STRUCTURE, DYNAMICS AND SUBSTRATE-INDUCED CONFORMATIONAL CHANGES OF *ESCHERICHIA COLI* MULTIDRUG TRANSPORTER (EMRE)

By

Sepan Tariq Hassan Amadi

Dissertation

Submitted to the Faculty of the

Graduate School of Vanderbilt University

in partial fulfillment of the requirements

for the degree of

DOCTOR OF PHILOSOPHY

in

Molecular Physiology and Biophysics

August, 2010

Nashville, Tennessee

Approved:

Albert Beth

Tony Weil

Phoebe Stewart

Charles Cobb

Borden Lacy

I dedicate this work to my parents, Professor Tariq Amadi and Associate Professor Faiza Armaghani, my sister, Lezan Amadi, and my husband Khaldoon Al-Naimi.

Their sacrifice, love, and support

is beyond anything I can imagine.

ACKNOWLEDGEMENTS

I could not have done this work without the help of my advisor, Prof. Hassane Mchaourab. I wish to express my deepest gratitude to him for his patience, encouragement, and his support all thorough my graduate study. His enthusiasm and dedication to Science has inspired me and taught me to always ask questions and strive for perfection.

I also want to thank the members of my examination committee: Prof. Albert Beth, Research Associate Prof. Charles Cobb, Assistant Prof. Borden Lacy, Prof. Phoebe Stewart, and Prof. Tony Weil, for their helpful discussions to my research. Their expertise in their field has provided me with an abundance of help for the thesis work.

I want to also thank members of Prof. Mchaourab's laboratory. Research Assistant Prof. Hanane Koteiche was the first person who showed me all the techniques in the lab. The project that I pursued for my PhD was a continuum of her work. Sanjay Mishra has helped me with sample preparation and a large portion of the fluorescence binding assay. Without his help I could not have completed the project in this time frame. I also want to thank all the graduate students, who have made each day in the lab exciting and full of surprises. Also, I want to thank the post-doctorates, and research assistants who have helped me along the way.

TABLE OF CONTENTS

LIST OF TABLES

LIST OF FIGURES

CHAPTER V

CHAPTER VI

CHAPTER VII

CHAPTER VIII

CHAPTER IX

LIST OF ABBREVIATIONS

Abbreviations	Description
ATP	Adenosine triphosphate
β-DDM	Dodecyl-β-D-maltoside
Bmr	*Bacillus subtilis* multidrug resistance regulator
Bpe-EmrE	Ethidium bromide resistance from *Brodetella pertussis*
BRC	C-terminal domain of *Bacillus subtillis* multidrug regulator
CCCP	Carbonyl cyanide m-cholorpheylhydrazone
CFP	Cerulean fluorescent protein
Cryo-EM	Cryogenic electron microscopy
DAT	dopamine transporter
DEER	Double electron-electron resonance
DQC	Double quantum coherence
DTT	Dithiotheritol
EmrE	Ethidium multidrug resistance from *Escherichia coli*
EPR	Electron paramagnetic resonance
GFP	Green fluorescent protein
HEPES	(4-(2-Hydroxyethyl)piperazine-1-ethanesulfonic acid)
Hsmr	*Halobacterium salinarum* multidrug resistance
IAP	porxyl-iodo acetamide
K+R bias	Lysine + Arginine bias
LPS	Lipopolysaccharide
MATE	Multidrug and toxic extrusion family
MDR	Multidrug resistance
MFS	Major facilitator superfamily
MRSA	Methicillin-resistance *Staphylococcus aureus*
MSL	Proxyl-maleimide spin label
MTSSL	methanethiosulfonate spin label
Mtu-SMR	*Myobacterium tuberculosis* small multidrug resistance protein
MvrC	Methyl viologen resistance from *Escherichia coli*

NBD	Nucleotide binding domain
NG	Nonyl-β-D-glucoside
NiEDDA	Nickel (II) ethylenediamine diacetate
OG	Octyl- β-D-glucoside
Pau-EmrE	Ethidium bromide resistance from *Pseudomonas aeruginosa*
PE	Phosphotidylethanolamine
P-gp	Phosphate glycoprotein
PhoA	Alkaline phosphatase
PMF	Proton motive force
PMSF	Phenylmethylsulfonyl fluoride
QAC	Quartenary Ammonium Compounds
RND	Resistance-nodulation-division superfamily
Sau-SMR	*Staphylococcus aureus* small multidrug resistance protein
SDSL	Site-directed spin labeling
SEC	Size exclusion chromatography
SERT	serotonin transporter
SMP	Small multidrug pump
SMR	Small multidrug resistance
Smr	*Staphylococcus aurius* multidrug resistance protein
SUG	Supressor of groEL
TMD	Transmembrane domain
TMS	Transmembrane segment
TPP^+	Tetraphenylphosphonium ion
VMAT	vesicular monamine transporter

CHAPTER I

INTRODUCTION

Multidrug Resistance

Living cells have long had machineries that protect them against toxic compounds present in the natural environment. The ability of some cells to gain resistance to new drugs is known as multidrug resistance. In 1928, an antimicrobial drug, penicillin was first discovered. This drug was highly effective against a wide variety of harmful micro-organisms (Fleming, 1980). Two decades later, penicillin resistance *Staphylococcus aureus* was discovered (Abraham & Chain, 1988).

For decades, pathogenic bacteria have been successfully kept in check by the use of various antibiotics. During the 1980s and 1990s infectious diseases such as tuberculosis reemerged, causing a serious public health problem. Alarming increases in antibiotic resistant bacteria were documented, including *Methicillin*-resistant S*taphylococcus aureus* (MRSA) from gram-positive bacteria as well as other dangerous bacteria such as *Acinetobacter baumanii*, *Enterococcus faecium*, *Klebsiella pneumoniae*, *Pseudomonas aeurginosa* and *Enterobacter* species (Taubes, 2008).

The problem is not restricted to antimicrobials, since 40% of human cancer tumors develop resistance to chemotherapeutic drugs. To successfully fight the increasing

numbers of drug resistant bacteria and tumor cells, extensive knowledge of the molecular mechanism of drug resistance is required.

Mechanisms of Resistance

Microbes have both intrinsic (natural) and acquired resistance to antimicrobials. Intrinsic resistance has been associated with the presence of an outer membrane barrier in gram-negative bacteria. The outer membrane decreases the rate of transmembrane diffusion of lipophilic solutes by narrowing its porin and lowering the fluidity of the lipopolysaccharide leaflet. However, equilibration across the barrier is achieved very rapidly (Nikaido, 1985, 1989). Therefore, additional mechanisms are needed to explain the level of intrinsic resistance. The second type of resistance is known as acquired resistance. Bacteria are susceptible to antibacterial agents, and undergo changes either by chromosome mutation or by passing their genes that encodes for resistance from one bacterium to another very rapidly. Strains emerged that are less susceptible or not at all susceptible to antibacterial drugs (Silver & Phung, 1996).

There are four primary mechanisms that give rise to multidrug resistance in bacteria, they include: (1) drug modification by enzymes of the targeted cell; (2) alteration of the cellular target through mutation or post-translational modification; (3) increased cell wall and outer membrane impermeability to drugs, that can be amplified by the loss of one or more porins; and (4) active efflux of drugs by membrane-bound multidrug efflux transporters.

Drugs can be hydrolyzed before reaching their targets, such as β-lactam antibiotics (penicillins and cephalosporins) that are hydrolyzed by bacterial β-lactamase

(Nikaido & Normark, 1987). This enzyme family expands its substrate range by a series of point mutations at different sites within the gene, causing a change in the interaction between the enzyme and its substrate (Jacoby & Carreras, 1990). In turn, the cycle of natural protein engineering that occurs in β-lactamase in response to changing antibiotics provides an obstacle in designing new and improved drugs against resistant bacteria. It has also been shown that resistance to a few antibiotics occurs by the acquisition of a gene encoding a new target enzyme that has much lower affinity for the antibiotics than the normal enzyme. This type of mechanism is known as target alteration (Maxwell, 1992).

Another mechanism of resistance depends on the malfunction in the transport of drugs, which depends on both the lipophilicity and the structure of the cell membrane (Hayes & Wolf, 1990). Thus, the permeability of drugs depends on the physiochemical properties of the membrane. It has been shown that hydrophobic antibiotics have a large effect on gram-positive bacteria compared to gram-negative bacteria due to a decrease in the diffusion rate of drugs across the outer membrane of gram-negative bacteria. This is attributed to the asymmetric structure of its lipid bilayer, where the outer and inner leaflets are comprised of lipopolysaccharide (LPS) and glycerophopholipids, respectively. The LPS layer its less fluidity and rigidity is thought to contribute to the ability of the outer membrane to exclude many hydrophobic antibiotics (Seydel, Labischinski, Kastowsky, & Brandenburg, 1993). Also, porin proteins have negatively and positively charged side chains at the lower and upper rim of the pore eyelet, which give rise to a transverse electric field. The electric field is suggested to separate polar and

non-polar solutes (Schulz, 1993; Weiss & Schulz, 1992). Consequently, the transverse field facilitates the permeation of hydrophilic compounds but expels hydrophobic ones.

The fourth mechanism is the active efflux of drugs by membrane-bound multidrug transporters (Figure 1). These transporters or proteins are present in all organisms. In bacteria, their genes are located on the chromosome, or transmissible genetic elements, such as plasmids that can confer an increase in resistance to antibiotics. Thus, the proteins that can transport several compounds are associated with multidrug resistance (MDR).

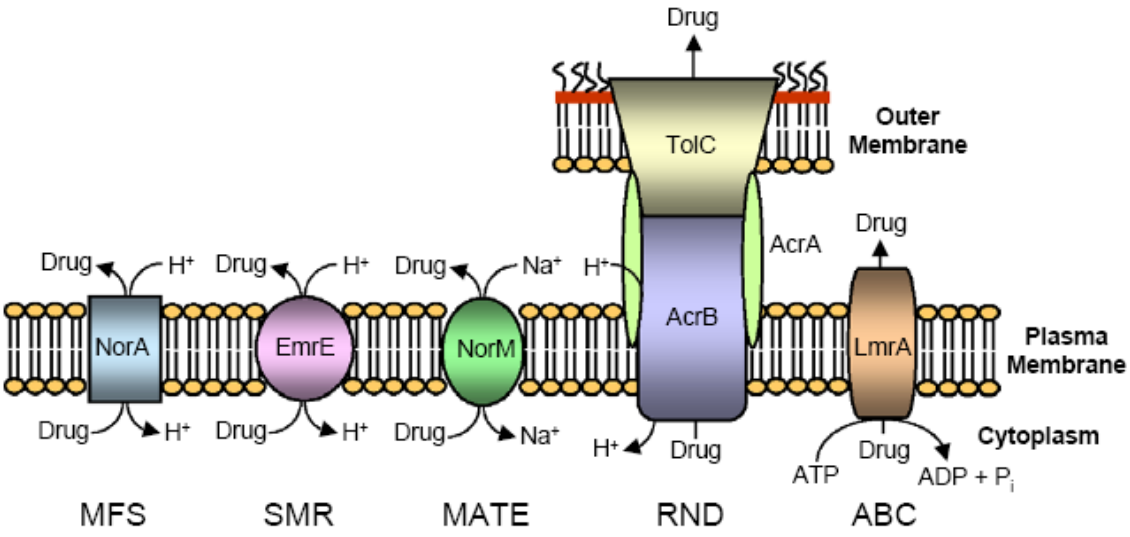

Figure 1: Schematic illustration of the main types of bacterial drug efflux pumps. Illustrated starting from the left, are: *Staphylococcus aureus* NorA, a member of the MFS superfamily; *Escherichia coli* EmrE, a member of the SMR superfamily; *Vibrio parahaemolyticus* NorM, a member of the MATE superfamily; *Escherichia coli* AcrAB-TolC, a member of the RND superfamily; and *Lactococcus lactis* LmrA, a member of the ABC superfamily (Kumar & Schweizer, 2005).

Multidrug Resistance Family

Multidrug transporters are divided into two major classes depending on their energy source for drug efflux. ATP-binding cassette (ABC) multidrug transporters use ATP hydrolysis to extrude drugs out of the cell while secondary multidrug transporters utilize electrochemical gradients of protons or sodium ions to drive the extrusion of drugs from the cell.

The functional unit of an ABC transporter contains two transmembrane domains (TMD) and two nucleotide ATP binding domains (NBD). The TMD's and NBD's can be expressed in a variety of arrangements. The four domains can be fused in a single polypeptide such as for P-glycoprotein (P-gp) (Aller et al., 2009) or can be expressed as half transporter with one TMD and one NBD. Each half dimerizes in order to have a functional transporter such as LmrA from *Lactococcus lactis* (Federici et al., 2007), MsbA from *E.coli* (Ward, Reyes, Yu, Roth, & Chang, 2007), and Sav1866 from *Staphylococcus aureus* (Dawson & Locher, 2006).

Dano was the first to suggest that the decrease in drug efficacy in multidrug resistance tumor cells is through active extrusion (Dano, 1973). Later, it was shown that the decrease in intracellular drug concentration is associated with the presence of a cell surface glycoprotein, known as P-glycoprotein (P-gp) (Juliano & Ling, 1976). It was recognized that Pgp is an ABC transporter protein that functions as an efflux pump (C. J. Chen et al., 1986). Diverse substrates are translocated by ABC transporters, ranging from chemotherapeutic drugs to naturally occurring chemical and biological compounds.

Most bacterial multidrug efflux systems are sensitive to agents that dissipate the proton motive force (PMF), triggering the expulsion of toxic compounds from the cells in

a coupled exchange with protons. During metabolism, the bacterial cell extrudes protons to the exterior. The generation of ATP and flagella movement are linked to solute transport via the bacterial cytoplasmic membrane. The combined potential, concentration or osmotic effect of the proton and its electropositivity, contribute to the proton motive force (PMF) (McDonnell & Russell, 1999).

PMF is composed of a chemical proton gradient (ΔpH, inside alkaline) and an electrical potential (Δψ, inside negative). In order to explore the energy characteristics of secondary multidrug transporters, experimental studies used ionophores which can selectively dissipate ΔpH and Δψ (Ng et al., 1994). These experiments provide insights into the drug/proton ratio governing the export process.

Secondary multidrug transporters are subdivided into four distinct families. The families include the major facilitator superfamily (MFS); the resistance nodulation-division-family (RND); the multidrug and toxic extrusion family (MATE); and the small multidrug resistance family (SMR).

The major facilitator superfamily is the largest and the most functionally diverse of the secondary multidrug transporters. Membrane proteins of this family are made of 12 or 14 transmembrane segments (TMS). An example is EmrD from *E.coli* that is involved in the shock adaptive response. Expression of EmrD protects the cell against uncouplers such as CCCP (carbonyl cyanide m-chlorophenylhydrazone), which is a protonophore that inhibits the PMF and in turn arrests the growth of *E.coli* (Naroditskaya, Schlosser, Fang, & Lewis, 1993). EmrD is homologous to two other MFS multidrug transporters; LmrP from *Lactococcus lactis* (Mazurkiewicz, Driessen, & Konings, 2004) and MdfA from *E.coli* (Adler & Bibi, 2005).

The most intensively studied member of the resistance-nodulation-division protein family is AcrB from *E.coli* (Zgurskaya & Nikaido, 1999). The functional AcrB transporter is a trimer, consisting of AcrA that has a role in membrane fusion and TolC which is a pore-like molecule that spans the outer membrane (Koronakis, Sharff, Koronakis, Luisi, & Hughes, 2000). AcrB translocates drugs into the TolC pore through which they cross both the periplasm and outer membrane. Many antibiotic targets are located in the periplasmic space. Therefore, to confer reistance against a broad spectrum of antibiotics, active transport must not only pump them out of the cytoplasm but also across the outer membrane of gram-negative bacteria.

The most recently identified secondary multidrug transporter family is MATE. The MATE family of transporters extrudes various drugs, especially cationic ones, through electroneutral exchange with protons. The first identified multidrug transporter of this family is from *Vibrio parahaemolyticus*, and denoted NorM (Morita et al., 1998).

In eukaryotes, a transporter of the MATE family known as MATE1 is responsible for the extrusion of organic cations, such as cationic drugs, some vitamins, and endogenous compounds such as choline and dopamine, thus is regarded as a multidrug or polyspecific exporter (Otsuka et al., 2005). When drugs reach the target cells upon absorption, they are then excreted from the kidney and liver (Pritchard & Miller, 1993). During this process, the drugs may pass through several cells using different transporter pathways (Inui, Masuda, & Saito, 2000; Tamai et al., 1999; Tsuji & Tamai, 1999; Ullrich, 1994). Final extrusion occurs at the brush border membranes of renal tubule cells and bile canaliculi.

Finally, the smallest of the secondary multidrug resistance family is the small multidrug resistance (SMR) (Chung & Saier, 2001). Members of the SMR family are distinct from the other transporter families in demonstrating transport of lipophilic compounds, primarily quaternary ammonium compounds (QAC) and a variety of antibiotics (Heir, Sundheim, & Holck, 1999). The structural model is composed of a tightly packed four-helix bundle (Arkin, Russ, Lebendiker, & Schuldiner, 1996; Edwards & Turner, 1998; Paulsen, Brown, & Skurray, 1996). SMR proteins demonstrate drug efflux via electrochemical proton gradient analogous to MFS. Therefore, SMR proteins have been classified as a proton-dependent multidrug efflux system (Littlejohn et al., 1992). One member of the SMR family is EmrE from *Escherichia coli*.

Regulation of Multidrug Transporters

All bacterial MDR transporters identified to date whose expression is under the control of a transcriptional regulatory protein are PMF-dependent exporters (Paulsen et al., 1996). Most of the MDR family of transporters belonging to the MFS and RND superfamilies are controlled by transcriptional regulatory proteins (see Table 1), such as the MDR gene regulator, BmrR (multidrug resistant regulator of *B subtilis*) (Ahmed, Borsch, Taylor, Vazquez-Laslop, & Neyfakh, 1994).

Multidrug transporter(s)	Regulator	Type
Blt	BltR	Activator
Blt, Bmr	Mta	Global activator
Bmr	BmrR	Activator
EmrB	EmrR	Repressor
QacA	QacR	Repressor
AcrB	MarA	Global activator
AcrB	AcrR	Repressor
AmrB	AmrR	Repressor
MexB	MexR	Repressor
MexD	NfxB	Repressor
MexF	MexT	Activator
MexZ	MexX	Repressor
MtrD	MtrA	Activator
MtrD	MtrR	Repressor

Table 1: **Reported transcriptional regulators that control the expression of multidrug transporters in bacteria.** Adapted from (Putman, Van Veen, Degener, & Konings, 2000).

The expression of *Staphylococcus aureus* multidrug efflux gene qacA is regulated by the transcribed repressor protein QacR (Grkovic, Brown, Roberts, Paulsen, & Skurray, 1998). However, members of the SMR family do not have their synthesis controlled at the transcriptional level. This could be a reflection of unknown physiological roles for the unregulated pumps in normal cellular metabolism (Grkovic, Brown, & Skurray, 2002). The small but continuous supply of these transporters can easily be controlled, either by low level production of the mRNA or by high turnover rates of the mRNA and/or the transport protein, without any additional regulatory controls. Understanding the

regulation of multidrug transporters may have an important role in the drug discovery process and for the development of combination therapies. Inhibition of these transporters may be achieved through targeting the regulatory networks that control expression.

Phylogeny of the SMR Family

SMR proteins are not all drug effluxers. This characteristic is a result of divergence of this family into three classes: small multidrug pumps (SMP) and suppressor of groEL mutation proteins (SUG) which is based in their conferred phenotype (Greener, Govezensky, & Zamir, 1993). The paired SMR (PSMR) protein group is a distinct group of SMR homologues. This group has been both identified and characterized based upon multidrug resistance and substrate transport. These SMR homologues are unique compared to the other subclass as they require co-expression of two separate SMR genes within the host bacterium. This group includes *Escherichia coli* YdgE and YdgF (Ninio, Rotem, & Schuldiner, 2001), *Bacillus subtillis* EbrA and EbrB (Kikukawa, Nara, Araiso, Miyauchi, & Kamo, 2006) YKKC and YKKD, and YvaE, YvdR and YvdS (Jack, Storms, Tchieu, Paulsen, & Saier, 2000)

In all cases the genes of members from each subclass have been identified on a variety of plasmids and transposable elements that provide high level resistance to a wide range of antibiotics such as β-lactams (Sidhu, Langsrud, & Holck, 2001), cephalosporin (Miriagou, Tassios, Legakis, & Tzouvelekis, 2004), dihydrofolate inhibitors (Burnside & Groot Obbink, 1996) as well as other aminoglycosides (Jeljaszewicz, Mlynarczyk, & Mlynarczyk, 2000). The frequency of their occurrence with other drug resistance genes strongly suggests that there is a tight genetic link between antibiotics and SMR resistance

genes (Sidhu et al., 2001). The co-selection of antibiotic and antiseptic resistance genes correlates with the increased usage of both antiseptics and antibiotics in clinical environments. Therefore, the spread of SMR homologues make them a critical protein to characterize and important candidates for transport mechanism studies.

SMP subclass proteins are primarily characterized in gram-negative (EmrE from *Escherichia coli*) and gram-positive (Smr from *Staphylococcus aureus*) bacteria as well as Archaea (Hsmr from *Halobacterium salinarum*) from the expression of a single gene. EmrE, a member of the SMR family, confers resistance to MvrC and Ebr (referred to as methyl viologen resistance protein, MvrC, and ethidium bromide resistance protein, Ebr) (Morimyo, Hongo, Hama-Inaba, & Machida, 1992; Purewal, 1991). Other characterized proteobacterial SMP proteins include *Pseudomonas aeruginosa* Pau-EmrE (γ-proteobacteria) (Li, Poole, & Nikaido, 2003) and *Brodetella pertussis* Bpe-EmrE (β-proteobacteria) (Ninio et al., 2001). Pau-EmrE and Bpe-EmrE share 45% and 50% identity with EmrE, respectively, and are fairly similar in protein length (107-110 amino acids).

The first SMR family member, Sau-SMR, was identified and characterized in the gram-positive bacteria, *Staphylococcus aureus* (Grinius & Goldberg, 1994). Mtu-SMR from *Mycobacterium tuberculosis* is the only class of SMR protein that has similar functionality to Sau-SMR. These two proteins have a substantial sequence identity of 41% and 38%, respectively, to EmrE.

EmrE: A Small Multidrug Transporter

Escherichia coli utilizes EmrE expression as a means of protection against toxic compounds such as ethidium, an intercalating dye (Lambert & Le Pecq, 1984). The EmrE gene was first identified and cloned on the basis of its ability to confer resistance to ethidium (Purewal, 1991; Purewal, Jones, & Midgley, 1990). The same gene under different pseudonym, mvrC was identified by Morimyo and colleagues in 1992 (Morimyo et al., 1992). The mvrC gene was cloned on the basis of its resistance to methyl viologen.

Subunit c of F_1F_0 ATP synthases was utilized for determining the nature of the energy required for extrusion of drugs by EmrE (Fillingame, 1992). In *E.coli* the F_1F_0 ATP synthases utilizes the energy of a transmembrane electrochemical proton gradient to catalyze ATP synthesis during oxidative phosphorylation. Therefore, to identify the driving force of EmrE, the *unc* operon strain deletion was used. It was then possible to manipulate independently both the proton electrochemical gradient (Δ_{H+}) and ATP. Effects of different agents on ethidium entry into the cell was tested (Yerushalmi, Lebendiker, & Schuldiner, 1995). Agents that inhibit Δ_{H+} but did not affect ATP levels in this strain induced ethidium entry into the cell, suggesting a failure of the extrusion machinery. In contrast, inhibitors that decrease ATP levels without any alteration on Δ_{H+} had no effect on ethidium uptake either. The experimental work strongly suggests that EmrE functions as a proton/substrate antiporter. This antiporter mechanism utilizes the electrochemical gradient of protons (Δ_{H+}) generated by a bacterial primary pump to extrude toxic cations and reduce their concentration in the cytoplasm (Yerushalmi et al., 1995).

Substrate Recognition

The SMR protein family has been shown to exhibit a wide range of drug binding affinities with nanomolar to micromolar K_D values. These values are associated with the sequence variation in the SMR family of proteins, some of which are found in human pathogens such as *Myobacterium tuberculosis* (TBsmr), *Pseudomonas aeruginosa* (PAsmr), and other pathogens such as *Bordetella pertussis* (BPsmr). For example, tetraphenylphosphonium (TPP^+) binding affinity among the SMR proteins ranges from either low binding to TBsmr (41% homologous to EmrE), and PAsmr (45% homologous to EmrE) to intermediate binding to BPsmr (58% homology to EmrE) (Ninio et al., 2001). The difference in the drug binding affinity of SMR homologues suggests a unique profile that is adapted to the activity of their host.

Grinius and Goldberg were the first to demonstrate that the efflux of substrate by SMR is energy dependent and is driven by a proton motive force (PMF) (Grinius & Goldberg, 1994; Littlejohn et al., 1992). In their experiments, Smr from *Staphylococcus aureus* was reconstituted into proteoliposomes and TPP^+ efflux was demonstrated via an electrochemical gradient. The result was confirmed for EmrE under similar experimental conditions (Yerushalmi et al., 1995). The nature of the compound affects the energy requirements for transport as observed in EmrE. Transport of monovalent lipophilic cations, such as TPP^+, appears to be electrogenic. In contrast, transport of divalent lipophilic cations such as methyl viologen (MV) is electroneutral (Rotem & Schuldiner, 2004). These findings suggest that SMR proteins depend on the energetic state of the cell and the proton gradient across the membrane. In addition, it offers important implications for the differences in drug resistance by host cells harbouring SMR proteins.

The Substrate Binding Site

The role of carboxylic acid residues in substrate recognition has been documented for many transporters that are not related to multidrug resistance, such as vesicular monamine transporters (VMAT's) (Merickel, Rosandich, Peter, & Edwards, 1995), serotonin transporters (SERT) (Kitayama et al., 1992), and plasma membrane dopamine transporters (DAT) (Barker, Moore, Rakhshan, & Blakely, 1999).

The bacterial multidrug transporter, lactose permease, is one of the best characterized coupled ion transporters. It has six residues, three of which are acidic amino acids that are important for active transport. E126 and R144 are involved in substrate binding and specificity (Frillingos & Kaback, 1996).

In addition, closely related multidrug efflux pump from the bacterial pathogen *Staphylococcus aureus*, QacA and QacB, were shown to have different substrate specificities due to a single amino acid substitution at position 323 (Paulsen et al., 1996). The acidic residue aspartate is present in QacA and is essential for substrate recognition (Mitchell, Brown, & Skurray, 1998; Paulsen et al., 1996). Mutating D323 to another acidic residue had no effect in the resistant phenotype while mutating to an alanine residue (similar to the residue position in QacB) reduces the resistance to divalent cations.

The *Bacillus subtillis* protein BmrR controls the transcription of the multidrug transporter gene bmr. It has been shown that the C-terminal domain of BmrR (BRC) has no sequence homology to other proteins of the same MerR family of transcription regulators. The apo-state of BRC reveals no pocket or cavity that would appear to serve as an obvious drug-binding site. However, the hydrophobic pocket of the protein revealed

a completely buried acidic residue, glutamate 134 (Glu134) (Figure 2). This residue is considered energetically unfavourable, yet in the structure the glutamic acid is hydrogen bonded to Tyrosine 33 (Tyr33) and Tyrosine 68 (Tyr68). This arrangement of amino acids makes it an attractive binding site for aromatic/hydrophobic cationic substrates, such as TPP^+ (Zheleznova, Markham, Neyfakh, & Brennan, 1999).

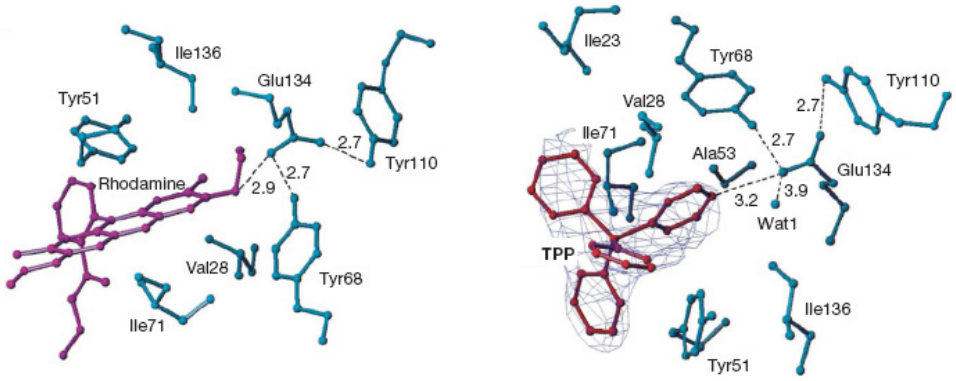

Figure 2: Drug binding site in BmrR. Residues that are involved in drug binding are shown in ball-and-stick configuration. Left: structure based model with bound rhodamine (purple ball and sticks). The key residue Glu 134 is shown. Right: structure based model with bound TPP^+ (in red) together with bound water molecule (Wat 1). Dashed lines are hydrogen bonds (Zheleznova et al., 1999).

EmrE contains eight charged residues, seven of them located in the hydrophilic loops and only one of them is a membrane-embedded charged residue, glutamate14 (Glu14 or E14), which is conserved in more than 200 homologous proteins in bacteria and archaea (Ninio et al., 2001; Sharoni, Steiner-Mordoch, & Schuldiner, 2005) are shown in Figure 3. Further characterization of the mutant showed that the replacement of E14 with a cysteine (Cys), glutamine (Gln), histidine (His), tyrosine (Tyr), or aspartic acid (Asp) has a large effect on the phenotype (Grinius & Goldberg, 1994; Yerushalmi &

Schuldiner, 2000a). Studies have also shown that out of the three acidic residues, only E14 (located in TM1) is important for drug transport activity (Muth & Schuldiner, 2000; Yerushalmi & Schuldiner, 2000b). E14 is thought to be involved in direct binding of both substrate and proton (Gutman, Steiner-Mordoch, & Schuldiner, 2003).

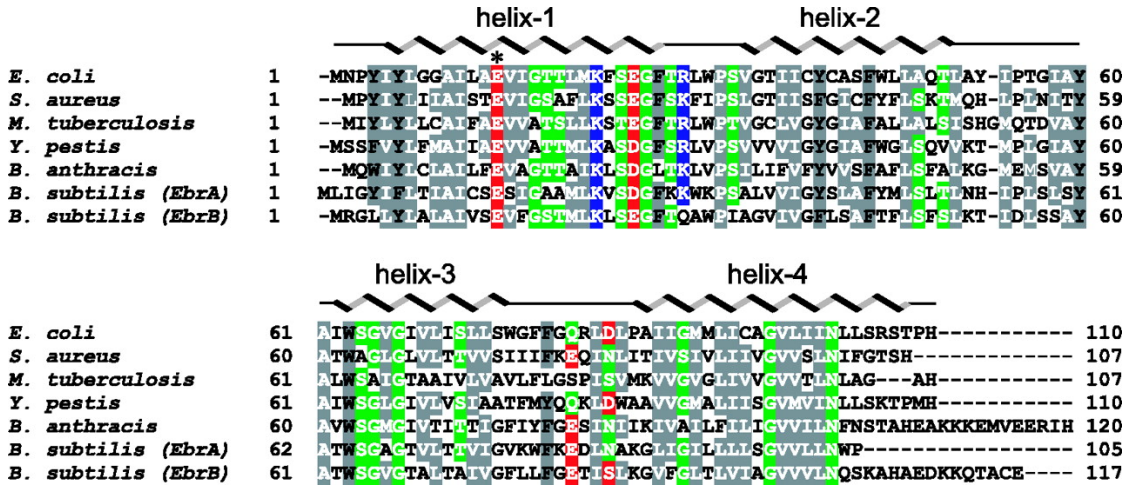

Figure 3: Amino acid sequence alignment of EmrE from *E.coli* shown with other homolog's from human pathogens. Conserved residues are coloured according to their acidic (red), basic (blue), polar (green), or hydrophobic (grey) character (Ma & Chang, 2004).

Evidence has shown that residues located in the vicinity of E14 in TM1 are part of the substrate-binding domain (Gutman et al., 2003). Further work has also shown that mutation of E14 to a cysteine results in an inactive protein while a mutation to an aspartate was able to bind substrate and transport it down its concentration gradient. The protein was, however, impaired in its ability to couple substrate flux to the proton gradient (Yerushalmi, Mordoch, & Schuldiner, 2001). This indicates that E14 plays a central role in both substrate and proton binding. It was shown that substrate binding to

wild type EmrE increases dramatically with increasing pH, suggesting that deprotonation of E14 is essential (Muth & Schuldiner, 2000; Yerushalmi et al., 2001). Furthermore, it was observed in detergent solubilised EmrE that substrate binding induces proton release (Soskine, Adam, & Schuldiner, 2004).

Several studies have demonstrated the equivalence of E14 in the dimer (Ninio, Elbaz, & Schuldiner, 2004; Weinglass et al., 2005) where both E14's are in similar hydrophobic environments. Tetraphenylphosphonium (TPP^+) is a substrate that binds with high affinity to EmrE. TPP^+ was shown to reduce chemical modification of E14 by more than 80%. The data suggests that E14 residues are in the functional unit of EmrE. The functional unit is in close proximity to the binding site (Ninio et al., 2004). This work was also supported by previous work in our lab that showed that a population of spin labels at position 14 from both monomers are in close proximity (Koteiche, Reeves, & McHaourab, 2003).

Biochemical evidence has shown that the E14 residue in TM1 has an unusually high pKa of 8.3-8.5 (Soskine et al., 2004) while the pKa of a glutamic acid residue in solution is 4.0. The large increase in pKa could be due to a decrease in the dielectric environment of E14 in EmrE. Furthermore, the dissociation constant (K_D) of the substrate is also sensitive to pH. An increase in pH from 6.2 to 8.8 results in a corresponding 200 fold decrease in K_D (Adam, Tayer, Rotem, Schreiber, & Schuldiner, 2007). The replacement E14 with aspartic acid results in a decrease in the pKa of the carboxyl and generates a protein that is independent of pH when substrate is bound. Consequently, at physiological pH the carboxyl is deprotonated. The protein is able to bind substrate but it cannot couple the substrate to the proton gradient (Soskine et al., 2004; Yerushalmi &

Schuldiner, 2000a). Overall, the single mutation of E14D transforms an antiporter mechanism in EmrE to a uniporter.

The findings presented above are summarized in Figure 4, which suggests a reaction path where the protonated EmrE (EH_2) plus the substrate (S) dissociates from E + $2H^+$ + S, and it rapidly forms ES + $2H^+$. That is, the binding of either the substrate or the protons requires the dissociation of the other.

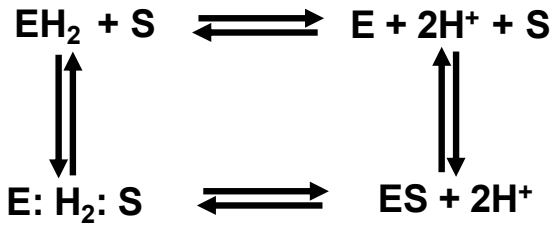

Figure 4: The substrate binding reaction cycle in EmrE. E, non protonated EmrE; EH_2, protonated EmrE; ES, substrate bound EmrE; E:H_2:S hypothetical ternary complex (Adam et al., 2007).

Structure Controversy

EmrE is an ion-coupled transporter. Although it is widely accepted that the monomer cannot transport drugs, the oligomeric state of EmrE has been controversial. The question was first addressed by direct measurements of substrate binding stoichiometry to the detergent solubilised EmrE. This resulted in high affinity of substrate binding in the nanomolar range, giving a ratio of EmrE:TPP^+ higher than two. The high ratio initially suggested that EmrE could be a trimer (Muth & Schuldiner, 2000). A possible explanation of the overestimation of the ratio of EmrE:TPP^+ was because the measurements made were at a very low concentration of EmrE that may have dissociated the dimer (Tate, Ubarretxena-Belandia, & Baldwin, 2003). Binding assays using higher

concentrations of EmrE *in vitro* confirmed a ratio of EmrE:TPP^+ of 2 (Elbaz, Tayer, Steinfels, Steiner-Mordoch, & Schuldiner, 2005; Tate et al., 2003). It is unclear if EmrE *in vivo* exists in a higher oligomeric state, but *in vitro* studies indicate the dimer is the basic functional unit.

A two-dimensional crystal of EmrE reconstituted in a lipid bilayer gave the first insight into the structure of the protein. The images of frozen hydrated crystals were collected by cryo-electron microscopy and a projection structure of EmrE was calculated to 7Å resolution (Tate, Kunji, Lebendiker, & Schuldiner, 2001). The structure from their projection map shows EmrE as a dimer comprised of highly tilted helices. They concluded that there was no obvious two-fold symmetry axis perpendicular to the membrane within the dimer, but there is a 2-fold axis in the plane of the membrane relating the two asymmetric structures to each other in the functional unit. The features of the electron density map were interpreted from a projection map of bacteriorhodopsin (bR) that has the same resolution as EmrE (Figure 5) (Grigorieff, Ceska, Downing, Baldwin, & Henderson, 1996).

In 2003 another EM model of substrate bound-EmrE was published (Tate et al., 2003). The data suggested that the substrate tetraphenylphosphonium (TPP^+) was bound at the monomer-monomer interface in the centre of the EmrE dimer. This binding caused a tilt in at least one transmembrane segment.

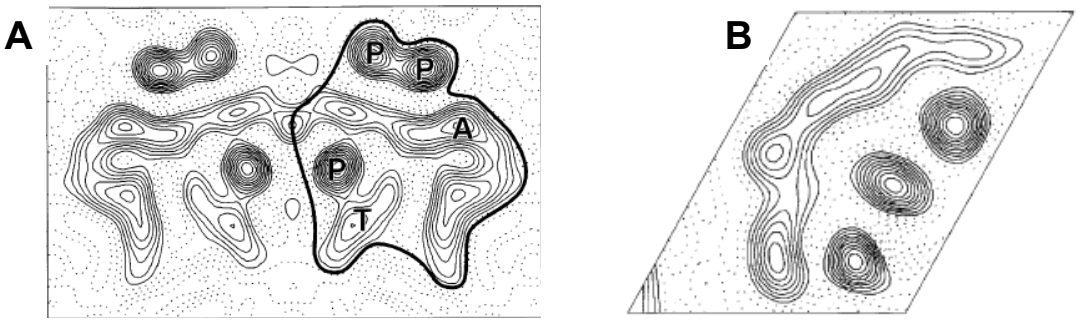

Figure 5: **Projection map of EmrE at 7 Å.** (A) A crystallographic dimer is shown from a projection map of EmrE at 7.0 Å resolution, with the asymmetric structure outlines. The asymmetric units are related by a 2-fold axis in the plane of the membrane, having different orientation in the membrane. P, an α-helix nearly perpendicular to the membrane plane; T, probably a single α-helix tilted with respect to the membrane normal; A, an arc of probably four tilted α-helix. (B) The projection map of bacteriorhodopsin at 7.0 Å resolution has been scaled exactly to EmrE, allowing a direct comparison of sizes (Tate et al., 2001).

In 2004 the high resolution X-ray structures of EmrE in the apo- and substrate bound TPP^+-state were published (Ma & Chang, 2004; Pornillos, Chen, Chen, & Chang, 2005). The crystal structure of EmrE in the apo-state was shown to be a tetrameric arrangement of two conformational heterodimers (Figure 6A). Helices 1, 2, and 3 from one subunit were rearranged in an approximately inverted orientation relative to the other monomer, forming a six-helix bundle with a hydrophobic core. Helix-4 from one subunit is nearly parallel to the membrane surface while the other is perpendicular (Ma & Chang, 2004). Subsequently, the crystal structure of EmrE in the presence of the substrate was published (Figure 6B) showing large structural differences from the apo-state. The substrate-bound state was shown to be homodimeric with substrate binding at the dimerization interface. Each of the subunits had opposite orientation in the membrane, forming an asymmetric antiparallel dimer (Pornillos et al., 2005).

(A) Apo-state

(B) Substrate-bound state

Figure 6: Retracted crystal structures of EmrE

(A) X-ray crystal structure of the apo-state EmrE at 3.7Å. Each heterodimer contains subunits with different conformation (shown in pink, black, blue and green). The residue Glu-14 is shown in red spheres. (B) X-ray crystal structure of the substrate-bound state at 3.8Å is composed of two subunits (subunit A in yellow and subunit B in green). The N and C-terminal of the two subunits are indicated, and one bound TPP (red).

The two crystal structures were later retracted in 2006. Prior to the retraction, the suggestion of an antiparallel topology of the monomers in a homodimeric membrane protein attracted widespread interest because of the implications regarding insertion and evolution of ion-coupled transporters.

The antiparallel rearrangement of the monomers has been supported by a reinterpretation of previously published electron density maps of 2-D crystals of EmrE, where parts of the structure are related by quasi-symmetry (Ubarretxena-Belandia, Baldwin, Schuldiner, & Tate, 2003).

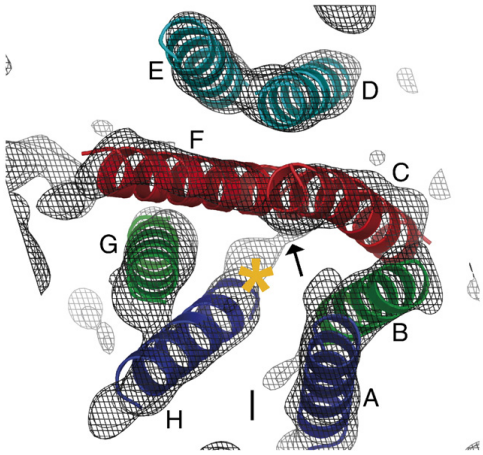

Figure 7: **The position of the α-helices of EmrE viewed perpendicular to the membrane plane.** The helices are labelled A-H. The grey mesh indicates electron density at 1.1σ. The arrow indicates the position where helices F and H are connected via what could be a rigid loop. The yellow asterisk mark the approximate in-plane position of the centre of the TPP^+ molecule (Fleishman et al., 2006).

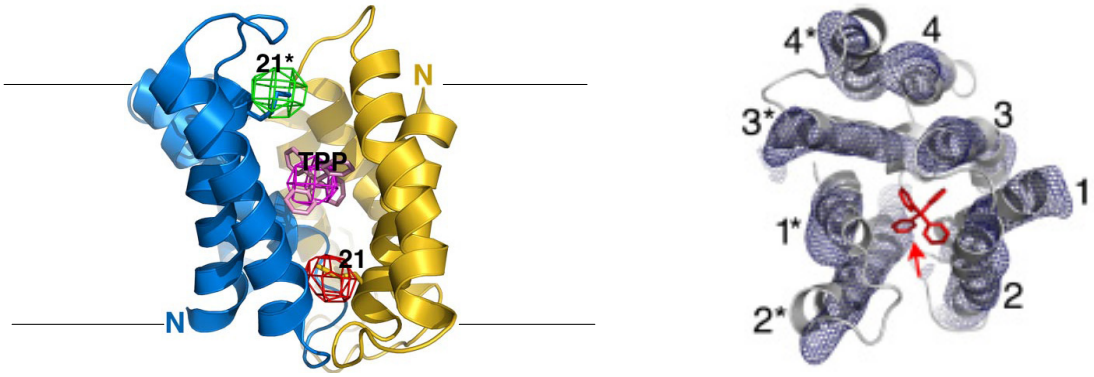

Figure 8: **EmrE binds TPP^+ as an antiparallel dimer.** Left panel is a front view of the EmrE transport in complex with TPP^+. The two monomers are shown in blue and yellow, and the bound TPP is pink. Anomalous Fourier density from SeMet (coloured red in one monomer and green in the other) markers in TM1 and the arsonium analogue of TPP (magenta). The N-termini of the monomers are labelled .Right panel is a stereo view ribbon representation of the EmrE-TPP x-ray structure docked into the EM density map. The TM helices are labelled, with the two monomers distinguished by asterisks. The bound TPP in the EM map is indicated by the red arrow (Y. J. Chen et al., 2007).

Using this symmetry relationship with sequence conservation data, transmembrane segments were assigned to the densities seen in the cryo-EM structure (Figure 7). In addition, after re-evaluating the crystal structure, in 2007 Chen and colleagues solved the corrected Cα model of the EmrE substrate bound crystal structure at a resolution of 3.8 Å suggesting an antiparallel homodimer (Figure 8) (Y. J. Chen et al., 2007). The structure showed a pseudo two-fold rotational axis running along the dimer interface and parallel to the membrane plane. The new crystal structure produced a Cα model that was similar to the Cα EM model derived from the 2-D crystals (Y. J. Chen et al., 2007). Figure 8 (right panel) shows the superimposed EM model with the X-ray structure of EmrE, where a 6 helix bundle surrounds the substrate (TPP^+) and two helices are further from the substrate binding site. The crystal structure was obtained by solubilizing the protein in Nonyl-β-D-Glucoside (NG), whereas the EM structure was obtained in lipids (dimyristoylphosphatidylcholine). Evidence has shown that detergents such as Octyl- and Nonyl-β-D-Glucoside cause a 10-30 fold decrease in the affinity of the substrate and a decrease in the number of binding sites (Soskine, Mark, Tayer, Mizrachi, & Schuldiner, 2006). It was also shown that both detergents when used in the preparation of the protein may have a large effect on the oligomeric state of EmrE causing an increase in its monomeric fraction. This suggests that the antiparallel orientation may reflect the arrangement of the monomers in the crystal (Schuldiner, 2007b; Soskine et al., 2006).

Topology of EmrE

In membrane proteins, the topology describes which segments of the polypeptide chain form TM helices and their orientation relative to the membrane. Not all membrane proteins have TM helices spanning the full length of the lipid bilayer, such as the Chloride channel ClC, and the Bovine Ca^{2+}- ATPase (Dutzler, Campbell, Cadene, Chait, & MacKinnon, 2002; Sorensen et al., 2004). A membrane protein of two subunits can either, theoretically, adopt a parallel or antiparallel orientation. A parallel orientation is when the N- and C-termini of both subunits in the dimer are on the same side of the membrane (i.e. adopt a single topology) such as LacY (Abramson et al., 2003), AcrB (Seeger et al., 2006). On the other hand, for an antiparallel orientation, the N- and C-termini of each subunit are on opposite sides of the membrane and thus adopt a dual topology, where the dimers are a mixture of both C_{in} and C_{out} (Schuldiner, 2007a).

The retraction of the crystal structure of EmrE in 2006 led to a controversy regarding the topology of the two monomers. It has been suggested that EmrE is likely to be an antiparallel dual topology homodimer composed of N_{in}-C_{in} and N_{out}-C_{out} monomers (Butler, Ubarretxena-Belandia, Warne, & Tate, 2004; Fleishman et al., 2006; Rapp, Granseth, Seppala, & von Heijne, 2006; Ubarretxena-Belandia et al., 2003). Other data had suggested a parallel dimer made of N_{in}-C_{in} monomers (Ninio et al., 2004; Soskine et al., 2006). The topology of membrane proteins has been shown to be governed by the positive inside rule, where loops rich in lysine (K) and arginine (R) tend to orient towards the cytoplasmic side of the membrane (Heijne, 1986). Thus, the dual topology of EmrE was largely speculated due to the weak topological signal of the protein (weak K+R bias) of -2. The topology of EmrE remains unresolved. Therefore, determining the topology of

EmrE is essential not only to understand its function but also to learn how the protein has evolved. In this section the details of this controversy will be clarified.

Biochemical results of crosslinking studies were consistent with parallel topology of the two monomers (Soskine, Steiner-Mordoch, & Schuldiner, 2002). Additionally, a second crosslinking experiment that used a rigid bifunctional crosslinking agent was introduced to a specific site in TM4 at a distance of about 35 to 45 Å, a distance that is too long for crosslinking in an antiparallel structure. Regardless of the distance, crosslinking was observed as expected from a parallel topology (Soskine et al., 2006). The crosslinked monomers displayed identical substrate binding properties to the non-crosslinked species in detergent as well as reconstituted into proteoliposomes (Soskine et al., 2006).

Further investigations have supported the parallel rearrangement of the monomers. A combination of both *in vivo* and *in vitro* studies were carried out on a genetic fusion construct, connecting the C-terminal of one monomer to the N-terminal of the second monomer by a linker that is either too hydrophilic or too short such that it cannot be compatible with an antiparallel topology (Steiner-Mordoch et al., 2008). The tandem dimer was shown to confer resistance to ethidium. Moreover, the purified protein bound TPP^+ with high affinity. It was also shown through a negative dominance study that mixing the tandem dimer with an inactive mutant does not inhibit the activity of the tandem dimer. This evidence supports the tandem dimer is the functional unit.

Genetic work has also been performed to investigate the topology of membrane proteins. A comprehensive global analysis of the topology of a large fraction of the *E.coli* membrane proteins were investigated by von Heijne and collaborators (Daley et al.,

2005). In this study two topology reporters were used: alkaline phosphatase (PhoA) that can fold into an active conformation only when present in the periplasm, and green fluorescent protein (GFP) which can only become fluorescent when present in the cytoplasm. Therefore, the location of the C-termini of the membrane proteins can be determined by making a PhoA and a GFP fusion. A high PhoA/low GFP activity indicates a periplasmic location, while a low PhoA/high GFP activity indicates a cytoplasmic location. Consequently, the C-terminal location (C_{in}, C_{out}) was determined in this manner for 502 of the 665 cloned proteins. The C-terminal assignment for 69 out of 71 proteins agreed with previously published work. However, EmrE was vaguely assigned as C_{out}. The rationale behind this assignment was that the GFP fluorescence was higher than background as it was for about 30 other proteins (Daley et al., 2005). To further support the dual topology concept, mutational studies were performed showing that the topology of the EmrE fusion proteins in the membrane is sensitive to the distribution of positively charged residues (lysine and arginine) in the protein (Rapp, Seppala, Granseth, & von Heijne, 2007). Manipulating the positively charged residues forces the protein to have either C_{out} or C_{in} topology (Rapp et al., 2006; Rapp et al., 2007). The expression of EmrE (C_{in}) and EmrE (C_{out}) (having three mutations each), individually (in single or double copy) does not confer resistance to EtBr. On the other hand, co-expression of these inactive mutants restores the ethidium bromide resistance phenotype to the same level as observed with wild-type EmrE (Rapp et al., 2007). The conclusion of these results suggests the formation of a functional, antiparallel heterodimer.

A recent publication from our lab (McHaourab, Mishra, Koteiche, & Amadi, 2008) challenged the conclusion of von Heijne and colleagues (Rapp et al., 2007) that the only determinant of EmrE topology is the positive inside rule. Therefore, in this study the topology of EmrE was investigated by manipulating the (K+R) bias and using the reporter protein cerulean fluorescent protein-CFP (Malo et al., 2007) to show the orientation of the two monomers by observing the fluorescnece of CFP *in vitro*. Moreover, site directed mutagenesis and EPR spectroscopy were used to derive structural constraints to observe the packing of the two EmrE monomers. The results showed four important facts. First, manipulation of the (K+R) bias did not change the interface between the monomers of EmrE. Second, the oligomeric state of the C_{in} mutants was similar to the cysteine less-EmrE (WT*) consistent with maintaining the dimer structure. Third, GFP fluorescence is dependent on the efficient folding of the tagged protein (Pedelacq, Cabantous, Tran, Terwilliger, & Waldo, 2006). The difference in level of the fluorescence between mutants may reflect misfolding of the chimeras. Fourth, results from the in vivo study of ethidium bromide resistance and in vitro study of TPP^+ binding show that the mutant that forces EmrE into N_{in}-C_{in} orientation had measurable resistance to ethidium bromide and also binding to TPP^+, respectively. Overall, the results demonstrated that the K+R bias is not the only determinant of CFP fluorescence.

The conclusion of von Heijne and colleagues was based upon the fact that the membrane insertion efficiency of all mutants was similar (Rapp et al., 2007) even though a direct analysis of membrane insertion was not performed.

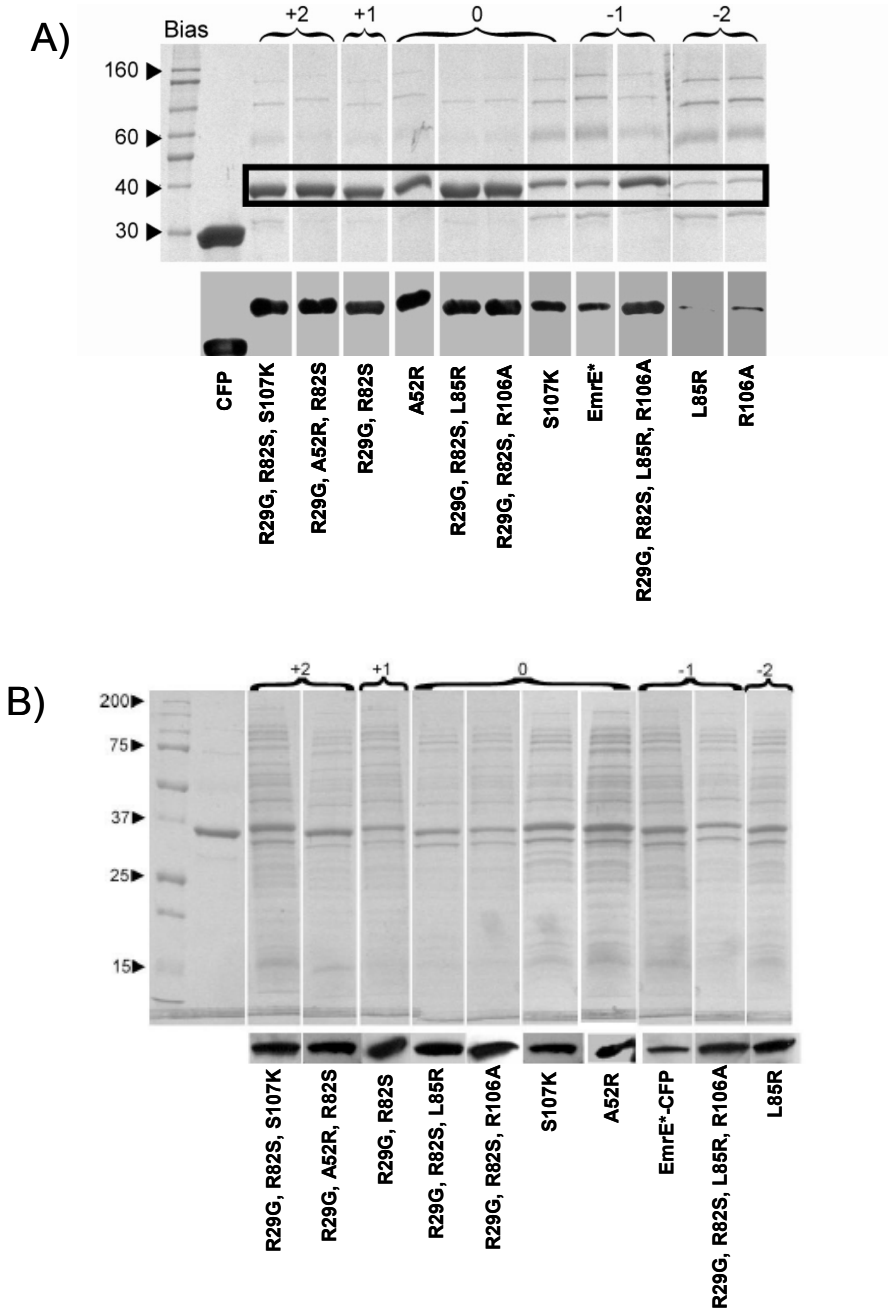

Figure 9: **SDS-PAGE and Western blot analysis of EmrE-CFP. A)** SDS-PAGE analysis of equal amounts of purified membrane inserted EmrE*-CFP shows the inconsistency in yield. Bottom panel is the Western blot analysis with antibodies against the C-terminal CFP. **B)** SDS-PAGE and Western blot analysis (bottom panel) of inclusion bodies pellets from 11 cultures. Lane 1 is purified EmrE*-CFP from the membrane fraction (McHaourab et al., 2008).

The highly fluorescent chimera reported by Rapp et al. was based on the R29G, a C_{in} mutation that induced more than 90% of the observed increase in GFP fluorescent (Rapp et al., 2006; Rapp et al., 2007), while the C_{out} mutants were based on L85R. However, the results in Figure 9A show that the nature of the substitution profoundly changes the level of insertion of the protein into the membrane, where some mutants partition into membrane fractions while others partition into inclusion bodies (Figure 9B). In addition, independent mutations having similar K+R biases had considerably different levels of CFP fluorescence, as well as an inverse effect relating temperature of expression with fluorescence, suggesting that thermodynamic stability is another contributing factor. Therefore, it was proposed that the favorable energetic of helix-helix interaction in the parallel dimer take priority over the unfavorable (K+R) bias in the near neutral region, leading to a native all C_{in} orientation. The study is also supported by other published work showing that membrane proteins are dependent on neighboring helices, the primary sequence, and interaction of helices with lipids (Bowie, 2004, 2005; Hessa et al., 2007; White & Wimley, 1999).

The evolutionary challenge of recognition and transport for a wide variety of substrates may have selected SMR heterodimers that originated from a gene duplication of more ancient homodimers. Therefore, after gene duplication a small number of mutations in the hydrophilic domains might be adequate to assume either parallel or antiparallel orientation of the monomers within the heterodimer (Schuldiner, 2007a). A protein with only a slightly modified sequence could extend the range of substrate specificity. Starting from the SMR heterodimers that can fuse to form larger proteins, the topology evolution of large proteins can be visualized.

The controversy regarding the interaction of the subunits in the SMR dimer, especially EmrE, and also its structure in detergent micelles, makes it an attractive model to investigate the conformational dynamics using biochemical and biophysical studies. These studies may resolve the disagreements that have been identified by different groups and also may provide additional information regarding conformational changes that occur during the transition from the apo-state to the substrate bound-state.

Research Overview

Over the past decades extensive study of EmrE from *Escherichia coli* has proved to be a valuable model system for the understanding of the coupling mechanism of the ion coupled transporter family (Adam et al., 2007; Schuldiner, 2007b; Soskine et al., 2004; Yerushalmi & Schuldiner, 2000a, 2000b). EmrE extrudes positively charged aromatic drugs in exchange for two protons generating bacterial resistance to a wide variety of toxic compounds (Schuldiner et al., 2001; Yerushalmi et al., 1995). The small size of this protein and the retention of its function upon solubilisation in detergent (Sikora & Turner, 2005; Soskine et al., 2006) make it a good model system for structural and functional studies that would contribute to the understanding of the mechanism of the SMR family of transporters.

In the last three years EmrE was center stage due to the controversy regarding its structure and topology. The crystal structure of EmrE in the apo-state was published by Chang and colleagues (Y. J. Chen et al., 2007). It was proposed that the conformation of the apo-state did not support known biochemical data. In addition, the helix packing in the non-native state could not be compared to the EmrE substrate bound-state crystal

structure (Y. J. Chen et al., 2007). It was believed that the structure of the apo-state was a non-native conformation that was stabilized by crystal contacts.

The EM model of the apo-state of EmrE (Tate et al., 2001) provided a glimpse towards assessing the helix packing and tertiary structure. Both the EM model and the substrate bound-state crystal structure of EmrE have shown that EmrE is a dimer with an antiparallel orientation of the two monomers. The low resolution of the two models made it difficult to precisely identify the residues for each of the transmembrane segments. In addition, conformational changes in the transmembrane segments were not investigated. The work described in this PhD dissertation explores the two conformational states of the SMR transporter in the apo-state and the substrate bound-state. It investigates the packing of the two monomers of EmrE in the dimer which will explain the EmrE topology at physiological pH. Two different environments were used to evaluate the EmrE structure of the substrate bound-state, detergent micelles and liposomes.

The main biophysical techniques used to investigate the structure and conformational changes are based on electron paramagnetic resonance spectroscopy (EPR) combined with site-directed spin labelling (SDSL). These combined methods have emerged as a powerful tool to investigate protein structure and dynamics, allowing resolution at a level of the backbone fold (Hubbell and Altenbach 1994). Additional structural information will be expressed in terms of the accessibility parameter (Π) (Altenbach, Froncisz, Hemker, McHaourab, & Hubbell, 2005) that will provide information on protein secondary structure, the tilt of the membrane protein, and position of the protein at the membrane interface (Hubbell, Gross, Langen, & Lietzow, 1998). Furthermore, pulse EPR methods will be used to investigate distances in the range of 20-

60 Å giving another dimension to the structural analysis of EmrE. All the above techniques will be used to obtain high resolution structural analysis that enables identification of the arrangements between the two monomers of EmrE.

CHAPTER II

ELECTRON PARAMAGNETIC RESONANCE SPECTROSCOPY

Theory of Electron Paramagnetic Resonance

Zeeman and Hyperfine Interactions

The science of electron paramagnetic resonance (EPR) spectroscopy deals with the interaction between unpaired electrons and an external magnetic field. The unpaired electron has an intrinsic magnetic moment, thus any rotating particle would have a vector known as angular momentum. In quantum mechanics, angular momentum is quantized so that the allowed magnitude is given by:

$$\left(J\left(J+1\right)\right)^{\frac{1}{2}}\hbar \qquad (1)$$

where J is the primary angular-momentum quantum number (J =0, 1, 2, 3, …..), $\hbar = \frac{h}{2\pi}$ which equal approximately 1.054 x 10^{-34} Js, (h is the Planck's constant). The magnitude of angular momentum along any selected direction is given by the secondary angular momentum quantum number M_J, that takes values of $M_J = \left(-J,-J+1,...0,.....1,,J-1,J\right)$.

The angular momentum of an unpaired electron is known as the spin angular momentum. For a single unpaired electron has a spin of ½, the primary spin angular momentum quantum number is S= ½ that corresponds to the doublet state (2S+1) since

unpaired electrons can have two states. These two states are the secondary spin quantum number, M_s that can either be ½ or -½. For two unpaired electrons, the primary spin angular momentum quantum number can either be S= 0 for a singlet state, or S= 1 for a triplet state. In contrast, a nucleus such as ^{14}N has a primary spin angular momentum quantum number I= 1, and a secondary spin quantum number M_I (M_I = -1, 0, +1).

In quantum mechanics, both the magnetic moment and the spin angular momentum are proportional to one another for particles that have non-zero magnetic moments:

$$\mu = \gamma S = \pm \frac{g\beta}{\hbar} S \tag{2}$$

γ, is the magnetogyric ratio converting angular momentum to magnetic moment, g is the Zeeman factor for the particles considered, β is the Bohr magneton (constant for a specific particle), and ± reflects whether the direction of both spin angular momentum and magnetic moment are parallel or anti-parallel. For an electron, γ is negative, while for nuclei it is positive.

These particles having different states with different secondary spin quantum numbers would have the same energy level if the external field is not imposed. When the external field is imposed, the energy of the magnetic dipole, including unpaired electrons is given by:

$$E = -\mu \hat{H} \tag{3}$$

$\hat{H}$ is the direction of the magnetic field. For an unpaired electron, the two values of M_s are ½ and -½. Then the two allowed spin states have the energy:

$$E = \pm \frac{1}{2} g_e \beta_e \hat{H} \tag{4}$$

This is referred to as the electronic Zeeman energy. The energy difference between the two electronic Zeeman levels is $g_e\beta_e\hat{H}$. The transition between these two energy levels can be induced by an electromagnetic field of appropriate frequency υ such that the photon energy $h\upsilon$ matches the energy separation (ΔE) that is described by the resonance equation:

$$\Delta E = h\upsilon = g_e \beta_e \hat{H} \tag{5}$$

If the interaction of the unpaired electron with the external applied magnetic field were the only effect, then all EPR spectra would consist of one line. However, in EPR the interaction between the unpaired electron and neighboring nuclear dipole moments, result in the splitting of the resonance. This interaction is known as the nuclear hyperfine interaction.

In a nitroxide spin label, the unpaired electron ($S=½$) interacts with the nitrogen ^{14}N nucleus ($I=1$) forming six spin states with different energy levels for nitroxid (Figure 1). Due to the selection rule of spin transitions $\Delta M_s = \pm 1$ and $\Delta M_I = 0$ for EPR absorption, there are three allowed transitions (Figure 1). In a field-sweep experiment at constant frequency, the resonance condition must be modified as:

$$\Delta E = h\upsilon = g_e \beta_e \hat{H} + M_I A \tag{6}$$

where M_I is the secondary spin quantum number of nitrogen having values of (+1, 0, -1) and A is the hyperfine interaction.

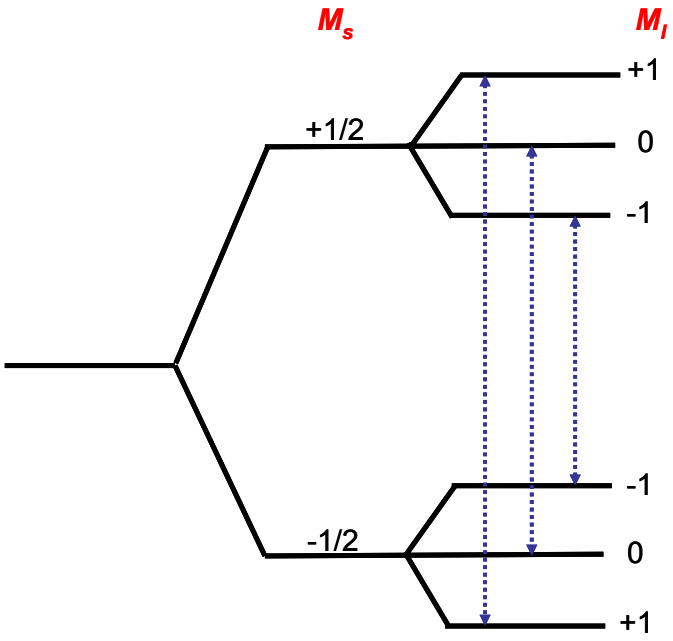

Figure 1: Energy levels due to Zeeman and hyperfine interactions. Energy levels and allowed EPR transitions shown in vertical blue arrows between different spin states. M_s is the secondary spin quantum number of the unpaired electron, and M_I is the secondary spin quantum number of nitrogen nucleus.

There are two important mechanisms that give rise to the hyperfine interaction; they are either isotropic (orientation independent) or anisotropic (dependent on the orientation of the magnetic field with respect to a molecular axis) interaction. The isotropic hyperfine Hamiltonian interaction is defined by:

$$\hat{H}_{iso} = \left(\frac{2\mu_0}{3}\right) g_e \beta_e g_n \beta_n \left|\Psi(0)\right|^2 \hat{S}\ \hat{I}\ = A_0 \hat{S}\ \hat{I} \qquad (7)$$

where $\Psi(0)$ is the wavefunction value of the unpaired electron at the position of the nucleus. A_0 is the isotropic hyperfine coupling constant that can be expressed in

magnetic field units and identified as the hyperfine splitting ($a_0 = \frac{A_0}{g_e \beta_e}$). $\hat{S}$ and $\hat{I}$ are the spin angular momentum of the electron and nucleus, respectively.

For the anisotropic hyperfine Hamiltonian, the interaction is expressed with respect to the dipolar interaction between the nucleus and the electron separated by a distance *r*:

$$\hat{H}_{dipolar} = -\left(\frac{\mu_0}{4\pi}\right) g_e \beta_e g_n \beta_n \left[\frac{\hat{S}\hat{I}}{r^3} - \left(\frac{3\hat{S}r\hat{I}r}{r^5}\right)\right] \tag{8}$$

Since the unpaired electron is in the pπ orbital of the nitroxide bond, the dependence of the dipolar Hamiltonian on the orientation is obtained by averaging over the electron spatial distribution. Both isotropic and anisotropic hyperfine terms can be combined and described as a tensor (*A*) having principle 3 x 3 unit matrix, corresponding to the principle axis of the nitroxide spin label (Figure 2).

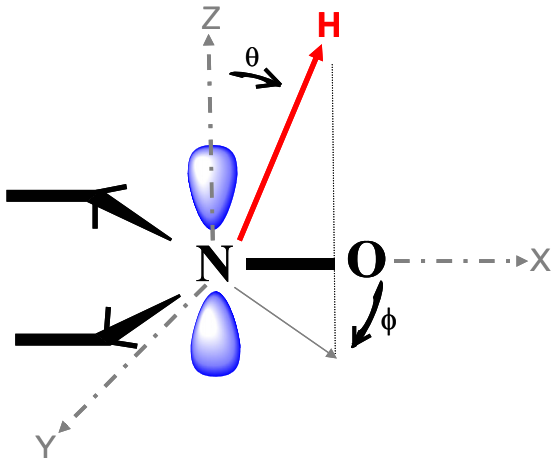

Figure 2: The principle axes of the nitroxide spin label.

In addition to the *A* tensor, the *g* factor is also orientation dependent (anisotropy). Therefore, the coupling between the electron-spin angular momentum and orbital angular momentum corresponds to the anisotropy of the *g* factor. The *g* tensor in the lab frame can be expressed as a 3 x 3 matrix:

$$g = \begin{vmatrix} gxx & 0 & 0 \\ 0 & gyy & 0 \\ 0 & 0 & gzz \end{vmatrix} \tag{9}$$

The above matrix corresponds to a rotation of the axes known as the principle axes. g_{xx} and g_{yy} are perpendicular to the symmetry axis *Z*, while g_{zz}, is parallel to the *Z* axis. Both the *g* tensor and the *A* tensor can be calculated by the random orientation of the nitroxide spin label in an external magnetic field:

$$g(\theta,\varphi) = g_{xx}\sin^2(\theta)\cos^2(\varphi) + g_{yy}\sin^2(\theta)\sin^2(\varphi) + g_{zz}\cos^2(\theta) \tag{10}$$

$$A^2(\theta,\varphi) = A_{xx}^2\sin^2(\theta)\cos^2(\varphi) + A_{yy}^2\sin^2(\theta)\sin^2(\varphi) + A_{zz}^2\cos^2(\theta) \tag{11}$$

The complete spin Hamiltonian for the nitroxide spin label combines the *A* tensor, electron Zeeman and nuclear Zeeman terms. Therefore,

$$\hat{H} = g_e\beta_e\hat{H}\hat{S} - g_n\beta_n\hat{H}\hat{I} + \hat{S}A\hat{I} \tag{12}$$

where $\hat{H}$ is the external magnetic field, $\hat{S}$ and $\hat{I}$ are the spin angular momentum of the electron and nitrogen nucleus, respectively. A is the hyperfine interaction tensor.

Overall, after approximation of the Hamiltonian and merging of orientation dependence of the A and g tensors, the resonance of the anisotropic condition becomes:

$$E = h\nu = g(\theta,\varphi)\beta\hat{H} + M_I A(\theta,\varphi) \tag{13}$$

Spin Relaxation

The difference in spin populations between the upper (M_s = ½) and lower (M_s =-½) energy states allows us to detect the resonance absorption that defines the intensity of the EPR signal. The ratio of the two populations is determined by the Boltzman distribution:

$$\frac{N_{1/2}}{N_{-1/2}} = e^{\frac{-\Delta E}{KT}} \tag{14}$$

Where $N_{1/2}$ and $N_{-1/2}$ are the spin populations of the two states, $\Delta E = E_{1/2} - E_{-1/2}$; K is the Boltzman distribution constant; T is the absolute temperature at thermal equilibrium.

A change in the magnetic field (H) or in temperature shifts the spin system from thermal equilibrium. The Boltzman equilibrium can be restored by an efficient relaxation pathway. The relaxation pathway can be measured by T_1, spin-lattice relaxation time (longitudinal relaxation time) or by T_2, spin-relaxation time (transverse relaxation time). The relaxation results from the random fluctuation of local magnetic field experienced by the spin. In quantum mechanics these two relaxation times can be calculated by the perturbation method. Alternatively, they can be measured experimentally.

The dynamics of the total spin magnetization vector can be described by the Bloch equations. This model gives a clear picture regarding the dynamics of the spin

systems. In an external magnetic field, $\hat{H}_o$, along the *z* axis, the bulk magnetization *M* is in the x-y plane. Therefore, when the oscillating electromagnetic field, $\hat{H}_1$ ($H_{1x} = H_1 \cos(wt)$, $H_{1y} = H_1 \sin(wt)$, $H_{1z} = 0$) is imposed in a direction perpendicular to the static magnetic field $\hat{H}_o$ (along z-axis), the Bloch equations are:

$$\frac{\partial M_x}{\partial t} = \gamma_e \left(H_0 M_y - M_z H_1 \cos(wt) \right) - \frac{M_x}{T_2} \tag{15}$$

$$\frac{\partial M_y}{\partial t} = \gamma_e \left(M_z H_1 \sin(wt) - H_0 M_x \right) - \frac{M_y}{T_2} \tag{16}$$

$$\frac{\partial M_z}{\partial t} = \gamma_e \left(M_z H_1 \sin(wt) - M_z H_1 \cos(wt) \right) + \frac{\left(M_{z^0} - M_z \right)}{T_1} \tag{17}$$

The steady state solutions of the Bloch equations in the rotation frame are:-

$$M_x = \frac{- M_{z^0} \left(\gamma_e H_1 (w_0 - w) T_2^2 \right)}{\left(1 + (w_0 - w)^2 T_2^2 + \gamma_e^2 H_1^2 T_1 T_2 \right)} \tag{18}$$

$$M_y = \frac{M_{z^0} \left(\gamma_e H_1 T_2^2 \right)}{\left(1 + (w_0 - w)^2 T_2^2 + \gamma_e^2 H_1^2 T_1 T_2 \right)} \tag{19}$$

$$M_z = \frac{M_{z^0} \left(1 + (w_0 - w)^2 T_2^2 \right)}{\left(1 + (w_0 - w)^2 T_2^2 + \gamma_e^2 H_1^2 T_1 T_2 \right)} \tag{20}$$

where ω_o is the larmor frequency of the spin. The actual spectrum is determined by the average power absorbed per cycle. Therefore, under field-sweep conditions, the absorption line of the M_y component is a Lorentzian function with half width at half height given by $\Gamma = \frac{1}{\gamma_e T_2} (1 + \gamma_e^2 H_1^2 T_1 T_2)^{1/2}$. The peak-to-peak width of the first derivative

equation is $\frac{2}{\sqrt{3}}\Gamma$. In non-saturation conditions where $\gamma_e^2 H_1^2 T_1 T_2 << 1$, the EPR central linwidth (ΔH_{pp}) is approximately $\frac{2}{\sqrt{3}\gamma_e T_2}$.

Spin-Spin Interactions

The basis of spin-spin interaction is the overlap of the orbital (electron exchange interaction) of the unpaired electrons and the dipolar interaction between the magnetic moment of the two spin labels.

In a two spin system, two magnetic moments can be constructed in two equivalent ways, an uncoupled representation (S1 and S2) and coupled representation (S). For two unpaired electrons there are four spin states. If the two unpaired electrons interact considerably, such that the electron orbital overlap, forming a bond or quickly collide with each other, the system separate in energy into triplet (S=1) and singlet (S=0) state (Hustedt & Beth, 1999). The interaction between the two unpaired electrons is known as the exchange-energy, *J*. This operator is represented by the spin Hamiltonian:

$$(\hat{H}_{exch})_{iso} = J_o \hat{S}_1 . \hat{S}_2 \qquad (21)$$

In practice, only the isotropic part of J_o is considered important. The isotropic electron-exchange coupling constant J_o is the analog of the isotropic hyperfine coupling parameter A_o.

In addition to the exchange interaction, there exists an anisotropic hyperfine dipolar interaction between two electronic magnetic dipoles. The magnetic dipole-dipole interaction is given by the Hamiltonian:

$$\hat{H}_{ss} = \left(\frac{\mu_0}{4\pi}\right) g_1 g_2 \beta_e^2 \left[\frac{\hat{S}_1 \hat{S}_2}{r^3} - \left(\frac{3\left(\hat{S}_1 r'\right)\left(\hat{S}_2 r\right)}{r^5}\right)\right] = \hat{S}_1 D \hat{S}_2 \qquad (22)$$

$\acute{r}$ is the interspin vector, r is the scalar length of the $\acute{r}$ vector, g_1 and g_2 are the tensor defining the zeeman interaction for spin 1 and spin 2, respectively; $\hat{S}1$ and $\hat{S}2$ are the spin angular momenta for spin 1 and spin 2, and D is the dipolar coupling tensor. As the g and A tensor, a 3x3 matrix D can be diagonalized. The inter-electron distance is larger than the size of the moleuclar orbital of the unpaired electron on the nitroxide, the D tensor is axially symmetric and the principle z-axis of the diagonalized D tensor aligns with the inter-electron vector (Hustedt & Beth, 1999). The dipolar interaction is $1/r^3$ dependent, therefore, when the distance between the two nitroxde decreases, the dipolar interaction increases, and vice versa. Overall, the distance measurement is dependent on the spin-spin interaction.

Pulse EPR

Magnetization in the Lab Frame

The lab frame in EPR is defined by the magnetic field B_o and is parallel to the z axis, the microwave magnetic field, B_1, is parallel to the x axis and the y axis is orthogonal to the x and z axes.

When an electron spin is placed in a magnetic field, a torque is exerted on the electron spin, causing the magnetic moment to precess about the magnetic field B_o. The angular frequency of the precession is commonly called the larmor frequency (ω_L), and it is related to the magnetic field by

$$\omega_L = -\gamma B_0 \tag{23}$$

When considering a large number of electron spins, the electrons are characterized by two quantum mechanical states, Ms= ± ½, one with its magnetic moment parallel to B_o and one antiparallel. The parallel state has lower energy and at thermal equilibrium, there is an excess of electron spins in the parallel state (Ms=-½) according to Boltzman distribution. Therefore, there should be a net magnetization parallel to the z axis. The electron spins are still precessing about the z axis, however, their orientations are random in the *x*-*y* plane. For a very large number of electron spins, the various transverse (i.e. in the x-y plane) components of the magnetic moments cancel each other out. The result is a stationary magnetization, M_0 parallel to B_0 (Figure 3).

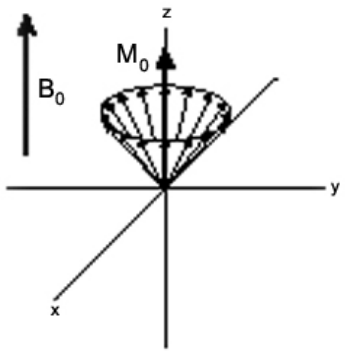

Figure 3: The Larmor precession and the resultant stationary magnetization

Magnetization in the Rotating Frame

EPR experiments are usually performed with a resonator using linearly polarized microwaves. The microwave resonator is designed to produce a microwave magnetic field, B_1, perpendicular to the applied magnetic field, B_o. In most cases $|B_1| << |B_o|$. At resonance, $\omega_L = \omega_o$, where ω_o is the microwave frequency. By rotating the coordinate system at an angular frequency ω_o, B_1 appears to be stationary and parallel to the *x* axis and the Larmor precession around the z axis is absent. Therefore, B_o disappears in the rotating frame while M rotates about the x axis following the right hand rule at a frequency $\omega_1 = -\gamma B_1$, where ω_1 is the Rabi Frequency.

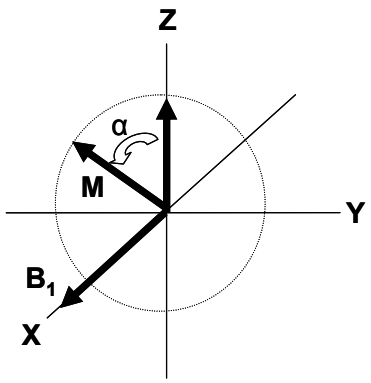

Figure 4: The tip angel of bulk magnetization in the rotating frame.

The angle by which *M* rotates in the yz plane is called the tip angle, $\alpha = -\gamma |B_1| t_p$. The tip angle depends on both the magnitude of B_1 and the length of the pulse (t_p) that is in the range of several nanoseconds. In continous wave EPR (CW-EPR), $t_p \rightarrow \infty$, B_1 has the constant amplitude with time. B_1 drives the spins back and forth between Ms= ±1/2. In

pulse EPR, pulses are often labeled by their tip angles as π/2 pulse and π pulse (i.e. 90 and 180 degrees).

Application of EPR Spectroscopy

Spin Labeling

Site-directed spin labeling (SDSL) has become a powerful tool in structural biology, combining both molecular biology with EPR spectroscopy (Altenbach, Marti, Khorana, & Hubbell, 1990). The basic strategy of SDSL is mutating all native cysteines (non-disulfide bonds) to an alanine or a serine followed by replacing the native residue (or residues) of interest with a cysteine. The cysteine residues in the protein of interest can be subsequently modified with a variety of sulfhydryl-specific nitroxide spin labels, such as proxyl-iodo acetamide (IAP) and proxyl-maleimide (MSL). The most currently utilized spin label is proxyl-methanethiosulfonate (unsaturated methane thio sulfonate) spin label (MTSSL) (Berliner, Grunwald, Hankovszky, & Hideg, 1982). The pyrroline derivative of MTSSL contains four methyl groups to protect the unpaired electron in the pπ orbital of the nitroxide from reducing agents (Figure 2), such as ascorbic acid. Therefore, the unsaturated methanethiosulfonate spin label (MTSSL) is the most commercially available spin label that generates a disulfide-linker nitroxide side chain, designated as R1. The R1 side chain is comparable to a tryptophan in molecular in size. In addition, they have a negligible influence on biological activity of a protein structure and function, especially for sites located on the surface of the protein (Bolin, Hanson, Wright, & Millhauser, 1998; McHaourab, Lietzow, Hideg, & Hubbell, 1996). For buried sites, the labeling efficiency decreases but in most cases they can accommodate the spin

label and restore packing of the protein core. In some cases spin labeling may affect the function of the protein but not the protein folding. Generally, protein structure is less affected than protein function by spin labeling as long as the cysteine mutation does not affect protein folding. If the protein is denatured or aggregated a unique EPR line shape would be observed. Thus, the shape of the EPR spectrum is an indication of the protein's native folding.

Mobility

The continuous wave (CW) EPR lineshape of the nitroxide side chain is sensitive to the local environment in the nanosecond time scale. The nitroxide dynamics is reflected by anisotropy of its motion and distribution of the motional states. Thus, the motion of the spin label attached to a protein is mainly manifested by the rotation correlation time, τ. τ is a measure of the average lifetime of a particular spatial orientation of the nitrogen p-orbital and $1/\tau$ is a measure of the rate of motion (Columbus & Hubbell, 2002). Consequently, the rotational motions that change the spin label orientation modulate the EPR line shape. Overall, the effect of rotational motion on CW-EPR line shape is illustrated in Figure 5. The effect of fast rotation (τ= 0.01ns) causes the CW-EPR spectral line shape to exhibit three sharp lines, while the central line position and the hyperfine splitting is determined by the relative orientation of the external static magnetic field. Therefore, when the rotation correlation time increases, the rate of motion decreases, thus, the central line and the overall spectrum are broadened. For the spectrum of a crystalline powder at the slow motion limit ($\tau = \infty$), each of the three lines experience extreme anisotropic motion.

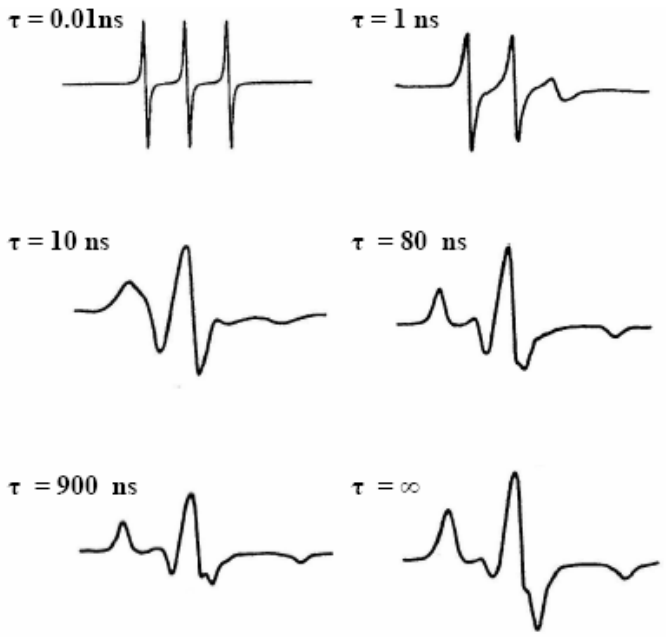

Figure 5: The effects of rotational motion of a nitroxide spin label on CW-EPR line shape.

When R1 is bound to a specific site on the protein backbone (Figure 6), the motion of the nitroxide ring will have a contribution from the rotational diffusion of the protein, the local backbone fluctuation and internal dynamic modes of the side chain. Experimental conditions have been used so that the contribution of protein rotation and tumbling can be reduced by increasing the viscosity of the solution (McHaourab et al., 1996). Under these conditions, the side chain mobility relative to the protein at room temperature is not affected. As a result, the χ_4/χ_5 model of R1 (Figure 6) on a helix, with no contact with nearby side chains, has been proposed according to crystallographic data, chemical modification of the R1 side chain, and fitting of the spectra to models for side chain motion (Columbus, Kalai, Jeko, Hideg, & Hubbell, 2001; Langen, Oh, Cascio, & Hubbell, 2000; McHaourab et al., 1996).

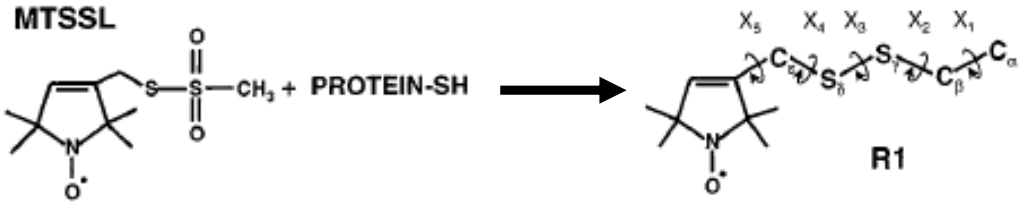

Figure 6: When a protein is labeled with MTSSL. The nitroxide moiety is tethered to the backbone via a side chain referred to as R1. The dihedral angles X_1-X_5 are shown. The Cα and Cβ are on the cysteine residue with the Cα position in the backbone (Borbat, McHaourab, & Freed, 2002).

In this model, the internal anisotropic motion is largely limited to torsional oscillations about the dihedral angles X_4 and X_5 since the S_δ sulfur atom forms a non covalent hydrogen bond with the Cα hydrogen atom in the protein backbone (Langen et al., 2000). The overall motion of the nitroxide remains strongly coupled to the motions of the backbone. Despite the complicated nature of the nitroxide dynamics, which is reflected by the anisotropy of the nitrogen p orbital motion and distribution of the motional states, EPR lineshapes have been analyzed using semiquantitative methods. The first is the inverse central line width of the central resonance line (ΔH_0^{-1}). Plotting this parameter as a function of residue number reveals secondary structure, since the periodicity of the spin label mobility refers to a sequence of surface, contact or buried sites (McHaourab et al., 1996; Perozo, Kloda, Cortes, & Martinac, 2001; Pfeiffer, Rink, Gerwert, Oesterhelt, & Steinhoff, 1999). Second, is the separation between the outer hyperfine extrema ($2A_{par}$) which can also be taken as a measure of label mobility (Figure 7).

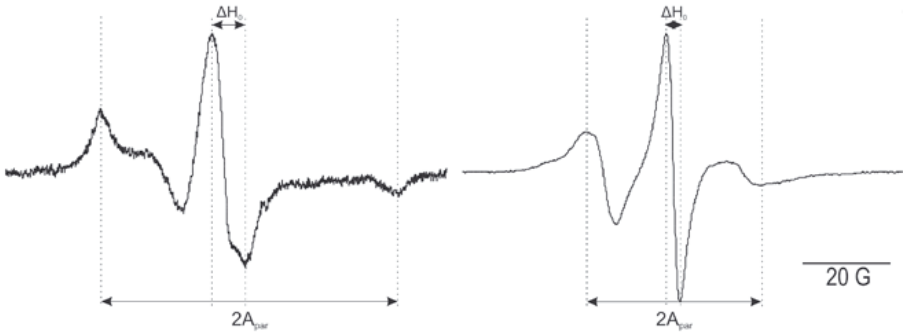

Figure 7: Spin label mobility revealed by EPR spectral line shape. On the left, motionally restricted spin label of buried side chain of a helix.On the right is an exposed side chain of the same helix. The separation between the outer hyperfine extrema ($2A_{par}$) and the peak-to-peak separation of the central line width (ΔH_o) provides a measure of label mobility (Czogalla, Pieciul, Jezierski, & Sikorski, 2007).

The second moment provides a measure of the overall breadth of the spectrum (Columbus & Hubbell, 2002; McHaourab et al., 1996). The reciprocal plot of $\left\langle H^2 \right\rangle^{-1}$ versus reciprocal central line width ΔH_0^{-1} is roughly linear and has been found to group side chains into defined types based on the plot from T4 lysozyme crystal structure (Figure 8).

The mobility increases in the order from buried sites, tertiary contact sites, and helix surface sites to loop sites, respectively. Some buried sites have low mobility that is consistent with sites located in a densely packed interior reflected by highly ordered R1 motion, while the loop sites are all located in a highly mobile region. The overlap between tertiary interaction sites, buried sites, and helix surface sites may be affected by the backbone dynamics superimposed on the effect of tertiary interactions. Mobility can also serve as a sensitive monitor of conformational changes in helices (Columbus & Hubbell, 2004), β-structure (Jayasinghe & Langen, 2004; Kusnetzow, Altenbach, &

Hubbell, 2006), and in the folding process (Cobb, Sonnichsen, McHaourab, & Surewicz, 2007; Koteiche & McHaourab, 1999; Morin et al., 2006).

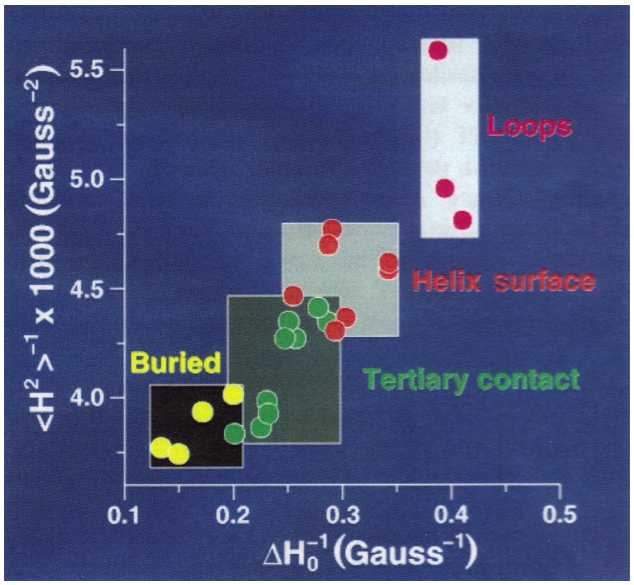

Figure 8: **Mobility map.** A mobility map constructed as a plot of the inverse second moment of the EPR spectrum ($\langle H^2 \rangle^{-1}$) versus inverse central line width (ΔH_o^{-1}), indicating the correlation between the measured parameters and regions of protein topology for selected R1 side chain positions in T4 lysozyme. Regions of buried sites, tertiary contact, helix surface, and loops are represented in yellow, green, red, and pink circles, respectively (McHaourab et al., 1996).

A quantitative understanding of the motions that generate a given line shape is accomplished by simulation of EPR spectra. The simulation will help to get a precise view of dynamics of the analyzed system (Barnes, Liang, McHaourab, Freed, & Hubbell, 1999; Borbat, Costa-Filho, Earle, Moscicki, & Freed, 2001; Livshits, Kurad, & Marsh, 2006). In addition, molecular dynamics EPR spectral simulation facilitates the study that influence the structure adjacent to the spin sites on the spectral lineshape (Steinhoff et al., 2000). Spectral simulations help determine whether the lineshape corresponds to

isotropic or anisotropic motion and also can be used to detect multiple components of the spectra.

Solvent Accessibility

One of the most informative features of the protein structure is solvent accessibility of side chain *R1* to paramagnetic reagents. Solvent accessibility is determined from collision frequency of the nitroxide with paramagnetic reagents such as oxygen and NiEDDA. The presence of a paramagnetic reagent provides an additional pathway for relaxation, which leads to a decrease of the spin lattice relaxation time T_1. The change in T_1 of the nitroxide can be characterized by the relative collision rate between the nitroxide and the paramagnetic exchange reagent *R*, known as the Heisenberg exchange, W_{ex}. The exchange reagent *R* that is used for measurement of solvent accessibility should have high water solubility, have limited accessibility to the interior of a well packed protein, should be electrically neutral, and should have similar size to the nitroxide itself. It is also important that the exchange between the nitroxide and *R* be in the strong exchange limit, where the rate is solely determined by the rate of diffusional encounter.

The interaction of the reagent with the nitroxide is only manifested by the Heisenberg exchange, with little contribution from distance dependent magnetic dipolar coupling. An interaction that occurs through space may provide an overestimation of solvent accessibility. This is insured for reagents with $T_{1R} < \tau_c$, where T_{1R} is the longitudinal relaxation time for the reagent and τ_c is the encounter complex lifetime.

Both O_2 and NiEDDA meet the above criteria as an exchange reagent for determining solvent accessibility.

For bimolecular encounter between a small nitroxide *N* and exchange reagents in solution, the Heisenberg exchange frequency, W_{ex}, experienced by a particular nitroxide is given by:

$$W_{ex} = k_{ex} C_R \tag{24}$$

where k_{ex} is the exchange rate constant and C_R is the concentration of *R*. In the strong exchange limit, where Heisenberg exchange is diffusion controlled,

$$W_{ex} = k_{ex} C_R = P_{\max} f K_D = P_{\max} f 4\pi \left(\frac{N_A}{1000} \right) (D_N + D_R) r_c \tag{25}$$

where $P_{\max}$ is the maximum exchange efficiency (P_{max}=1, when the strong exchange limit and $T_{1R} < \tau_c$ are satisfied). The steric factor, K_D, is the diffusion-controlled rate constant, and D_N and D_R are diffusion constants for the nitroxide and the reagent, respectively. The collision radius, r_c, is $r_N + r_R$, where r_N and r_R are effective radii of the nitroxide and reagent, respectively. For a nitroxide bound to a protein the translational diffusion becomes that of the protein, and thus $D_N + D_R \approx D_R$. However, the nitroxide retains rotational freedom about the bonds of the tether. *R* and the nitroxide are still viewed as a colliding species, rather than *R* and the spin labeled protein, the definition of collision radius, r_c, is retained. The local protein environment and interaction of the nitroxide with the protein are reduced by the number of effective collisions below those characteristics of the nitroxide in solution, and all such effects are collectively accounted for by a factor

ρ (accessibility factor). Thus, for a protein associated nitroxide, W_{ex}^{P} in the strong exchange limit is

$$W_{ex}^{P} = \rho f 4\pi \left(\frac{N_A}{1000} \right) D_R r_C C_R \tag{26}$$

$$\rho = \frac{W_{ex}^{P}}{f k_D^{P} C_R} = \frac{W_{ex}^{P} k_D}{W_{ex} k_D^{P}} = \frac{k_{ex}^{P} k_D}{k_{ex} k_D^{P}} = \frac{k_{ex}^{P}}{k_{ex}} \left(\frac{D_R + D_N}{D_R} \right) \tag{27}$$

for a small, electrically neutral but polar exchange reagent, ρ varies from zero for a nitroxide buried in the protein to a limiting value of infinity for a nitroxide at a completely exposed site on the protein surface.

For exchange reagents with $T_{1R} < \tau_c$, T_{1e} Heisenberg exchange leads to equal changes in T_{1e} and T_{2e} of the nitroxide

$$W_{ex} = \Delta \left(\frac{1}{T_{1e}} \right) = \Delta \left(\frac{1}{T_{2e}} \right) = k_{ex} C_R \tag{28}$$

Measurements of either T_{2e} or T_{1e} can be employed for experimental determination of W_{ex}. Methods based on T_{2e} rely on the fact that Heisenberg exchange leads to Lorentzian line broadening. The broadening can be determined as the width at half height of the Lorentzian line ($\Delta H_{1/2}$) that, when convoluted with the spectrum in the absence of collision, yields the interacting spectrum. Alternatively, the broadening can be directly measured as the increase in peak-to-peak central line width of the first derivative EPR spectrum ($\Delta\Delta H_{PP}$) under non saturated condition

$$\Delta\Delta H_{PP} = \frac{2}{\sqrt{3}\ |\gamma_e| T_2} = \frac{\Delta H_{1/2}}{\sqrt{3}} \tag{29}$$

$$W_{ex} = \Delta\left(\frac{1}{T_2}\right) = \frac{\sqrt{3}|\gamma_e|\Delta\Delta H_{PP}}{2} \tag{30}$$

In CW saturation EPR, the amplitude (A) of the first derivative central resonance (M_I= 0) line is measured as a function of microwave power (P)

$$A = \frac{I\sqrt{P}}{\left(1 + \frac{\left(2^{1/\varepsilon} - 1\right)P}{P_{1/2}}\right)^{\varepsilon}} \tag{31}$$

$$P_{1/2} = \frac{\left(2^{2/3} - 1\right)}{\Lambda^2 \gamma_e^2 T_1 T_2} \tag{32}$$

γ_e is the gyromagnetic ratio of the electron ($\gamma_e = \frac{2\pi g\beta}{h} = \frac{g\beta}{\hbar}$), ε is the line shape adjustment parameter (ranging from ε = 1.5 for the homogenous saturation limit to ε = 0.5 for a completely inhomogeneous saturation limit), Λ is an instrumental factor, I is the scaling factor, and $P_{1/2}$ is the half saturation power, where the incident microwave power where the first derivative amplitude is reduced to half of its unsaturated value. For the common case where $W_{ex} << \frac{1}{T_{2e}}$, where T_{2e} is a constant, and

$$\Delta P_{1/2} = P_{1/2} - P^0_{1/2} = \frac{\left(2^{2/3} - 1\right)}{\Lambda^2 \gamma_e^2 T_{1e} T_{2e}} = \frac{\left(2^{2/3} - 1\right)}{\Lambda^2 \gamma_e^2}\left(\frac{1}{T_1 T_2} - \frac{1}{T_1^0 T_2^0}\right) \tag{33}$$

$$= \frac{\left(2^{2/3} - 1\right)}{\Lambda^2 \gamma_e^2 T_2}\left(\frac{1}{T_1 T_2} - \frac{1}{T_1^0 T_2^0}\right) = \frac{\left(2^{2/3} - 1\right)}{\Lambda^2 \gamma_e^2 T_2} W_{ex} \tag{34}$$

therefore,

$$\Delta P_{1/2} \quad \alpha \quad \frac{W_{ex}}{T_2} \quad \alpha \quad W_{ex} \quad \alpha \quad \rho \tag{35}$$

For the purpose of normalization and to standardize measurements from different resonators, a dimensionless accessibility parameter Π is defined as

$$\Pi = \frac{\left(\frac{\Delta P_{1/2}}{\Delta H_{PP}} \right)}{\left(\frac{P_{1/2}^{DPPH}}{\Delta H_{PP}^{DPPH}} \right)} = \alpha W_{ex} \tag{36}$$

DPPH (Diphenylpicryhydrazide) is selected as the reference to normalize for variations in resonance frequency (Altenbach et al., 2005).

The protein environment has a local effect on the collision rate of the nitroxide side chain and the exchange reagent. In turn, the accessibility of a spin labeled site is highly sensitive to the local environment. Therefore, one can determine secondary structure of a protein along the polypeptide chain revealing an α helical or a β sheet fold with an accessibility Π pattern that is likely to show an approximate periodicity of 3.6 and 2, respectively.

Solvent accessibility is a powerful tool for probing the secondary, tertiary, and protein folding such as water soluble α-crystallin (Berengian, Bova, & McHaourab, 1997; McHaourab, Berengian, & Koteiche, 1997), prokaryotic voltage-dependent K^+ channel (KvAP) (Cuello, Cortes, & Perozo, 2004), and also conformational changes in dynamics processes such as Bacterial rhodopsin (Thorgeirsson et al., 1997), multidrug transporter MsbA (Dong, Yang, & McHaourab, 2005), and mechanosensitive channel, MscS (Vasquez, Sotomayor, Cordero-Morales, Schulten, & Perozo, 2008; Vasquez, Sotomayor, Cortes et al., 2008).

Spin-Spin Distance

When a pair of nitroxides is introduced at selected sites on a protein the magnetic dipole interactions between them can be analyzed using EPR spectroscopy, to measure the distance distribution between the two spin labeled sites. The spin Hamiltonian of two interacting nitroxide spin labels is given by:

$$\hat{H} = \beta_e H_0 g_1 \hat{S}_1 + \beta_e H_0 g_2 \hat{S}_2 - \omega_n \left(I_{1z} + I_{2z}\right) + \gamma_e \hat{I}_1 A_1 \hat{S}_1 + \gamma_e \hat{I}_2 A_2 \hat{S}_2 + \hat{S}_1 D \hat{S}_2 + J \hat{S}_1 \hat{S}_2 \quad (37)$$

The two nitroxides are labeled as 1 and 2, where β_e is the Bohr magneton, g1 and g2 are the zeeman tensors defining the interaction of the electron spin of nitroxide 1 ($\hat{S}_1$) and nitroxide 2 ($\hat{S}_2$) with the magnetic field H_o, ω_n is the Larmor frequency of the nitrogen nucleus, A_1 and A_2 are the hyperfine tensors defining the interaction of the nitrogen nuclear spins ($\hat{I}_1$ or $\hat{I}_2$) with $\hat{S}_1$ or $\hat{S}_2$, D is dipolar coupling tensor, and J is the scalar exchange interaction between electron spins. In this Hamiltonian, the unpaired electron density is highly localized to the N-O bond of the nitroxide. The principal axes of the g and A tensors of a spin label are essentially coincident and are well defined within the molecular frame of the nitroxide. Given that the inter-electron distance to be observed is normally considerably larger than the size of the molecular orbital of the unpaired electron on the nitroxide, the D tensor is axially symmetric, with the principal z-axis of the diagonalized D-tensor aligned with the inter-electron vector; term in D are proportional to $1/ R^3$, where R is the inter-electron distance. Significant J coupling can only arise for inter-nitroxide distances less than 10 Å.

These distances or distance distributions can be used to build structural models of a protein as well as structural changes related to protein function. To obtain the distance distribution between two nitroxide is a complicated task. It is crucial to determine the global motion of the protein and the local motion of the nitroxides since CW-EPR spectra are strongly dependent on the relative orientation and distribution of the two probes. Therefore, three cases have been addressed to deal with distance measurement between nitroxide spin labels (Hustedt & Beth, 1999).

The first case deals with statically arranged spins. The distance between the two nitroxides and its orientation adopts a fixed, static value and the protein has a global rotational correlation time of $\geq 1\mu s$. The inter-nitroxide distance, R, and all five angles (ξ, and η for one nitroxide, and α, β, and γ for the second nitroxide) define the steric geometry of the two probes. For a given set of 6 variables directly calculating from the Hamiltonian in equation 37 of two interacting spins can generate the EPR spectrum.

Research that falls into this case are the extensive tertiary interaction of the nitroxide R1 side chain (McHaourab, Kalai, Hideg, & Hubbell, 1999), and the binding of substrate with high affinity to a large protein complex (Beth et al., 1984).

The second case deals with statically disordered spins. The two nitroxides adopt a static distribution of orientations with respect to one another. Both the local rotational motion of the nitroxides and the global rotation occur on a time scale $\geq 1\mu s$. The number of applications that fall in this case is limited. However, by slowing the dynamics of side chain motion and the global tumbling by carrying out studies at low temperature or in viscous media, large applications that fall under case 3 will meet the requirements of case 2. An example is the situation of a protein < 20 kDa in size and has a small rotation

correlation time (Hubbell, McHaourab, Altenbach, & Lietzow, 1996; McHaourab et al., 1996). The rotational modulation of the dipolar interaction and the homogenous line broadening is given as:

$$\Delta B_{dd} = \left(\frac{3}{10}\right)\left(\frac{\gamma^4 h^3 \tau}{g\beta r^6}\right)\left(3 + \frac{5}{1+\upsilon^2\tau^2} + \frac{2}{1+4\upsilon^2\tau^2}\right) \tag{38}$$

where τ is the rotation correlation time of the inner spin vector; r is the inter-spin distance, υ is the frequency of the external magnetic field (microwave). In the frozen state, the two nitroxides are separated by the distance r and the sum of individual crystallites is disordered with certain distribution, known as Pake pattern. The EPR absorption lines are then split by $2B$ in the magnetic field $2\Delta B = 1.5 g_e \beta_e$ (Pake, 1948). Therefore, the dipolar coupled line shape can be described by the convolution of two non-interacting nitroxides with a Pake broadening function of the nitroxide side chain and the change in conformation of the protein:

$$\Pi(B) = S(B) \otimes M(B) = \int_{-\infty}^{\infty} S(B')M(B' - B)dB' \tag{39}$$

where $\Pi(B)$ is the spectrum of double-labeled protein, $S(B)$ is the average spectra of the two single labeled proteins (non-interacting). $M(B)$ is the weighed average broadening function with respect to distance r between the two nitroxides. By applying Fourier transformation on both sides of equation (39) and the convolution theorem one obtains $M(B)$. Knowing $\Pi(B)$ and $S(B)$, we get:

$$\Pi^*(w) = S^*(w)M^*(w) \tag{40}$$

where $^{*}(w)$ represents the Fourier transformation of the corresponding function, therefore:

$$M(B) = \frac{1}{\sqrt{2}\pi} \int_{-\infty}^{\infty} \exp(2i\pi wB) \frac{\Pi^{*}(w)}{S^{*}(w)} dw \tag{41}$$

Thus, the average splitting $\langle 2B \rangle$ and average distance $\langle r \rangle$ are:

$$\langle 2B \rangle = \frac{\int_{-\infty}^{\infty} |2B| M(B) dB}{\int_{-\infty}^{\infty} M(B) dB} \tag{42}$$

$$\langle r \rangle = \left(\frac{0.75\left(\frac{3}{2}\right) g_e \beta_e}{\langle 2B \rangle} \right)^{\frac{1}{3}} \tag{43}$$

The convolution-deconvolution method involves the estimation of inter-spin nitroxide distance for either a solid, at *RT*, or a frozen solution. This approach neglects the effect of the *g* and *A* tensors. Also, the inter-electron vector with respect to the nitroxide is randomly and isotropically distributed over a sphere. This cannot be valid as the attachment of the nitroxide to the protein backbone leads to one or both nitroxides being restricted to a specific orientation relative to the inter-electron vector. In this case, the *g* tensor, hyperfine *A* tensor and dipolar coupling *D* tensor of the spin Hamiltonian are all determined by a set of angles (Hustedt et al., 2006).

The third case is related to the effect of dynamics. Mchaourab et al. (McHaourab et al., 1997) developed a method, based on the fast motion relaxation theory (the motion completely averages the anisotropy of the *g* and hyperfine tensors), for analyzing line broadening due to nitroxide-nitroxide dipolar coupling in the intermediate to fast motion

range. This study was performed on a small globular protein, T4 Lysozyme, with an isotropic correlation time of 6 ns. For double mutants where the inter-nitroxide distance could be estimated from the known crystal structure, the observed line broadening due to dipolar coupling was proportional to $1/R^6$ (because the relaxation effects will be proportional to the square of the dipolar coupling). As the distance increases the spectral broadening decreases faster than in the second case ($1/ R^3$). Overall, in the fast motion, when the energy of interaction is much lower than the reorientation of the dipolar interaction of the two nitroxides, R1, the dipolar splitting is nearly averaged to zero.

To measure the inter-nitroxide distance of more than 25 Å, a time domain EPR method was developed to overcome the limit of distance measurement by CW-EPR arising from inhomogeneous broadening of the EPR line. The two advantages of using time domain pulse EPR method are:

1. To increase the distance ranging from 20-60 Å.
2. To simplify the probelm since the dipolar interaction between the two nitroxide spin labels is observed without a dominant effect of the hyperfine and *g*-tensors.

A number of pulse methods have been developed for measuring the distance from 20-60 Å between two nitroxides in the frozen state. Among the techniques that have been used for biological samples are double electron-electron resonance (DEER) (Pannier, Veit, Godt, Jeschke, & Spiess, 2000) and double quantum coherence (DQC) (Borbat et al., 2002). In DQC, EPR utilizes a DQC pulse sequence to preserve the contribution to the double quantum echo signal solely from the dipolar interaction between the two spins. The intensity of the echo is recorded as a function of time and a Fourier transform of the

echo generates the dipolar coupled Pake pattern spectrum that is directly related to the distance between the two spin labeled sites (Borbat et al., 2001).

The work in this thesis project was performed using a 4 pulse DEER (Pannier et al., 2000). In DEER the system consists of two electron spins, S_A and S_B. The resonance microwave frequency of A is υ_A and the one containing resonance frequency υ_B will be the B spin. The four pulse pattern experiment is shown in Figure 9.

At time 0 ns, spin packet A is excited first with a $\pi/2$ pulse that tips the magnetization of spin A into the xy plane, where the spin packet precesses with angular rate of υ_A. The presence of field inhomogeneties due to unresolved dipolar couplings of nearby spins, results in slightly different angular rates and causes de-phasing of the spins. At time τ_1, a π pulse is applied to spin A causing the spins to flip the magnetization 180˚, resulting in refocusing spin A and leading to spin echo at $2\tau_1$. Spin A continues to precess in the xy plane but a second π pulse is applied after an evolution time of $\tau_2(2\tau_1+\tau_2)$ and leads to a refocusing of the A spin magnetization at time $2\tau_1+2\tau_2$ after the last phase, with smaller amplitude as the phase coherence is lost due to spin-spin relaxation ($\pi/2$-π pulse generates a Hahn echo).

The dipolar interaction can be studied if an additional π pulse applied at time $(2\tau_2+t)$ is applied to spin B, therefore flipping the B spins and thus reverses the dipolar contribution experienced by the A spins from $\frac{1}{2}\upsilon_{AB}$ to $-\frac{1}{2}\upsilon_{AB}$. As a result, spin A cannot be fully refocused due to the variable time of flipping the B spins.

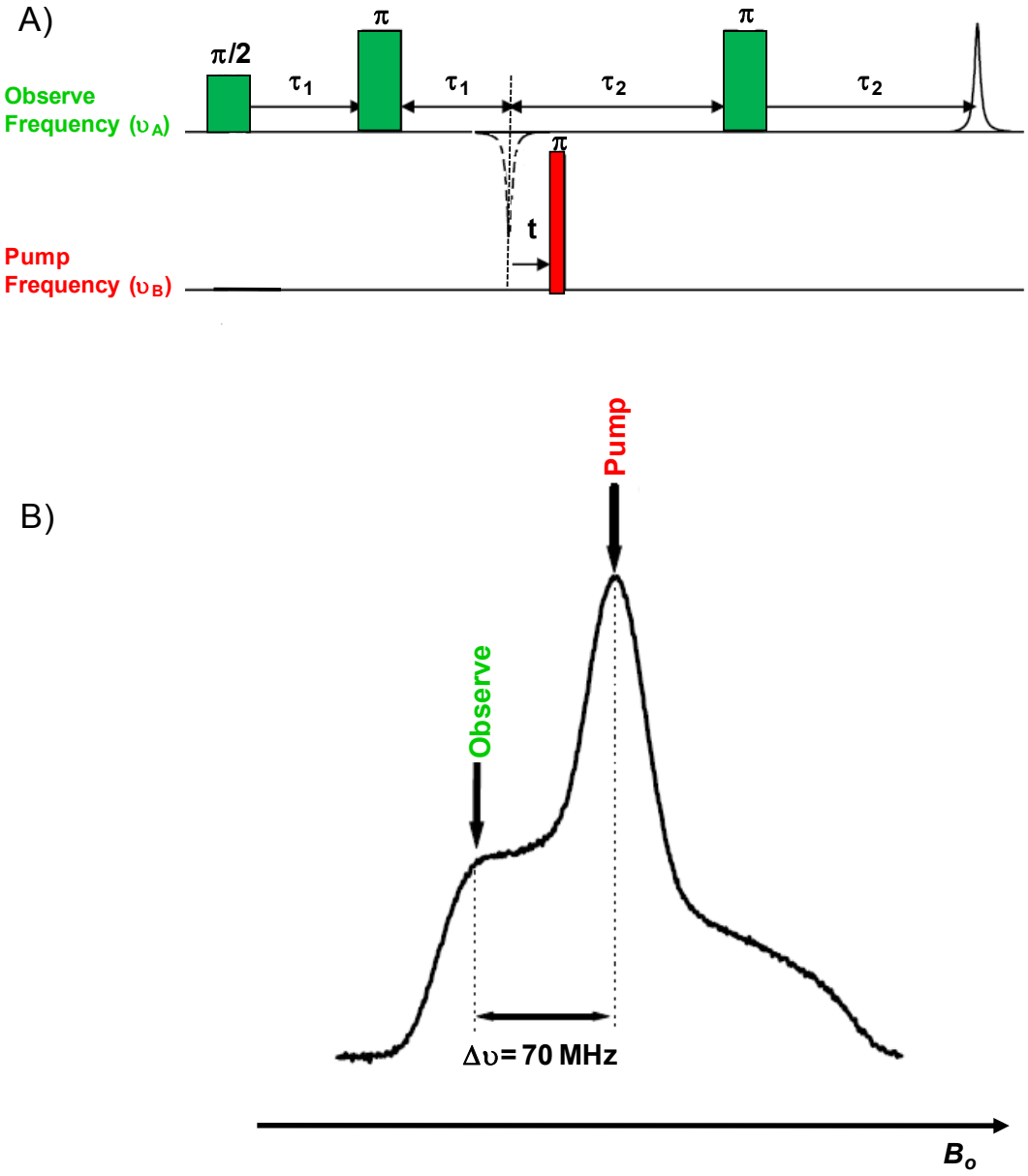

Figure 9: **Four-pulse DEER. A)** A diagram shows the EPR pulse sequence for the 4-pulse DEER. Spin A is excited by the observing microwave pulse (green bar) and spin B is excited by the pumping microwave pulse (red bar). When spin B is close to spin A, spin A senses the excited spin B (π pulse at υ_B) and inverts the local dipolar field of spin A, therefore, an electron spin echo at position A (dotted echo) is observed. When a second π pulse is applied that inverts spin B, a change is observed in the local magnetic field and refocusing at the A spins. At variable time t the pumping pulse of spin B is applied, the refocused echo intensity of spin A oscillates with a frequency ω_{AB} (Banham et al., 2008). **B)** The diagram shows the excitation profiles of the microwave pulses in the DEER experiment.

It is important to realize that the 4 pulse DEER experiment is a constant time experiment, thus, the second π pulse is applied to avoid distortion of the signal or dead time due to the overlap in a short time after the π/2 pulse.

After the $2\tau_1 + 2\tau_2$ the echo intensity of spin *A* oscillates with:

$$I = I_0 \cos(-\upsilon_{AB} t) \qquad (44)$$

I_o and I are the initial and final echo intensity of spin *A* that oscillates with $\cos(-\upsilon_{AB} t)$. Thus, the DEER signal is the echo intensity as the pumping π pulse is swept between the two π pulses.

It is important to correctly choose the magnetic field for observing and pumping frequency in order to obtain the best DEER result. One of the important criteria is that the bandwidths of the observable and pump pulses must not overlap. Typically, the frequency difference between the observable and pump pulses must differ at least 70 MHz to avoid overlap, as shown in Figure 9.

In principal, to detect longer distances than 60-80 Å, one could extend the evolution period (i.e. time between the π pulses). The evolution period is restricted by the phase memory time (Tm) or the spin-spin relaxation time (T_2) of the nitroxide labels. In practice, the time between the pulses is limited to 2 μsec for a protonated nitroxide. Therefore, the maximum distance measured by DEER is limited to 60-80 Å. One of the advantages of the DEER signal is the easy way to estimate the average distance from the oscillation of the refocused echo intensity containing the information regarding the dipolar interaction. Thus, the analysis of the inter-spin distance and distance distribution can be obtained either from the Pake pattern after Fourier transformation (as mentioned above) or from de-convolution method and the data fitting model.

In summary, the use of SDSL EPR techniques has become a powerful tool not only to obtain the global structure but also functional dynamics of a protein. Proteins can also be studied in their native environment (i.e. in solution for water soluble proteins or reconstituted proteoliposomes for membrane proteins).

CHAPTER III

MATERIAL AND METHODS

EmrE Gene Cloning and Site directed Mutagenesis

The EmrE gene was kindly provided by Geoffrey Chang (Scripps Institute, La Jolla, CA) in pET15b^{+} expression vector (Novagen, California, USA). The gene was located in the multiple cloning sites between two restriction sites Nde I and BamH I, and a 6-histidine tag at the N-terminus of the cloned EmrE gene.

The wild type EmrE has three native cysteine residues at position 39, 41, and 95 that were replaced by alanine residues using the QuikChange Mutagenesis Kit (Stratagene, La Jolla, CA). The new construct was named (EmrE-CLA, or WT*). Single cysteine mutants were made for all 110 amino acids of EmrE using WT* as the background. All the mutants were confirmed by sequencing at the Vanderbilt DNA Sequencing Facility.

Protein Expression

The plasmids containing EmrE cysteine mutants were transformed into BL21 Gold (DE3) *E.coli* competent cells (Stratagene, La Jolla, CA). EmrE mutants were over-expressed in one liter minimal medium (1g ammonium sulfate, 4.5g potassium phosphate monobasic, 10.5 g potassium phosphate dibasic, 0.5 g sodium citrate). The medium was supplemented with 1 mM magnesium sulfate (autoclaved 45 minutes), 100 μg/ml ampicilin (filter sterilized), 2.5 μg/ml thiamine (filter sterilized), 0.5% glycerol (v/v,

autoclaved 45 minutes), and 1 ml amino acid mixture (Gibco-BRL, Maryland, USA). Briefly, 30 ml of overnight seed culture in LB medium was used to inoculate the minimal medium. Cells were grown at 37°C until A_{600} ~1.5 was reached. Protein expression was induced with 1mM IPTG and cells were grown at 28°C for 5 hours (for some mutants the expression temperature was lowered to 20°C overnight).

Cells were harvested by centrifugation at 3500 x g for 15 minutes. The cell pellets were resuspended in lysis buffer (10 mM Tris, 250 mM sucrose, 150 mM choline chloride, 2.5 mM $MgSO_4$, 0.02% NaN_3, pH 7.5) supplemented with 10 mM DTT, 45 μg DNAse, and 10 μM PMSF. The cells were sonicated and homogenized using EmulsiFlex-C5 (Avestin). The lysates were centrifuged at 9000 x g for 5 minutes to remove cell debris. The supernatants were centrifuged for 1 hour at 388,000 x g to pellet cell membranes. The membrane pellets were solubilized with 1.5% n-dodecyl-β-D-maltopyranoside (β-DDM, Anatrace, Ohio, USA) in resuspension buffer (50 mM sodium phosphate monobasic, 300 mM sodium chloride, and 10 mM imidazole, pH 8). The insoluble components were removed by ultracentrifugation for 1 hour at 388,000 x g and the supernatant was used for EmrE purification.

Two steps were used to purify EmrE mutants. First, the His-tagged EmrE was purified using Ni-NTA resin as described by the manufacturer (Qiagen, Valencia, CA). Purified mutants of EmrE were spin-labeled with a 20-fold molar excess of 1-oxyl-2,2,5,5-tetramethyl-Δ3-pyrroline-3-methyl-methanethiosulfonate spin label (MTSSL; Toronto Research Chemicals, Ontario, Canada) and incubated at room temperature for 2 hours followed by a second and a third addition of 10-fold molar excess of spin label every two hours. After 6 hours at room temperature, the samples were stored at 4°C on

ice overnight. Under labeled mutants were spin labeled with 0.5-fold molar excess of MTSSL and incubated at room temperature for 1.5 hours then added 20-fold molar excess of diamagnetic spin label (1-Acetyl-2,2,5,5-tetramethyl-Δ3-pyrroline-3-methyl) Methane thiosulfonate (Toronto Research Chemicals, Ontario, Canada) and stored overnight at 4 °C. Second, the samples were concentrated 3-fold and further purified by size-exclusion chromatography (SEC) employing a superdex-200 column (Amersham Biosciences, New Jersey, USA) in SEC buffer (50 mM sodium phosphate monobasic, 50 mM NaCl, and 0.02% β-DDM, and 0.02% NaN_3 pH 7.2). Protein concentration was determined by UV absorption at 280nm using an extinction coefficient of 29450 $M^{-1}cm^{-1}$. The two step purification was sufficient to achieve single band purity as is evident by SDS-PAGE (Figure 1).

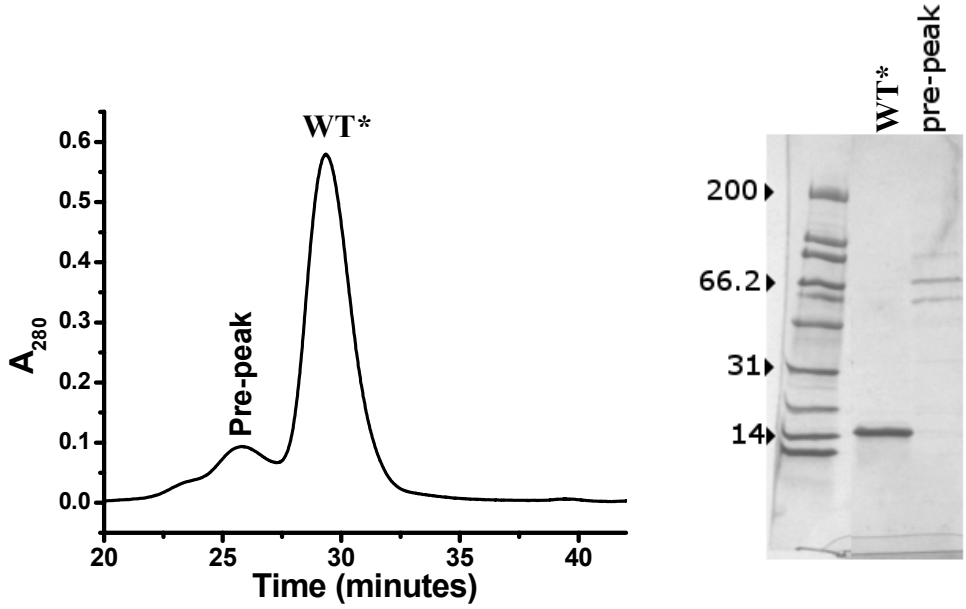

Figure 1: Purified EmrE. Left panel is the gel filtration profile of WT* (EmrE-CLA). The right panel is the SDS-PAGE gel of purified WT* protein stained with comassine blue.

Protein Reconstitution

Asolectin (purchased from Avanti Polar Lipids, Alabama, USA) was dissolved in chloroform resulting in a final lipid concentration of 20 mg/ml. Traces of solvent were removed by a rotary evaporation and left in a desiccator overnight. The dried film of asolectin was hydrated in the reconstitution buffer (50 mM HEPES, 50 mM sodium chloride, 2 mM magnesium chloride, pH 7.5) to a final lipid concentration of 10 mg/ml. The hydrated lipid was vigorously vortexed and subjected to cycles of freeze (incubation in dry ice/ methanol bath) and thaw (incubate at 37°C) 5 times. Unilamellar asolectin liposomes were made by extruding asolectin through a 50 nm Nuclepore Track-Etched Membrane filter (Whatman) 10 times. The unilamellar liposomes were destabilized by 2mM β-DDM and mixed with 0.3-0.5 mg labeled protein at 500 to 1000-fold molar excess of lipid over protein. The detergent concentration was adjusted to 1.3- 1.5 mM such that lipid: detergent ratio was ~4000. The mixture was incubated with gentle agitation at 4°C for 2 hours, and then was diluted to 10ml with reconstitution buffer. Bio-Beads SM2 (Bio-Rad, California, USA) were added into the sample at the quantity of 80 mg per milliliter initial mixture and incubated for two hours at 4°C with the addition of fresh Bio-Beads twice at a two hour intervals followed by overnight incubation at 4°C. The reconstituted proteoliposomes were collected by ultracentrifugation at 388,000 x g for 45 minutes at 4°C and the pellet was resuspended with reconstitution buffer.

The proteoliposome protein concentration was determined with the DC protein assay kit (Bio-Rad, Buckaklian et al, 2003). Proteoliposomes were diluted to about 1 μg/μl of protein in reconstitution buffer. Twenty-five microliters of diluted proteoliposomes were mixed with 125 μl working reagent A. One milliliter of reagent B

was added to each tube and vortexed immediately. The solution was incubated at room temperature for 15 minutes, and absorbance at 750 nm was measured. Bovine serum albumin (BSA) was used as the standard, and liposome without EmrE protein was used as control. The BSA standard curve is shown in Figure 2.

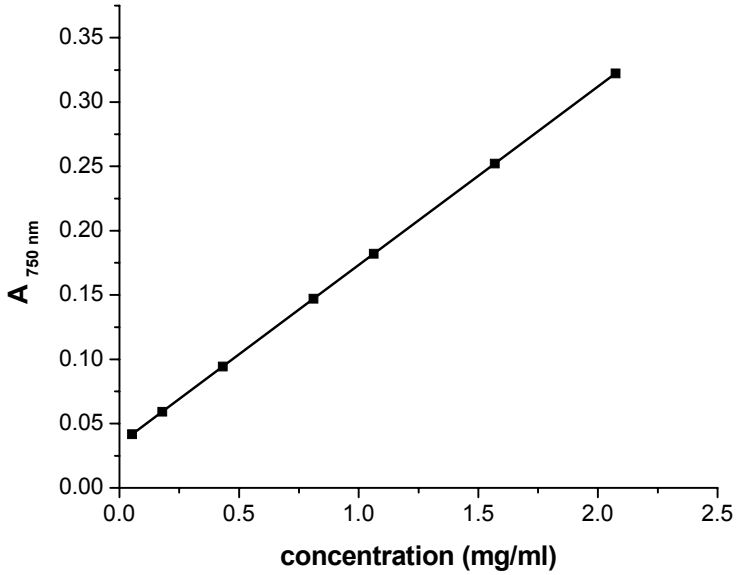

Figure 2: Standard curve of the Bio-Rad DC protein assay.

Continuous Wave (CW)-EPR Measurements

X-band (9.8 GHz) CW-EPR spectra were collected using a Varian spectrometer equipped with a loop-gap resonator at room temperature. The samples were prepared at 100 μM spin concentration, then drawn into a round capillary of size 0.6 I.D. X 0.84 O.D. (VitroCom, Mt Lks, NJ) and sealed with Cha-seal (Chase scientific). The magnetic field scan range was set to 100, 160, or 200 Gauss sweep width, and the incident microwave power was set at 2mW. All spectra contained 1024 data points collected at 100 kHz Zeeman field modulation frequency of 1.6 Gauss amplitude (peak-to-peak). The spectra

were collected with EWWin 4.21 EPRware (Scientific Software Services, Michigan, USA), and analyzed with the program HMEPR version 4 written by Richard Stein (Vanderbilt University).

Solvent Accessibility

For power saturation experiments, reconstituted spin labeled samples were loaded into a gas-permeable TPX capillary (Medical Advances, Wisconsin, USA), and data was collected using Bruker ELEXSYS spectrometer equipped with a dielectric resonator (BrukerBiospin, Billerica, MA). The field scan of the central resonance line for each mutant was carried out at 25 Gauss. The amplitude of the central resonance line was obtained with a microwave power of 1, 2, 3, 4, 10, 16, 25, 40, 63, 79.6, and 100 mW, respectively. The power saturation experimental data were collected and analyzed by non-linear curve-fitting using Origin 7.1 software (OriginLab Corporation, Massachusetts, USA) to obtain the spectral amplitude (A) versus the square root of the microwave power $\left(\sqrt{P}\right)$ according to the following equation (Altenbach et al., 2005):

$$A = \frac{I\sqrt{P}}{\left(1 + \frac{\left(2^{1/\varepsilon} - 1\right)P}{P_{1/2}}\right)^{\varepsilon}}$$

where A is the peak-to-peak amplitude of the central line; I and ε are adjustable parameters; $P_{1/2}$ is the half-saturation power; and P is the power of the incident

electromagnetic wave. The NiEDDA and oxygen accessibility (Π) were calculated by the following equation:

$$\Pi = \frac{\left(\frac{\Delta P_{1/2}}{\Delta H_o}\right)}{\left(\frac{P_{1/2}^{T4L}}{\Delta H_0^{T4L}}\right)}$$

where Π is the accessibility, $\Delta P_{1/2}$ is the difference of the half saturation power in the presence and absence of paramagnetic reagents (50mM NiEDDA or 20% O_2), $P_{1/2}^{T4L}$ is the T4L half saturation power in the absence of paramagnetic reagent (T4L was selected as a reference to normalize for variations in the resonance frequency) and ΔH_o is the central line width.

Distance Measurements

Double electron-electron resonance (DEER) was used to measure long-range distances (25 Å -80 Å) between two nitroxide spin labeled residues. The experiments were performed on an X-band (9.5 GHz) Bruker E680 pulse EPR instrument (Bruker Spectrospin, Billerica, MA) using a 4 pulse sequence (Pannier et al., 2000). Spin labeled EmrE samples were concentrated to 200 μM and supplemented with 30% (v/v) glycerol. DEER measurements were carried out at 83°K using a 16 nanosecond 90° (π/2) pulse and a 32 nanosecond 180° (π) pulse and an 800 nanosecond shot repetition time (SRT) in an over-coupled dielectric resonator (ER4118X-MD5, Bruker Biospin, Billerica, MA). The

DEER signals was analyzed by Tikhonov regularization (Chiang, Borbat, & Freed, 2005) of the software DeerAnalysis 2008 to determine the average distances and distributions in distance, P(r).

Fluorescence Binding

The extent of binding of tetraphenylphosphonium (TPP^+) was estimated by quenching of native intrinsic tryptophan (Trp) fluorescence emission (Elbaz et al., 2005). Tryptophan emission spectra were recorded at room temperature. Each spin labeled EmrE mutant diluted to 3 μM with SEC buffer (50 mM sodium phosphate monobasic, 50 mM NaCl, and 0.02% β-DDM, pH 7.2) without and with 2x and 4x molar excess of the substrate at 295 nm excitation and 310-350 nm emission using a quartz cuvette (1cm path length). The experiment was carried out on an L-format Photon Technology International Fluorometer. Maximum fluorescence intensity was obtained from the emission curves by in-house software ("LambdaMax" written by Marco Bortolus) and analyzed using Origin 7.1 software (OriginLab Corporation, Massachusetts, USA) to obtain relative fluorescence with and without the substrate for each EmrE mutants.

Subunit exchange

Purified EmrE mutant and cysteine-less EmrE were concentrated 4 fold and mixed at a ratio of 1:2. The mixture was then injected into a desalting column (HiTrap, GE Healthcare) equilibrated with SEC buffer (50 mM sodium phosphate monobasic, 50 mM NaCl, and 0.02% β-DDM, and 0.02% NaN_3 pH 7.2) supplemented with 0.8 mole fraction of sodium dodecyl sulfate (SDS). The eluted mixture was incubated at room

temperature for 10 minutes. To refold the sample it was injected back onto a Superdex-200 column equilibrated with SEC buffer (50 mM sodium phosphate monobasic, 50 mM NaCl, and 0.02% β-DDM, and 0.02% NaN_3 pH 7.2). CW-EPR spectra of the sample with and without SDS were collected at room temperature. The magnetic field scan range was set to 160, 200, or 250 Gauss sweep width, and the incident microwave power was set at 9 mW.

CHAPTER IV

FUNCTIONAL CHARACTERISTICS OF EMRE

Introduction

The main goal of this thesis was to compare the structure of EmrE obtained via SDSL and EPR spectroscopy to the crystal structure and the EM model (Y. J. Chen et al., 2007; Fleishman et al., 2006). Since the SDSL method involves mutating each residue of EmrE one at a time to cysteine it is important to measure the activity of each mutant to insure the mutations and the subsequent spin labeling have minimal effect. Thus, a second goal of the work presented in this chapter is to evaluate the functional consequence of the cysteine mutations and subsequent spin labeling.

EmrE is part of the multi-drug transporter family that recognizes a broad range of substrates with high affinity and removes them from the cytoplasm. EmrE extrudes various drugs in exchange for protons, causing bacterial resistance to these compounds (Grinius & Goldberg, 1994; Paulsen et al., 1996). Therefore, both binding and translocation of the substrate are important functional characteristics of EmrE mutants.

In vivo and *in vitro* assays are used to evaluate EmrE mutants. To assess *in vivo* transport activity, previous work has judged the ability of cells expressing mutant proteins to grow in the presence of toxic compounds (Mordoch, Granot, Lebendiker, & Schuldiner, 1999). It was shown that most sites can be replaced with cysteines without

serious impairment of function, with the exception of mutant sites that are located at positions 11, 14, 18, 60 and 63 that seem to be important for activity (Yerushalmi, Lebendiker, & Schuldiner, 1996). Therefore, the selective growth of cells containing EmrE that is resistant to a specific substrate gives a qualitative measurement of activity.

Previous studies have also shown that out of the 8 charged residues of EmrE, only one acidic residue at position 14 when replaced with cysteine, causes complete loss of activity (Morimyo et al., 1992). This was supported and confirmed in other multidrug transporters (Edgar & Bibi, 1999; Paulsen et al., 1996), suggesting that the central role of the acidic residue in multidrug transporters is in recognizing positively charged substrates (Yerushalmi & Schuldiner, 2000b).

In vivo activity is qualitative, since a mutant that is inactive may indicate a role for that site in the mechanism of translocation, but could also indicate a role in stability, folding, or decreasing the affinity for the substrate. An *in vitro* assay gives direct evidence with respect to substrate binding for each mutant of EmrE.

The TPP^+ dissociation constant for binding to wild-type EmrE in solution was determined to be (20 ± 15 nM), which was similar to EmrE-His (10 ± 3 nM) bound (Muth & Schuldiner, 2000). Therefore, the high affinity of TPP^+ towards EmrE makes it a good substrate for analyzing activity of EmrE *in vitro*. Previous work on the binding sites of transcription factors (Godsey, Zheleznova Heldwein, & Brennan, 2002; Neyfakh, 2002) has shown an interaction of the substrates with aromatic residues. Aromatic residues such as tryptophan can interact with cations through strong, non-covalent force (Zacharias & Dougherty, 2002). It has been suggested that the aromatic residues in a protein can pull the cationic substrate out of water into a hydrophobic environment. This

was also suggested in EmrE, where the three aromatic residues (Trp63, Tyr40, and Tyr60) in each monomer stabilize the carboxyls of Glu14 in the binding cavity, the low dielectric constant of the protein interior created by the hydrophobic and aromatic residues (at least three from each monomer) would strongly favor the electrostatic interaction between the negatively charged glutamate and a positively charged drug (Elbaz et al., 2005; Rotem, Steiner-Mordoch, & Schuldiner, 2006).

The focus of this chapter will be to analyze each of the cysteine mutants and the spin labeled mutants for activity using *in vivo* and *in vitro* assays, leading to a better understanding of the functionality of each site in EmrE in comparison to previous published work.

Experimental Methods

Ethidium Resistance Assay

The *in vivo* assay was carried out by Dr. Hanane Koteiche and the results are presented in this chapter for completeness. The DNA containing the EmrE open reading frame was amplified from *E.coli* MG1655 and cloned into the NdeI and HindIII sites of plasmid pET20b$^+$. The EmrE gene is controlled by the T7 promoter in pET20b$^+$ vector. This promoter is known for background 'leaky' expression; unlike the highly regulated pET15b$^+$ vector containing the T7 lac promoter that controls basal expression (Studier, Rosenberg, Dunn, & Dubendorff, 1990). All 110 single cysteine mutants were made in a cysteine-less (WT*) background using QuikChange Mutagenesis (Stratagene, La Jolla, CA). All mutants were confirmed by the Vanderbilt DNA Sequencing facility.

The ability of mutants to confer resistance was determined as previously described (Mordoch et al., 1999). Overnight cultures of *E.coli* expressing mutant EmrE's were grown to saturation ~4.0 OD_{600}. The cultures were then diluted 10-, 10^3, and 10^6-fold, and 5µl of the dilutions was spotted on LB-amp plates containing 200µg/ml ethidium bromide. Growth was examined after incubation at 37°C for 24 hours.

The mutants were classified into three groups based on the growth profile of the transformed cells. A resistance phenotype at all dilutions (10-10^6) was interpreted as 100 % active EmrE; growth only in the 10-10^3 dilution was considered 50 % active; while abnormal phenotype in the 10-10^3 dilution, was recorded as compromised activity. If the cells did not grow in any dilutions then they were concidered to be inactive mutants. Assays were repeated twice.

Intrinsic Tryptophan Fluorescence

Details of this method are described in Chapter III. To obtain similar fluorescent intensities, all the spin labeled samples were diluted to a final concentration of 3 µM in 0.02 % w/v β-DDM, pH 7.2 phosphate buffer. Each EmrE spin labeled sample was incubated at room temperature for 20 minutes after the addition of 2x or 4x molar access of TPP^+. For the high concentration experiments, the spin labeled samples were diluted to a final concentration of 20 µM and each sample had the addition of 4x and 6x molar acess of TPP^+. A substantial portion/part of these experiments was carried out by Sanjay Mishra.

Purification of EmrE using different buffers

Details of the purification of EmrE are given in Chapter III. All mutants were purified in a phosphate buffer (50 mM NaH_2PO_4, 50 mM NaCl, 250 mM imidazole, 0.02 % NaN_3, and 0.08 % β-DDM, pH 7.2). Cys-less EmrE (WT*) was also purified in comparable Tris buffer (20 mM Tris, 20 mM NaCl, and 0.3 % (w/v) NG or 0.02 % β-DDM at pH 7.2 and 8) (Chen. et al. 2007). SDS-PAGE (4-20 %) was used to confirm the homogeneity of the purified WT* protein.

Results and Discussion

Stability of the EmrE Dimer

Previously, it has been shown that the exposure of detergent solubilized EmrE to high temperature for a specific amount of time causes only a 20-30% decrease in the ability of EmrE to bind and transport substrate (Soskine et al., 2006) suggesting a highly stable structure. However, the requirement of the proper detergent is quite stringent. For instance, it was shown that using the detergent nonyl-glucoside (NG) instead of dodecyl-β-D-maltoside (β-DDM) to purify EmrE, caused a 10 fold decrease in the binding of TPP^+, suggesting an effect on the oligomeric state of the protein (Soskine et al., 2006).

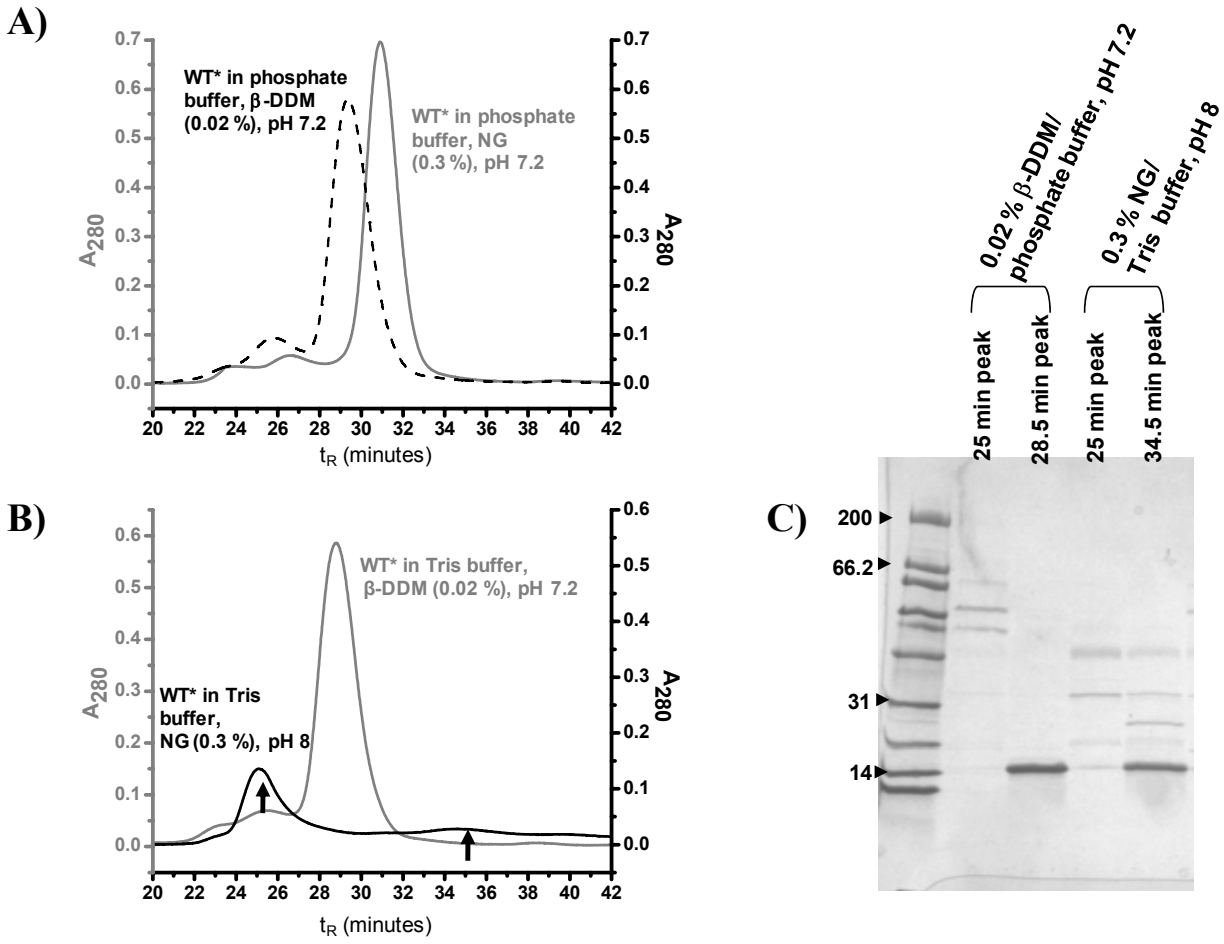

Figure 1: SEC profile of EmrE-CLA (WT*) using different buffer components.

A) The retention time (t_R) of WT* purified with similar buffer and pH but different detergent. The profile of WT* in β-DDM is shown in black dotted trace, and of NG is shown in grey trace.

B) The retention time (t_R) of WT* purified with similar buffer, but different pH and detergent. The profile of EmrE-CLA in β-DDM, pH 7.2 is shown in grey trace, and in NG, pH 8.0 is shown in black trace.

C) SDS-PAGE of WT* purified using different detergent component at different retention times.

This is relevant because the crystal structure of EmrE was obtained from protein purified and crystallized in a Tris buffer containing 0.3 % w/v (NG) at pH 8.0 (Y. J. Chen et al., 2007). An important question that we addressed is: could the content of the buffer, pH, or the detergent have an influence on EmrE oligomer structure? To answer this question, we analyzed the effect of detergent and pH on the dimer structure using size exclusion chromatography (SEC). At pH 7.2, we found that substitution of NG for β-DDM had a slight effect on the retention time, as shown in Figure 1A. In contrast, for Figures 1B and C, the detergent had a large influence in the retention time of the cys-less EmrE (WT*) when purified with buffer containing 0.3 % NG detergent micelles, at pH 8, showing a shift in the retention time , t_R, to ~34.5 minutes. Notably, we observed substantial loss of protein implying either precipitation or irreversible interactions with the column. The longer retention time suggests that NG destabilized the EmrE dimer.

These results demonstrate that the detergent used to purify EmrE for crystallization (Y. J. Chen et al., 2007) has a large influence on the oligomerization state. Previous work has shown that other membrane proteins purified with β-DDM are much more stable than when purified with NG (Serrano-Vega, Magnani, Shibata, & Tate, 2008). Both detergents are nonionic, but the length of the hydrocarbon side chain of NG is 9 while in β-DDM it is 12. Therefore, the length of the hydrocarbon chain has an effect in stabilizing the highly hydrophobic EmrE (i.e. when comparing NG micelles to β-DDM micelles) as supported by a recent publication confirming that different detergent micelles have a great influence on the structural dynamics of membrane proteins (Columbus et al., 2009).

Overall, it is clear that the use of NG is likely to destabilize the dimer structure. The detergent NG could be the reason behind the misfolding of the apo-state. Since the exact buffer in the crystal is not known, a definite determination of whether EmrE is a dimer in the TPP^+ bound crystal is not possible. At the high concentration used during crystallization, TPP^+ (Y. J. Chen et al., 2007) may stabilize the dimer or bind to the monomer.

All purified spin labeled mutants were analyzed by SEC. Most had similar retention time to the WT* of ~28 minutes, as shown in Figure 2 (dotted trace profile), suggesting a destabilization by the mutation and subsequent labeling. Exceptions are spin labeled sites 90, 94, 97, and 101 (Figure 2, G90C-SL is shown as an example) where an increase in the aggregation fraction at a retention time of ~25 minutes was observed.

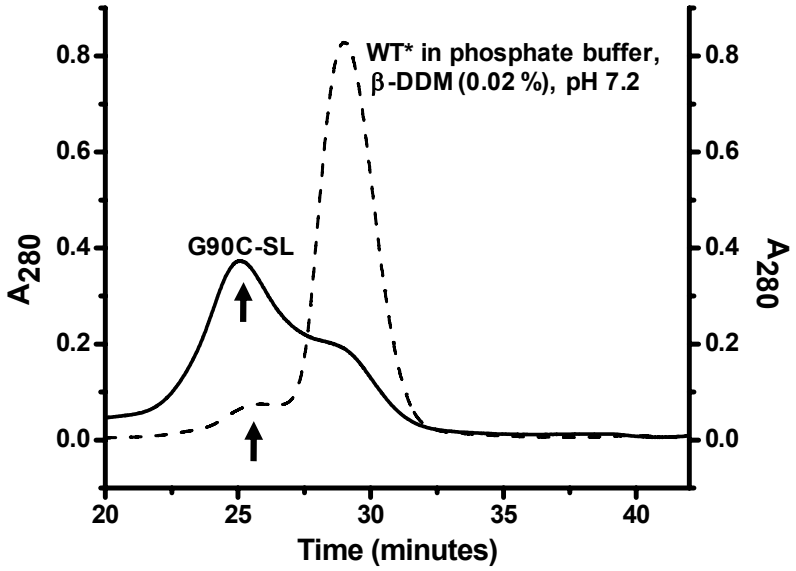

Figure 2: Elution profile of stable and unstable mutants of EmrE. SEC profile of EmrE cys-less (WT*) (black dotted trace) compared to G90C-SL, an unstable mutant (black trace). Arrow points to the aggregation peak.

These four mutants are all located in TM4 and are one helical turn away from one another, thus, facing the same side of the helix. This result suggests that the oligomeric state of TM4 is compromised when these sites are mutated and spin labeled.

Activity of EmrE Mutants

Sequential cysteine mutants spanning the full length of EmrE (i.e. 110 amino acids) were constructed in a cysteine less mutant of EmrE where its three native cysteines at position 39, 41, and 95 were mutated to alanine. Cysless EmrE has been shown to have similar activity to the native EmrE in vivo and in proteoliposomes (Lebendiker & Schuldiner, 1996).

An *in vivo* functional assay was used to test whether the cysteine mutants of EmrE were able to confer resistance to ethidium bromide. The *in vivo* activity of EmrE mutants is determined by three important characterizations. First, the affinity of the substrate towards the mutant protein; second, the coupling of substrate to proton movement; and third the oligomeric structure of EmrE, the loss of which impairs transport. Examining the cysteine mutants of EmrE *in vivo* would therefore provide another dimension when exploring the structure of EmrE.

From the 110 residues analyzed by Hanane Koteiche, 80 % of the EmrE cysteine mutants retained their activity, and 10 % of the cysteine mutants were inactive (sites 10, 14, 17, 18, 60, 63, 67, 90, 97, 101, and 102). The rest, 7 %, were only 50 % active (sites 3, 4, 7, 22, 47, 55, 57 and 94), and only 2 % had compromised activity (sites 40 and 54).

Previous published work has shown that sites on TM1 located at a distance of about one helical turn from E14, such as residues 10 and 18, were nonfunctional and seem to be in the drug binding pathway (Koteiche et al., 2003). Mutated sites located in

TM3 (sites 60, 63, and 67) and in TM4 (sites 90, 97, 101, and 102) were also inactive. Site 60 is a tyrosine and site 63 is a tryptophan, and these two aromatic sites have been shown to be important for substrate binding and translocation (Elbaz et al., 2005; Rotem et al., 2006). Furthermore, sites 67, 90, and 97 that showed no resistance to ethidium bromide are all glycine residues. Biochemical evidence has shown that the glycine residue at site 67 in TM3 is important for the flexibility of the helix and may participate in the translocation of the substrate (Elbaz, Salomon, & Schuldiner, 2008). The glycine sites at positions 90 and 97 of TM4 seem to have an important role in the dimerization of EmrE (Elbaz et al., 2008; Gottschalk, Soskine, Schuldiner, & Kessler, 2004; Soskine et al., 2002), which has also been confirmed by the SEC profiles presented above. The data also show that the replacement of TM2 residues with cysteines did not yield an inactive protein, suggesting that TM2 residues may have an important role in stabilizing the substrate but not in the transport activity of EmrE.

Intrinsic Tryptophan Fluorescence for Cys-less and Spin Label Mutants of EmrE

One of the main goals of this thesis project is to compare the structure of EmrE upon the binding of the TPP^+ at physiological pH with the crystal structure of the substrate-bound state determined at pH 8. Therefore, it is important to independently confirm that the spin labeled mutants can bind TPP^+. For this purpose, we used a tryptophan fluorescence quenching assay introduced by Schuldiner and colleagues (Elbaz et al., 2005). EmrE has four tryptophan residues, with tryptophan 63 fully conserved within the SMR family of transporters (Ninio et al., 2001).

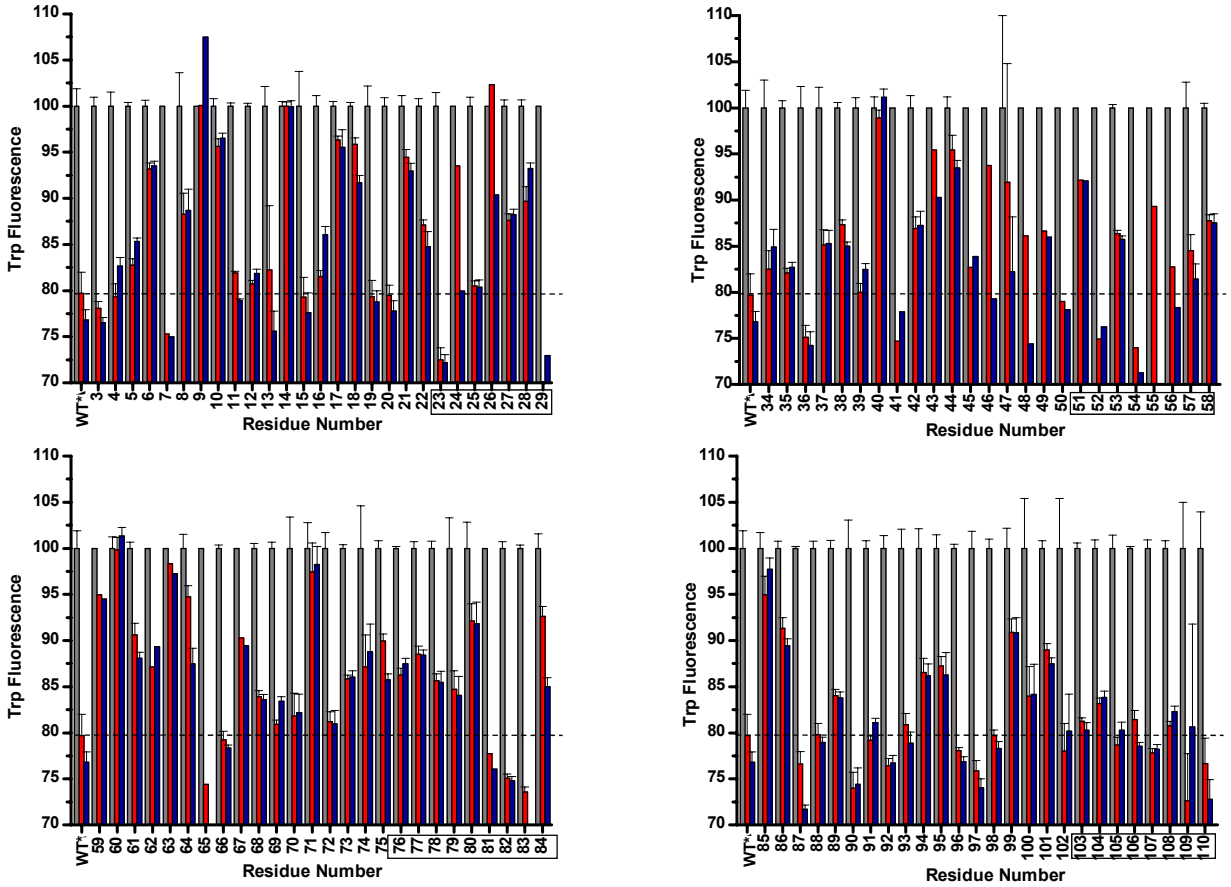

Figure 3: *In vitro* functional activity of each spin label mutants of EmrE.
A bar graph of the Trp fluorescence properties of each spin labeled mutants of EmrE shown in the absence (grey), or in the presence of saturating amount of TPP^+, 6 μM and 12 μM, shown in red and blue bar graph, respectively. The four graphs signifies the location of the mutants; upper left panel is the TM1, upper right panel is TM2, lower left panel is TM3, and lower right panel is the TM4 mutants. The loop region is outlined by a rectangle for each of the TMS. The horizontal dotted grey line shows the cutoff of the quenching in comparison to WT*.

This is the only tryptophan in EmrE that could sense substrate binding and/or conformational change following the binding reaction (Elbaz et al., 2005). For each spin labeled mutant the magnitude of the decrease in the fluorescent intensity compared to the cysless-EmrE (WT*) was collected (Figure 3).

The addition of saturating amounts of TPP^+ to the WT* induced significant quenching (~22 %) of the Trp fluorescence (Figure 3) with no detectable shift in the emission maxima, suggesting that there are no major changes in the hydrophobic environment. The majority of the spin labeled mutants seems to show relative quenching with respect to its apo-state, with the exception of some mutants that will be described below.

The tryptophan at position 63 is conserved in the SMR family of transporters, for which, Trp quenching is only observed at higher concentrations of TPP^+, as shown in Figure 3. This confirms that the tryptophan at position 63 is involved in the function of the protein and most likely in substrate binding. Moreover, the *in vivo* activity shows that W63C has a damaging effect on the resistance to ethidium, suggesting that this site is important in both binding and translocation of the substrate. Similarly, for E14C-SL, a residue that is an absolute requirement for substrate binding and translocation, the addition of saturating amounts of substrate did not change the fluorescence with respect to its apo-state. In the case of sites 40, 44, and 60, the addition of TPP^+ showed similar Trp emissions to their apo-state. However, Trp quenching is restored by increasing the concentration of EmrE and TPP^+ as shown in Figure 4, suggesting that the three mutant sites reduce the affinity for TPP^+.

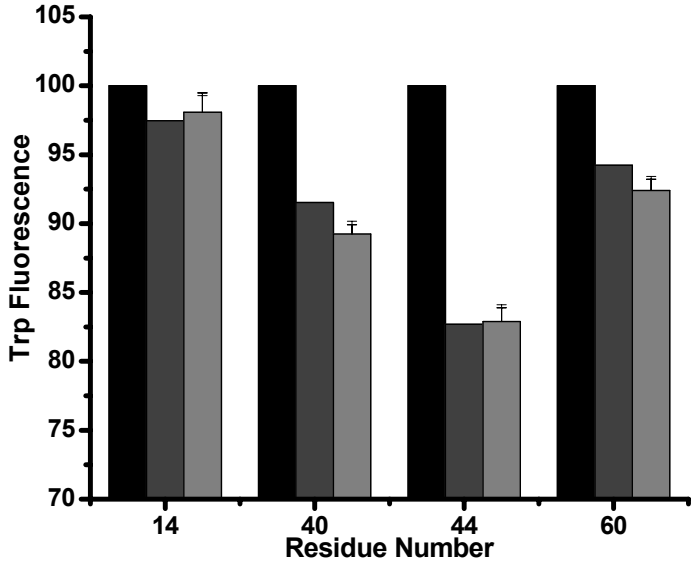

Figure 4: *In vitro* functional activity of spin label mutants using higher concentrations of EmrE. The bargraph represents the apo-state EmrE (black bar) and in the presence of 4x (dark grey) and 6x (ligh grey) molar excess of TPP^+.

Generally, the *in vitro* functional study is well correlated with the *in vivo* data, suggesting that the mutants of EmrE in detergent micelles have similar functional characteristics to those of the mutants in cells.

Conclusion

In this chapter, each of the cysteine mutants of EmrE was characterized using a qualitative *in vivo* assay. Some of these mutants located in TM1, TM3 and TM4 were nonfuctional, which suggests that they might play a role in either insertion, stability of folding, or in the catalytic cycle. On the other hand, TM2 cysteine mutant sites were fully functional, suggesting that these sites do not play a role in the translocation of the substrate but may play a role in stabilizing the substrate prior to translocation.

The oligomeric state of spin labeled cysteine mutants of each of the 110 sites of EmrE were analyzed and compared to its unlabeled cysless-EmrE (WT*) using size exclusion chromatography (SEC). Most of the purified spin labeled mutants had similar retention times to WT*, suggesting that the oligomeric state was not perturbed. However, certain sites located in TM4 showed an increase in the aggregation fraction compared to that of WT*, suggesting a change in the oligomeric state of the protein. This result correlates well with the *in vivo* assay, suggesting that TM4 might play a role in folding.

Extracting and purifying WT* in different buffers showed that the eluted protein sample was unstable when using NG instead of β-DDM. This conclusion might imply that the crystal packing of EmrE in the dimer that is located in the unit cell is not the native-state of EmrE. This data is also supported by previous work suggesting that using NG decreases the fraction of the functional protein. The tryptophan fluorescence data of the spin labeled sites of EmrE showed that most of the mutants bind TPP^{+}.

CHAPTER V

CONFORMATIONAL DYNAMICS OF APO EMRE IN LIPID BILAYERS

Introduction

One of the challenges in crystallographie analysis of secondary multidrug transporters is their hydrophobic nature and flexibility. In the past decade, several crystal structures of secondary multidrug transporters were published such as Lactose permease (Lac Y) and EmrD (Abramson et al., 2003; Yin, He, Szewczyk, Nguyen, & Chang, 2006) from the MFS family, and AcrB from *E.coli* and MexB (Murakami, Nakashima, Yamashita, Matsumoto, & Yamaguchi, 2006; Sennhauser, Bukowska, Briand, & Grutter, 2009) from the RND family of transporters. The only published crystal structure of EmrE in the absence of substrate (apo-state) was soon retracted in 2006 due to faulty analysis of the software (Ma & Chang, 2007).

One of the first models of EmrE in the apo-state was determined by cryo-EM and image reconstruction of 2D crystals (Tate et al., 2001). The projection map with overall dimensions of approximately 31 x 40 Å at 7 Å resolution (see Figure 5, Chapter I) was shown to represent an asymmetric dimer related by a 2-fold axis in the plane of the membrane with no obvious 2-fold symmetry axis perpendicular to the membrane. Thus, the monomers have identical amino acid but do not have identical structures in the functional unit.

In 2003 Tate and colleagues determined the three dimensional structure of EmrE in the substrate bound-state from 2-D crystals at 7.5 Å. The substrate-bound EmrE crystal was more ordered and well defined than the apo-state crystals. Nevertheless, the projection of the substrate bound-state was proposed to be identical to the apo-state. The asymmetric homodimer of EmrE was composed of eight transmembrane helices (TM) in total (four TM helices from each monomer) (Ubarretxena-Belandia et al., 2003). The low resolution of the structure made it difficult to assign the helices to specific segment of primary structure. Yet, the presence of a pseudo two fold axis in the plane of the membrane suggested novel architecture of the two monomers consisting of an antiparallel dimer.

In 2007 the crystal structure of the apo-state of EmrE was recalculated by using anomalous diffraction from mercurial derivatives to 4.5 Å resolution (Y. J. Chen et al., 2007), Figure 1A. The asymmetric units contained distorted monomers. The first three helices form a three-helix bundle that packs against the equivalent helices forming a dimer.

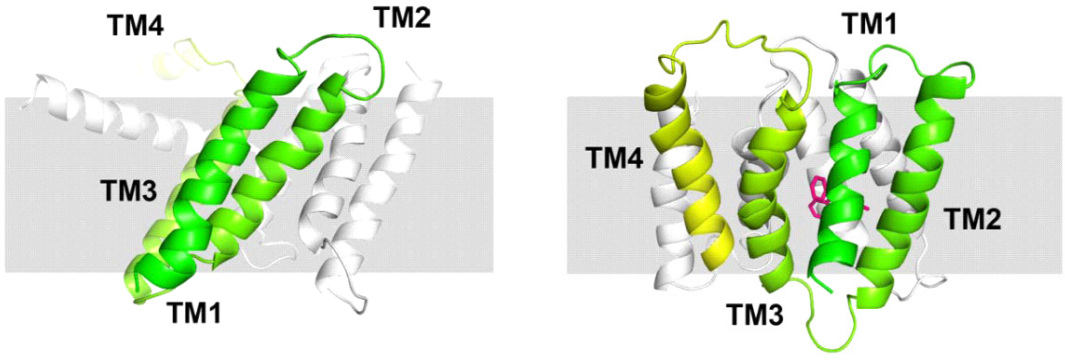

Figure 1: Crystal structures of EmrE. (A) Ribbon representation of the distorted apo-EmrE dimer. One monomer is rendered in color gradient with the TM helices labeled, and the other monomer is shown in grey. **(B)** Side view of EmrE-TPP^+ dimer. The dimensions of the bilayer are shown by the gray shading (Y. J. Chen et al., 2007).

The fourth helix from each monomer interacts with one another and project laterally from the main body of the dimer. Since the apo-EmrE was crystallized at pH 4, it was proposed that the non-native conformation reflects partial denaturation of the protein. Indeed, our size exclusion chromatography data (see Chapter IV) suggests that the dimer dissociates in the detergent (nonyl-glucoside) used for crystallization. To date, the crystal structure of native EmrE in the apo-state has not been published where the resolution was high enough to confirm not only the packing of the helices, but also the location of the amino acids and their contributions to the substrate binding site.

To gain insight into the conformation of EmrE in liposomes (a native like-environment), the structural dynamics of EmrE were investigated using site-directed spin labeling (SDSL) and EPR spectroscopy. Both spin label motion and solvent accessibility which reflect local environment in the dimer, were analyzed. The analysis distinguishes sites that are either at the dimer interface, buried within the protein, exposed to the aqueous environment or to the membrane milieu. In this chapter a thorough investigation of spin label mobility and accessibility to oxygen and NiEDDA is reported to deduce the structural dynamics from an EPR perspective and compare it to the overall crystal structure of the substrate bound-state.

Experimental Methods

EPR spectra of spin labeled mutants reconstituted in liposomes were collected on a Varian E9 equipped with a loop gap resonator as described in chapter II. Power saturation was performed on Bruker Elexsys spectrometer equipped with a dielectric resonator; the $P_{1/2}$ was obtained by curve fitting to the equation:

$$A = \frac{I\sqrt{P}}{\left(1 + \frac{\left(2^{1/\varepsilon} - 1\right)P}{P_{1/2}}\right)^{\varepsilon}}$$

where A is the peak-to-peak amplitude, ε is the line shape adjustment parameter, I is the scaling factor, $P_{1/2}$ is the half saturation power, and P is the power of the incident electromagnetic wave.

The solvent accessibility data of each position in the segment was mapped onto the crystal structure of EmrE in the substrate bound-state (Y. J. Chen et al., 2007) using the UCSF Chimera package from the Computer Graphic Laboratory, University of California, San Francisco (Pettersen et al., 2004; Sanner, Olson, & Spehner, 1996).

The immersion depth (Φ) was calculated using the equation:

$$\Phi = \ln\left(\frac{\Pi(O_2)}{\Pi(NiEDDA)}\right)$$

The immersion depth is related to the standard state chemical potential of the reagent at any depth, independent of viscosity or steric constraints forced by the environment and also independent of the EPR lineshape. Therefore, the ratio of two paramagnetic reagents such as oxygen and NiEDDA would relate to the relative measure of depth in the bilayer, that is, on distance through the concentration gradient (Altenbach, Greenhalgh, Khorana, & Hubbell, 1994).

Results and Discussion

EmrE Structural Constraints

CW EPR spectra of the spin labeled EmrE mutants in the apo-state along the full length of the protein were recorded at room temperature. The regions include TM1 (residues 3 to 22), loop 1 (residues 23 to 29), TM2 (residues 30 to 49), loop 2 (residues 50 to 58), TM3 (residues 59 to 75), loop 3 (residues 76 to 84), TM4 (residues 85 to 103), and loop 4 (residues 104 to 110).

The local steric restrictions on the mobility of the nitroxide probe is reflected in the EPR spectral line shapes shown in Figures 2, 4, 6, and 9. The mobility refers to the reorientation of the spin label relative to the protein backbone. In a sterically packed environment such as the protein core, the spin label will have restricted mobility leading to spectral broadening and the appearance of outer splittings as described in Chapter II. On the protein surface, the lack of tertiary contacts results in high mobility. The mobility can be quantified by the inverse of the central resonance line width (ΔH_o^{-1}). ΔH_o^{-1} values for each TMS of EmrE are shown in Figures 3 A, 5 A, 8 A, and 10 A.

Additional information can be obtained by investigating the accessibility parameter (Π) of the spin label to reagents of different solvation. The two reagents that were used are molecular oxygen, which is highly soluble in the low dielectric lipid environment, and NiEDDA (Nickel(II)ethylenediaminediacetate), a water-soluble reagent. Each transmembrane helix will have an accessibility pattern that describes its position relative to the bilayer. High oxygen accessibility indicates that the nitroxide spin label is exposed to the lipid bilayer, while high NiEDDA accessibility signifies the exposure of the nitroxide spin label to the aqueous environment. NiEDDA and oxygen

accessibility (Π(NiEDDA) and Π(O_2)) (see chapter II for the definition of Π) profiles of the full length reconstituted EmrE in the apo-state for each of the four helices are shown in the lower panel of Figures 3 B, 5 B, 8 B, and 10 B.

Mobility and Accessibility of Transmembrane Helix One (TM1)

The profiles of the mobility, NiEDDA and oxygen accessibility of TM1 in detergent micelles have been previously published (Koteiche et al. 2003). A visual inspection of the EPR spectral line shape of TM1 in liposomes, as shown in Figure 2, reveals that residues on the same side of the helix (i, i+4) relative to site 3 are in tertiary contacts leading to an immobilized line shapes. Sites 6, 10 and 14, which are on the same side of the helix, show a gradual increase in steric constraints at the dimer interface to a point where the two spin labels are close enough to be within van der Waals contact at position 14. Along this face of the helix, EPR spectra at sites 14 and 18 show strong dipolar coupling. The EPR spectrum of 14 show a broad (arrows, shown in Figure 2) and a narrow component reflecting two populations of spins each separated by a different distance. The broad component feature was suggested to represent two spin labels in close proximity (Koteiche et al., 2003; McHaourab et al., 1997), whereas the narrow component represents spins that are separated by distance of ≥ 20 Å. Moreover, the spectrum of T18C-SL shows a broadening of the spectrum that falls in the range of ≤ 15 Å in distance.

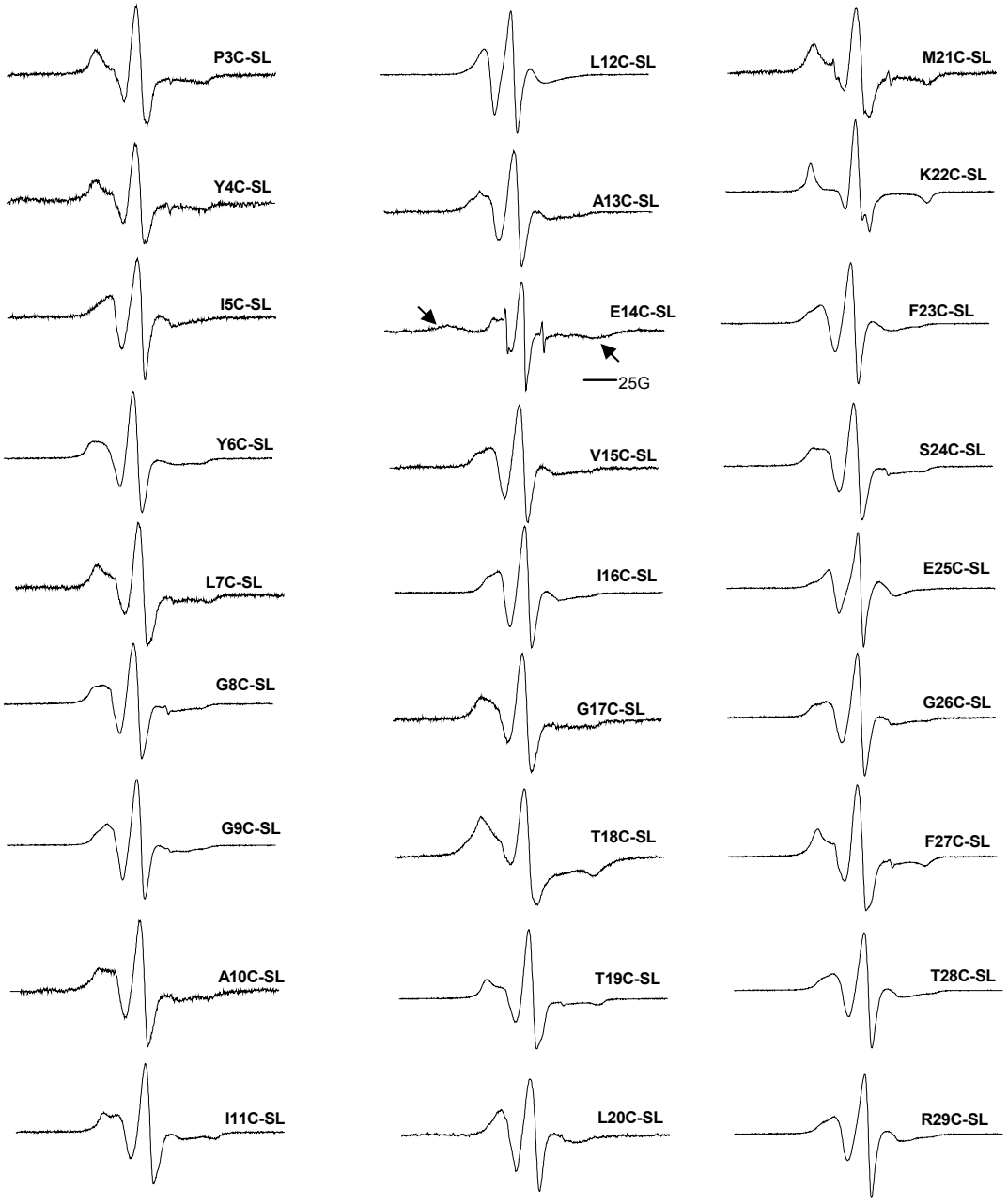

Figure 2: EPR spectra of TM1. X-band CW EPR spectra of EmrE mutants along TM1 (residue 3 to 22), and Loop 1 (residues 23 to 29) reconstituted in liposomes. All spectra were recorded with a 160 G scan width with the exception of site 14 was recorded with a scan width of 250 G.

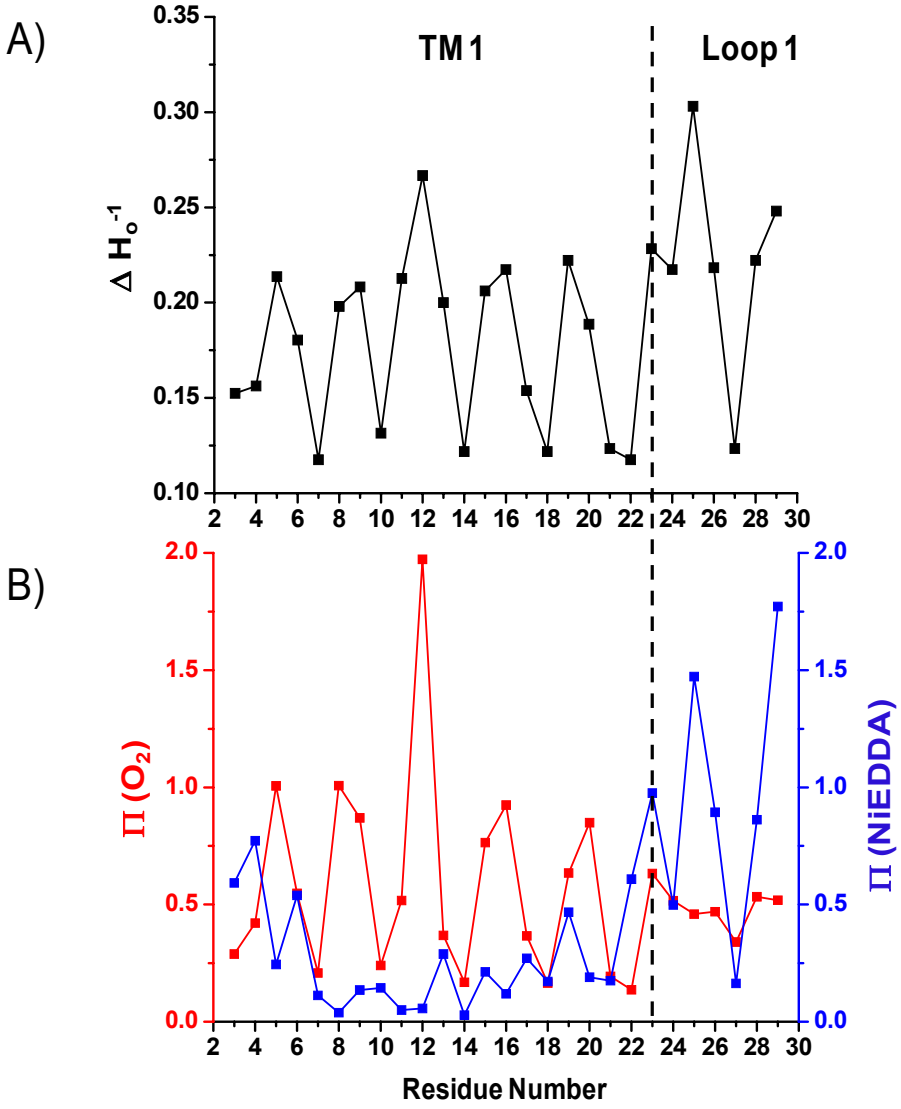

Figure 3: Mobility and accessibility profile of TM1. A) Inverse central linewidth (ΔH_o^{-1}). **B)** O_2 accessibility ($\Pi(O_2)$, red), and NiEDDA accessibility (Π (NiEDDA), blue) parameters along TM1 (3-22), and Loop 1 (23-29) reconstituted in liposomes. The different regions are separated by a vertical black dotted line.

Sites 21 and 22 that are one turn away from site 18 show a highly immobilized EPR spectral line shape as reflected by the prominent outer splittings at the low and high field extrema. The lack of spin-spin coupling emphasizes that sites located at the C-terminal are further apart from the dimer interface and are interacting with other helices in the

vicinity of TM1. Conversely, sites 12, 15, 16, and 20 and the loop region 23 to 29, with the exception of site 27, show little, if any restriction in mobility. These results support the conclusion previously proposed (Koteiche et al., 2003), that TM1 is in an X-shaped arrangement where the close contact of sites 14 and 18 at the dimer interface would be lining the binding chamber.

In Figure 3, both mobility (ΔH_o^{-1}) and oxygen accessibility indicate a 3.6 residue periodicity along TM1 reflecting an α-helical secondary structure. Furthermore, the oxygen accessibility ($\Pi(O_2)$) profile shows increasing amplitude at successive maxima reflecting the oxygen concentration gradient towards the middle of the lipid bilayer. The highest $\Pi(O_2)$ is at residue 12 which also possesses a highly mobile spectral line shape indicative of a residue facing the lipid milieu near the middle of the bilayer. Therefore, site 12 provides the reference position of the protein relative to the middle of the lipid bilayer. Residues with maximum oxygen accessibility such as 5, 8, 12, 16, and 20 face the lipid bilayer and have high spectral mobility (ΔH_o^{-1}). The helical surface defined by oxygen accessibility minima at residues 10, 14, and 18 seem to participate in tertiary contacts.

In the loop region connecting TM1 to TM2 following residue 22, the periodicity is lost and the spin label mobility is uniformly high. Sites 25 and 29 show the highest NiEDDA accessibility, suggesting that these two sites are located beyond the lipid-water interface. Only residue 27 in this loop shows low NiEDDA accessibility. Coincident low mobility suggests that the spin label at this position is in tertiary contacts with the surrounding region. Overall, the accessibility parameters are in good agreement with the CW-EPR spectral line shape. Also, the results of the liposomes samples of TM1 are

similar to the published data of the spin labeled samples in detergent micelle (Koteiche et al., 2003).

Mobility and Accessibility of Transmembrane Helix Two (TM2)

The loop merges into transmembrane 2 at around residue 30 where distinct 3.6 residue periodicity in $\Pi(O_2)$ resumes. In Figure 4 highly mobile spectral line shapes are observed at the N-terminal region of TM2, sites 30 to 35, suggesting that the spin labeled sites are undergoing fast motion with no tertiary contacts. This conclusion is also supported by high accessibility to oxygen observed on both faces of the helix (grey dotted vertical lines in Figure 5B). In contrast, the following helical turns show distinct evidence of tertiary contacts. Immobilized line shapes and low oxygen accessibility define the packed face of TM2 consisting of residues 36, 40, 44, 47, and 51. Distinct dipolar splittings are observed in the EPR spectrum for sites 40 and 44 indicating an inter-probe distance of less than 10 Å. Furthermore, both sites have low oxygen accessibility consistent with a buried environment.

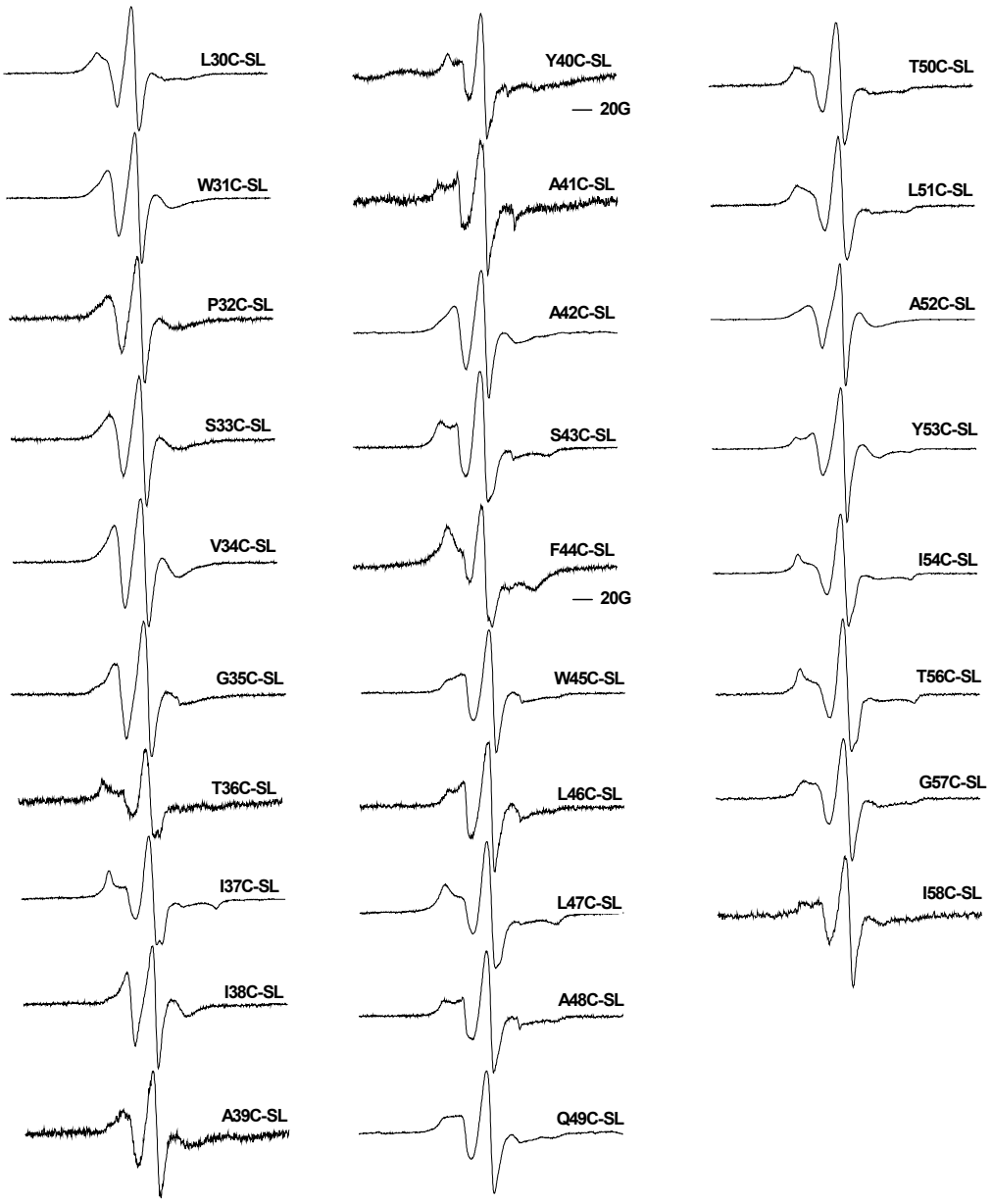

Figure 4: EPR spectra of TM 2. X-band CW EPR spectra along TM2 (residue 30 to 49), and Loop 2 (residues 50 to 58) reconstituted in liposomes. All spectra were recorded with a 160 G scan width with the exception of sites 40 and 44 were recorded with scan width of 200 G.

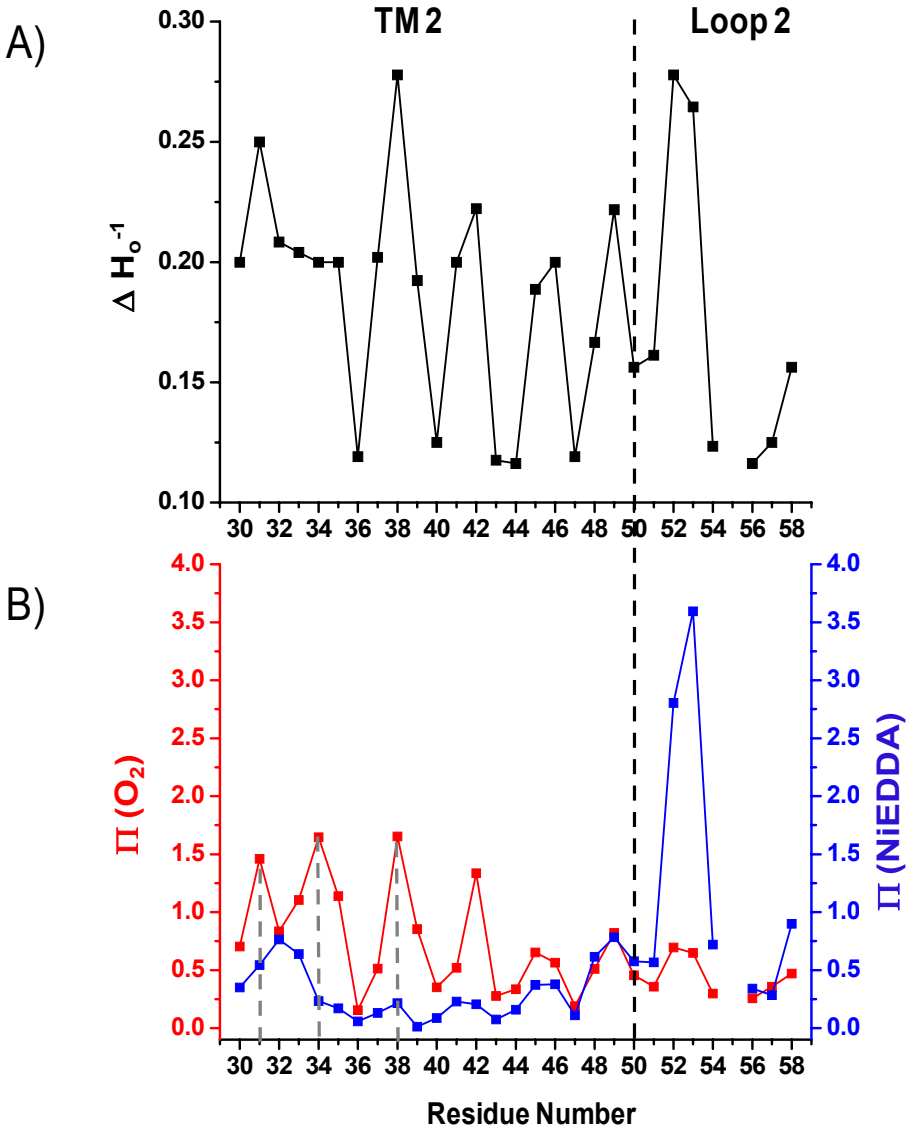

Figure 5: Mobility and accessibility profile of TM2. A) Inverse central linewidth (ΔH_o^{-1}). **B)** O_2 accessibility ($\Pi(O_2)$, red), and NiEDDA accessibility (Π (NiEDDA), blue) parameters along TM2 (30-49), Loop 2 (50-58) of EmrE. The different regions are separated by a vertical black dotted line.

A loss of the 3.6 periodicity is observed in the oxygen accessibility profile for sites 51-58. These sites are in the loop region connection TM2 to TM3. In parallel, NiEDDA accessibility increases at sites 52 and 53 suggesting locations well beyond the membrane-water interface compared to the other loops of EmrE that seem to be localized at the membrane interface. Sites 54 to 58 report extensive motional restriction that is reflected by a decrease in Π(NiEDDA) suggesting that the loop is located in the lipid bilayer connecting to TM3.

Mobility and Accessibility of Transmembrane Helix Three (TM3)

The N-terminal regions of TM3 from both monomers are in close proximity, as reflected by the broadened spectral line shape at positions 60 and 64 (see Figure 6). The side chains of residue 64 are within 6.9 Å in the crystal structure as a result of a distortion of one of the helices (Figure 7). Furthermore, the N-termini of these antiparallel helices are pulled towards the middle of the membrane bringing residue 60 from each monomer into close proximity. Agreement with the EPR data requires helix rotation to allow for the projection of the spin labels towards each other. Further down the TM helix, residue 68 which faces the same side of the helix as 60 and 64 does not show evidence of spin-spin coupling suggesting that only the first turn of TM3 helices are in close contact at the dimer interface. However, the spin label at this site has low mobility (ΔH_o^{-1}) and low oxygen accessibility (see Figure 8 A and B, respectively) consistent with tertiary contacts.

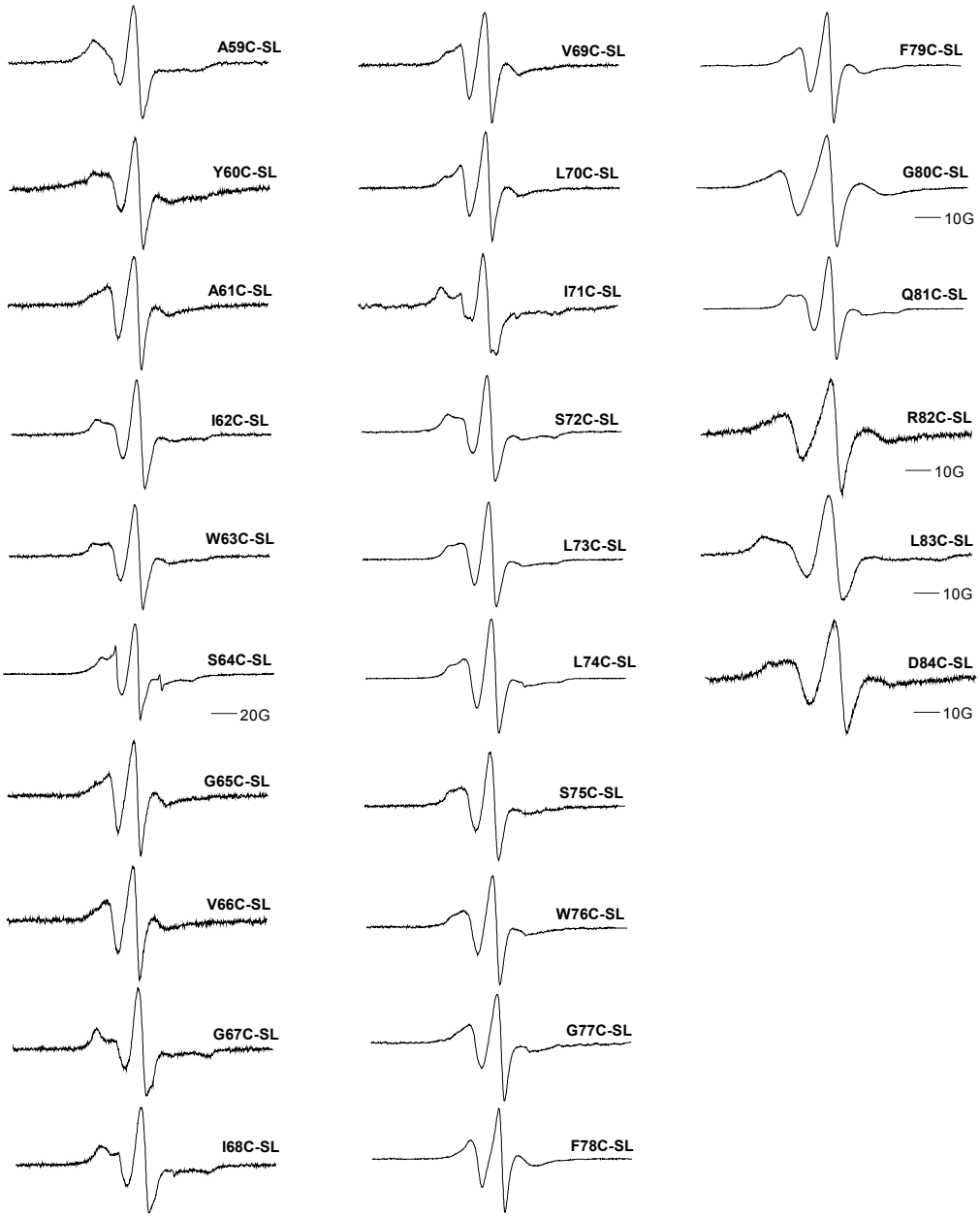

Figure 6: EPR spectra of TM 3. X-band CW EPR spectra along TM3 (residue 59 to 75), and Loop 3 (residue 76 to 84) reconstituted in liposomes. All spectra were recorded with a 160 G scan width with the exception of site 64, which was recorded with a scan width of 200 G, and sites 80, and 82-84 were recorded with scan width of 100 G.

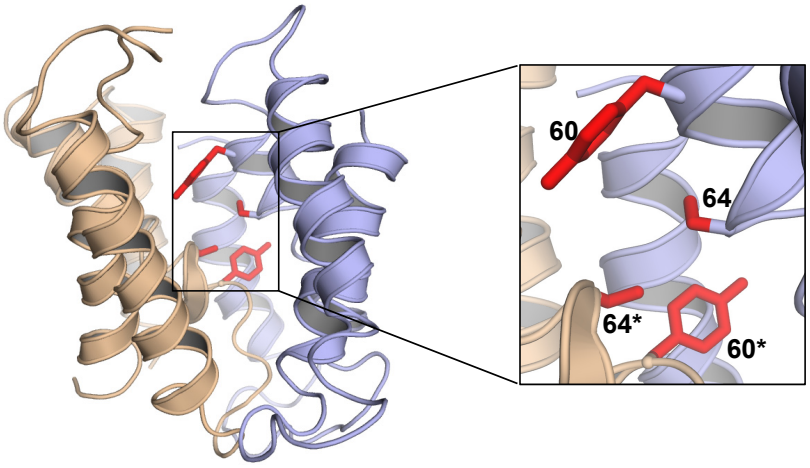

Figure 7: Location of residues 60 and 64 in the crystal structure. The two monomers are shown in blue and wheat. Residues 60 and 64 are represented in sticks (red). The residue in the second monomer is shown in asterisks.

Maximum oxygen accessibility is observed at positions 65, 66, 69, and 70, defining the helix surface facing the lipid bilayer and coinciding with the highest mobility (ΔH_o^{-1}). Based on the crystal structure, the C-terminal turns of TM3 are expected to be closer to the lipid-water interface leading to a decrease in oxygen accessibility. This was not the case, since spin labeled sites 72 to 76 are highly mobile, report a high level of oxygen accessibility, and a loss of the 3.6 periodicity of the α-helix secondary structure. These interesting characteristics suggest that this small segment is not helical and is exposed to the lipid bilayer. This may indicate that the loop region following TM3 is longer than expected, starting in the lipid bilayer at site 73 and continues towards site 79, where it reaches the lipid-water interface. A gradual increase is detected in NiEDDA accessibility, with spin labeled site 80 showing the maximum collision rate. The loop reenters the lipid bilayer at site 81 to 84, where a decrease in NiEDDA accessibility and an increase in steric restrictions are observed.

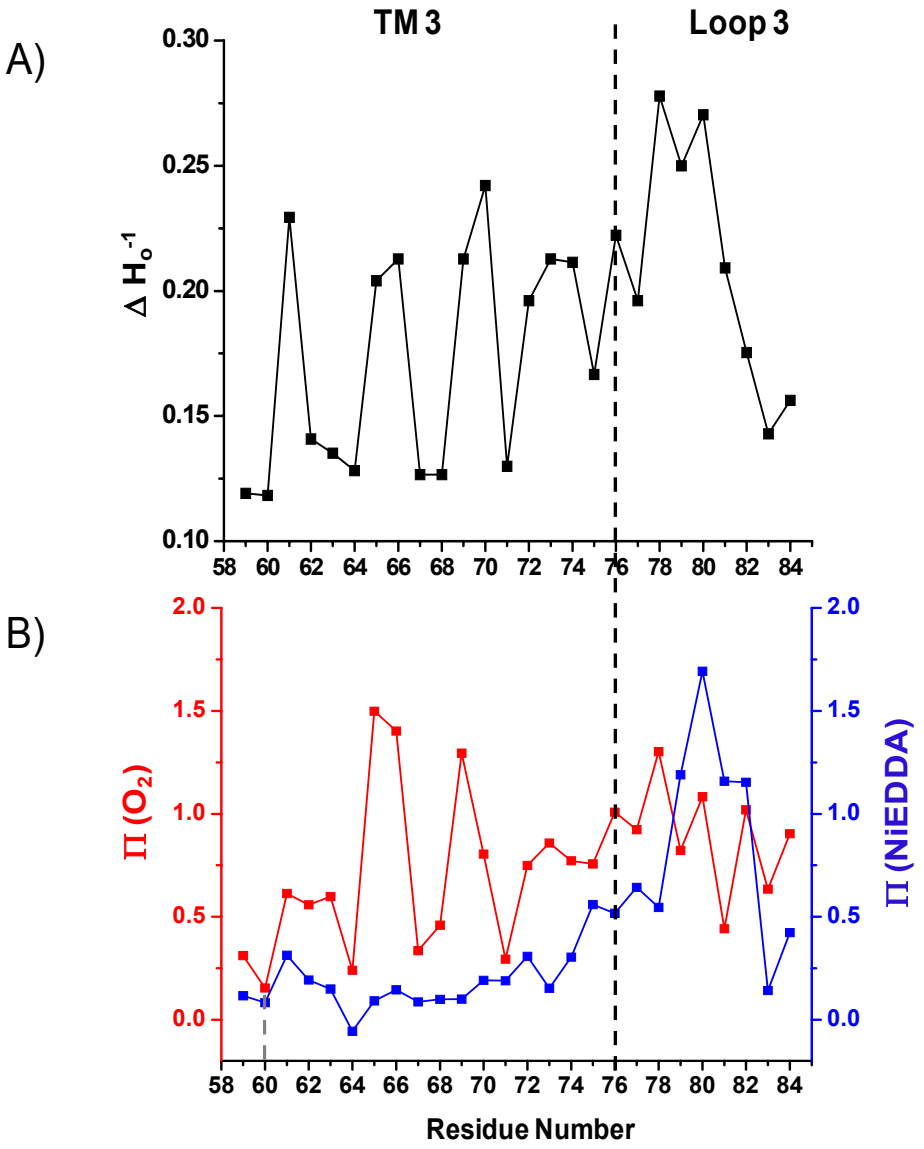

Figure 8: Mobility and accessibility profile of TM3. A) Inverse central linewidth (ΔH_o^{-1}). **B)** O_2 accessibility ($\Pi(O_2)$, red), and NiEDDA accessibility (Π (NiEDDA), blue) parameters along TM3 (59-75), Loop 3 (76-84) of EmrE. The different regions are separated by a vertical black dotted line. The vertical grey line indicates the only site that is close at the dimer interface.

In general, TM3 is highly hydrophobic and from the mobility analysis appears to be surrounded by other helices. Furthermore, the loss of periodicity between sites 73 and 76 suggests that TM3 has either a specific motif (such as a helix-turn-helix or a helix-

loop-helix) or it may be that TM3 is shorter than the crystal structure predicts. In the latter case, a longer loop connecting TM3 to TM4 extends from the lipid bilayer at site 73 and moves toward the aqueous environment at position 80.

Mobility and Accessibility of Transmembrane Helix Four (TM4)

The crystal structure and the low resolution model constructed from cryo-electron crystallography data placed both TM4 helices at the dimer interface (Chen, et al. 2007, and Tate, et al. 2001, Figure 5, Chapter I). However, no spin-spin interactions between symmetry-related nitroxides across the dimer interface were detected along this helix (see Figure 9). This would be especially evident at 93 and 97 since these two residues are in close proximity in the crystal structure, with Cα distances of 10.5 Å and 6 Å, respectively. However, this was not reported from the EPR spectral line shape, leading us to hypothesize that the packing of TM4 segments in the apo-state in solution is different from the proposed crystal structure of the substrate bound-state.

The accessibility data in Figure 10 B shows that residues 89, 93, 96, and 99 are facing the lipid bilayer, and have similar high values of $\Pi(O_2)$. Moreover, both EPR spectral line shapes and (ΔH_o^{-1}) (Figure 10 A) suggests that these sites do not have extensive tertiary contacts.

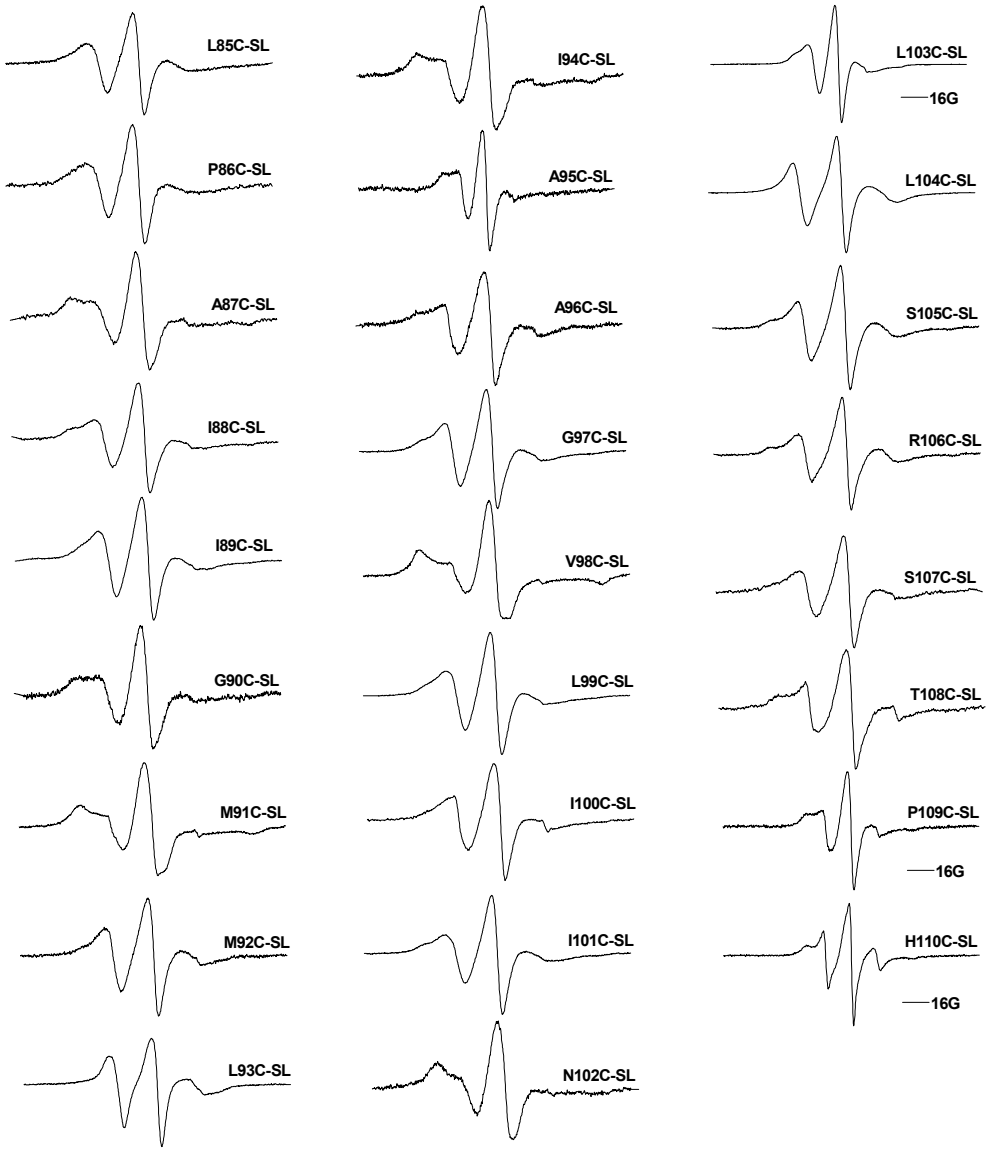

Figure 9: EPR spectra of TM4. X-band CW EPR spectra along TM4 (residue 85 to 103), and Loop 4 (residue 104 to 110) reconstituted in liposomes. All spectra were recorded with a 100 G scan width with the exception of sites 95, 103, 109, and 110 were recorded with scan width of 160 G.

Conversely, sites 87, 91, 94, 98, and 102 have similar low Π(O2) characteristics of sites that are in tertiary contacts, according to the immobilized spectral line shape (Figure 9). Thus, the accessibility data along TM4 suggests that one side of the helix is lipid facing while the other side is in tertiary contacts with other protein segments. It is possible that TM4 is tilted more than 11° relative to the membrane normal (Ubarretxena-Belandia et al., 2003), resulting in similar oxygen accessibility for the sites facing the membrane lipid bilayer.

The values of NiEDDA accessibility at the N-terminal of TM4 (residues 85-88) are higher than for sites 89-99, suggesting that the N-terminal region is near the lipid-water interface. Conversely, the C-terminal region (103-110) shows the highest NiEDDA accessibility especially for sites 106 and 109 indicative of sites beyond the lipid-water interface. Thus, it could be that the sites beyond 103 are in the loop region or represent an extended TM4 helix.

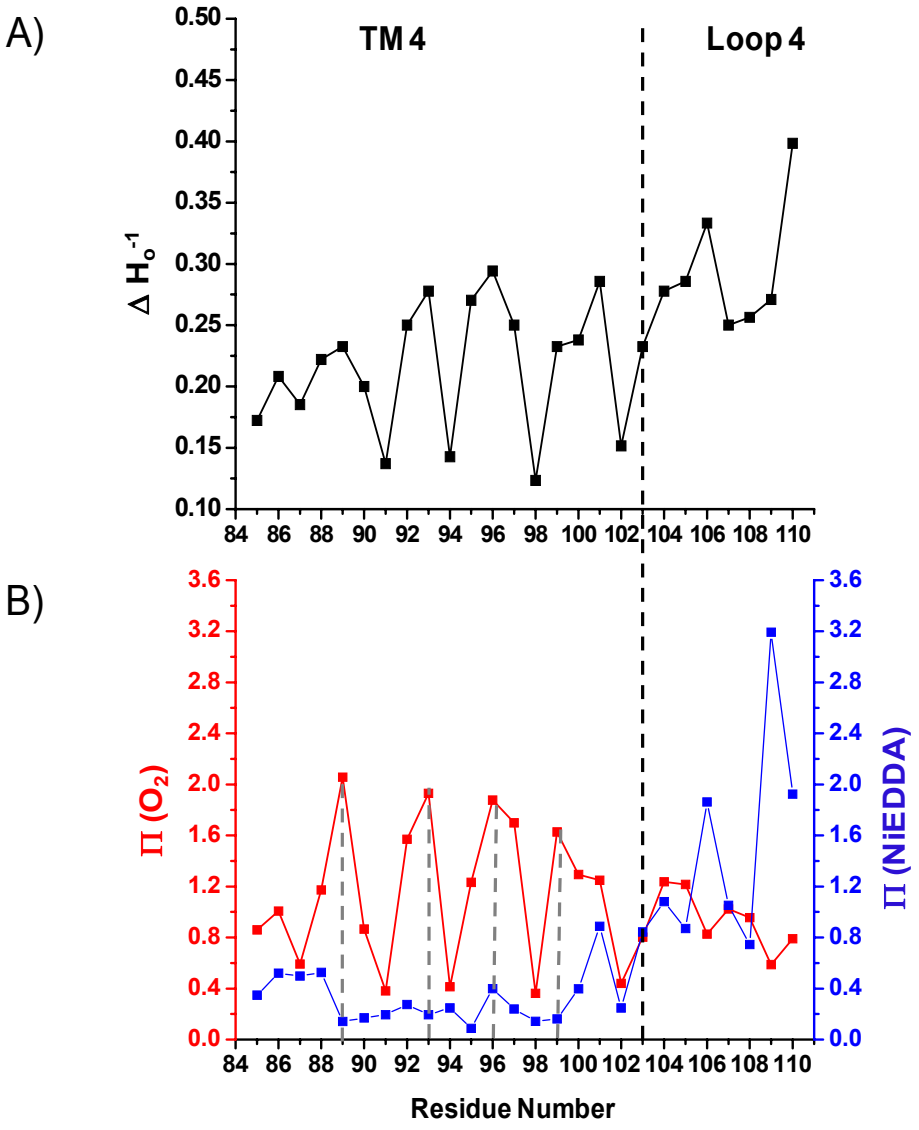

Figure 10: Mobility and accessibility profile of TM4. A) Inverse central linewidth (ΔH_o^{-1}). **B)** O_2 accessibility ($\Pi(O_2)$, red), and NiEDDA accessibility (Π (NiEDDA), blue) parameters along TM4 (85-102), Loop 4 (103-110) reconstituted in liposomes. The different regions are separated by a vertical black dotted line. The vertical grey lines indicate the sites that are facing the lipid bilayer.

EmrE Topology within the Lipid Bilayer

Even though the collision frequencies of NiEDDA along the transmembrane segments of EmrE are low, there is still evidence that some regions along the transmembrane segments are in contact with the aqueous phase as described in the accessibility sections. Overall, the four transmembrane segments of EmrE are highly hydrophobic as shown by the environmental parameters of oxygen and NiEDDA accessibility. The results are supported by several other published works (Edwards & Turner, 1998; Schwaiger et al., 1998) emphasizing the hydrophobic nature of EmrE.

The length of each helix of EmrE was estimated from the periodicity of the accessibility data (see Table 1, below) that was described in the previous sections.

TMS	Amino acid length	Length of TMS (Å)
1	20	28.5
2	20	28.5
3	17	24
4	19	27

Table 1: Length of the transmembrane segments (TMS) from the experimental data of EmrE.

The thickness of the hydrocarbon core of the lipid membrane is ~30-40 Å (Jaud S, et al. 2009). On average a transmembrane segment of 20 amino acids would extend the full length of the lipid bilayer as long as the helix is parallel to the membrane normal (Jaud et al., 2009). Table 1 indicates that only TM1 and TM2 and TM4 extend across the full length of the lipid bilayer, while TM3 seems to be the shortest.

Another approach for localizing the transmembrane helices in the lipid bilayer is by using the immersion depth (Φ) in membranes. This measurement takes advantage of the concentration gradients of paramagnetic relaxing agents (O_2 and NiEDDA) in the lipid bilayer (Altenbach et al., 1994). Generally, a depth (Φ) of 0 indicates sites that are at the lipid-water interface, while a positive (Φ), indicates sites that are in the lipid bilayer. Depths were obtained for all the residues in TM1, 2, 3, and 4, as shown in Figure 11 A and B. TM1 and TM2 are the only two transmembrane helices that span the full length of the lipid bilayer. TM3 (Figure 11B) is in the lipid bilayer since all the spin labeled sites have positive immersion depth values. Given the disposition of the N-terminus of TM3 well below the membrane/water interface, it would be expected that the C-terminal would have negative immersion depth value. Our data suggests that this segment bends back towards the bilayer probably facilitated by a kink in the helix. This proposed configuration of TM3 rationalizes the distances between spin labels determined in Chapter VIII.

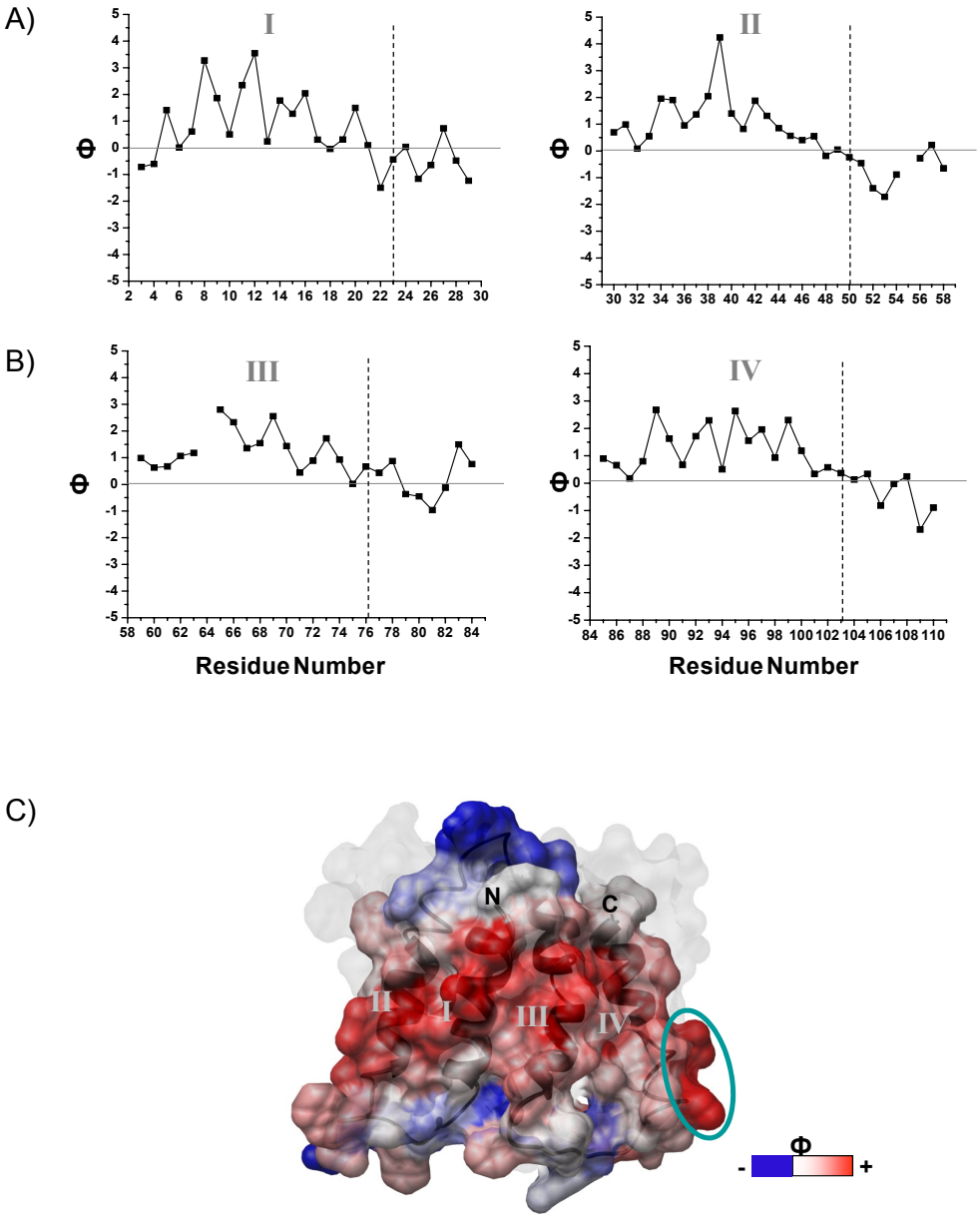

Figure 11: The immersion depth of the full length EmrE. A) The immersion depth (Φ) of TM1, and TM2. B) The immersion depth of TM 3, and TM4 (numbered in roman numerals). The grey horizontal line indicates the lipid-water interface. The separation of regions is shown by black vertical dotted line. C) The depth (Φ) of all 110 residues mapped on a surface representation of one subunit of the crystal structure. The second subunit is shown in grey surface. The cyan oval points to a region in the N-terminal of TM4, sites 89, 92, and 93. The depth (Φ) is represented by three colors: blue sites located in the aqueous environment, white sites in the lipid-water interface, and red sites located in the middle of the lipid bilayer. The N- and C-terminal of EmrE indicates by N and C.

The depth parameters were mapped onto the crystal structure of EmrE in the TPP^+ bound-state using UCSF Chimera package (Pettersen et al., 2004; Sanner et al., 1996), as shown in Figure 11 C. Segments located in the lipid bilayer are shown in red while those in water are colored in blue. The mapping reinforces the points discussed above including the discrepancy between the EPR parameters along TM4 and the crystal structure. The dark red color at the N-terminus of this helix (circled in cyan) indicates that this segment is deep within the lipid bilayer, whereas, in the crystal structure these sites are located near the lipid-water interface. In general, the accessibility, mobility, and depth data seem to confirm that the packing of TM4 in the lipid bilayer in the apo-state deviates from the helical packing of TM4 helices in the crystal structure of the substrate bound-state.

Mapping the Accessibility Data to the Crystal Structure of EmrE

Both oxygen and NiEDDA accessibility (Figure 12 and 13, respectively) were mapped onto the two asymmetric subunits of the crystal structure of EmrE in the TPP^+ bound-state using the UCSF Chimera (Pettersen et al., 2004; Sanner et al., 1996). There are multiple EmrE regions where the EPR parameters in the apo-state deviates from what are expected based on their environments in the crystal structure.

The oxygen accessibility (Figure 12) reports that one side of transmembrane helix one (TM1) is facing the lipid bilayer and samples the oxygen concentration gradient while the opposite side of the helix seems to show very low or no oxygen accessibility, such as residue E14 (Figure 12) supporting the crystal structure.

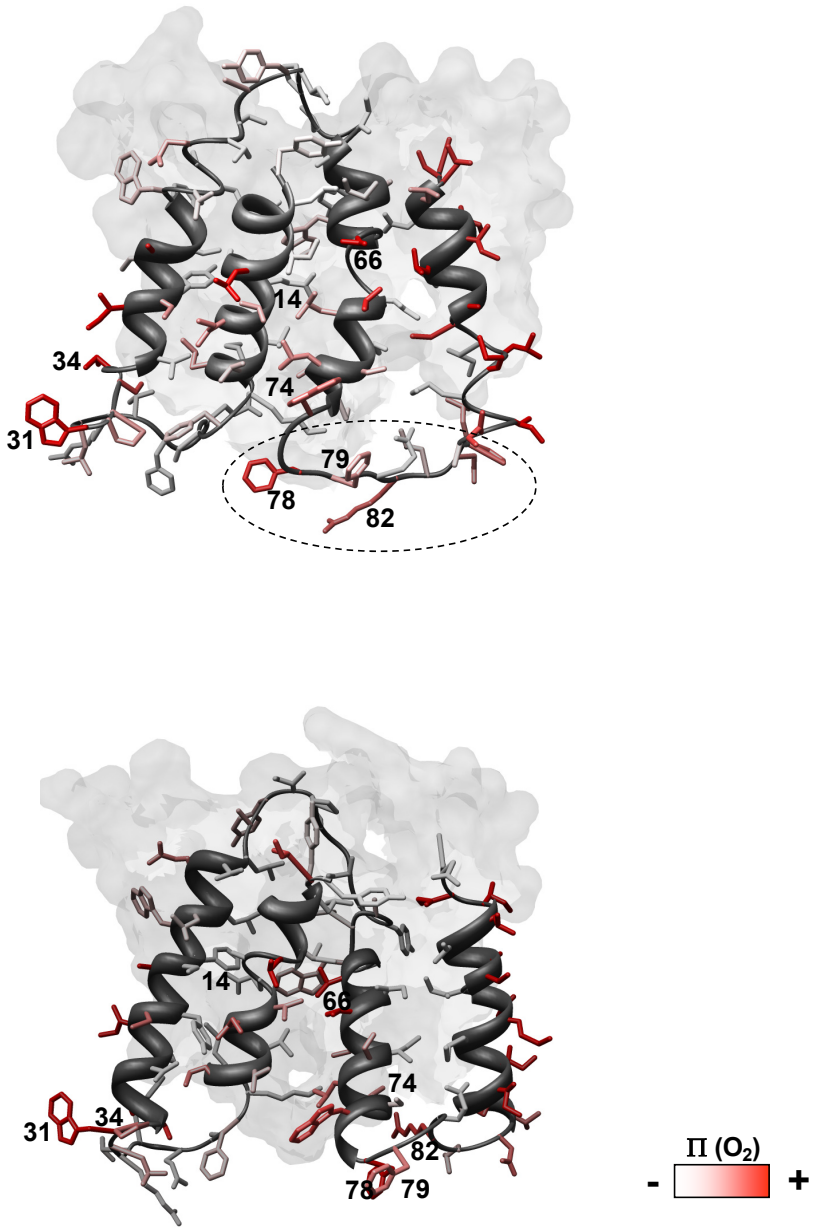

Figure 12: Mapping the oxygen accessibility of apo-EmrE onto the crystal structure of the TPP^+ bound-state. The $\Pi(O_2)$ data of the 110 sites (represented by sticks) of EmrE mapped on a surface representation of the two subunits (upper and lower panel) of the crystal structure. The second subunit in each panel is shown as a surface. The asymmetry in loop 3 from both subunits is shown in oval dotted line. The $\Pi(O_2)$ is encoded by two colors: white stands for small $\Pi(O_2)$; red stands for large $\Pi(O_2)$.

TM2 accessibility data in the absence of TPP^+ is not compatible with the disposition of TM2 in the crystal structure, suggesting a change of this segment upon substrate binding. The maximum oxygen accessibility is mapped to residues 34 and 38, yet according to the crystal structure, residues 31 and 34 are located in the loop region for one of the two monomers. The accessibility is in agreement with the CW-EPR line shape, signifying that the sites with high oxygen accessibility have a highly mobile spin labeled side chain, confirming that the N-terminus of TM2 is more tilted than what is reported in the crystal structure.

It has been suggested by the EM model that TM3 in one monomer has a tilt of 24° and in the second monomer 38°, with respect to the membrane normal (Ubarretxena-Belandia, et al. 2003). This was also supported by the crystal structure of the substrate-bound state superimposed on to the density map of the EM model (Y. J. Chen et al., 2007) showing that TM3 of one monomer seems to be less kinked than the segment in the second monomer. Thus, the inconsistency between the accessibility data and the crystal structure is well observed for residues 66 to 76, especially residue 74. It appears that these residues at the C-terminus having maximum oxygen accessibility are buried in the crystal structure while the minimas are lipid facing in the crystal structure. The discrepancy continues through the loop connecting to TM4 (76-84) where significant accessibility to O_2 and NiEDDA can only be rationalized by a highly dynamic backbone allowing large movement of the loop between the aqueous and the lipid environment. The asymmetry between the two monomers may have an important role in the mechanism of transport, where one monomer functions independently from the other.

Mapping TM4 oxygen accessibility data suggests that one side of the helix is exposed to the lipid bilayer while the other is in tertiary contacts. If TM4 is perpendicular to the membrane normal (as is shown for TM1), there would be a decrease in the collision rates with oxygen at sites further from the middle of the lipid bilayer. However, the pattern of oxygen accessibility is similar for the sites facing the lipid bilayer. This suggests that the TM4 segment is at a steep angle to the membrane normal, much higher than proposed by the EM model (Fleishman et al., 2006; Ubarretxena-Belandia et al., 2003).

The NiEDDA accessibility data were also mapped onto the crystal structure, as shown in Figure 13. In general, high NiEDDA accessibility signifies an area that is either in a cytoplasmic or periplasmic milieu. It is known that the NiEDDA accessibility is 180˚ out of phase in comparison to the oxygen accessibility for a symmetrically solvated helix that is perpendicular to the membrane normal (Hubbell et al., 1998).

When mapping the NiEDDA accessibility onto the crystal structure measurable collision to the reagent is observed mostly at the termini of TM1, TM2 segments at certain sites show minimal oxygen exposure. In contrast, the termini of TM3 and TM4 such as residue 79 to 82 seems to have measurable collision to both oxygen and NiEDDA (in phase) (see above for explanation).

The sites 103-105 that are located in TM4 shows high NiEDDA accessibility that could only be mapped to one monomer since these residues are not resolved in the other, suggesting a dynamic backbone. The data implies that TM4 is at an angle with respect to the membrane normal, therefore, residues 103-105 might well be at the lipid-water interface giving rise to a similar collision rate to NiEDDA and oxygen.

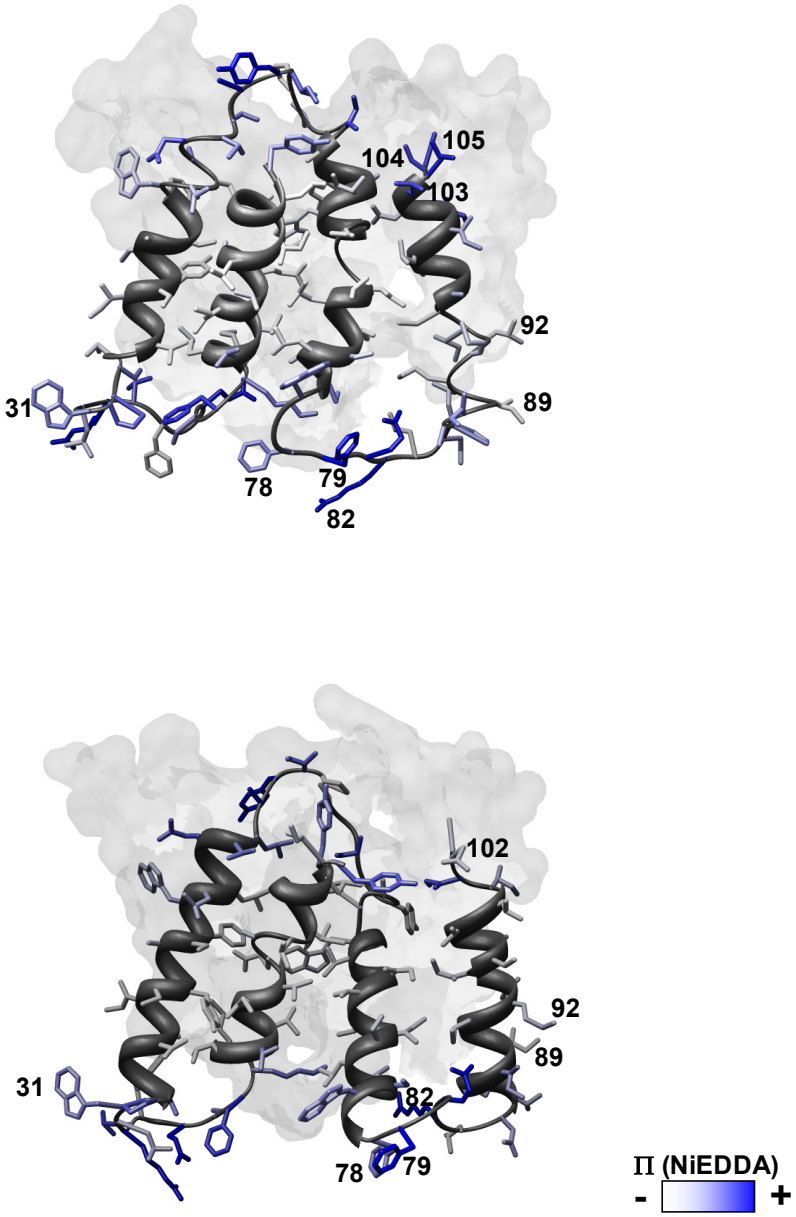

Figure 13: Mapping the NiEDDA accessibility of apo-EmrE onto the crystal structure of the TPP^+ bound-state. The Π(NiEDDA) data of the 110 sites (represented by sticks) of EmrE mapped on the two subunits (upper and lower panel) of the crystal structure. The second subunit in each panel is shown as a surface. The Π(NiEDDA) is encoded by two colors: white stands for a small Π(NiEDDA); blue stands for a large Π(NiEDDA).

The sites beyond 105 show an increase in NiEDDA accessibility that suggests that this part of the helix appears out of the lipid bilayer.

Conclusion

In this study, EmrE was reconstituted into liposomes which mimic the native environment. The purpose was to assess the similarity of the structural restraints obtained by EPR spectroscopy to the crystal structure of EmrE in the TPP^+ bound-state.

SDSL and EPR spectroscopy were used to study EmrE in liposomes in the apo-state and evaluate its conformational dynamics. The CW-EPR data of sites located in TM1, 2, and 3 confirms that the apo-state of EmrE exists as a dimer due to the dipolar interaction of certain sites that are in close proximity within the dimerization unit. The proximity along the three transmembrane segments appears to be consistent with the crystal structure. However, the flexibility of TM3 may account for the discrepancy between the EPR data and the crystal structure. Finally, the EPR data of TM4 sites suggest that they are futher apart at the dimer inteface than what has been proposed by the crystal structure of EmrE.

It is important to note that the reported results of the apo-state are compared to the crystal structure of the substrate bound state. Therefore, the inconsistencies between the EPR data and the crystal structure in this study may well be due to conformational changes that take place upon the binding of TPP^+. The experimental data of the substrate bound-state of EmrE will be assessed and analyzed in the next chapter.

CHAPTER VI

CONFORMATIONAL DYNAMICS OF EMRE UPON TETRAPHENYLPHOSPHONIUM (TPP^+) BINDING

Introduction

A number of studies have investigated the conformational changes of EmrE upon substrate binding (Korkhov & Tate, 2008; Tate et al., 2003). One of those studies reported a two dimensional crystal of EmrE bound to TPP^+ in the presence of lipid (Tate et al., 2003). The average images that were collected by electron cryo-microscopy of both the native EmrE and the substrate bound-state were compared (Figure 1). The differences in the density between the two images showed alteration in structural elements as a result of TPP^+ binding. Two density regions were associated with substrate binding. The first, a positive density (circled in red) predicted to be the bound TPP^+. The second, a positive density (circled in green) represents the movement of helix H, causing the ends of this helix to move away from the center of the EmrE dimer. The position of the TPP^+ along the axis perpendicular to the membrane plane was not certain due to the low resolution (Ubarretxena-Belandia et al., 2003). This small change was strikingly different from other family members of multidrug transporters that showed large conformational changes (Chang & Roth, 2001; Rosenberg et al., 2001).

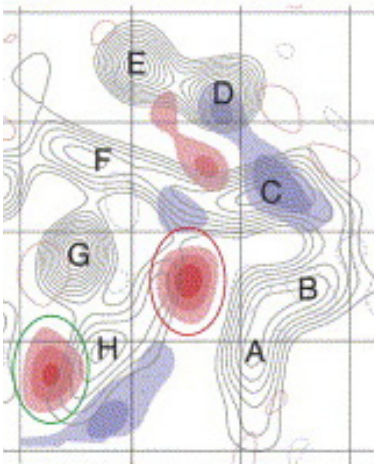

Figure 1: Structure of EmrE determined by cryo-EM. The density difference obtained by subtracting the native state EmrE and TPP^+ bound state. The positive differences are in red and negative differences are in blue. The density representing TPP^+ is ringed in red and the density difference identifying the conformational change in Helix H upon TPP^+ binding is ringed in green.

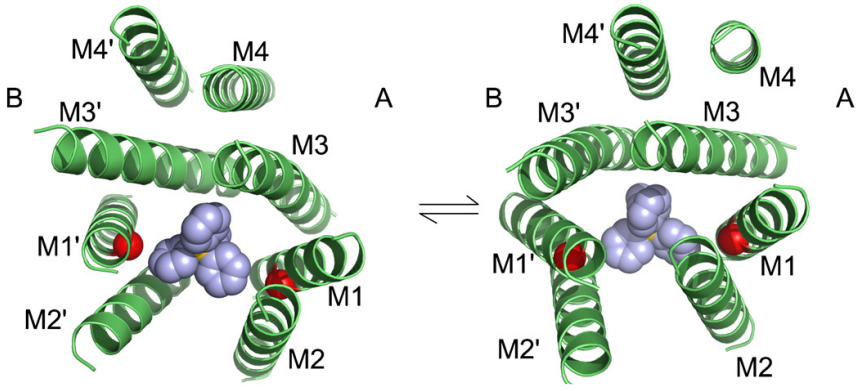

Cytoplasmic-facing **Periplasmic-facing**

Figure 2: Proposed model of conformational change of the EmrE dimer based on the cryo-EM structure during substrate binding and translocation. The cytoplasmic- and periplasmic-facing EmrE showing the two monomers (A and B) in green with red sphere indentifying E14. Each of the TM helices are assigned as M1-M4 for one monomer and M1'-M4' for the second monomer. TPP^+ is docked manually, shown in purple (Fleishman et al. 2006).

The second study was the published crystal structure of EmrE in the substrate bound-state (Y. J. Chen et al., 2007), that yielded a similar helix arrangements to the EM model mentioned above (Tate, 2006). In addition, the helices from the X-ray structure were superimposable on the EM model with an average root mean square deviation (rmsd) of 1.4 Å over equivalent Cα atoms. The crystal structure of the substrate bound-state was, however, different from the apo-state in pair-wise helix packing and the monomer/monomer packing interface. It was suggested that the apo-state crystal structure represents the minimal energy fold for helices 1-3 after *in vivo* synthesis (Korkhov & Tate, 2008) whereas helix 4 is in contact with neighboring crystallographic tetramer instead of a mobile transbilayer orientation (as shown in Figure 1, chapter V). This discrepancy between the apo-state and the substrate bound-state crystal structure (Y. J. Chen et al., 2007) provides compelling rational to investigate the conformational changes of EmrE upon the binding of the substrate.

From the model of TPP^+ bound EmrE (Fleishman et al., 2006) derived from the EM density, a mechanism of binding and translocation was proposed. In this model the drug binds to the cytoplasmic-facing binding pocket causing a conformational change which closes the cytoplasmic–facing binding pocket and opens towards the periplasmic side. It was suggested that the transition of the substrate from the cytoplasmic-facing to the periplasmic-facing EmrE involves three important structural changes. First, TM1-TM3 helices in both monomers reorient by ~20° with respect to the in-plane axis of symmetry. Second, TM3 undergoes kinking and straightening facilitated by a GXG motif. Third, there is small translation of TM1-3 in both monomers with respect to TM4 helices (Figure 2). The periplasmic and cytoplasmic facing conformation of the TPP^+

bound EmrE are essentially identical but rotated by 180° and would require a single substrate binding mode.

The model proposed above was based on the approximate positions of individual amino acids obtained only by biophysical experiments on EmrE and its homologues. Therefore, it was necessary in this chapter to make a detailed analysis of the conformational changes for each site of EmrE and its contribution to the binding of TPP^+ that will either support or contradict the models proposed.

The techniques used to explore the conformational changes of EmrE in a native-like environment produced by binding of the substrate TPP^+ are a combination of EPR-power saturation studies, lineshape analysis and double electron-electron resonance (DEER) spectroscopy experiments. The significance of this work lies in establishing the important conformational changes within the TM helices in the native-like environment of lipid bilayers.

Experimental Methods

EPR spectra were obtained on a Varian spectrometer equipped with a loop-gap resonator as described in chapter III. Tetraphenylphosphonium was used as a substrate for EmrE binding experiments as follows; TPP^+ was added to a final concentration of 16mM to7 μl proteoliposomes (~100 μM EmrE) and then the mixture was incubated at room temperature for 20 minutes so that all the TPP^+ is bound to EmrE.

For distance measurements, the substrate was mixed with EmrE in detergent micelles. TPP^+ was added to a final concentration of 1 mM to 55 μl (200 μM EmrE)

sample in detergent containing 30% glycerol. The sample was incubated at room temperature for 20 minutes before collecting data at 83 °K (-190˚C).

Results and Discussion

TPP^+ Binding Induces Conformational Changes

The CW-EPR spectral line shape of spin labeled EmrE mutants in the presence of the substrate TPP^+ reveals significant changes compared to the apo-state indicating that TPP^+ binding causes local structural rearrangements of specific regions located throughout the transmembrane domains of EmrE. These results are consistent with biochemical evidence showing that particular sites from each helix have an important role in binding of TPP^+ (Elbaz et al., 2005; Rotem et al., 2006; Yerushalmi & Schuldiner, 2000a) even though the sites that contribute to the binding might vary when using other substrates; as it has been shown in the different binding modes when using zwitterionic, neutral, or divalent cationic substrates to bacterial multidrug regulators and MDR transporters (Godsey et al., 2002; Lewinson & Bibi, 2001). TPP^+ was, however, chosen for its high affinity in binding to EmrE (Muth & Schuldiner, 2000) that makes it a unique candidate in investigating the conformational changes arise during substrate binding.

Mobility and Accessibility of TM1

It has been proposed from the previous chapter that the two monomers of TM1 pack against each other in the apo-state. This conclusion confirmed previously published work in detergent micelles (Koteiche et al., 2003), suggesting that the packing interface is a V-shaped chamber where the N-terminal sites are further from the dimer interface. Furthermore, biochemical evidence has shown that the N-termini of TM1s are accessible to the aqueous environment and do not interact directly with the substrate (Sharoni et al., 2005). Consistent with these results, the spectral line shape upon TPP^+ binding of the N-terminus of TM1 (residues 3-6) and the loop region, connecting TM1 to TM2 (residues 23 to 29) are similar to that of the apo-state, indicating no changes to the structure in these regions. Sites proposed to be lining the binding chamber (10, 11, 13, and 16) demonstrate an increase in the order of the spin label in comparison to the apo-state, as shown in Figure 3. Furthermore, upon the addition of the substrate, the distance between the spin label sites at position 18 located at the dimer interface increases. This was reflected by the loss of spectral broadening. In contrast, at sites 21 and 22, substrate binding causes a decrease in the order of the spin label. These observations suggest that the sites facing the same side as E14, such as sites 10, 11, and 18 show the largest conformational change upon substrate binding. The experimental data is also supported by biochemical evidence, which suggests that the substitution of I11 and T18 by cysteines led to compromised transport activity (Mordoch et al., 1999).

Figure 3: **Conformational changes upon substrate binding reflected in the EPR spectra of mutants along TM 1.** CW EPR spectra of spin-labeled mutants in TM 1 (residues 3 to 22), loop 1 (residues 23 to 29) reconstituted in liposomes are plotted in the presence (red trace) and absence (black trace) of TPP^+. All spectra were recorded at room temperature, with 160 Gauss scan width.

To provide a quantitative measure of mobility changes, the reciprocal of the central line width (ΔH_o^{-1}) is reported in Figure 4. Residues 8, 10, and 11 report increase in steric contacts with other regions of the protein as shown from the change in ΔH_o^{-1} minimum. However, smaller changes are observed for sites 15, 16, 19, and 20 compared to the apo-state, suggesting that these sites which are located towards the C-terminal of TM1 are less sensitive to the direct binding of the substrate.

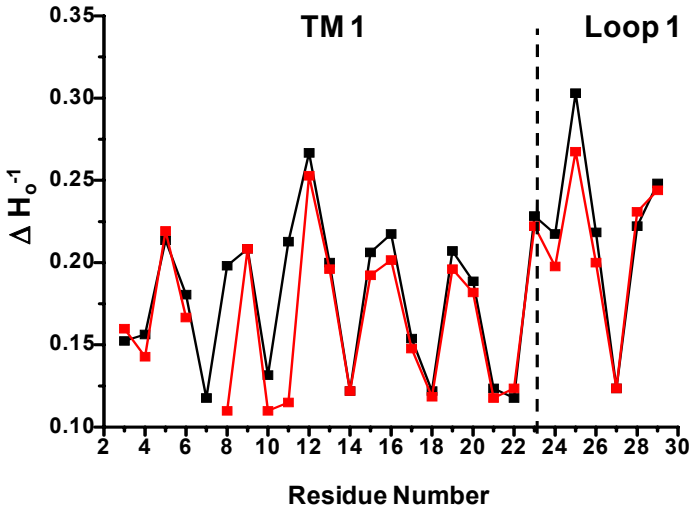

Figure 4: Mobility changes in TM1 upon TPP^+ binding. Inverse central line width (ΔH_o^{-1}) of TM1 (residues 3-22) and loop 1 (residues 23-29) in TPP^+ bound-state (red trace) and the apo-state (black trace). The black dotted vertical line represents the boundary between the two regions.

To better understand the structural basis of these changes in mobility, spin label accessibility to NiEDDA and molecular oxygen were investigated as shown in Figure 5 and Figure 6. For NiEDDA, a reagent exclusively soluble in the aqueous phase, the sites located in the vicinity of the proposed substrate binding pocket such as sites 9-12, and 15-

22 showed small changes in Π (NiEDDA). Changes in NiEDDA accessibility along TM1 at sites 10, 12, 16, 17, and 20 are relatively small suggesting that the changes in mobility do not alter the solvation profile in the vicinity of TM1. The largest changes in Π (NiEDDA) are at sites located in the loop region connecting TM1 to TM2 especially for sites 23 and 25. By comparison, large site-specific changes in oxygen accessibility are observed (Figure 6). The direction of the changes is in agreement with the mobility changes. Spin labels located at positions 8 and 15 report the largest changes in $\Pi(O_2)$. In the apo-state, these two sites are facing the lipid bilayer and are one turn away from site 12. Upon the binding of the substrate the oxygen accessibility decreases. This observation correlates well with the spectral line shape, since the addition of the substrate increases the tertiary contact with surrounding sites. In contrast, spin labeled site 15 shows little change in the spectral lineshape upon binding of the substrate, suggesting that the spin label site is only affected by the change in the environment without an alteration in mobility. The overall oxygen accessibility profile of TM1 upon binding of the substrate does not show any phase shift, which indicates that there is no global helix rotation.

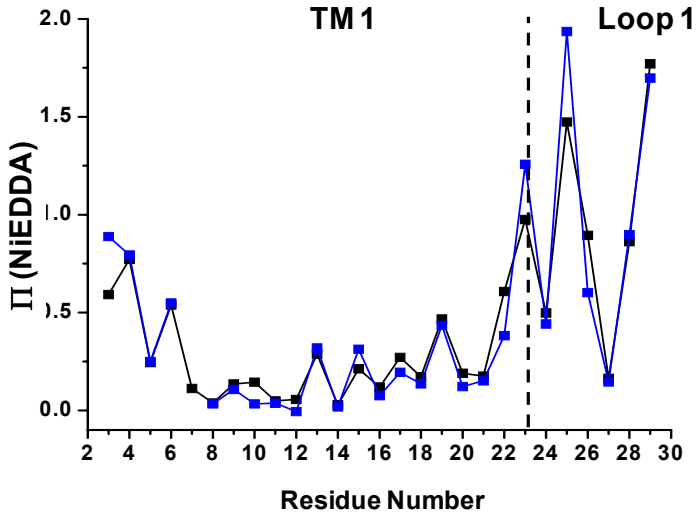

Figure 5: NiEDDA accessibility changes of TM1 upon TPP^+ binding. The NiEDDA accessibility of TM1 and Loop 1 in the TPP^+ bound-state (blue trace) and in the apo-state (black trace). The black dotted vertical line represents the boundary between the two regions.

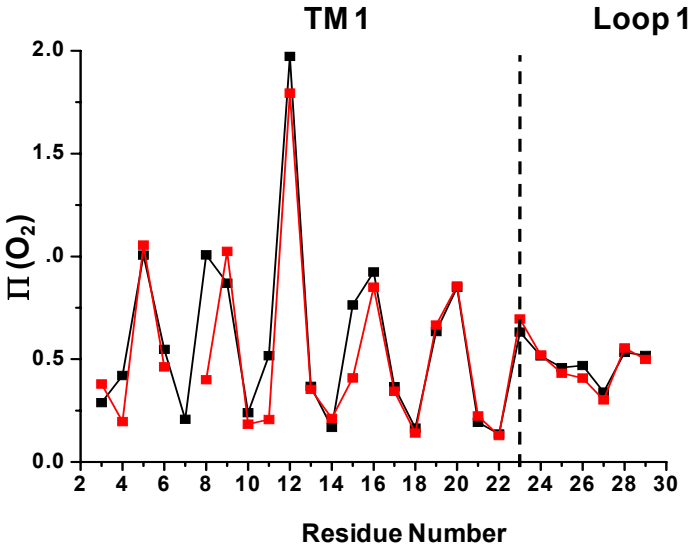

Figure 6: Oxygen accessibility changes of TM1 upon TPP^+ binding. The oxygen accessibility of TM1 and Loop 1 in the TPP^+ bound-state (red trace) and in the apo-state (black trace). The black dotted vertical line represents the boundary between the two regions.

TM1 Conformational Changes are Substrate-Specific

In vivo activity (see Chapter IV) and previous published work have confirmed mutation of E14 detrimentally affects the activity of EmrE (Weinglass et al., 2005). We took advantage of this observation to establish the specificity of TPP^+ induced conformational change. For this purpose, an E14A mutation was introduced into selected spin labeled EmrE mutants.

In the apo-state of EmrE, the spectral line shape at sites 18 exhibits low mobility and dipolar splittings at the dimer interface. In the presence of TPP^+, the pair of nitroxide at position 18 looses the spin-spin interaction, suggesting that the site move further apart and becomes in tertiary contact with surrounding sites, reflected by an immobilized spectral line shape. Introduction of the E14A background mutation affected the spectral line shape of the spin labeled site at positions 18 in the apo-state and reduced dipolar coupling. Furthermore, the spectral line shape in the presence of substrate was identical to the apo-state (Figure 7 B). This result confirms that the spectral changes are a consequence of specific substrate binding.

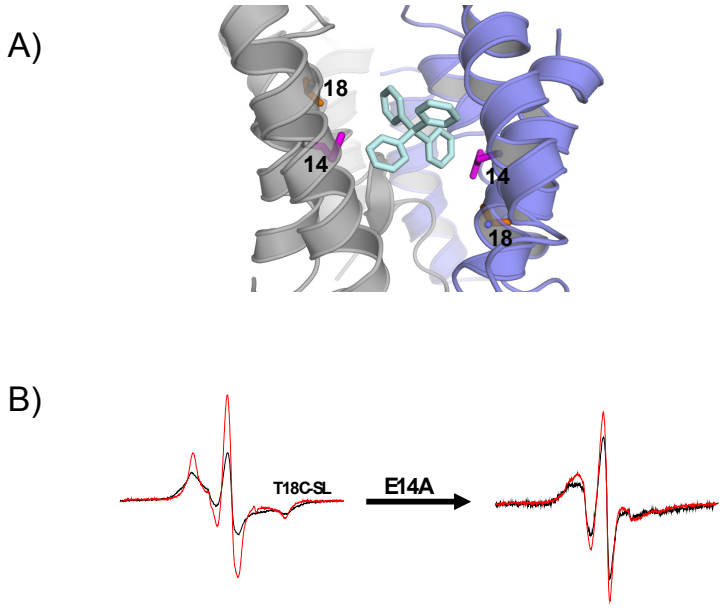

Figure 7: Interaction of sites in TM 1 located in the substrate binding pathway. A) A ribbon representation of the two subunits of EmrE (grey and blue). Sites 14 and 18 are colored in magenta and orange, respectively. TPP^+ (colored in light cyan) is in the center of the binding pocket. **B)** CW-EPR spectra of spin labeled mutant of site 18 plotted in the presence (red trace) and absence of TPP^+ (black trace). The spectra were recorded at room temperature, with 160 Gauss scan width.

Mobility and Accessibility of the TM2 Helix

The EPR spectra of spin labeled EmrE mutants of TM2 (residues 30-49) and loop 2 (residues 50-58) bound to TPP^+ are shown in Figure 8. Conformational changes induced by TPP^+ binding are reflected at certain sites of the helix, such as at the N-terminus (site 31 to 33). However, the C-terminal region and part of the loop region (sites 48 to 53), show no change in spectral line shapes. Sites located on the side of the helix involved in tertiary contact, such as sites 36, 37, 40, and 44 shows the most significant change in the spectral line shape upon substrate binding.

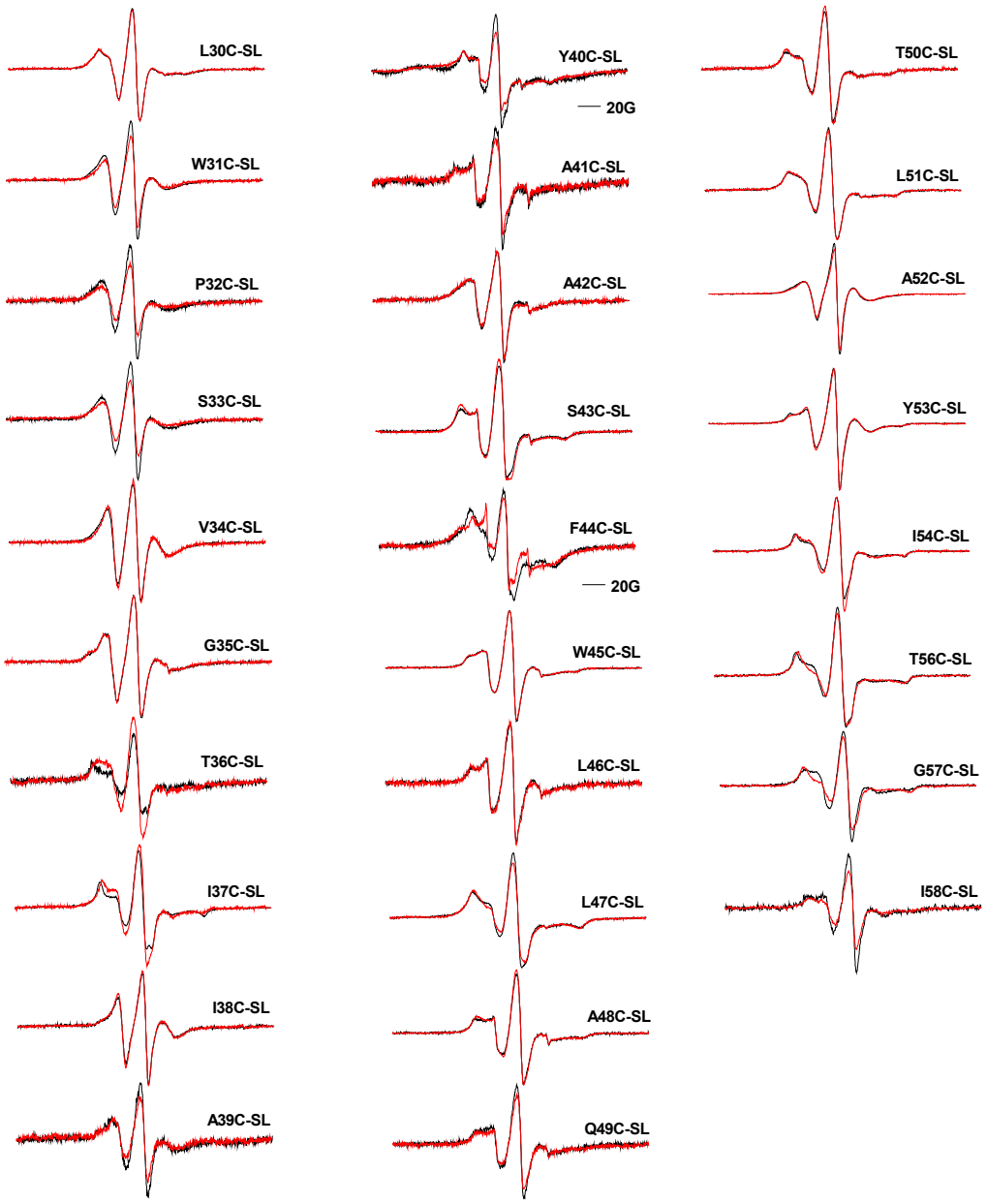

Figure 8: **Conformational changes upon substrate binding reflected in the EPR spectra of mutants along TM 2.** CW EPR spectra of spin-labeled mutants in TM 2 (residues 30 to 49), loop 2 (residues 50 to 58) reconstituted in liposomes are plotted in the presence (red trace) and absence (black trace) of TPP^+. All spectra were recorded at room temperature, with 160 Gauss scan width, except sites 40 and 44 which were recorded with a 200 Gauss scan width.

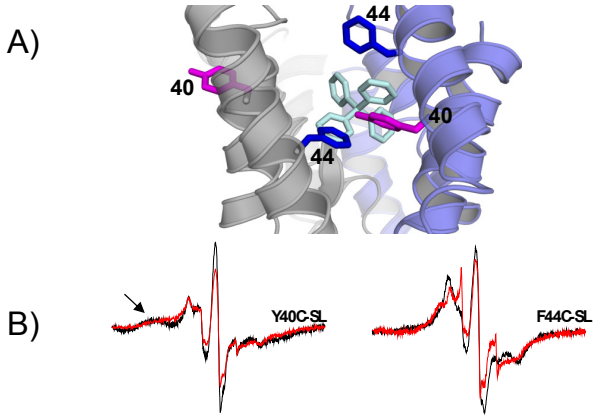

Figure 9: Interaction of sites in TM 2 located in the substrate binding pathway. A) A ribbon representation of the two subunits of EmrE (grey and blue). Sites 40 and 44 are colored in magenta and blue, respectively. TPP^+ (colored in light cyan) is in the center of the binding pocket. **B)** CW-EPR spectra of spin labeled mutant of site 40 (lower left), and 44 (lower right) plotted in the presence (red trace) and absence of TPP^+ (black trace). The two spectra were recorded at room temperature, with 200 Gauss scan width.

The spectral changes at sites 40 and 44 indicate that TM2 undergoes a rearrangement when substrate is bound. Strong spin-spin interaction in the apo-state, as evident from the broadening of the spectral line shape, suggests that both spin labeled sites are located within close distance at the dimer interface. However, in the substrate-bound crystal structure site 40 of each monomer is facing away from one another (Figure 9 A), indicating a change in orientation of this site upon the binding of the substrate. Indeed, upon binding of the substrate, site 40 from each monomer moves apart, as shown from the decrease in the intensity of the broad spectral features (see arrow in Figure 9 B). This may suggest two possible scenarios. Either there is a change in the orientation of TM2 upon the binding of the substrate, which is consistent with the reduction in spin-spin coupling, or the crystal structure of the substrate bound-state EmrE is a snap shot of one of several intermediates. On the other hand, site 44 seems to move closer when the

substrate is bound, which is evident from the increase in the spin-spin interaction at the dimer interface (red trace, Figure 9 B). Sequence analysis has shown Y40 and F44 to be conserved within the SMR family of transporters (Arkin et al., 1996; Rotem et al., 2006), suggesting that both aromatic residues have an important role in the activity of EmrE and also in stabilizing the binding pocket with and without TPP^+ (Zheleznova et al., 1999). The *in vitro* fluorescence data (Figure 3, Chapter IV) of the two spin labeled sites suggest that both spin labeled mutants at position 40 and 44 seems to bind to TPP^+ but with lower affinity.

The reciprocal of the central line width (ΔH_o^{-1}) for TM2 sites is reported in Figure 10. The decrease in ΔH_o^{-1} at residue 31-33 does not represent a change in the level of tertiary interactions. Rather, the broadening observed across the spectrum may reflect a reduction in the flexibility of the backbone. In contrast, the increase in ΔH_o^{-1} at position 36 is associated with a change in the line shape reflected by a reduction in steric restriction. This observation is consistent with the location of residue 36 on each monomer that is on the same side as site 40. Sites 46-54 located in the C-terminal region show very little change in ΔH_o^{-1}, suggesting that the C-terminal of TM2 is less sensitive to the binding of the substrate. The end of TM2 loop region, sites 56-58, shows an increase in steric contact. All these changes deduced from the mobility parameters are consistent with the EPR spectral line shapes.

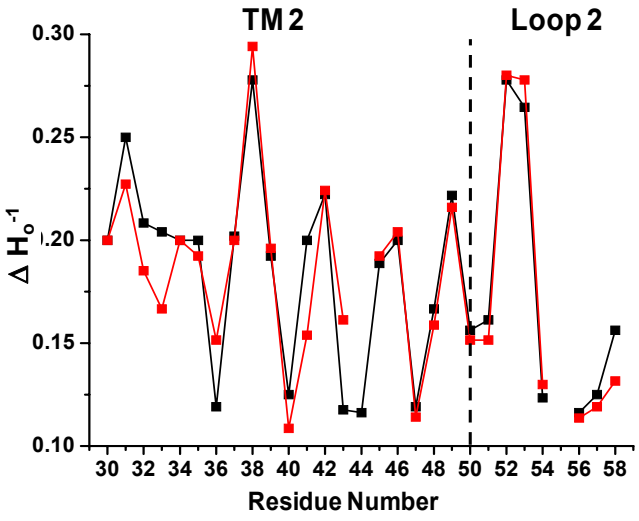

Figure 10: Mobility changes in TM2 upon TPP^+ binding. Inverse central line width (ΔH_o^{-1}) of TM2 (residues 30-49) and loop 2 (residues 50-58) in TPP^+ bound-state (red trace) and apo-state (black trace). The black dotted vertical line represents the boundary between the two regions.

To further investigate the change along TM2 environmental parameters such as oxygen and NiEDDA accessibility were measured and compared to their values in the apo-state. The local changes in Π(NiEDDA), shown in Figure 11, for the spin label at positions 30 to 35 at the N-terminus of TM2 reflects a decrease in the collision rate with NiEDDA and as a consequence a decrease in water exposure. The loop region connecting TM2 to TM3 shows the largest increase in the collision rate of NiEDDA towards sites 52 and 53, while the remaining loop region is unchanged. Residues 54-58 (Figure 8 and 10), report an increase in tertiary contacts when TPP^+ is bound, although a small change in Π (NiEDDA) is observed. As a result, these changes suggest repacking of the loop region induced by TPP^+ binding.

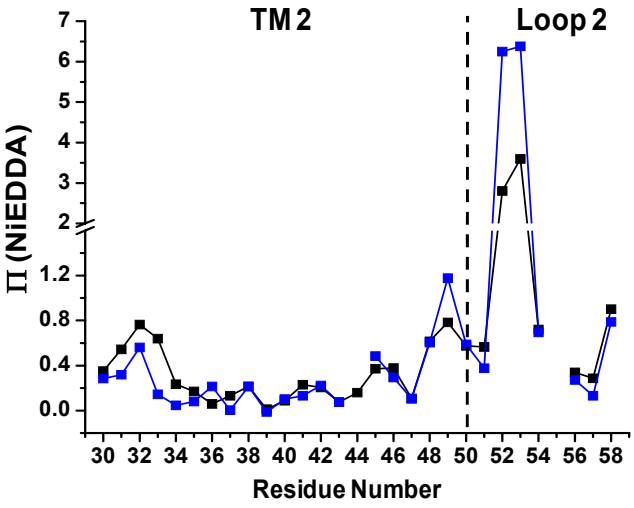

Figure 11: NiEDDA accessibility changes of TM2 upon TPP^+ binding. The NiEDDA accessibility of TM2 and Loop 2 in the TPP^+ bound-state (blue trace) and the apo-state (black trace). The black dotted vertical line represents the boundary between the two regions.

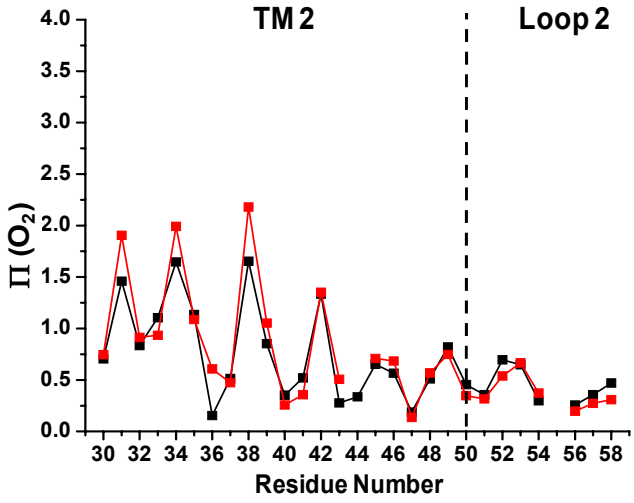

Figure 12: Oxygen accessibility changes of TM2 upon TPP^+ binding. The oxygen accessibility of TM2 and Loop 2 in the TPP^+ bound-state (red trace) and the apo-state (black trace). The black dotted vertical line represents the boundary between the two regions.

Changes in oxygen accessibility (Figure 12) correlates with those of NiEDDA accessibility at the N-terminus of TM2. An increase in oxygen accessibility upon substrate binding coincides with a decrease in the collision rate of NiEDDA suggesting that this part of the helix moves further into the lipid bilayer. Further into the helix, the spin label at position 36, which is one turn away from site 40, also show an increase in oxygen accessibility. This is consistent with the EPR spectral line shape and the mobility changes shown in Figures 8 and 10, where the binding of the substrate causes the spin label at position 36 to increase in mobility. In contrast to the changes observed in the N-terminal region, the C-terminal and the loop region shows very little change with respect to the apo-state.

Mobility and Accessibility of TM3 Helix

EPR spectral line shape changes of each spin labeled mutant along TM3 are shown in Figure 13. Sites located at the N-terminus of TM3 show a conformational change when TPP^+ is bound. It was mentioned in chapter V that residue 60 is at the dimer interface and is located near the N-terminus of TM3. The binding of the substrate marginally increases the dipolar coupling between the two spin labels at the dimer interface. This is also observed for site 61, where substrate binding causes the spin labeled sites to move closer toward one another as evident from a decrease in the spectral amplitude and broadening of the line shape. The conformational changes are detected in the EPR parameters of residues facing the same side of the helix as residue 60, specifically 63, 64 and 68.

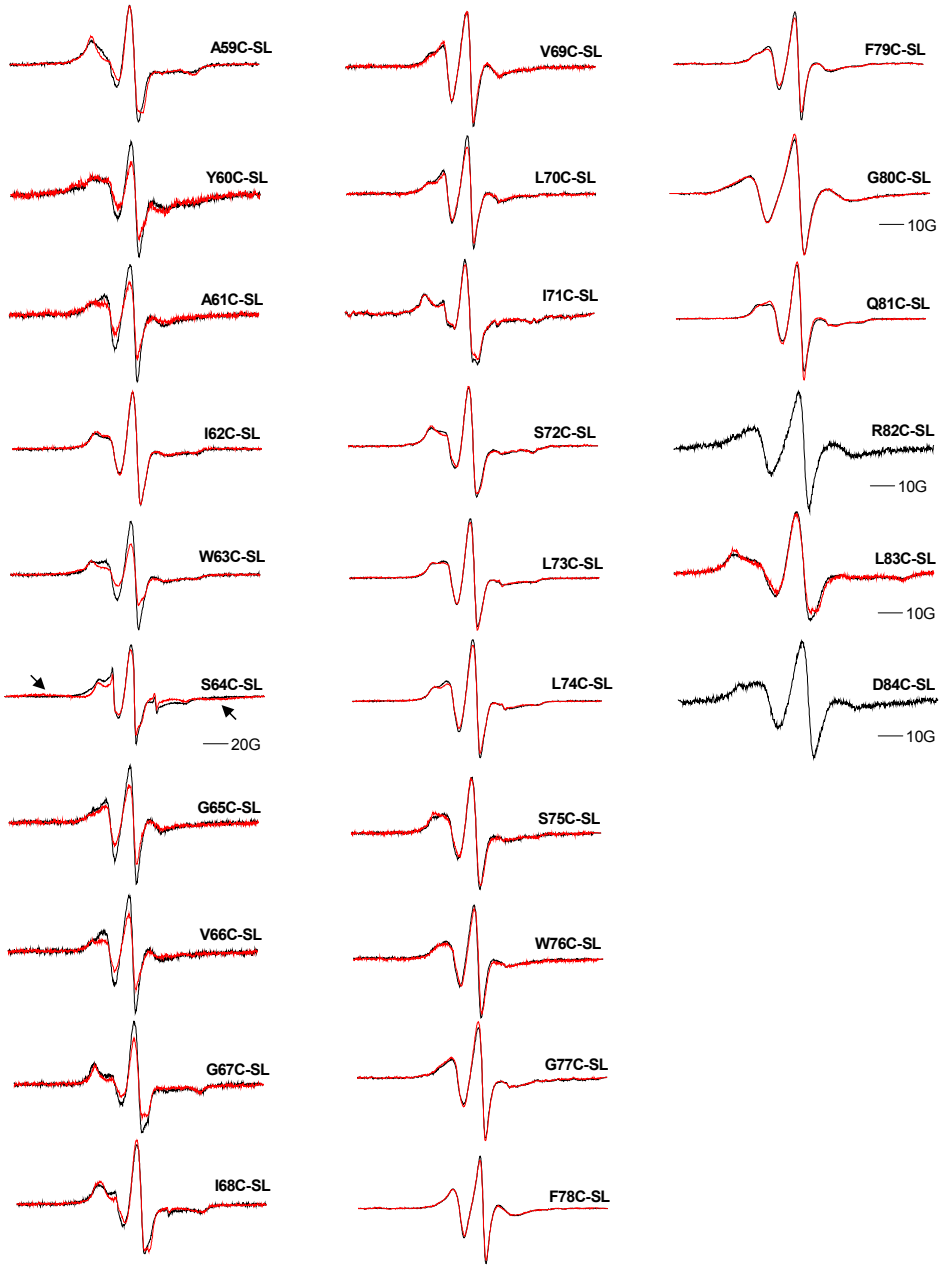

Figure 13: **Conformational changes upon substrate binding reflected in the EPR spectra of mutants along TM3.** CW EPR spectra of spin-labeled mutants in TM 3 (residues 59 to 75), loop 3 (residues 76 to 84) reconstituted in liposomes are plotted in the presence (red trace) and absence (black trace) of TPP^+. All spectra were recorded at room temperature, with 160 Gauss scan width, except sites 80, and 82-84 were recorded with 100 Gauss and 64 with 200 Gauss.

At site 64, the addition of the substrate causes the spin labels to move closer toward one another, as reflected by an increase in the spectral broadening observed at the low and high field of the spectral line shape (see arrow in Figure 14 B). The spectrum, similar to that of 14 and 40 spectral line shapes (see Figure 2, chapter V), has two distance components. One component is due to van der Waals contact between the labels, while the second is at a distance more than 20 Å apart. Therefore, the largest changes upon the binding of TPP^+ are observed at sites located at the N-terminus of TM3 towards the middle of the helix.

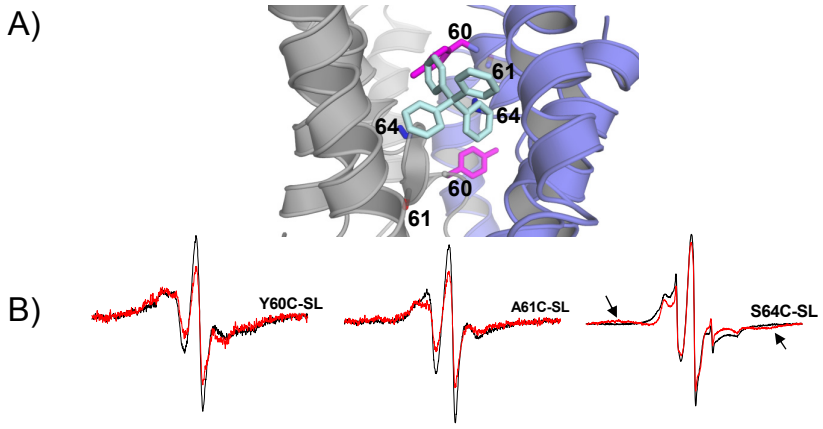

Figure 14: Interaction of sites in TM3 located in the substrate binding pathway. A) A ribbon representation of the two subunits of EmrE (grey and blue). Sites 60, 61, and 64 are colored in magenta, red and blue, respectively. TPP^+ (colored in light cyan) is in the center of the binding pocket. **B)** CW-EPR spectra of spin labeled mutant of site 60 (left), 61 (center), and 64 plotted in the presence (red trace) and absence (black trace) of TPP^+.

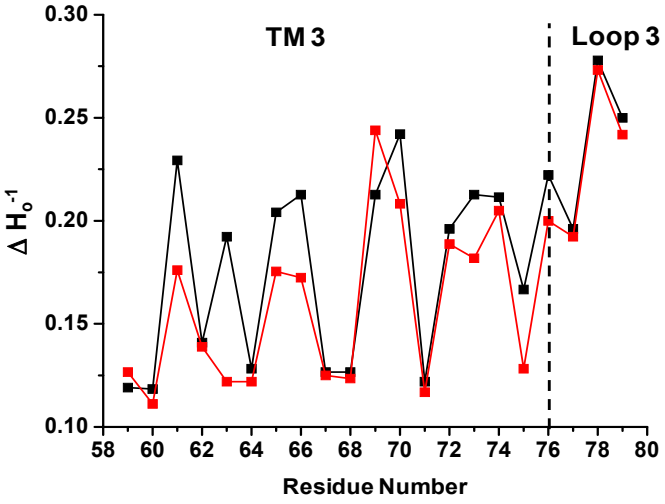

Figure 15: Mobility changes in TM3 upon TPP$^+$ binding. Inverse central line width (ΔH_o^{-1}) of TM3 (residues 59-75) and part of loop 3 (residues 76-79) in TPP$^+$ bound-state (red trace) and the apo-state (black trace). The black dotted vertical line represents the boundary between the two regions.

The quantitative measurement of the mobility of sites in TM3 is reported in Figure 15. Most of the sites in TM3 show a change in ΔH_o^{-1} in the presence of TPP$^+$, especially for sites that are located in the N-terminus (60-66) and less towards the C-terminal. The N-terminal region of TM3 is surrounded by other helices, thus the sites that showed a decrease in ΔH_o^{-1} suggest that the spin label sites increase in steric contacts upon the binding of the substrate.

Changes reported for TM3 are consistent with two lines of biochemical evidence. First, Y60, is highly conserved within the SMR family (Ninio et al., 2001). The replacement of Y60 with an aromatic residue such as phenylalanine results in an inactive protein (Yerushalmi et al., 1996). This has also been confirmed in our lab, where mutation of Y60 to a cysteine did not yield a functional phenotype on solid media (see

Chapter IV). An *in vitro* binding activity assay has shown that the replacement of Y60 with cysteine has a detectable TPP^+ binding activity only at high concentrations (Figure 4, Chapter IV). Also, previous published data have proposed that the tyrosine residue at position 60 has a major role in the transport activity where the hydroxyl group must be positioned in the exact place for its influence to be optimal (Rotem et al., 2006). Second, the two glycine residues at position 65 and 67 (GXG or GG1 motif; two glycine residues separated by one amino acid) are also conserved in the SMR family of multidrug transporters (Liu, Engelman, & Gerstein, 2002). Replacement of G67 with another amino acid yields a protein that does not confer resistance (Elbaz et al., 2008) (also see Chapter IV). In addition, glycine residues introduced in other proton-coupled transporters such as lactose permease (Weinglass, Smirnova, & Kaback, 2001) led to an increase in conformational flexibility. Moreover, the motif GXG also exists in potassium channels, and acts as a gating hinge (Jiang et al., 2002). Thus, TM3 may well participate in both the structural and functional aspects of EmrE. It is noted that the changes in the EPR spectral line shape may not be due to direct contacts with the substrate but could be due to backbone conformational dynamics (evidence supporting this interpretation will be presented in Figure 18).

NiEDDA accessibility of TM3 is shown in Figure 16. The overall accessibility is low and the pattern is not periodic, consistent with TM3 being predominantly in the lipid bilayer. The change in NiEDDA accessibility observed at the C-terminal and loop region (74-79), specifically for site 79, suggests that this site moves towards the lipid-water interface upon TPP^+ binding.

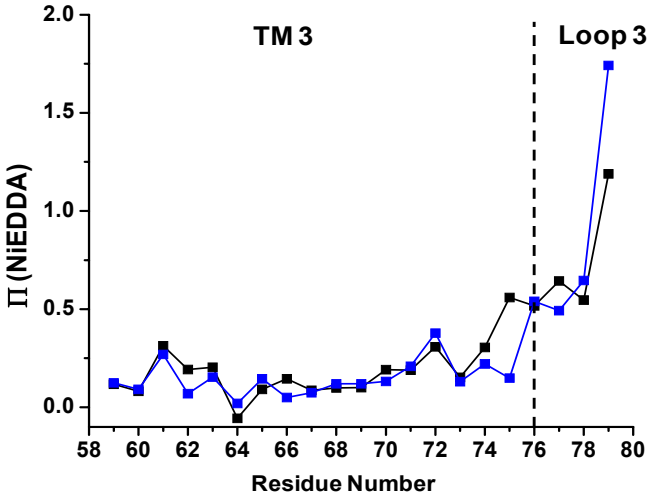

Figure 16: NiEDDA accessibility changes of TM3 upon TPP^+ binding. The NiEDDA accessibility of TM3 in the TPP^+ bound-state (blue trace) and in the apo-state (black trace). The black dotted vertical line represents the boundary between the two regions.

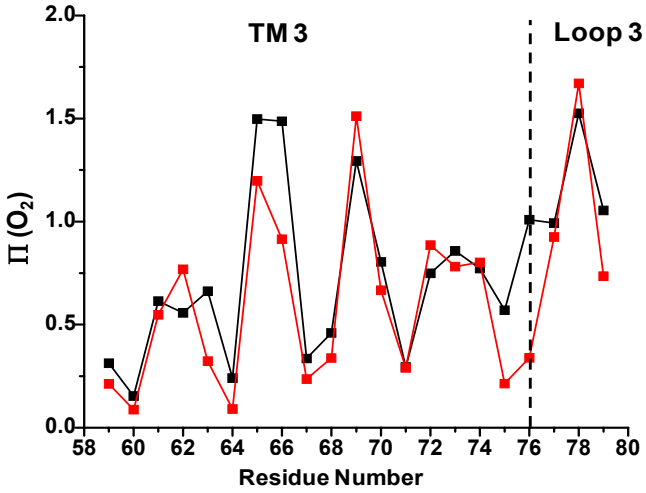

Figure 17: Oxygen accessibility changes of TM3 upon TPP^+ binding. The oxygen accessibility of TM3 in the TPP^+ bound-state (red trace) and in the apo-state (black trace). The black dotted vertical line represents the boundary between the two regions.

The oxygen accessibility of TM3 is shown in Figure 17. The phase of the periodic pattern along TM3 sites in the substrate bound-state is very similar to the apo-state, suggesting the absence of significant rigid body rotation. Sites 60-68 show a decrease in $\Pi(O_2)$ upon the binding of TPP^+, which when correlated with the EPR spectral line shapes, suggest that the increase in steric contacts causes a decrease in oxygen accessibility. The C-terminus of TM3, especially near the loop region (75 and 76) shows a decrease in oxygen accessibility that is in phase with NiEDDA accessibility upon TPP^+ binding. This suggests that the C-terminal and the loop region change their packing due to the flexibility of the helix when the substrate is bound. To further investigate the flexibility of TM3, especially at the C-terminus, distances were measured between spin labels at sites 68, 71, 74, and 76 (Figure 18 A).

Given that EmrE is a dimer, there would be two equivalent cysteine residues. After spin labeling, the two spin labeled probes might show spin-spin interaction such as for site 60. If the distance between the two spin labeled sites is more than 25Å, DEER is used to measure the dipolar interaction. The distance measurement is an important constraint for the analysis and determination of protein structure and conformational changes that will give both magnitude and direction of global movements.

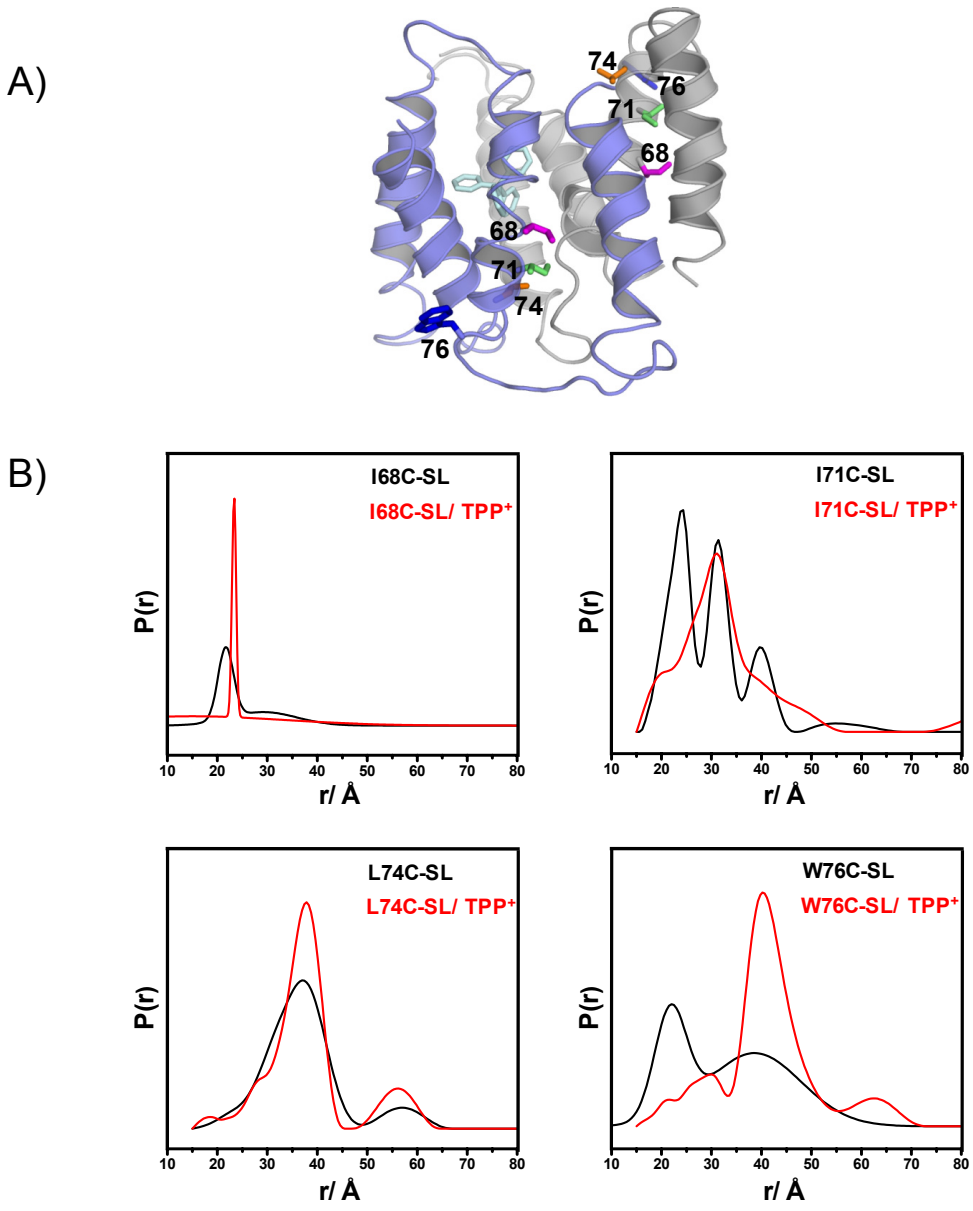

Figure 18: **DEER distance measurements of inter-probe residues located in TM3 with and without TPP$^+$. A)** A ribbon representation of the two subunits of EmrE (grey and blue). The TPP$^+$ is shown in light cyan. The location of sites 68, 71, 74, 76 are colored in magenta, green, orange, and blue, respectively. **B)** The distance distribution from the DEER experiments of the spin labeled site 68 (upper left), 71 (upper right), 74 (lower left) and 76 (lower right), in the presence (red trace) and absence (black trace) of TPP$^+$.

The DEER analysis suggests that the binding of the substrate decreases the width of the distance distribution. The multi-modal distance distribution (Figure 18 B) in the apo-state of sites 71, 74, and 76, indicates multiple conformers of EmrE of by the structure of the loop connecting TM3 and TM4. The change in the shape of the distance distribution may be facilitated by glycine residues located at positions 65 and 67 of TM3 (Elbaz et al., 2008), forming a flexible joint in the helix. As a result, the binding of TPP^+ seems to increase the order of the distance distribution for sites that are located at the C-terminal of TM3. Overall, TM3 is a highly flexible helix and its flexibility is decreased when TPP^+ is bound.

The model shown in Figure 1 had proposed that the transition of the substrate from the cytoplasmic-facing to the periplasmic-facing EmrE involves kinking and straightening of TM3 which was in agreement with the results mentioned above. However, the DEER results seem to indicate that the transition between the two sides of the lipid bilayer is not a one-step conversion but may involve intermediates between the two states. This was well illustrated for the spin label at site 64 upon the binding of the substrate, where the EPR spectral line shape suggests the existence of two components. The two components are indicative of possible heterogeneity in the EmrE dimer.

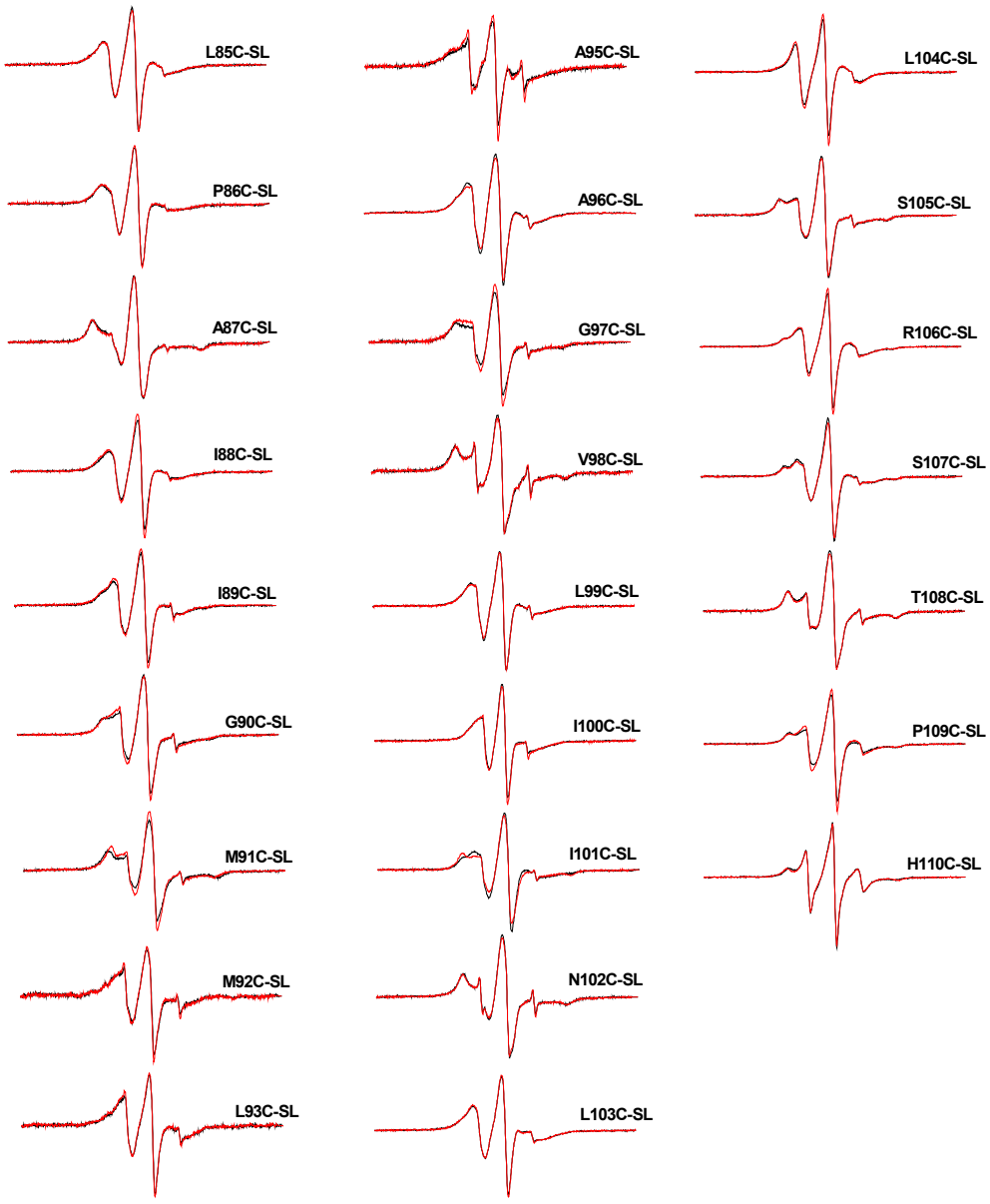

Figure 19: **Conformational changes upon substrate binding reflected in the EPR spectra of mutants along TM4.** CW EPR spectra of spin-labeled mutants in TM 4 (residues 85 to 103), loop 4 (residues 104 to 110) in detergent micelle are plotted in the presence (red trace) and absence (black trace) of TPP^+. All spectra were recorded at room temperature, with 160 Gauss scan width.

Mobility of TM4 Helix

Little if any changes in the EPR spectral line shapes of TM4 (residues 85 to 103) and loop 4 (residue 104 to 110), are induced by TPP^+ binding in detergent micelles as shown in Figure 19. This suggests that the TM4 helix does not undergo rigid body movement upon TPP^+ binding. As a result, we did not further investigate the changes in mobility of TM4 reconstituted in liposomes. Several studies demonstrating that the sites located in TM4 do not contribute to substrate binding (Gottschalk et al., 2004; Soskine et al., 2002). However, TM4 may have a significant function in dimerization, since two essential glycine residues at position 90 and 97 are conserved and form a protein motif, GG7, where the glycines residues are separated by six other residues. This motif was observed in transport/channel-like membrane proteins (Liu et al., 2002). Substituting the glycines to cysteines in these positions increases aggregation (see Figure 2, Chapter IV).

Mapping the Changes in O_2 and NiEDDA Accessibility with TPP^+ bound

To visualize the overall pattern of the average conformational changes revealed by the oxygen and NiEDDA accessibility data in a structural context, both were mapped onto the TPP^+ bound-crystal structure of EmrE (Figure 20). Changes in oxygen and NiEDDA accessibility were calculated by subtracting the accessibility of the TPP^+ bound-state from the apo-state to observe the largest changes when the substrate is bound to EmrE.

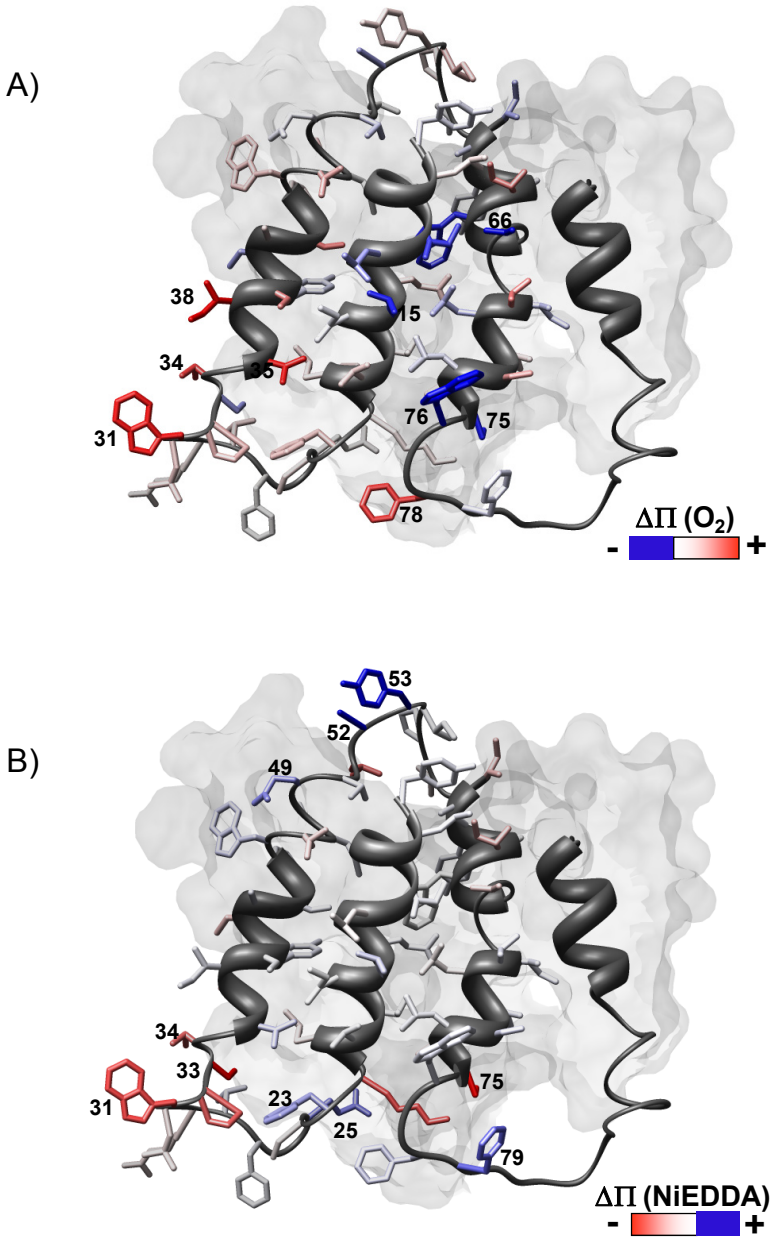

Figure 20: **Mapping the ΔΠ(O_2) and ΔΠ(NiEDDA) onto the crystal structure of TPP^+ bound EmrE. A)** ΔΠ (O2) along residues 6-79. The residues are represented by sticks. The (ΔΠ (O2)) is encoded by three colors: blue stands for decrease, white stands for no change, and red stands for increase in O_2 accessibility.
B) ΔΠ (NiEDDA) along residues 6-79. The residues are represented by sticks. The ΔΠ (NiEDDA) is encoded by three colors: red stands for decrease, white stands for no change, and blue stands for increase in NiEDDA accessibility.

The mapped changes in the oxygen accessibility ($\Delta\Pi(O_2)$) are shown in Figure 20 A. An overview of the data shows that sites located within the lipid bilayer have the largest change when the substrate is bound.

The changes observed describe a pathway through which the substrate may permeate. Thus, the middle of TM1, the N-terminus of TM2, and the full length of TM3 show the largest change in oxygen accessibility. For TM1, the changes are observed at residues 8, 11, 12, and 15 that are near the region of the substrate binding pocket. The N-terminus of TM2 moves further apart from the dimer interface, while the C-terminus of the helix shows less change. This implies that the N-terminus might accommodate the hydrophobic substrate to enter the lipid bilayer. In TM3, the changes in the N-terminus accessibility are related to the close contact of the sites in the first turn of the helix at the dimer interface. In the C-terminus the changes are related to the complete movement of the loop region connecting TM3 to TM4.

The change in NiEDDA accessibility ($\Delta\Pi$(NiEDDA)) is reported in Figure 20 B. There were no changes observed for sites located near the drug binding pathway. This indicates that TPP^+ binding has little effect on the hydration of the transmembrane segments. The changes are only observed at specific sites located in the loop regions connecting each of the four transmembrane segments. These changes in NiEDDA are in accordance with the $\Delta\Pi$ (O_2), suggesting that the movement of the transmembrane segments induced by TPP^+ binding causes the repacking of the loop regions.

Evaluating the Alternating Access Model of EmrE

Alternating access models propose that substrate transport entails a change in the orientation of the substrate binding site between the two sides of the membrane. This in turn would lead to translocation of the substrate. The results presented in this chapter suggest not global but local conformational changes upon the binding of TPP^+ to EmrE. Most of the changes in the EPR spectral line shapes are observed at sites that are near the substrate binding pocket such as sites 10, 18, and 64. However, one of the alternating access models, the rocker-switch model, proposes a motion of rocking or tilting around the binding site near the center of the membrane. The sites that are in direct contact with the substrate changes position the least in comparison to the motion at the extreme ends of the TMSs (Forrest & Rudnick, 2009). In our EPR result section of the first three TM helices of EmrE, the changes in the accessibility do not show any phase shift that would suggest a rotation of the transmembrane helices. The accessibility data suggest local changes in the N- and C-terminus of the TM helices that are related to changes in steric contacts with other sites of surrounding helices. This suggests a small tilt in the transmembrane helices. The changes, especially for TM3 in the N-terminus may serve to stabilize the substrate, while its flexible C-terminal region possibly serves to occlude the substrate from one side of the membrane; thus, TM3 has an important structural function that needs further investigation.

EmrE is made of two identical monomers that have been proposed by both the EM model and the crystal structure to be arranged in an antiparallel asymmetric dimer. In most cases, however, membrane transport proteins that use alternating access have internal structural symmetry but not sequence symmetry (Forrest et al., 2008; Huang,

Lemieux, Song, Auer, & Wang, 2003; Zhou, Guan, Freites, & Kaback, 2008). For EmrE, an alternating access mechanism implies that identical residues on either side of the membrane would undergo distinct interactions with neighboring residues. The inverted monomers of EmrE may create a pathway that is symmetrical from either side of the membrane. This agrees with the proposed model of EmrE bound to TPP^+ (Fleishman et al., 2006) where both the periplasmic- and cytoplasmic-facing side are identical but inverted by 180°.

One question that persists is how can two identical monomers possess different conformations and interactions? Previously, it was suggested that one monomer during the transport cycle may be unstable, and therefore requires the second monomer to stabilize it (Ubarretxena-Belandia et al., 2003). To elucidate the importance of the asymmetry of EmrE would require a higher resolution structure of different conformational states.

Conclusion

The TPP^+ induced structural changes of EmrE in liposomes were investigated using SDSL EPR spectroscopy to characterize the local dynamics, accessibility, and distance of the spin labels in the dimer. The changes in the EPR data between the apo- and substrate bound-intermediates of EmrE in liposomes were compared to the crystal structure in detergent micelles.

The EPR data mapped onto the crystal structure of the substrate bound-state report changes distributed on both sides of the asymmetric dimer. The changes were prominent in the N-terminus of TM2 and along the full length of TM3. The tilt at the N-

terminus of TM2 provides direct access to the bilayer from which hydrophobic substrates may enter. For TM3, the N-terminus moves closer towards the dimer interface, while the C-terminal and the loop region connecting TM3 to TM4 undergoes large amplitude motion. In TM1 the sites that were in direct contact with the substrate such as site 10 and 18 showed large distance changes. Hence, the data reported in this chapter contradicts the proposed model that is shown in Figure 2 (Fleishman et al., 2006), where there is no net change in residues environment, or proximity across the dimer interface during the transition from one side of the membrane to the other.

CHAPTER VII

HELIX PACKING IN THE EMRE MONOMER

Introduction

The accessibility data reported in Chapter V and VI revealed fundamental discrepancies between the crystal structure and the liposome structure. These include local steric packing in regions of helices 2 and 4 and the orientation of helix 3 relative to the lipid phase. While these differences may reflect the effects of detergent solubilization on the structure, they can also be a consequence of the low resolution of the published crystal structure deposited as a Cα carbon trace. The apo- and substrate bound-state were solubilized and crystalized using nonyl glucoside (NG) detergent micelle. Experimental data suggested that using NG to solubilize EmrE increases the monomeric fraction, leading to weaker interaction between the monomers in the functional EmrE dimer (see Figure 1, Chapter IV). Therefore, the interface between adjacent helices within each monomer may also be distorted. Conversely, solubilizing EmrE with β-DDM detergent micelle showed an increase in the stability of the EmrE dimer (Soskine et al., 2006; Soskine et al., 2002). In this chapter, we explore the veracity of the crystallographic model by determining the relative proximity between helices in the monomer.

Confidence in the crystal structure is based on the position of the selenomethionine (SeMet) at positions 21, 91 and 92 in each monomer. The Se heavy

atom was used to solve the phase problem, emphasizing that the pair of SeMet residues in the dimer are consistent with an antiparallel orientation. In addition, the Cα model of the crystal structure is practically identical to the Cα model derived from the 2D crystals (Y. J. Chen et al., 2007). The antiparallel orientation of the two monomers was investigated previously by studying the global topology analysis of a large fraction of the *E.coli* membrane proteins using reporter proteins (Daley et al., 2005). Reporter proteins, alkaline phosphatase (PhoA) that can only fold into an active protein when present in the periplasm (Manoil & Beckwith, 1986), and the green fluorescent protein (GFP) that fluoresces only when present in the cytoplasm (Feilmeier, Iseminger, Schroeder, Webber, & Phillips, 2000) were used to locate the C-terminus of membrane proteins. The results suggested that EmrE may have dual topology, suggesting architecture similar to the internal structural symmetry found in several membrane proteins, such as the ClC channel and aquaporin (Dutzler et al., 2002; Murata et al., 2000). The topology data were also supported by mutational studies, showing that EmrE fused to the reporter proteins in the membrane is sensitive to the distribution of positive charges (Rapp et al., 2006; Rapp et al., 2007).

Using mutations in positive charge distribution of EmrE similar to those done by von Heijne and collaborators (Rapp et al., 2007), a recent publication from our laboratory concluded that the helix-helix interaction supersedes the positive bias near the neutral region (McHaourab et al., 2008). This is also supported by previous studies showing that the folding of the membrane protein seems to be defined by many forces, such as the insertion of the TM helices of the protein into the bilayer, interactions within the protein itself, and also the interactions of the lipid and protein (Bowie, 2005; Hessa et al., 2007;

L. Zhang et al., 2007). Existing biochemical data is more consistent with parallel assembly of the EmrE monomers. Ninio and colleagues concluded both in a whole cell and under native conditions that the loops connecting transmembrane segments one and two of EmrE are in the periplasmic side while the two sites located near the C-terminal end are in the cytoplasmic side (Ninio et al., 2004). Previous work had also used a unique approach where the monomers are connected tail to head (C-terminus of the first with N-terminus of the second monomer) by a defined linker that was not compatible with antiparallel topology. The fused dimer of EmrE (tandem-EmrE) showed indistinguishable functional characteristics to the wild-type EmrE, concluding that the tandem-EmrE has parallel topology (Steiner-Mordoch et al., 2008). These results clearly show that parallel topology EmrE is functional. In contrast, the functionality of the antiparallel dual topology dimer has not yet been proven.

In summary, compelling evidence for an antiparallel monomer packing from EM analysis and the symmetry of the SeMet densities in the crystal structure are balanced by biochemical data supporting a parallel orientation. There are also concerns regarding the effects of detergent solubilization on the crystal structure. It is, therefore, important to analyze the arrangement of helices in the EmrE monomer since the in plane symmetry is only compatible with specific topologies. One of the goals of this chapter is to challenge the monomer packing model deduced from the crystal structure and supported by the EM-based computational model. For this purpose, spin label pairs were introduced at sites predicted to be separated by less than 20 Å in neighboring helices. The pattern of proximity deduced from CW-EPR analysis and DEER confirm the topology of helices 1-

3 in the monomer. However, the EPR distance restraints suggest significant distortion in the crystal structure.

Experimental Methods

The double cysteine mutants were made on a cysteine-less EmrE (WT*) background. Purification and labeling were done as described in Chapter III. All the EPR spectra of the detergent samples for the spin labeled double mutants have a final protein concentration of 100μM obtained on a Varian EPR spectrometer equipped with a loop gap resonator as described in chapter III. DEER was used to collect the distance measurements for the double spin labeled samples at a final protein concentration of 200 μM containing 30% glycerol. All DEER distance data were collected at 83°K (-190°C).

Subunit Exchange

The detergent purified doubly labeled samples were mixed with unlabeled cysteineless-EmrE (EmrE-CLA) at a molar ration of 1:2. The mixture was desalted on a desalting column (HiTrap, GE Healthcare) pre-equilibrated with SEC buffer (50 mM sodium phosphate monobasic, 50 mM NaCl, and 0.02% β-DDM, and 0.02% NaN_3, pH 7.2) containing 0.8 mole fraction of sodium dodecyl sulfate (SDS). After desalting, the unfolded mixture was incubated at room temperature for 15 minutes, and then refolded by passing it through a SEC superdex-200 column equilibrated with SEC buffer without SDS. The CW-EPR spectra of the refolded and the unfolded samples were obtained on a EMX Bruker spectrometer. The above procedure was repeated for a negative control sample without the addition of WT*.

Molecular Modeling

A molecular model of the side chains from the known crystal structure of EmrE (PDB ID: 3B5D; (Chen, 2007)) was manually constructed by Nathan Alexander in Meiler's lab at Vanderbilt University.

The distance between a pair of nitroxides (NO-NO) was estimated using the $\chi_4\chi_5$ model, as shown in Figure 6, Chapter II (Columbus et al., 2001; Langen et al., 2000). This model takes into consideration that the first three bonds (χ_1, χ_2, χ_3) between the Cα of the spin cysteine and the nitroxide ring are fixed, while the dominant contribution to the motion of the nitroxide is about the χ_4 and χ_5 bonds.

These distances were calculated using the program "CalDihedral.exe" designed by Marco Bortolus. The position of the label is calculated by projecting along the α-β carbon bond at a desired distance. To account for the tether flexibility, error estimation is calculated assuming that a label can be found in a cone whose vortex is centered on the α-carbon. Therefore, the program takes into account the projection of the α-β carbon and the tilt in the cone. This would reconcile the distance obtained by EPR experiments with the backbone distance.

Results and Discussion

Characterization of the Double Mutants

The packing of the helices of EmrE in the monomer and the orientation of its residues were investigated. Nitroxide spin labels were introduced at cysteine pairs between all possible helix pairs, TM1 and TM2, TM1 and TM3, TM1 and TM4, TM2 and TM3, TM2 and TM4, and finally between TM3 and TM4.

The spin label double mutants were fully characterized using a tryptophan fluorescence quenching assay (Elbaz et al., 2005), as described in Chapter IV. The tryptophan at position 63 is sensitive to substrate binding and/or conformational changes. Thus, the tryptophan fluorescence of each of the double spin label mutants was measured in the presence of TPP^+ and the level of quenching compared to the cysteine less-EmrE (WT*). The addition of saturating amounts of TPP^+ to each of the double mutants induced quenching of tryptophan florescence that was similar to WT* (Figure 1) with no detectable shift in the emission maxima. Overall, the structure of EmrE was not compromised by the double cysteine substitutions.

In addition, the hydrodynamic profiles of the double mutants was compared to the WT* using size exclusion chromatography (SEC) (data not shown). The purified spin labeled mutants had similar retention time to WT*, signifying no disruption of the dimeric structure.

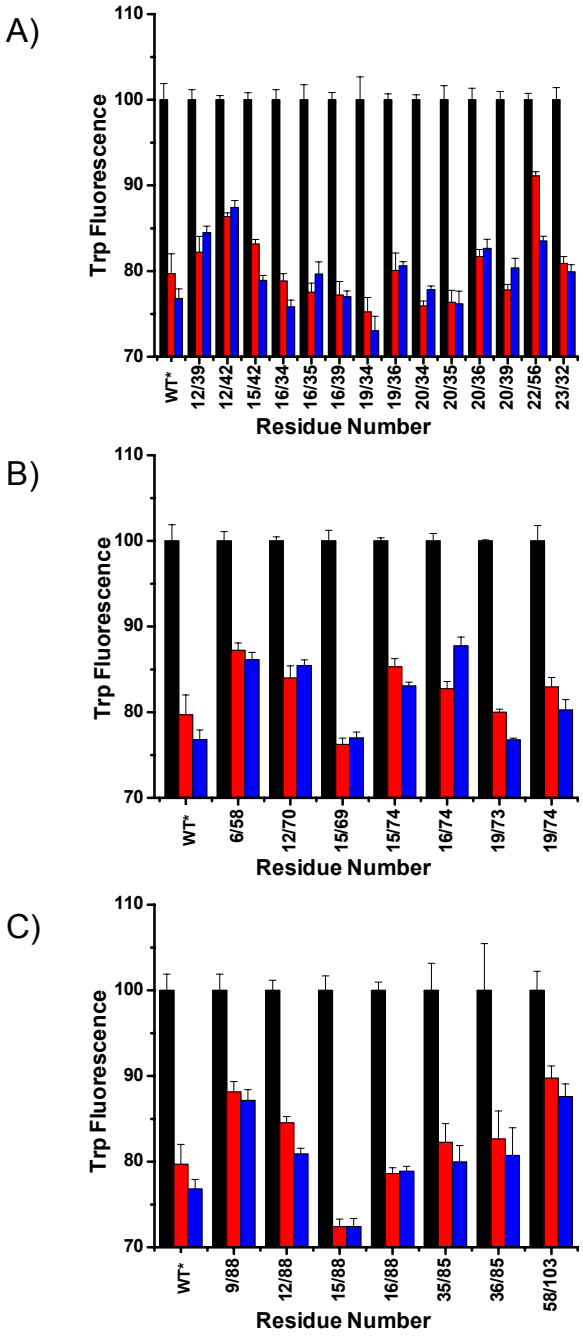

Figure 1: *In vitro* substrate binding of the double spin labeled mutants of EmrE. A bar graph of EmrE tryptophan (Trp) florescence in the absence (black bar) or in the presence of saturated amount of TPP^+, 6 μM and 12 μM in red and blue bar, respectively. The three graphs signify the location of the double spin label mutants in the TMS; **A)** TM1/TM2, **B)** TM1/TM3, **C)** TM1/TM4, TM2/TM4, and TM3/TM4. All mutants were compared to the unlabeled cysteine-less EmrE (WT*).

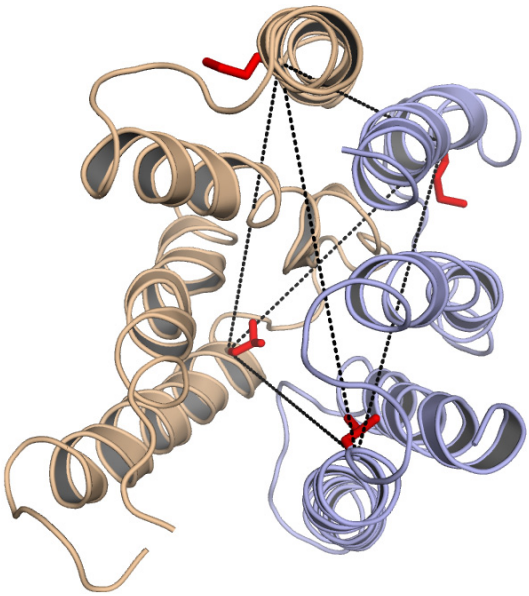

Figure 2: Pair-wise distances relating spin labels in the EmrE dimer. Structure of EmrE viewed perpendicular to the membrane plane. The two monomers of EmrE are colored in blue and wheat. The red sticks represent two sites located in each monomer. The black dotted lines represent the distance measured within the monomer or between monomers.

Methodology

EmrE is a dimer, thus the interpretation of the chosen double mutants in the monomer is complicated. Each of the two monomers would have two spin labeled sites, a total of 4 spin labeled sites in the dimer, and therefore six distance probabilities, as shown in Figure 2. This is not an issue for short range distance (8-20 Å) since in general the inter-monomer distances tend to be outside the range of dipolar coupling interactions and thus do not contribute to the spectral broadening of the EPR lineshape. For the measurements of distance between the chosen double labeled sites separated by a distance between 25 to 60 Å, double electron electron resonance (DEER) is used (review by (Pannier et al., 2000), also see introduction to EPR measurements, Chapter II). To

overcome the complexity of the resulting distance distribution, each of the intra-doubly labeled sites were normalized then compared to the DEER distance distribution of the inter-singly labeled sites to identify their contribution to the average intra-distance distribution in the monomer.

For the intra-spin labeled sites that are separated by a distance of less than 18 Å showing strong spin-spin interaction the measurements can only be determined by CW-EPR spectra. A convolution method utilizing a spectrum comprised of the sum of the corresponding single mutants was used to determine the distance distribution (Rabenstein & Shin, 1995).

Is EmrE Domain Swapped?

Domain swapping is an efficient way of forming oligomers since the interactions of the helices within the monomer are used in the dimer. Evidence of domain swapping was first observed in G-protein coupled receptor activation mechanisms (Gouldson, Snell, & Reynolds, 1997). The published EM model and the crystal structure of the substrate bound-state of EmrE did not reveal evidence of domain swapping (Y. J. Chen et al., 2007; Fleishman et al., 2006). As a result, interpenetration of helices from one monomer with helices from another monomer (i.e. domain swapped) was ruled out.

To confirm that EmrE helices are not swapped in the dimer, we selected pairs of mutants, 16/39 and 19/74 between helices 1 and 2, and 1 and 3. Only 16/39 was predicted to be in close proximity in the crystal structure. As a control, we selected a double mutant combining sites 22 and 56 at the dimer interface. The EPR spectra of all three doubly labeled sites are broadened by dipolar coupling (Figure 3, blue trace), indicative of nitroxides that are in close proximity.

To definitively demonstrate that spin-spin coupling arises from proximity within the monomer, each of the doubly labeled mutants was unfolded using SDS as a denaturant to dissociate the dimer (Lau & Bowie, 1997). The unfolded EPR spectra (dotted grey trace for only 19/74 and 22/56) are shown in Figure 3 A and 3 C, respectively. Mixing the denatured 19/74, 16/39 and 22/56 with the denatured unlabeled cysteine-less EmrE (WT*) followed by refolding did not eliminate the spectral broadening especially for site 19/74, which confirms the spin-spin interaction arises from the close proximity of the two nitroxide at position 19 and 74 within the monomer. In contrast, the spectrum of the positive control 22/56 showed a complete loss of spectral broadening confirming that both sites 22 and 56 are located at the dimer interface (Figure 3 C). A relatively limited loss of broadening in the 16/39 pair results from the elimination of spin-spin coupling at site 39 across the dimer interface (Figure 3 B).

The data suggests that TM1 and TM3 are not swapped in the dimer. Yet, the increase in amplitude of the central resonance line of 16/39 when mixed with the WT* (Figure 3 B) indicates that either the TM2 helices are swapped in the dimer, or the spectral broadening of 16/39 has contribution from dipolar coupling at site 39 at the dimer interface.

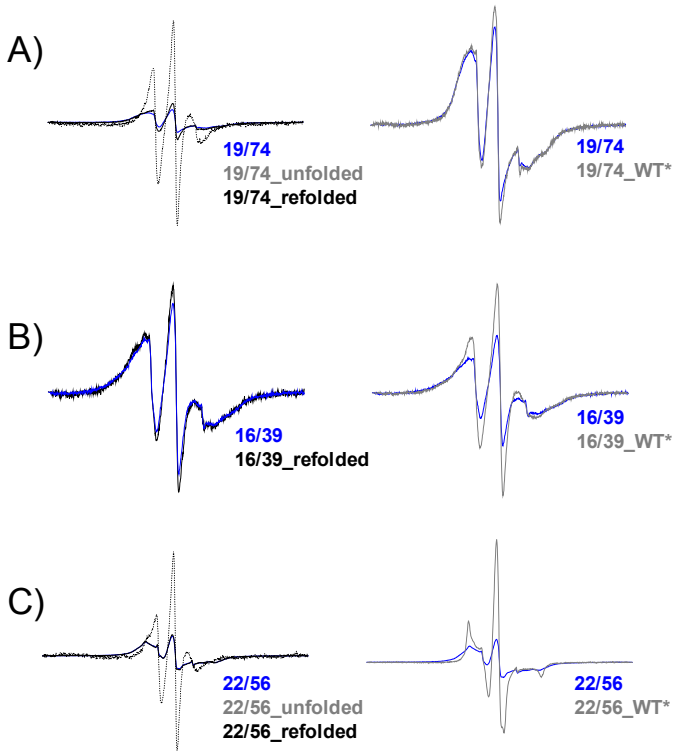

Figure 3: CW-EPR spectra for the subunit exchange of the intra- and inter-spin label sites. The EPR spectra of **A)** 19/74; **B)** 16/39; **C)** 22/56, shown in blue trace. The unfolded spectra are shown in dotted grey trace with the exception of 16/39 (spectra was not collected). The spectra of the refolded sample are shown in black trace. The grey solid trace spectra are the subunit exchange of the doubly labeled sites with WT*.

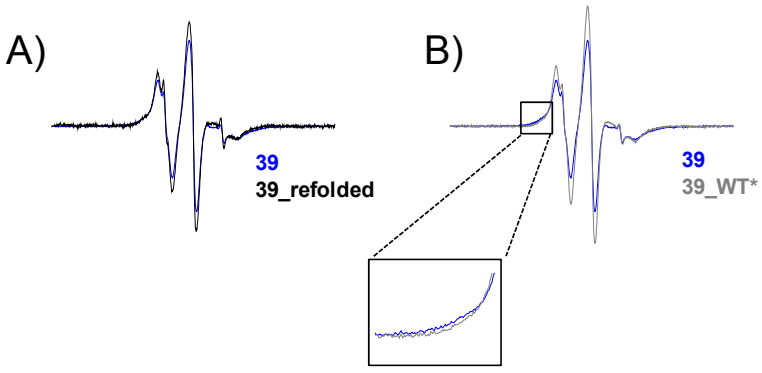

Figure 4: CW-EPR spectra for the subunit exchange of the spin label site 39. A) Spectral line shape of spin labeled site 39 is shown in blue trace. The refolded spectra (black trace). **B)** The subunit exchange spectra of 39 with WT* is shown in grey trace The inset is showing the high field spectral line shape change.

To explore the latter possibility, EPR spectra of the site 39 mutant refolded in the presence and absence of WT* were obtained (Figure 4 B). The result shows a decrease in the broadening of the spectral line shape (inset, Figure 4 B). Together with the analysis of Figure 3, this data suggests that TM2 is not swapped in the dimer.

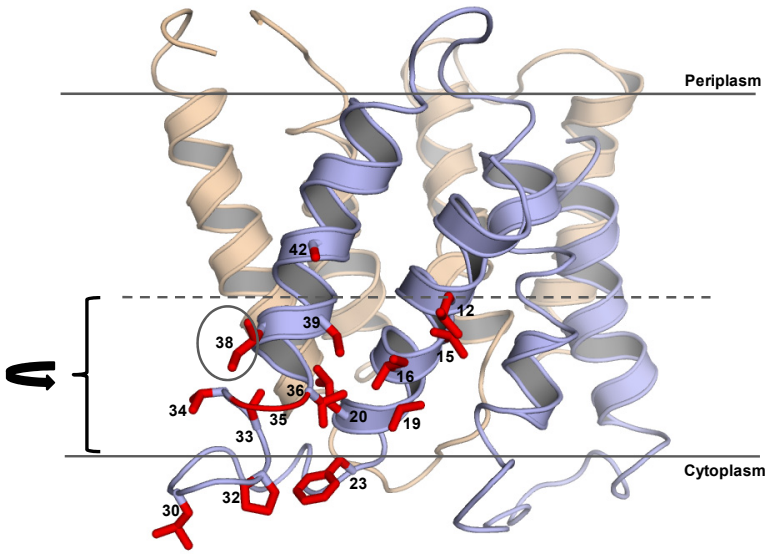

Figure 5: Double mutants for TM1/TM2 packing modeled onto the EmrE crystal structure. The two monomers are represented in blue and wheat colored ribbons**.** The mutation sites in both transmembrane segments are shown as red sticks for only one monomer. The horizontal dashed line (light grey) shows the location of sites in the middle of the bilayer. The predicted lipid bilayer is indicated by two horizontal lines. The black arrow shows the predicted rotation of the helix from experimental data.

The spin labeled double mutants was fully characterized for the spatial arrangement of the transmembrane segments in the monomer by CW-EPR. The line shapes are shown in Figures 6, 7, 10, 12, and 13. For a subset of mutants, distances were measured by DEER as illustrated in Figure 8 and reported in detail in Tables 1, 2, and 3.

The corresponding CW-EPR spectra of the double mutants upon TPP^+ binding are shown in the appendix. In general, the spectral line shapes were similar to those of the apo-state.

Intra-Monomer Distances between Residues Located in TM1 and TM2

Evidence from several biochemical and biophysical studies have proposed that sites located in both TM1 and TM2 have an important contribution to the activity of EmrE, including stabilizing, binding, and translocation of the substrate (Rotem et al., 2006; Sharoni et al., 2005; Yerushalmi et al., 2001). In contrast, the spatial proximity of these two TM segments in the monomer has not been validated. The published crystal structure of EmrE in the apo-state is proposed to be in a misfolded form. The only structural evidence that has been published regarding the two transmembrane segments is from the crystal structure of the substrate bound-state where it has been proposed that TM1 and TM2 are in close proximity in the monomer.

The sites that were chosen to investigate the proximity of TM1 and TM2 are show in Figures 5. The spectral line shape of each of the double mutants is shown in Figure 6 and 7. To avoid destabilizing the monomer fold, spin labels were introduced at the lipid-exposed surface of the helices as defined by the oxygen accessibility profile in Chapter V. CW-EPR spectra for each of the double labeled mutants were collected in the apo- and TPP^+ bound-states (see the appendix, pages 210 and 211). All the chosen pairs in this chapter did not show large changes in spectral line shape upon substrate binding. Thus, the spectral line shape of the apo-state doubly-labeled mutants was compared to the crystal structure of the substrate bound-state.

Out of the 17 chosen sites only 7 (Figure 6) showed spectral broadening consistent with two spin labels in close proximity (quantitative analysis of the CW-EPR spectra is shown in the appendix, page 209). This is reflected by a decrease in spectral amplitude (and line width increase) of the CW-EPR spectra of the doubly labeled mutants with respect to the sum of the single mutants. In the apo-state accessibility data (Chapter V), site 12 had the highest oxygen accessibility, indicative of a site that is in the center of the TM1 helix and facing the lipid bilayer. Sites 16 and 20 are one and two turns away from site 12, respectively, facing the lipid bilayer. The spectra of 12/39, 16/39, and 20/39 are broadened relative to the EPR spectrum of the sum of singles. Spectral simulation yields distances consistent with the direct packing of the two helices.

To further investigate the TM1/TM2 interface, spin labels were introduced at sites 16/38 and 15/38. Broadening was evident in the spectrum of 16/38 while the spectrum of the 15/38 double mutant and sum of singles are superimposable. Thus, residue 15 is away from the interface with TM2 consistent with the handedness implied by the crystal structure. Inconsistencies between the experimental data and the crystal structure are observed at a number of sites. These are highlighted in Figure 7 where the line shapes of the double mutants are similar to the corresponding sum of the single mutants, suggesting that none of the spin labels are in close contact as predicted by the crystal structure.

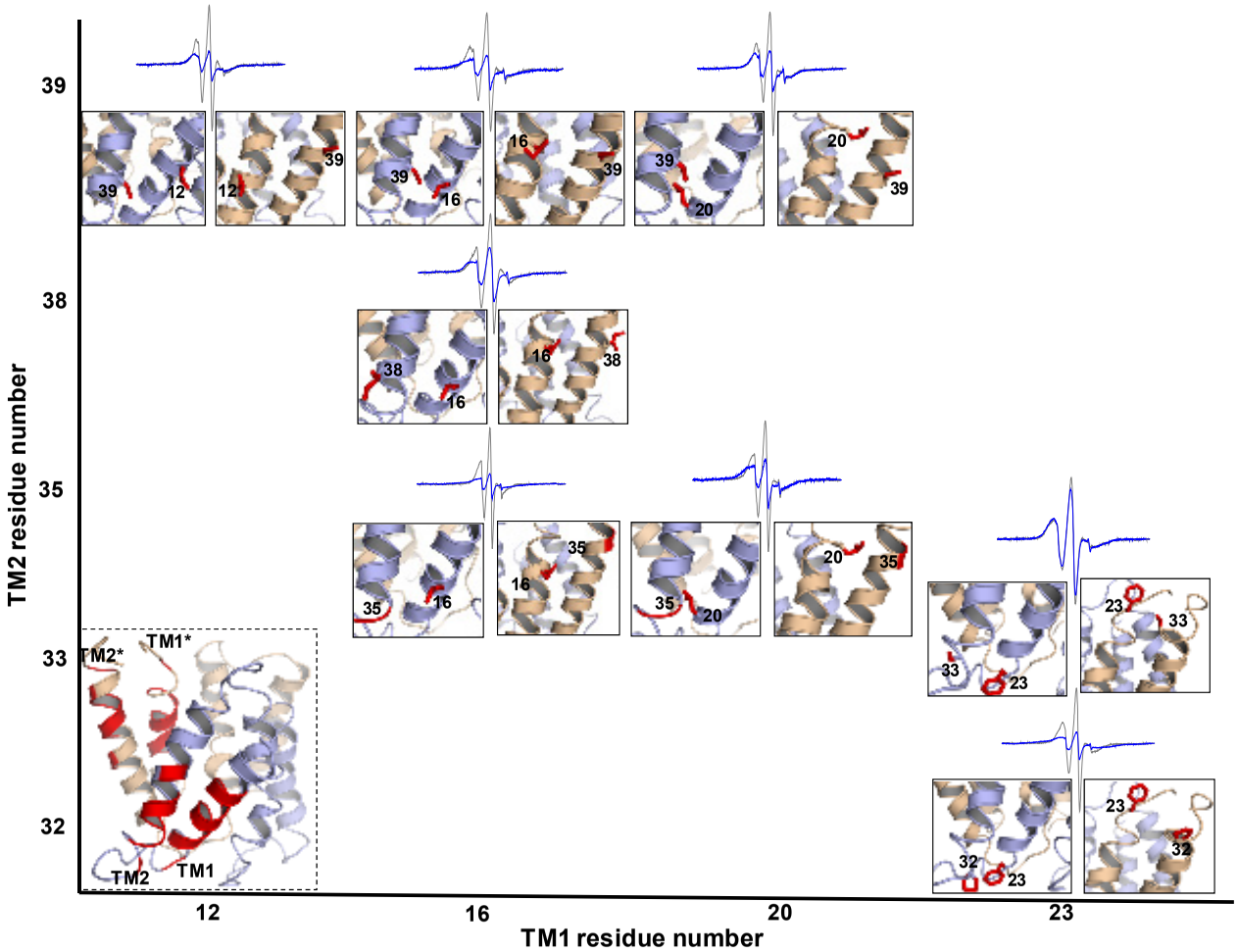

Figure 6: Matrices of the chosen spin label sites within TM1 and TM2, located at close proximity. The bottom left panel is a ribbon diagram of the two subunits colored in blue and wheat. The location of TM1 and TM2 in each subunit is labeled. The red colored regions are the location of the chosen sites. The location of the two sites is shown in red sticks in both monomers. The CW-EPR spectra of the double spin labeled sites (blue trace) and sum of single mutants (grey trace).

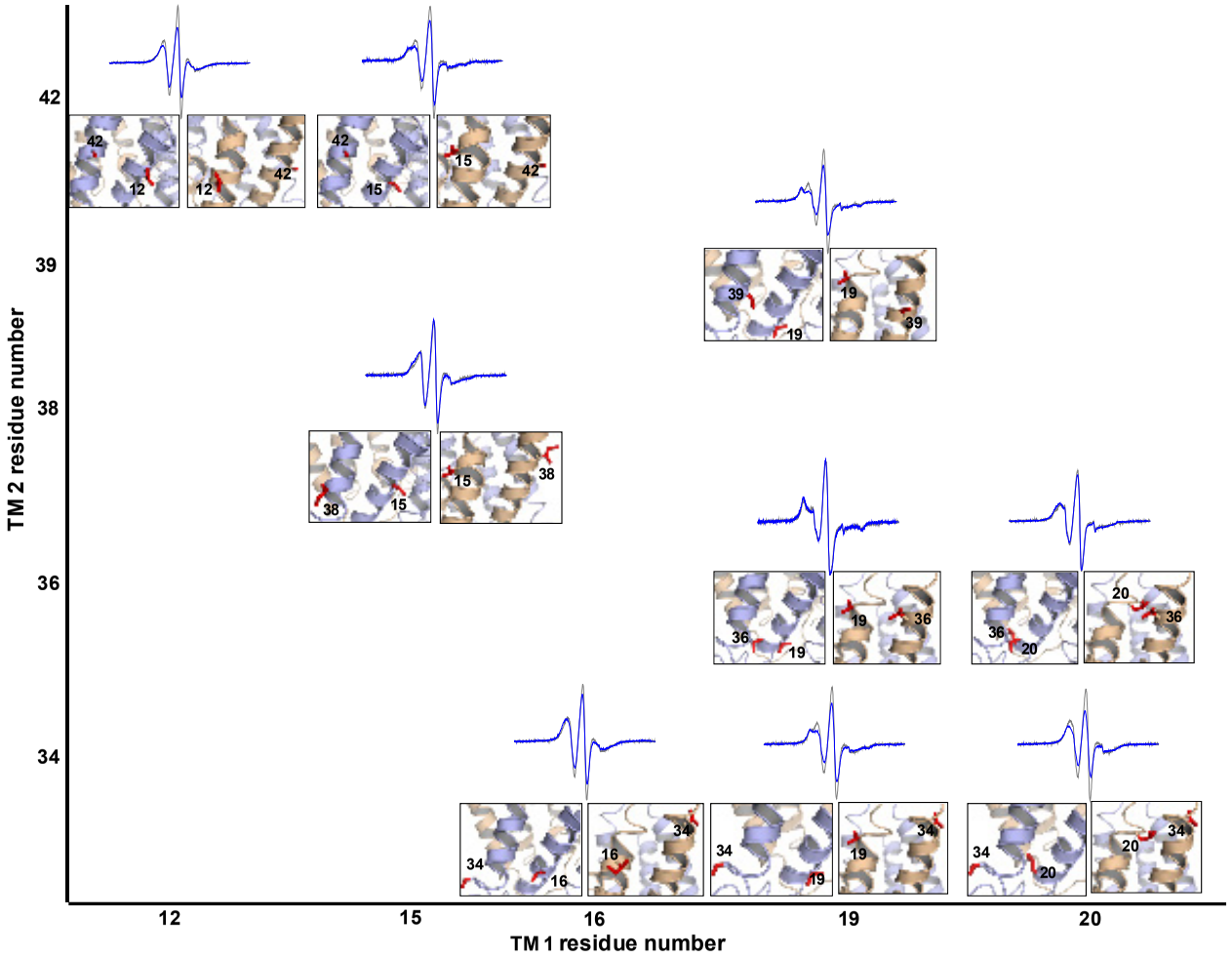

Figure 7: Matrices of the chosen spin label sites within TM1 and TM2, located further apart. The location of the two sites is shown in red sticks in both monomers. The CW-EPR spectra of the double spin labeled sites (blue trace) and sum of single mutants (grey trace).

This is evident when comparing the EPR spectra of the doubly labeled mutant 20/36 (Figure 7) with 20/35 (Figure 6). Two of these chosen sites 20 and 36 seem to be in close contact in the crystal structure while site 35 is facing away from site 20. EPR spectra of 20/36 showed no indication of spin-spin interaction, in contrast to the EPR spectrum of 20/35. Similarly the pairs 23/32 and 23/33 (Figure 6) are proposed from the crystal structure to be well within the range of strong dipolar coupling. Nevertheless, the EPR spectral line shapes show only 23/32 in close proximity in the monomer as indicated by spectral broadening. It is noted that the crystal structure had proposed both residues 32 and 33 are located in the loop region connecting TM1 to TM2; however the accessibility data (see Chapter V) suggest that these two sites are within the N-terminus of TM2.

To support the qualitative interpretation from the EPR spectral line shape in Figure 7, distances were measured using DEER. DEER is not affected by under labeling which could mask the dipolar coupling in CW-EPR analysis. As mentioned previously, to avoid the contribution of the multiple distance distributions expected from the labeled double mutants, the DEER distance distributions were compared to the corresponding single mutants. Only the peak distance of the intra-spin labeled distance was extracted and presented for the rest of the mutants (shown in Table 1 and Figure 8). Average distances were then compared to the distance predicted from the crystal structure. The spin label was modeled onto the wild type crystal structure to extrapolate the position of the label (see experimental methods). Table 1 shows that the experimental data does not agree with the molecular modeling of the spin labeled side chains at each of the chosen sites based on the static crystal structure. In some cases, such as the doubly labeled site 20/36, the two residues in the monomer are at a distance of less than 11Å. The average

distance calculated from the EPR spectrum is ~ 20 Å. The pattern of deviation between the EPR data and the crystal structure suggests that there are fundamental distortions at the N-terminus of helix-2.

Residue #	R (Å)	σ (Å)	Ca- Ca (Å) Monomer A	Ca- Ca (Å) Monomer B	NO-NO (Å) Monomer A	NO-NO (Å) Monomer B
12/42	19	8.6	9.7	12.8	7	18.7
15/38	24	7.8	12.4	14.2	16.7	26.3
15/42	25	7	11.4	13.2	10.4	19.8
16/34	22	7.8	11.7	12.5	17.7	19.6
19/34	22	8	12	11.5	19.85	22.7
19/36	23	7.6	8.6	9.5	9.8	7
19/39	18	8.3	9.6	11.6	3	8.7
20/34	18	9.1	8.7	7.7	11	14.5
20/36	20	9.7	9.6	6.3	10.3	10.3
23/33	23	2	7.63	7.04	10.8	8.4

Table 1: Intra-monomer distance between selected sites located in TM1 and TM2 determined by DEER. The grey shaded columns are the experimental average distance (R) and the width of the distance distribution (σ). The rest of the four columns are the calculated distances from the crystal structure, Cα-Cα and the spin labeled probe (NO-NO) modeled onto the crystal structure for each of the two monomers (A and B).

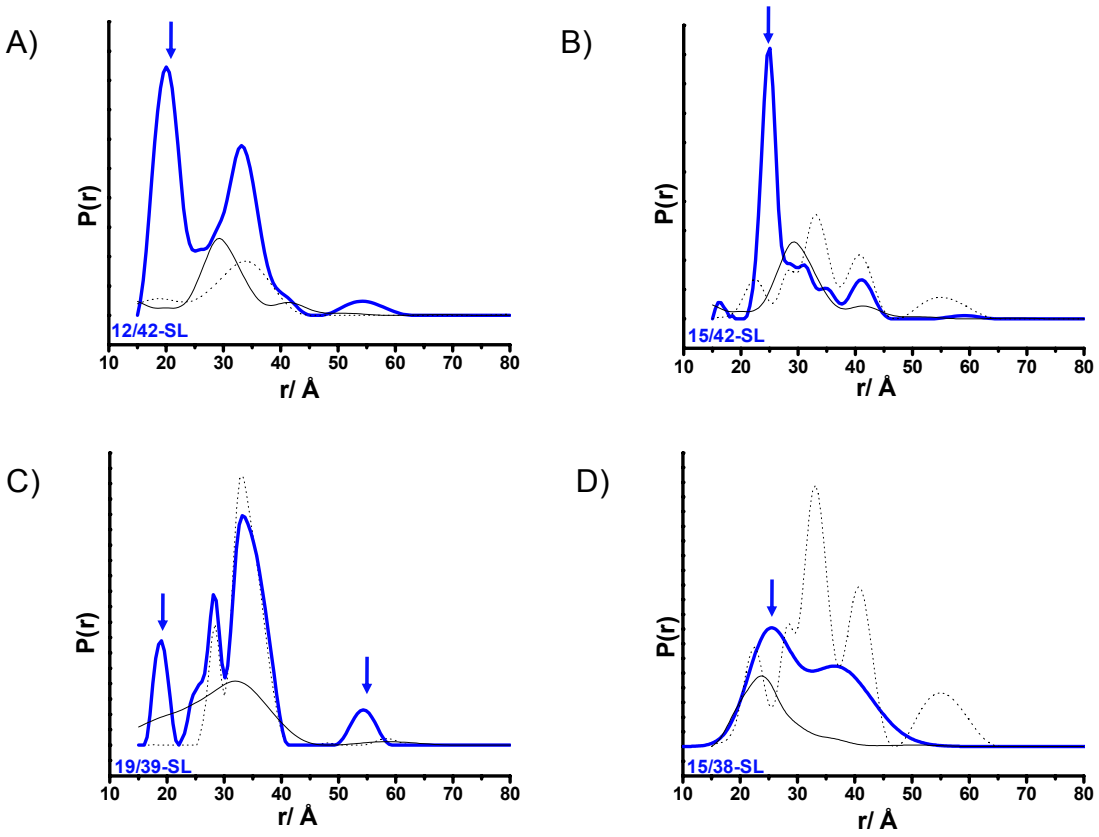

Figure 8: Distances between TM1 and TM2 determined by DEER. The distance distribution of the double labeled mutants is shown in the blue trace. The dotted black trace and black line are the distance distribution of the corresponding single mutants. Distance distribution are shown for; **A)** 12/42; **B)** 15/42; **C)** 19/39; **D)** 15/38. The peak average distance distribution for each site is shown in blue arrow.

The deviation of the EPR data from the crystal structure suggest that the N-terminus of the TM2 helix from both monomers in the crystal structure may well be tilted with respect to the lipid bilayer. The tilt in the transmembrane helix would support the results reported in Figure 6 and 7. In addition, the simple rotation (see Figure 5, black arrow) of TM2 would also correlate well with the high oxygen accessibility data from the

previous chapter suggesting that both 34 and 38 are facing the lipid bilayer with no tertiary contact.

To further support the data and the conclusions above, double mutants were chosen between TM1 and TM3 to test if similar trends can be observed and to confirm the orientation of the two monomers within the dimer of EmrE.

Packing of TM1 and TM3

Given the proposed dynamic role of TM3 (Fleishman et al., 2006) confirmed by the results in Chapters V and VI, it is important to determine its relative location in the monomer. Towards this goal, double cysteine mutants were introduced at positions 6/58, 12/70, 15/69, 15/74, 19/73, 16/74, 19/74, and 22/74 (see Figure 9 for the location of these sites in the crystal structure). Each of the double cysteine mutants were spin labeled, and CW-EPR spectra were collected as shown in Figure 10. Most of the chosen doubly labeled sites showed similar spectral line shapes to the corresponding sum of the single mutants. This suggests that the doubly labeled sites in the monomer are further apart than the proposed packing in the crystal structure.

The EPR spectral line shape of the doubly labeled sites at position 15/74, 16/74, 19/74, and 22/74 show broadening as would be expected for two spin labeled sites that are separated by less than 20 Å apart. This is in disagreement with the crystal structure, especially for the 22/74 pair where the sites are predicted to be facing away from each other (Figure 9).

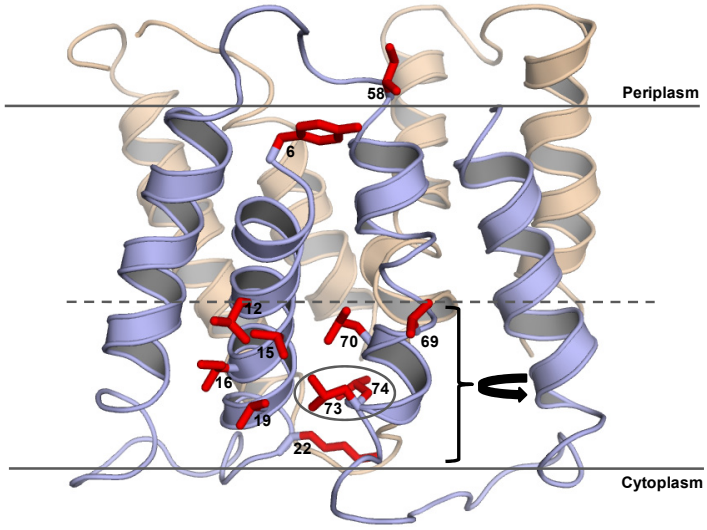

Figure 9: Double mutants for TM1/TM3 packing modeled onto the EmrE crystal structure. The two monomers are represented in blue and wheat colored ribbons**.** The mutation sites in both transmembrane segments are shown as red sticks for only one monomer. The horizontal dashed line (light grey) shows the location of sites in the middle of the bilayer. The predicted lipid bilayer is indicated by two horizontal lines. The black arrow shows the predicted rotation of the helix from experimental data.

The subunit exchange experiment shown in Figure 3, confirms that the spin-spin interaction of the two sites 19 and 74 arises from their interaction in the monomer. In contrast, hardly any broadening is observed in the 19/73 spectrum where the two spin labels are predicted to be 10 Å of one another in the crystal structure. In Chapter V the accessibility data showed site 74 to have high oxygen accessibility, suggesting that this site is facing the lipid membrane and not facing away from the lipid bilayer as suggested by the crystal structure. This orientation of TM3 would be consistent with the close proximity of site 74 with 15, 16, 19, and 22.

For the pairs 6/58, 12/70, 15/69, 15/74, 16/74, and 19/73 which did not show extensive spectral broadening, DEER experiments were carried out. Results of these experiments are compiled in Table 2 and analyzed to determine the average distance within the monomer. The table also compares the experimental data with the Cα-Cα and spin label distances measured from the crystal structure as described above.

The experimental distance distributions do not correlate with the distance measured from the molecular modeling of the spin labeled side chain (NO-NO) at each site based on the crystal structure. The distance measured by DEER for the chosen sites of TM1/ TM3 showed a wide distribution of distances (Table 2).

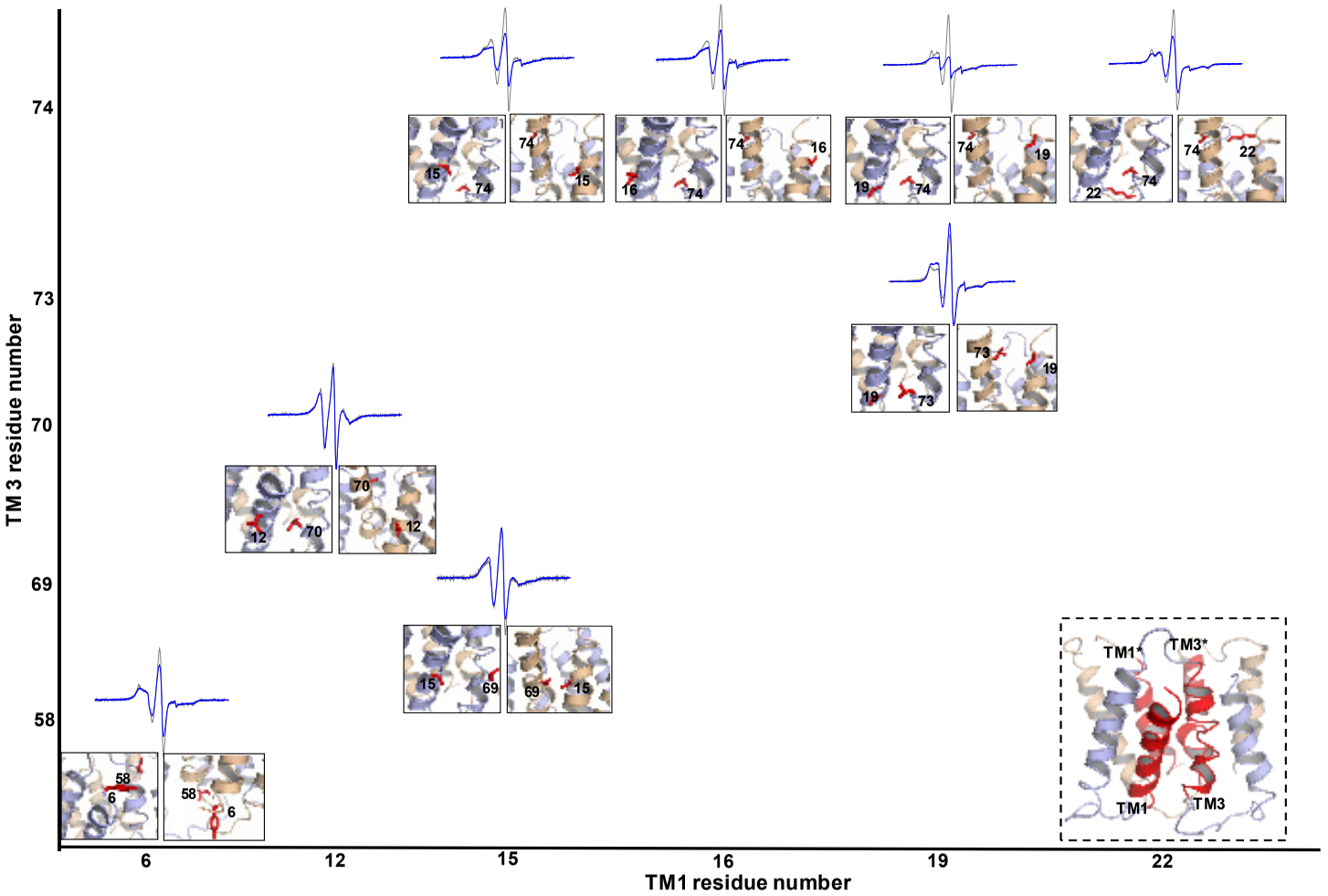

Figure 10: Matrices of the chosen spin label sites within TM1 and TM3. The bottom left panel is a ribbon diagram of the two subunits colored in blue and wheat. The location of TM1 and TM3 in each subunit is labeled. The red colored regions are the location of the chosen sites. The location of the two sites is shown in red sticks in both monomers. The CW-EPR spectra of the double spin labeled sites (blue trace) and sum of single mutants (grey trace).

Residue #	R (Å)	σ (Å)	Cα- Cα (Å) Monomer A	Cα- Cα (Å) Monomer B	NO-NO (Å) Monomer A	NO-NO (Å) Monomer B
6/58	35.9	12.4	11.5	10.8	3.7	5
12/70	33	8.2	8.7	10.5	14.6	21.6
15/69	26.4	10.3	9.2	6.8	9.3	5.6
15/74	34	11.4	7.7	12.2	18.9	19.2
16/74	15	10.8	9	13.7	21.9	25.9
19/73	31.6	10.3	7.4	8.6	7.9	11.2
19/74	7.9 [1]	6	6.4	10.8	18.6	19.8
22/74	17 [1]	6	7.1	11.4	6.8	11.4

Table 2: Intra-monomer distance between selected sites located in TM1 and TM3 determined by DEER. The grey shaded columns are the experimental average distance and the width of the distance distribution (σ). CW-EPR average distance obtained by the convolution method[1]. The rest of the four columns are the calculated distances from the crystal structure, Cα-Cα and the spin labeled probe (NO-NO) modeled onto the crystal structure for each of the two monomers (A and B).

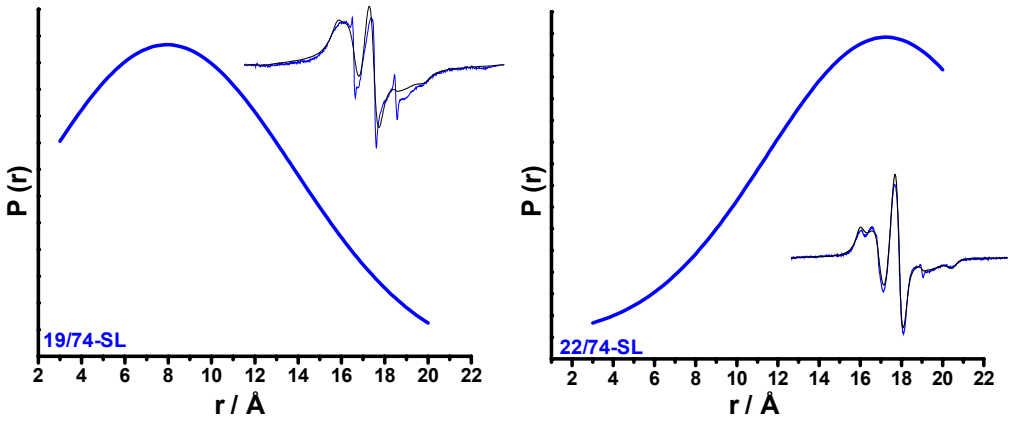

Figure 11: Distance distribution using CW-EPR. The distance distribution from the convolution method (Rabenstein & Shin, 1995) is shown for both 19/74 and 22/74. The CW-EPR spectra of 19/74 and 22/74 collected with a scan width of 200 G and 160 G, respectively. Double labeled mutant (blue trace), simulated spectra (black trace).

The broad distance distribution may be due to the proposed flexibility of TM3, thus, only the peak average distance distribution of the intra-spin labeled site 16/74 was determined. Both pairs 19/74 and 22/74 were analyzed using CW-EPR for the pair of nitroxides through the convolution method (Rabenstein & Shin, 1995), as shown in Figure 11 and Table 2. These two doubly labeled sites average distance do not agree with the nitroxide spin label modeled onto the crystal structure. In general, the measured distances of the chosen pair of nitroxides between TM1 and TM3 in the monomer are not in agreement with the crystal structure

Together, both the accessibility data (chapter V) and the data presented here, confirmed that sites 70, 73, and 74 are not at the dimer interface but are facing the lipid bilayer. This suggests that the C-terminus of the TM3 helix in the crystal structure must be rotated counterclockwise (see Figure 9, black arrow) to support the results mentioned above. Furthermore, previous chapters and biochemical evidence (Elbaz et al., 2008) have shown that the TM3 helix is highly flexible, thus the crystal structure of the substrate bound-state of EmrE may well be a snap shot of one intermediate that was not observed in the solution structure examined here.

Packing of TM2 and TM3

To further investigate how the helices are arranged in the monomer, we analyzed the dipolar interaction in the 38/74 and 47/62 pairs relating TM2 and TM3. The CW-EPR spectra of each of the two pairs of nitroxide spin labels are shown in the appendix (see appendix, page 211). In both cases, spectra of the double mutants were similar to the corresponding sum of the single mutants, suggesting that the sites are more than 20 Å apart. Since the doubly labeled site 38/74 is further in distance than 19/74, the

arrangement of the transmembrane helices is in agreement with the crystal structure and the EM model, where the TM1 helix is sandwiched between TM2 and TM3 on each side.

Intra-Monomer Distances between Residues Located in TM1/TM4, TM2/TM4, and TM3/TM4

The location of TM4 relative to the membrane normal has been controversial. The crystal structure of the substrate bound-state shows TM4 to be perpendicular with respect to the membrane plane. It is, therefore, important to investigate the distance between spin label pairs located in TM1/TM4, TM2/TM4 and TM3/TM4 in the monomer which will add another dimension to the apo-state model of EmrE. Towards this goal, double cysteine residues were introduced at: 12/88, 15/88, 16/88 for TM1/TM4; 32/85, 35/88, 36/89 for TM2/TM4; 58/103 for TM3/TM4. Each of the doubly labeled mutants was spin-labeled and CW-EPR spectra (Figure 12 and Figure 13) and distances for each of the double mutants were determined using DEER. The distributions of distances for the intra-spin labeled sites are shown in Table 3 (see appendix for detail of the distance distribution of each of the doubly labeled mutants).

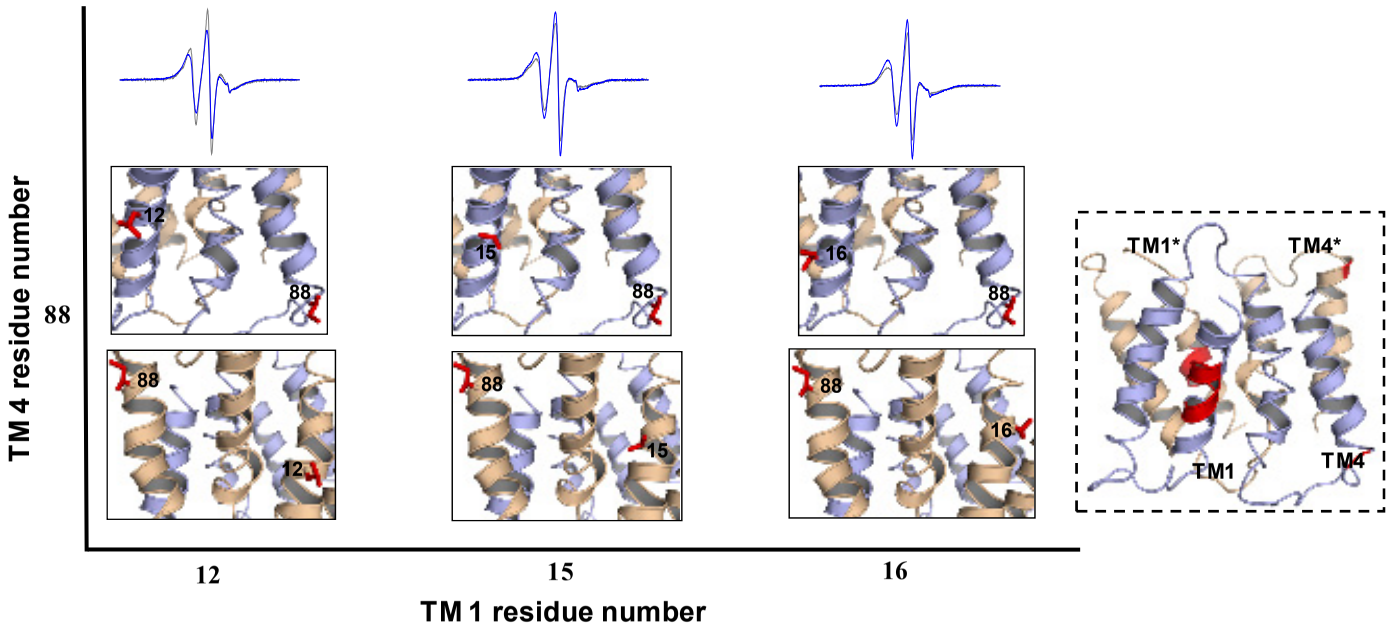

Figure 12: Matrices of the chosen spin label sites within TM1 and TM4. The far right panel is a ribbon diagram of the two subunits colored in blue and wheat. The location of TM1 and TM4 in each subunit is labeled. The red colored regions are the location of the chosen sites. The location of the two sites is shown in red sticks in both monomers. The CW-EPR spectra of the double spin labeled sites (blue trace) and sum of single mutants (grey trace).

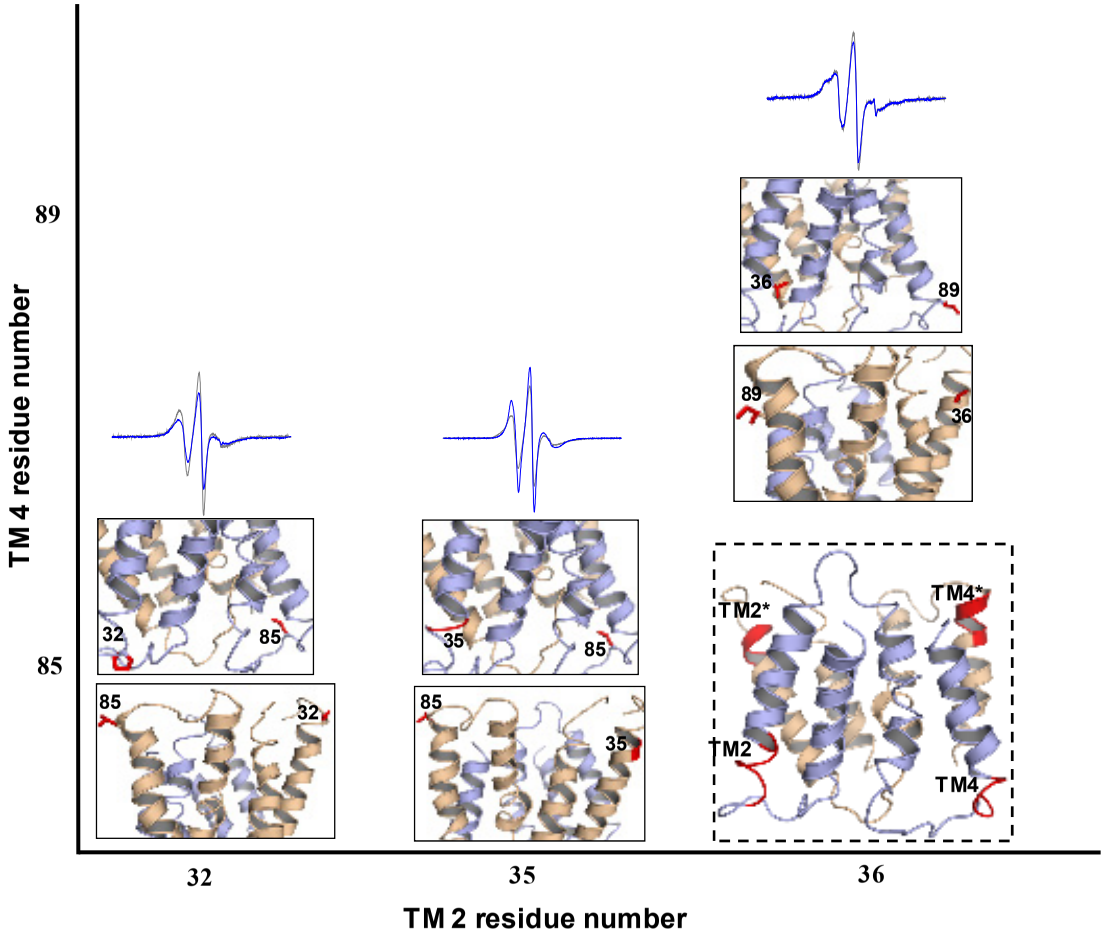

Figure 13: Matrices of the chosen spin label sites within TM2 and TM4. The bottom right panel is a ribbon diagram of the two subunits colored in blue and wheat. The location of TM2 and TM4 in each subunit is labeled. The red colored regions are the location of the chosen sites. The location of the two sites is shown in red sticks in both monomers. The CW-EPR spectra of the double spin labeled sites (blue trace) and sum of single mutants (grey trace).

Residue #	R (Å)	σ (Å)	Ca-Ca (Å) Monomer A	Ca-Ca (Å) Monomer B	NO-NO (Å) Monomer A	NO-NO (Å) Monomer B
12/88	22.5	9.1	23.5	22.5	30.3	31.9
15/88	23.5	8.8	20.6	20.6	24.8	20.6
16/88	24.5	9.7	23	23.4	31	36.6
32/85	47	11.7	30.6	35.4	22.8	39.2
35/85	34.6	10.8	32.8	36.9	30.3	38.9
36/89	30.7	9.9	30.8	32.4	30.6	33
58/103	18	10.3	7.2	-	15.8	-

Table 3: Intra-monomer distance between selected sites located in TM1/TM4, TM2/TM4, and TM3/TM4 determined by DEER. The grey shaded columns are the experimental average distance and the width of the distance distribution (σ). The rest of the four columns are the calculated distances from the crystal structure, Cα-Cα and the spin labeled probe (NO-NO) modeled onto the crystal structure for each of the two monomers (A and B).

The average distances of the three chosen double mutant sites between TM1/ TM4 (Table 3) are not in agreement with the spin label modeled onto the crystal structure, especially for sites 12/88 and 16/88, which shows a distance of more than 30 Å. This suggests that the N-terminus of TM4 is closer to TM1 than is suggested by the crystal structure of the substrate bound-state. In Chapter V, we had mentioned that TM4 is tilted relative to the membrane plane; therefore, the distances correlate with the accessibility data.

As for the double mutants between TM2/TM4, since the distance distribution of the double mutant sites were similar to the corresponding single mutants (see appendix,

page 212), thus, we could not make a final conclusion. However, the distance distribution suggests that the TM2 helix is furthest away from the TM4 helix, while the TM3 helix is the closest to the TM4 helix.

Overall, TM4 is further from the three transmembrane segments and may only contribute structurally as has been proposed for a homologue of EmrE, Hsmr, where TM4 is required for oligomerization (Poulsen, Rath, & Deber, 2009).

Evaluating the Monomer in the Crystal Structure

Several studies have used CW-EPR or pulse EPR techniques (McHaourab et al., 1997; Rabenstein & Shin, 1995) to derive structural models. The distance constraints obtained from CW-EPR or DEER methods can be used to assess structure models, such as the crystal structure and the EM model of EmrE.

Based on the sites examined in this Chapter, a number of observations can be made; The packing of the helices in the monomer was in agreement with both the crystal structure and the EM model, where TM1 and TM3 are between TM2 and TM4 (Y. J. Chen et al., 2007; Fleishman et al., 2006). This assignment of the helices suggests that the two monomers can form a dimer in an antiparallel orientation. Recent work has suggested that since conserved sites must face the core of the protein (Korkhov & Tate, 2008), the second monomer must be inverted to bring the conserved sites to face the center with similar interactions to the first monomer, forming a functional dimer. In contrast, published work using a tandem-EmrE where a linker connected the two monomers by a linker was compatible with parallel topology, and this construct had similar functional characteristics to the wild-type EmrE (Steiner-Mordoch et al., 2008). However, the

tandem-EmrE results do not rule out a dimer of dimer that is antiparallel. In addition, the crystal structure had observed a two fold symmetry axis relating two dimers but it was not shown (Y. J. Chen et al., 2007). These contradictions are still to be resolved.

The EPR results describing the detailed packing of the helices within the monomer did not correlate well with the crystal structure. One of these reasons would be the difference in the detergent used by the crystal structure (Nonyl-β-D-glucoside) versus Dodecyl-β-D-maltoside used in this experimental work (see details in Chapter IV). The NG, having a shorter hydrocarbon chain length has an effect in destabilizing the hydrophobic transmembrane segments of EmrE. Recent published work has proposed that different detergents can cause an increase in flexibility at similar sites within the same helix (Columbus et al., 2009). Thus, the use of different detergent micelles has an effect not only on helix-helix interactions but also on helix-micelle interactions. This could explain the difference in the packing of TM2 and TM3 with respect to TM1. Second, the crystal structure had published only the Cα trace of TPP^+-bound EmrE. Thus, the modeled residues might also deviate from the real projection in the crystal structure. However, these changes are minor when comparing the distances for the selected residues of EmrE in solution with respect to the static crystal structure.

The intra-monomer probe distances were in good agreement with the EPR spectral line shapes. For sites with a broadened spectral line shapes, such as 19/74 (Figure 11), showed a distance of < 15 Å, while sites that had mobile spectral line shapes such as 12/70 (see Table 2, and Figure 10) reflects a distance of > 25 Å. Yet, the broad distribution of distances observed may either be related to the asymmetry of the two

monomers within the EmrE dimer, or the flexibility and the dynamic contribution from the backbone fluctuation. This will be further clarified in the subsequent Chapter.

Conclusion

In this chapter, site-directed spin labeling (SDSL), in combination with CW-EPR and pulse EPR methods, was used to investigate the orientation and packing of the helices within the EmrE monomer. The 34 double mutants selected were strategically chosen so as not to interfere with the packing of EmrE in the monomer or in the dimer. The data suggests that the packing and orientation of TM2 and TM3 with respect to TM1 in the monomer deviates from the crystal structure. Thus, from the experimental results of the chosen sites of TM2 and TM3, both transmembrane segment need to be oriented counterclockwise to a certain degree with respect to TM1, which might in some cases support the static crystal structure. However, in other cases the average distance deviates greatly from the crystal structure even when rotating the transmembrane segments would not correspond to the crystal structure. Overall, the location of the transmembrane segments in the monomer supports both the crystal structure and EM model but does not support the packing interface between the transmembrane segments within the monomer.

CHAPTER VIII

PACKING OF EMRE MONOMERS IN THE DIMER. INSIGHT FROM LONG RANGE DISTANCE MEASUREMENTS BETWEEN SPIN LABELS

Introduction

Defining the structure and dynamics of EmrE is fundamental for the mechanistic description of its function. Although x-ray crystallography has yielded deep insights into the structure of proteins, constraints needed for growing crystals cannot provide dynamic information under physiological conditions. In the case of EmrE, the orientation of the two monomers in the dimer has emerged as a focal point of contention. EmrE structures, determined from 2 and 3 dimensional crystals, provide compelling evidence supporting an antiparallel orientation of the monomers (Y. J. Chen et al., 2007; Tate et al., 2001). In addition, the sequence determinants of membrane topology, the arginine and lysine contents of EmrE loops (i.e. the K+R bias), do not favor a unique orientation in the membrane implying that EmrE could inserts with dual topology (Rapp et al., 2007). However, experiments designed to verify or alter the relative orientation of the monomers were inconclusive (McHaourab et al., 2008).

In contrast, a body of biochemical data supports a parallel orientation of the dimer. These include the design and construction of functional EmrE chimeras where monomers are linked by short polar loops that are not favored energetically to cross the bilayer (Steiner-Mordoch et al., 2008). Furthermore, sites predicted to be on opposite

sides of the membranes in the antiparallel dimer model can be cross-linked without significant perturbation of transport (Soskine et al., 2002).

In Chapter VI, double electron-electron resonance (DEER) was used to obtain distances for regions in TM3 in order to define conformational changes induced by TPP^+ binding. Narrowing of the distance distribution and a decrease in the average distance was observed. The experiments demonstrated that careful analysis of the shape of the distance profile can provide detailed information regarding conformational sampling of the ensemble of structures.

In this chapter, an extensive spin labeling EPR analysis in detergent micelle using DEER spectroscopy was carried out (Borbat et al., 2001; Borbat et al., 2007; Hubbell, Cafiso, & Altenbach, 2000; Jeschke et al., 2005). The experimental distances were compared to the Cα and the spin labeled probe modeled onto the crystal structure of the substrate bound-state of EmrE. The shape of the distance distributions reveal multiple conformations of EmrE due to motion of the backbone to which the nitroxide label is attached. Two questions are addressed in this chapter: the first is whether the EmrE dimer consists of antiparallel monomers and the second is the nature of the conformational changes induced by substrate binding.

The crystal structure of the substrate bound-state of EmrE in detergent micelles (Y. J. Chen et al., 2007) provides a starting point to evaluate the conformational state of EmrE. The experimental work will evaluate not only the crystal structure of the substrate bound-state of EmrE in the mechanistic chain of events but also its deviation relative to the apo-state.

Experimental Methods

Double Electron-Electron Resonance (DEER)

The double cysteine mutants were made on a cysteine-less EmrE background. Purification and labeling were done as described in chapter III. The detergent samples for DEER measurements were concentrated to a final protein concentration 140-200 μM containing 30% glycerol (w/v). For the substrate bound-state of EmrE, a final concentration of 1 mM of TPP^+ was added. All distance data were collected at 83°K (-190°C) using four-pulse DEER protocol (Pannier et al., 2000). DEER signals were analyzed by Tikhonov regularization (Chiang et al., 2005) using DeerAnalysis 2008 software to determine average distances (r) and distribution of distances P(r).

Molecular Modeling

Modeling of double-labeled mutants with MTSL is based on the crystal structure of the substrate bound-state of EmrE (PDB ID: 3B5D; (Chen et al., 2007). The dihedral angles (χ_1, χ_2, χ_3) between the Cα of the spin labeled cysteine and the nitroxide ring were fixed. The disulfide-linked nitroxide side chain was estimated using the $\chi_4\chi_5$ model (Langen et al. 2000) where χ_4 and χ_5 were varied to explore conformational space. The relative distances between the two nitroxide radicals were calculated using the CalDihedral in-house program (see detail in Chapter VII, experimental methods).

Results and Discussion

Distance Fingerprint of Antiparallel Packing

The published crystal structure of EmrE in the substrate bound-state had only reported the Cα trace of the four α-helices (Y. J. Chen et al., 2007). Figure 1 show the Cα inter-subunit distance for each site that is resolved by the crystal structure (sites 6 to 102). An interesting pattern is observed in Figure 1. The sites with distances greater than 30 Å are located in the loops connecting each of the four TMSs and located on opposite side of the lipid bilayer in the crystal structure. For each TM helix, the sites of close distances are located near the center of the helices.

Figure 1B shows the predicted distances between spin labels modeled onto the crystal structure of TPP^+-bound EmrE. The modeled distances agree well in trend but not in magnitude with the Cα-Cα distances for sites located in TM2, TM3, and TM4. For TM1, the pattern is distorted for sites in the middle of the helix where the projection of the spin label leads to distances close to 30 Å. This reflects the tilt of the two helices relative to the membrane normal and the shorter separation between the helical axes.

One caveat with this approach is that at buried sites, the spin labels are likely to have different orientations relative to the alpha carbon than predicted by the simple cone model used here. However, exact modeling of the spin label rotamers at sterically restricted sites has not been carried out and is beyond the scope of this dissertation. Therefore, the pattern of distances between the modeled spin labels will be compared to the experimental distances with emphasis on exposed sites in the TM helices and loops.

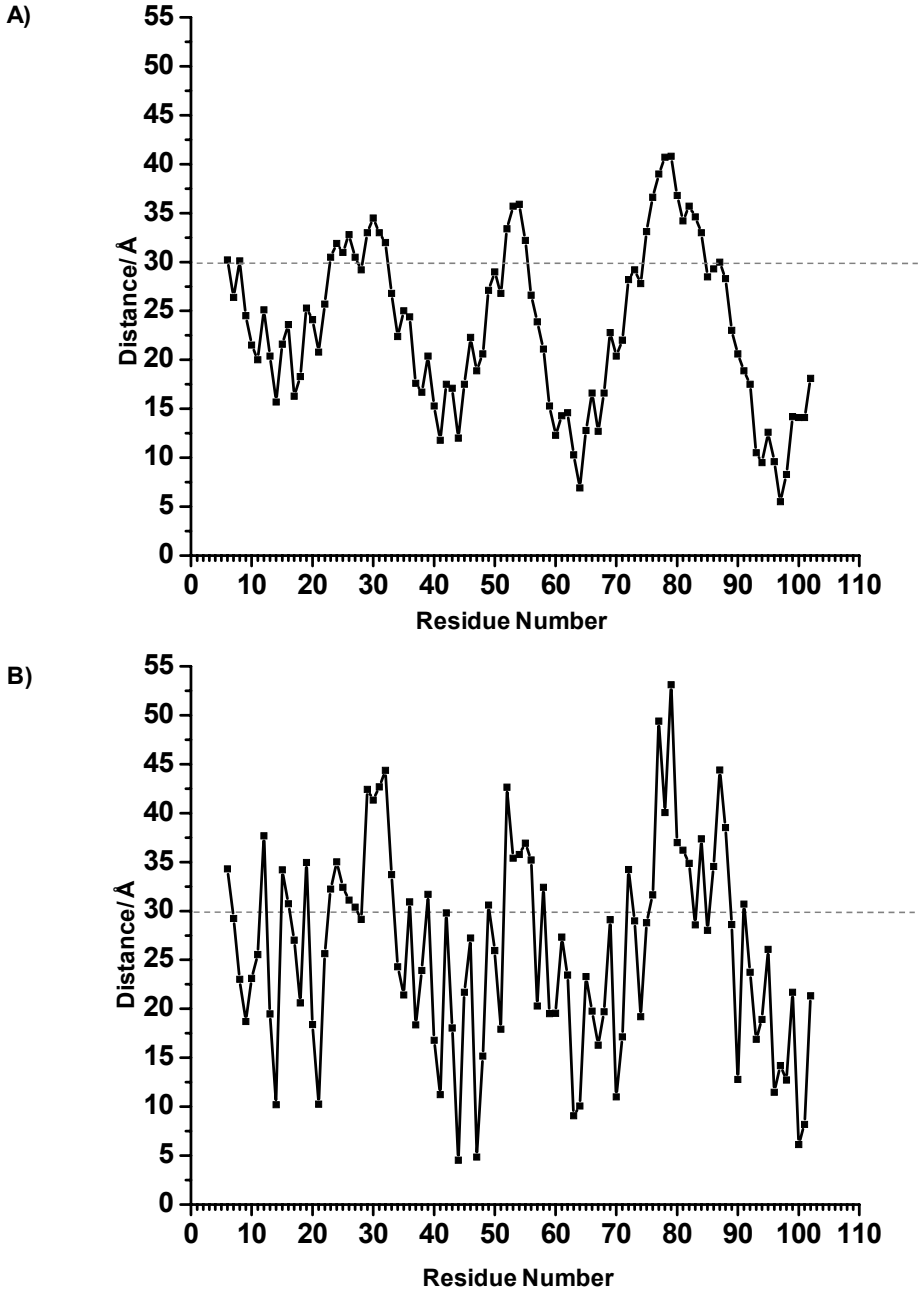

Figure 1: Calculated distances from the crystal structure. A) The calculated Cα-Cα distance between EmrE residues 6 to 102. B) The calculated inter-spin label nitroxide distances modeled onto the crystal structure for each residues from 6 to 102. The horizontal grey dotted lines show that distances above 30 Å are in the loop regions while those below 30 Å are within the transmembrane segments.

Distance Analysis of EmrE Structure in Detergent Micelles

To test whether the experimental distances between the inter spin labeled sites are similar to those predicted by the crystal structure of the substrate bound-state, 59 different sites were chosen where the spin labels are predicted to be more than 20 Å apart. The chosen sites are from TM1 (6, 8, 9, 12, 13, 15, 16, 19, 20, 21, 22, 23, 25, 26, 27, 28, and 29); from TM2 (31, 32, 33, 34, 35, 36, 38, 39, 42, 43, 46, 47, 52, 53, 54, 56, 57, and 58); from TM3 (59, 61, 62, 66, 67, 68, 69, 71, 73, 74, 76, 77, 78, 79, 81, 82, and 83); and from TM4 (85, 88, 89, 91, 99. 100, 102). Each of the 59 single cysteine mutants were spin labeled, and the distance between symmetry related pairs were measured using DEER. Data were analyzed to determine the average inter-spin label distances.

The table in the appendix of the inter-spin label interaction (see appendix, pages 213 and 214) summarizes distances and the distribution of distances for the spin label mutants in TM1, TM2, TM3 and TM4 determined in the apo-state and for some in the substrate bound-state. The differences in the average distance between the two states are very small, as will be shown in the next section. The distances that were collected were divided into two categories; the first consists of sites where single component distance distributions are observed, and the second consist of sites where multiple component distance distributions are observed. These two categories will be discussed separately below.

Single Component Distance Distributions

From the 59 different sites that were chosen for distance measurements only 22 sites showed single component distance distributions that can be compared to the calculated distance of the crystal structure (Figure 2).

These sites are: for TM1 (6, 8, 9, 16, 20, 21, 22, 23, 27, and 29); for TM2 (32, 33, 34, 38, 42 and 53); and for TM4 (82, 85, 88, 89, 99, and 102). In some sites the average distance of the TPP^+ bound-state was measured for comparison with the apo-state (see Figure 2 and the tabel in the appendix, pages 213 and 214). The average distance between the two states did not change. Therefore, we will focus on the experimental data of the apo-state and compare it to the crystal structure of the TPP^+ bound-state.

All these residues are located at the N- or C-terminal regions in the crystal structure. When compared to the predicted distances, substantial deviations (up to 10 Å) are noted at some sites specifically in TM1. At sites 21, 22, and 27 where the spin label is involved in steric contacts and therefore its location relative to the Cα is not well defined, the distances are likely to deviate from the cone model. Hence, the packing of the side chain would possibly determine the orientation, and in turn the average distance and the distribution of distances (Alexander, Bortolus, Al-Mestarihi, McHaourab, & Meiler, 2008).

For the sites located in the N-terminal TM2 helix (sites 32-34, Figure 2B), the experimental distances and the calculated distances are similar.

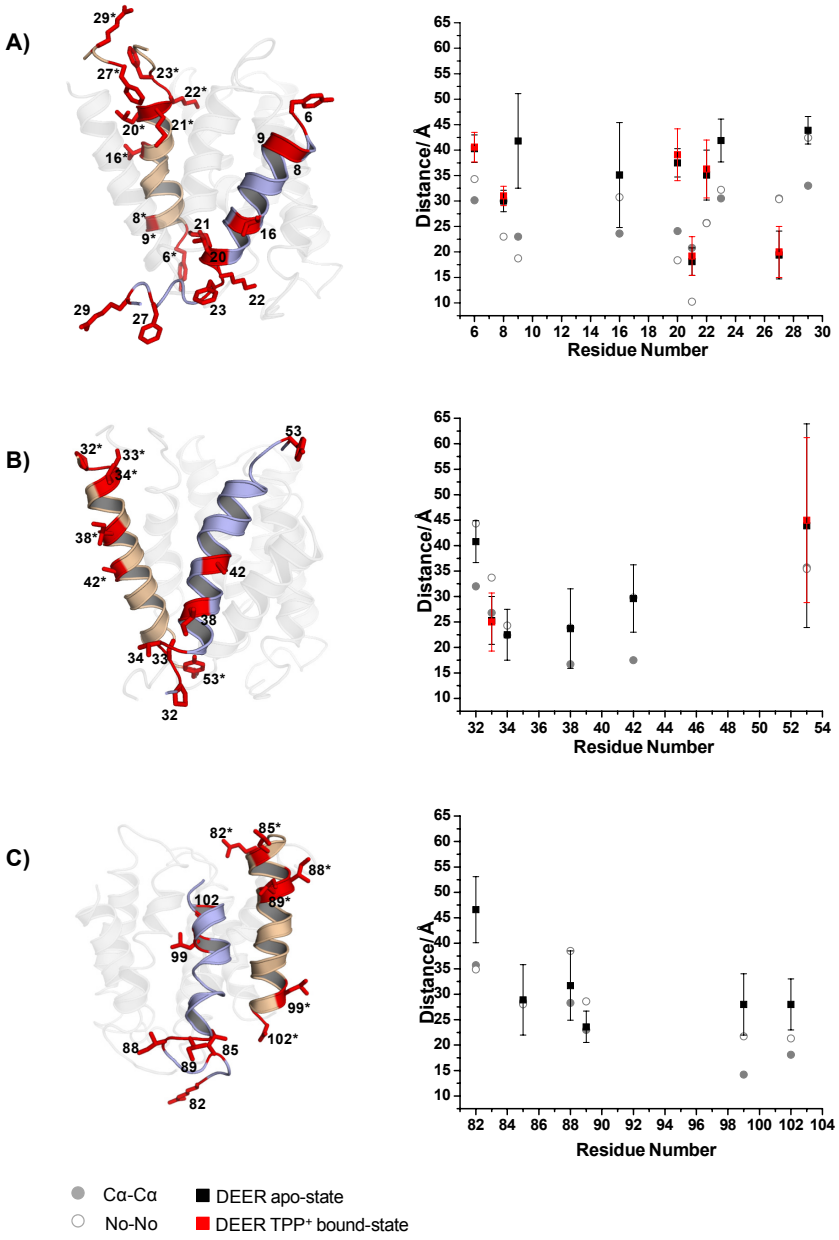

Figure 2: Comparison of experimental distances to the crystal structure of TPP^+ bound-state. The left column shows the ribbon diagram of each TM helices highlighted in blue and wheat for each monomer, for clarity. The chosen regions for distance measurements are highlighted in red, they are A) TM1 sites; 6, 8, 9, 16, 21, 22, 23, 27, and 29. B) TM2 sites; 32, 33, 34, 38, 42, and 53. C) TM4 sites; 82, 85, 88, 89, 99, and 102. The sites in the second monomer are distinguished by asterisk. The right column is the inter-spin label experimental distance determined by DEER of the apo-state (black squares) and TPP^+ bound-state (red squares). The vertical bars are the width of the distance distribution from fitting the experminetal data. Grey empty circle are the calculated distances by modeling the spin label onto the crystal structure at each position. The calculated Cα-Cα distances from the crystal structure are the grey filled circle.

However, moving towards the middle and the C-terminal the distances vary suggesting a change in the backbone packing. Site 53 that is located in the loop region connecting TM2 to TM3 shows a large distribution of distances suggesting that this part of the loop is flexible.

At a number of sites in TM4, the distances deviate from the crystal structure, suggesting that the backbone of TM4 helices in the apo-state is further apart. The difference could also pertain to the packing of the helices in the dimer. The DEER data is in support of EPR accessibility (see Chapter VI) suggesting that TM4 may have a larger average tilt relative to the membrane normal than what is observed in the substrate-bound crystal structure.

Overall, the experimental distances of specific regions of EmrE are in accordance with the modeled spin label onto the crystal structure for sites that are located only in N-termini of TM2s, but not for TM1, C-termini of TM2s and TM4, suggesting a difference in the helical packing for certain regions. In all the single component distances that have been collected and shown in Figure 2, none were from sites located in TM3. TM3 are in the second category of distances, which show multi-component distance distributions.

Multi-Modal Distance Distributions: Dynamics of TM3

The two questions that are crucial in understanding the structure of EmrE is; First, why do most of the data that were collected for distance measurements of EmrE have multiple component average distances and second, if the multiple distance components are a reflection of flexibility of the EmrE backbone, how are the distances affected when the substrate (TPP^+) is bound?

Recent published work has shown that DEER distance distributions provide information about conformational ensemble and equilibria (Blackburn et al., 2009; Smirnova et al., 2007; Zou & McHaourab, 2009). Hence, the observation of two or more distance populations between symmetry related spin labels, indicative of minor and major spin populations in the spectroscopic ensemble. On the other hand, the wide distance distributions are indicative of flexibility or the sampling of different local conformations. In EmrE, 37 sites out of the 59 sites were collected for distance measurements and located in TM1, TM2, TM3 and TM4 (See appendix, for detail of the distance distributions) all showed multiple component distance distributions in the apo-state. In most of these cases the differences in the distances suggest that it does not arise from multiple conformations of the label. Rather, our model suggests that throughout the apo-EmrE structure a constant motion of the backbone occurs. This conformational flexibility of apo-EmrE may have an important role in facilitating the binding of substrates to different sizes and structures.

Consistent with the accessibility and mobility data described in Chapter VI, distance distributions of spin labels along TM3 suggest a highly flexible backbone. The multiple component distributions are illustrated in Figure 3 for site 77 and 78. Other sites were presented in Chapter VI, Figure 18 and the rest are in the appendix (pages 218 and 219). These represent functionally relevant conformational equilibria that are supported by the effects of TPP^+ binding. Sites located in TM3 (68, 69, 71, 73, and 74) and the loop region connecting TM3 to TM4 (76 to 79) show changes in the shape and width of the distance distributions. In some cases, such as site 71 and 76, there was also an increase in

the average distance. The shift to longer distance induced by TPP^+ binding was also evident for sites 19, 20 and 21 of the TM1 helix.

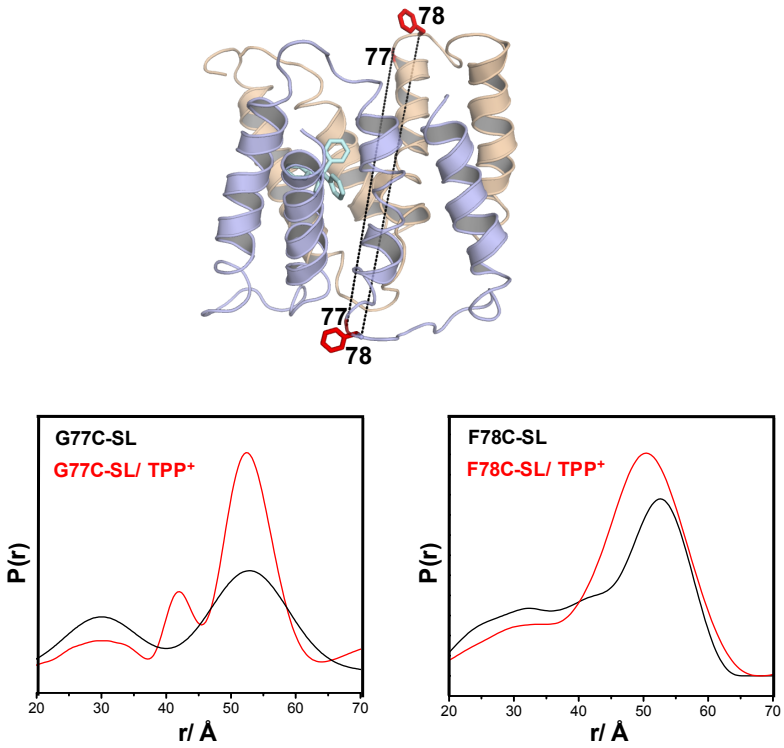

Figure 3: **DEER distance measurements of inter-probe residues of 77 and 78 located in TM3 with and without TPP^+.** A ribbon representation of the two subunits of EmrE is shown in grey and wheat. The TPP^+ is shown in light cyan. The location of sites 77 and 78 are represented by red sticks. The black dotted line shows the distance between the Cα-Cα for each site in the dimer. The distance distribution from the DEER experiments of the spin labeled site 77 (left) and78 (right) in the presence (red trace) and absence (black trace) of TPP^+.

The experimental distances are all measured in frozen solution which in principle captures all the conformations of the nitroxide at room temperature. Although, specific conformations at low temperature might be more favorable than others, the multiple distance components observed at most sites of EmrE suggest that there is a conformational equilibrium that adds complexity to the structural topology of EmrE.

Further work is needed to evaluate the complex distance distribution by collecting data using different microwave frequencies in the presence of other substrates. More importantly, the use of molecular modeling should provide a perspective on the nature of the conformational ensemble.

Short Range Distance Analysis of the Dimer Interface

The asymmetry of the two monomers that form a dimer in the crystal structure shows that one side is further apart than the opposite side, which suggests the transporter is facing one side of the bilayer. Thus, choosing double mutants that are in close proximity at the dimer interface would elucidate the asymmetry. The chosen mutants were 21/48 between TM1 and TM2, and in the loop region connecting TM1 to TM2 they are: 22/53, 23/53, and 26/52 (Figure 4).

The inter-probe interaction at the dimer interface did not agree with the close proximity that is shown in the crystal structure. Since there is asymmetry in the crystal structure the spectral line shape should reveal multiple spin label populations that would suggest different conformational geometry in the packing of the interface, however, this was not observed.

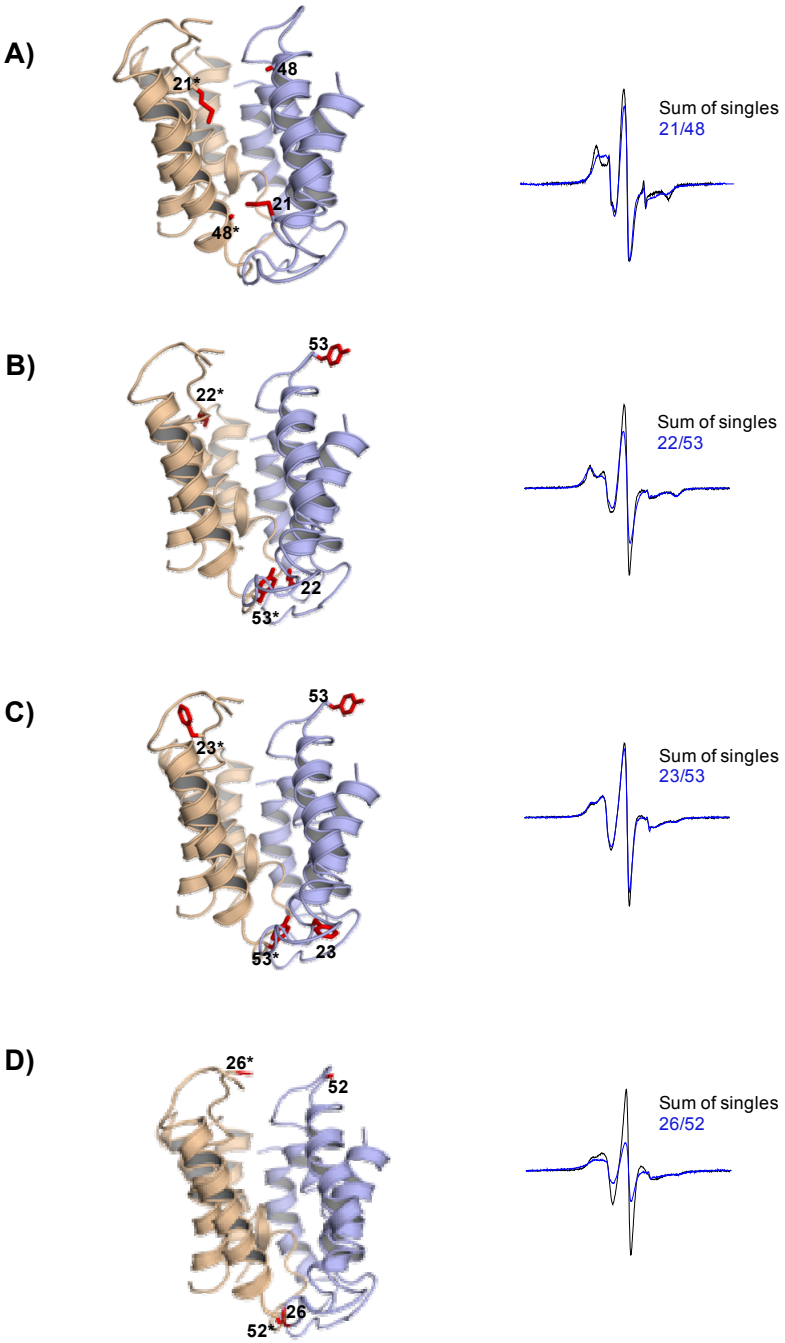

Figure 4: **Inter-probe interactions of TM1 and TM2 sites at the dimer interface.** Sites **A)** 21/48, **B)** 22/53, and **C)** 23/53, and **D)** 26/52 are represented by red sticks on the ribbon diagram of the substrate-bound EmrE crystal structure. Each subunit is shown in grey and wheat. The CW-EPR spectra for each double spin label site are shown in blue trace. The corresponding sum of single mutants is shown in black trace. All spectra were recorded at room temperature with a scan width of 160 Gauss.

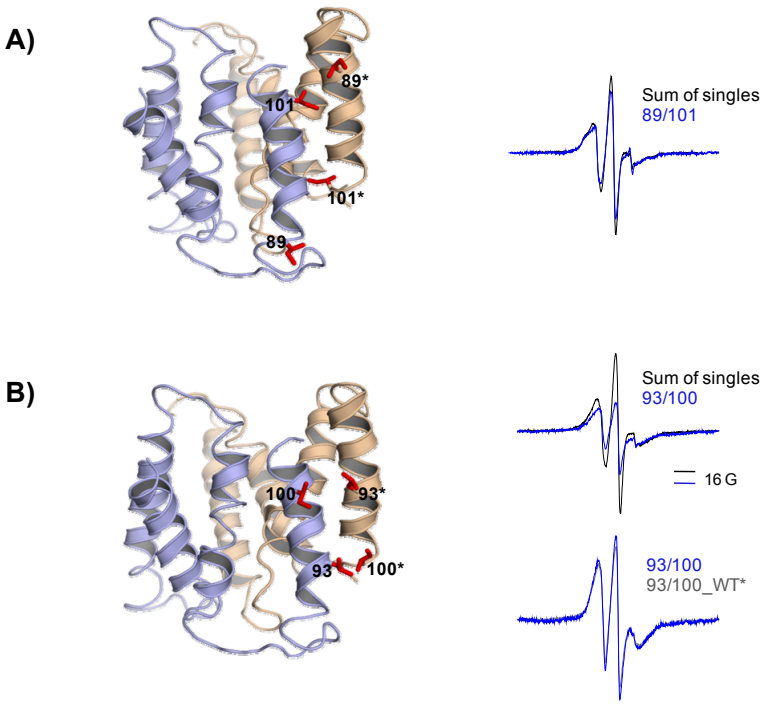

Figure 5: **Inter-probe interactions of TM4 sites at the dimer interface. A)** 89/101 and **B)** 93/100 are represented by red sticks on the ribbon diagram of the substrate-bound EmrE crystal structure. Each subunit is shown in grey and wheat. The CW-EPR spectra for each double spin label site are shown in blue trace. All spectra were recorded at room temperature with scan width of 200 Gauss with the exception of the spectra of sum of singles and 93/100 (top right panel of B) was recorded with a scan width of 160 Gauss. The grey trace spectral line shape (lower right panel of B) is the subunit exchange of 93/100 with cysteine-less EmrE (WT*).

To characterize the packing of TM4 at the dimer interface, pairs of spin labels were introduced at sites predicted to be in close proximity in the crystal structure. Figure 5A and B shows two double spin lablel mutants located at position 93/100 and 89/101. In Chapter V the mobility data of the TM4 helix shows that symmetry related sites along TM4 are further apart than suggested in the crystal structure. Consistent with this result, the CW-EPR spectral line shape of site 89/101 does not show any broadening indicating that the spin labels are more than 20 Å apart. The spectrum was similar to the sum of the corresponding single mutants.

Conversely, 93/100 (Figure 5B) showed a broadened spectral line shape, suggesting close proximity via inter-monomer or intra-monomer interactions. This unique mutant of 93/100 has similar intra- and inter-monomer distances of 15 Å in the crystal structure. The two interactions can be resolved using subunit exchange with unlabeled cysteine-less EmrE (WT*) (see detail of the method in Chapter III). If the broadening that is observed is due to inter-monomer interaction it would be expected that subunit exchange would lead to an increase in signal amplitude. The result reveals an intra-monomer interaction of 93/100, where subunit exchange sample had similar spectral line shape to the double spin label site of 93/100. This confirms that TM4's are further apart than suggested in the crystal structure.

Conclusion

The main goal of this chapter is to compare distances between symmetry related spin labels in detergent micelles with the calculated distances from the structure of EmrE in the substrate bound-state. In most cases, the experimental distances did not agree in trend and magnitude with the Cα-Cα distances of the crystal structure, suggesting a difference in the backbone order.

The overall consensus from the distance measurements shows the dynamic flexibility of the EmrE backbone in the apo-state. The dynamic flexibility is an important feature of EmrE that confers the ability to bind to a variety of structurally dissimilar substrates.

In the substrate bound-state of EmrE, the C-termini of TM1 sites show an increase in average distance, suggesting that the C-terminal region of TM1 is moving further apart

upon the binding of the substrate. However, sites located in TM2 and TM3 shows very little change in average distances between the two intermediate states but a decrease in flexibility of the backbone. The decrease in flexibility of EmrE induced by TPP^+ may initiate an intermediate for the vectorial translocation of the substrate across the membrane bilayer.

In general, the crystal structure is a snap-shot of one of several intermediate states of EmrE due to its flexibility. Therefore, it is not unexpected that the experimental distances collected in solution would deviate from the static crystal structure.

CHAPTER IX

SUMMARY AND PERSPECTIVES

The work presented in this dissertation addresses three fundamental questions relevant to the transport mechanism of EmrE:

1. How can we reconcile the EPR data with the crystal structure of EmrE in the substrate bound-state?

2. What conformational changes of EmrE are observed in the presence of TPP^+, how does it compare with the apo-state EPR data, and with the crystal structure of the TPP^+ bound-state?

3. What is the topology of EmrE?

The consensus antiporter mechanism (Figure 1) proposes that substrate in the cytoplasm would bind to unprotonated glutamate at position 14 (E14) of EmrE. A conformational change occurs causing the binding site to face the periplasm. In the periplasm the pH is more acidic, E14 becomes protonated and leads to the release of the substrate.

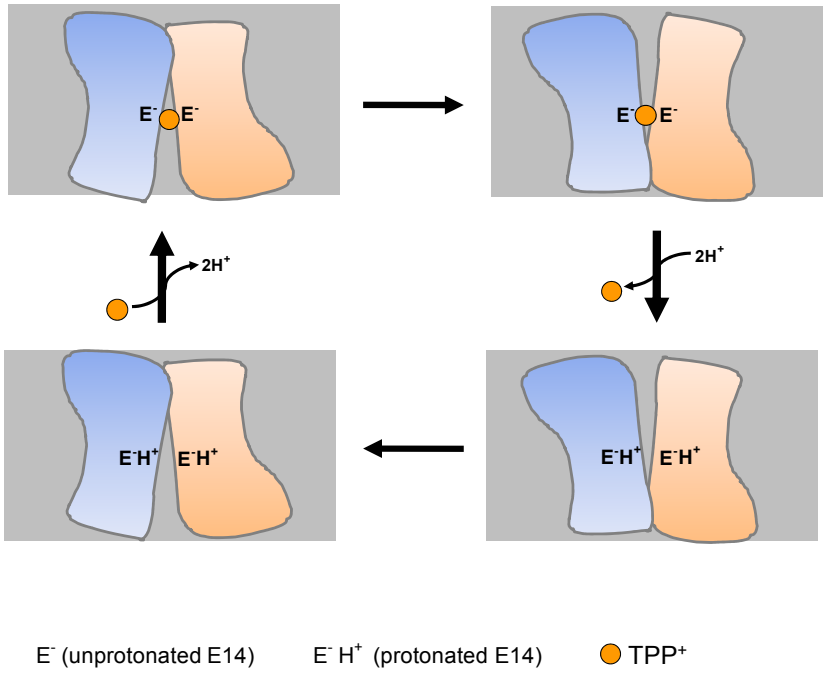

Figure 1: Proposed mechanism for transport by EmrE. The two asymmetric monomers are shown in blue and orange. E^-H^+ is the protonated glutamate residue at position 14. E^- is the unprotonated glutamate residue. The approximate dimensions of the lipid bilayer are shown by the grey shading.

Reconciling the EPR data of EmrE Apo-State with the Crystal Structure of the Substrate Bound-State

The published crystal structure reports that EmrE is an asymmetric dimer composed of four transmembrane helices / monomer packed in an antiparallel orientation (Y. J. Chen et al., 2007). The substrate is bound in the center of the first three helices from each monomer, while the fourth transmembrane helices are perpendicular to the membrane plane. In contrast, the distorted crystal structure of EmrE in the apo-state at pH 4.0 shows that TM4 helices are extending away from the main body of the dimer (Y. J. Chen et al., 2007).

The EPR data in the absence of substrate showed a deviation from the crystal structure of the substrate bound-EmrE for TM3, and TM4, whereas TM1 and TM2 had a similar arrangement at the dimer interface. Even though the buried environment of these sites hinders a quantitative comparison with the crystal structure, the focus was on whether the pattern of proximity agrees with the pairwise packing of helices in the crystal structure. Distance and orientation are the critical factors in such assessment since in the simplest model, the labels project along the Cα-Cβ bond. The spin labels for TM1 at site 14 are therefore expected to directly point towards each other thus rationalizing the broadened population. Site 18 shows dipolar coupling only in the apo-state and not in the substrate bound-state. This observation suggests that TPP^+ binding involves local rearrangement. For TM2 the only difference between the EPR data and the crystal stucture is related to sites 31, 34, and 38. All 3 sites show accessibility to high concentration of oxygen indicative of a region facing the lipid bilayer.

The crystal structure of EmrE shows an antiparallel dimer, in which site 63 is located in the first turn of the N-termini of TM3s at the dimer interface, with a distance separation of 10 Å. However, the EPR data did not show any spin-spin interactions for this site. The only two sites showing dipolar coupling were spin labeled sites 60 and 64. The C-terminal region of TM3 (73-76) was accessible to oxygen, suggesting a location within the lipid bilayer.

The interaction of sites located in TM1 and TM3 within the monomer shows that sites 19/74, and 22/74 have strong dipolar contact but not 19/73, suggesting that site 74 is facing the lipid bilayer and in close contact to site 19 and 22 of TM1. In the crystal structure, site 74 is facing away from the lipid membrane, while site 73 is facing the lipid

bilayer and in close contact to site 19. Overall, the deviation of TM3 topology between the crystal structure and the EPR data is related to the flexibility of the helix, thus, the crystal structure is perhaps showing one snap shot of several intermediates.

Both the crystal structure of the substrate bound-state and the EM model had shown that TM4 is perpendicular to the membrane plane. However, the EPR accessibility data does not support a helix that is perpendicular to the lipid bilayer, since most of the sites facing the lipid bilayer have similar collision rates to oxygen without a gradient where the highest oxygen accessibility would be at the center of the TM segments. The EPR data in the native like environment (reconstituted EmrE in liposomes), under which TM4 helices are at a steep angle with respect to the membrane plane or a surface helix parallel to the membrane plane compared to the crystal structure of the TPP^{+}-bound EmrE. The difference may well pertain to the flexibility of this region, thus, the static crystal structure is observing one conformation for TM4 while the EPR data represents an average over the ensemble of all conformation within the lipid bilayer.

At a number of sites, the EPR lineshapes and DEER data suggest the presence of at least two distinct conformations of EmrE. One explanation of the EPR data is the asymmetric structure of the two monomers, specifically for residues located in TM3 and TM4. The second explanation is that the EmrE dimer has a parallel topology. This may explain why site 60 and 64 that are located at the N-terminus of TM3 showed spin-spin interaction. For these sites to be in close proximity in an antiparallel orientation of the EmrE dimer they must be located below the lipid-water interface.

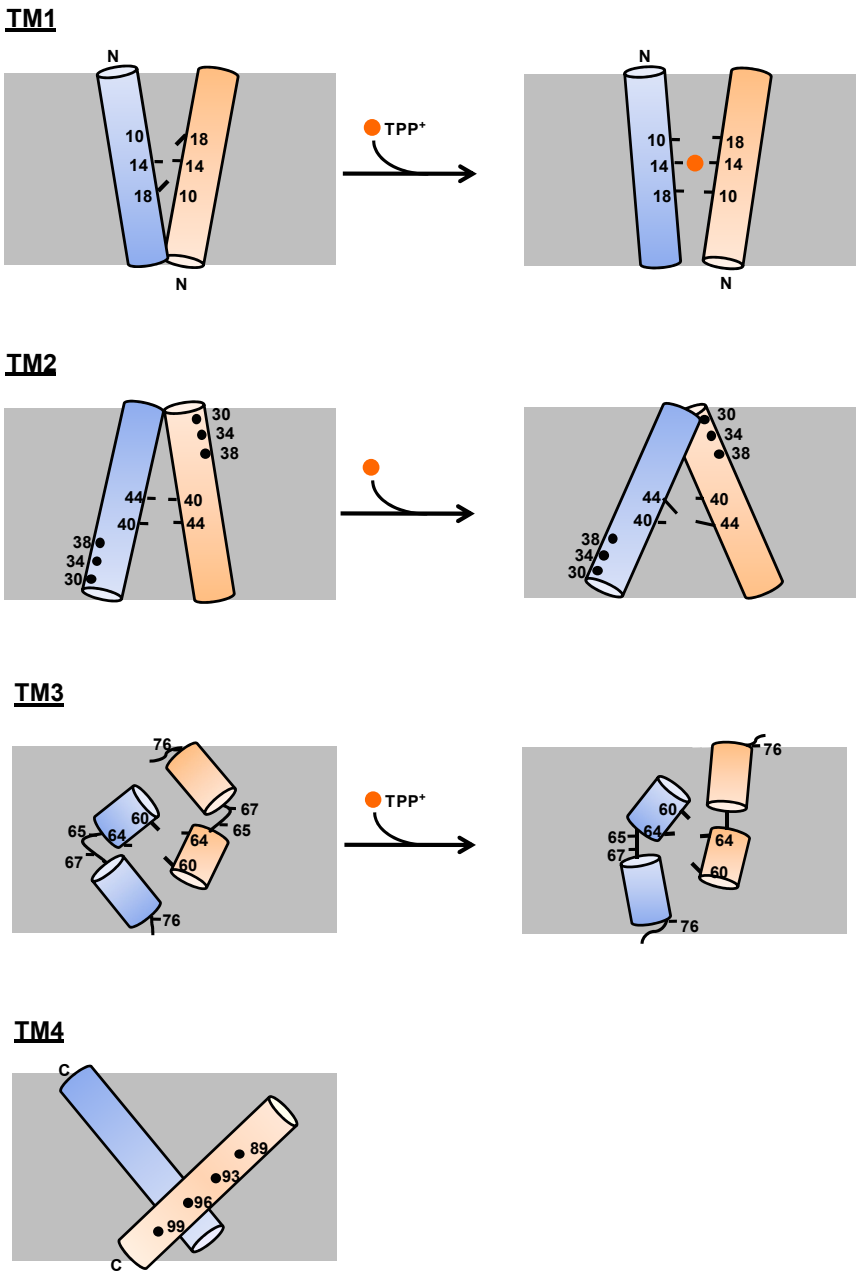

Figure 2: Diagram of each transmembrane segment in the apo- and substrate bound-state. Each TMS in the dimer is shown as cylinder and viewed parallel to the membrane plane. The TMS in one monomer is colored in blue, and the other in orange. TPP^+ is shown in orange sphere. The approximate dimensions of the lipid bilayer are shown by the grey shading.

As a result, the C-terminal region and the loop connecting TM3 to TM4 would be in the water phase. The antiparallel model, however, does not explain the high oxygen accessibility observed in this region.

Predicted Model of Conformational Changes for each Helix Induced by TPP^+ Binding

Figure 2 shows a model of the proposed changes observed for each helix upon TPP^+ binding from the EPR data. TM1 sites facing the binding pocket such as sites 10, 14 and 18 are in direct contact with TPP^+. Site 10 increases steric contact with other sites in the region while site 18 loses its dipolar coupling involving local rearrangements upon the binding of the substrate. These changes in lineshape were also observed for sites in the C-terminus of TM1 (19, 21, and 22).

Along TM2, site 44 increases the dipolar coupling while site 40 loses its spin-spin contact upon the addition of the substrate. This observation resolves the crystal structure projection of site 40 where one of the labels is away from the dimer interface. The N-terminus of TM2 increases in tilt when substrate binds reflected by an increase in O_2 accessibility for sites 30, 34, and 38. The differences between the EPR data and the crystal structure of the substrate bound-state are in TM3 and TM4. We predict, from the data upon substrate binding, site 64 at the N-terminus face one another at the dimer interface. This would explain the broadened spin populations observed in the spectral line shape. Changes are also observed along the full length of TM3, where there is a backbone rearrangement. We have proposed that the hinge between the N- and C-terminus of TM3 is at position 65 and 67. Consequently, the region (68-78) shows a change not in the rotamer of the spin label but in backbone dynamics. The DEER data for the region (68-

76) shows a decrease in the width of the distance distribution in the TPP^+-bound EmrE, suggesting that the C-terminal region of TM3 has an overall backbone mobility that decreases upon substrate binding to EmrE.

In the absence of substrate, TM4 showed substantial tilt relative to the membrane normal (see final model in Figure 2) as evident from the pattern of oxygen accessibility. The maximum values decrease towards the C-terminus and the helical periodicity is lost after residue 103 with no tertiary contact. The increase in Π (NiEDDA) beyond site 103 suggests that this region of the helix is emerging out of the membrane. The region 104-110 is not resolved in the crystal structure of the TPP^+ bound-state may suggest a flexible backbone.

Topology of EmrE

The data showed that the arrangement of the helices in each monomer was assigned similar to the crystal structure, where TM1 and TM3 were flanked by TM2 and TM4. The tertiary structure of the two monomers has been proposed previously to have only an inverted orientation within the membrane (Korkhov & Tate, 2008). This is because conserved residues such as site 14, 44, and 60 must point towards the center of the EmrE dimer to make specific interactions such as helix-helix and helix-substrate interactions. If the two monomers were parallel then each helix must be related by a translation, followed by a rotation of 180° about the individual helical axis to place each of the conserved sites in the center of the dimer. This causes the interface of the helices within each monomer to have different packing specificity, which to this day has never been seen with other membrane proteins.

It is also important to realize that previous published work from our lab (McHaourab et al., 2008) emphasized that EmrE topology does not only depend on the K+R bias as has been proposed previously (Heijne, 1986) but also the helix-helix interaction and helix-membrane interaction that has an important role in the orientation of membrane proteins. The main disagreement in the topology of EmrE from our published data came from observing dipolar coupling along TM3 at position 60 and 75 that were interpreted as indicative of parallel packing of two TM3s at the dimer interface (McHaourab et al., 2008). When the finding that spin labels at residue 64 have strong dipolar coupling, the data could be brought into closer agreement with an antiparallel model if the N-terminus of TM3 is located well below the membrane-water interface, placing site 60 and 64 in close proximity.

The flexibility of EmrE made it difficult to identify the exact topology of the two monomers of EmrE. A reason for the predicted models of each trasmembrane segments of EmrE in Figure 2 to be in an antiparallel topology was related to a double mutant 22/56 (see chapter VII). The EPR spectral line shape showed the close proximity of these two sites can only arise at the dimer interface (inverted monomers) and not within the monomer, as was proven by subunit exchange. Furthermore, the persistence of second populations in the dipolar coupled spectra reveals conformations of EmrE with different packing interfaces. However, the pattern of proximity along TM1 and TM2 suggest that one EmrE conformation is similar to the TPP^{+}-bound crystal structure. Flexibility and dynamics are invoked to rationalize the discrepancy between EPR data along TM3 and its crystallographic conformation.

For future work, the topology of EmrE can be further investigated by comparing it to another SMR family of transporter such as EbrA and EbrB proteins that are significantly homologous to each other and to EmrE (Zhang et al., 2007). It has also been suggested that EbrA/B form an antiparallel topology (Kikukawa, Miyauchi, Araiso, Kamo, & Nara, 2007). Thus, the homologous protein may elucidate the topology of EmrE.

Future work

Substrate Translocation

The thesis work gave detailed insight into the structure and dynamics of EmrE in the apo-state and the substrate bound-state. Future work is needed to investigate conformational changes using different substrates to elucidate the question of how cans a small membrane protein like EmrE extrude such a wide variety of substrates. Understanding the different conformational changes of EmrE require additional study of mechanism of transport. Previous work has shown that imposing an electrochemical gradient ($\Delta\mu_{H+}$) across the lipid bilayer causes the substrate to transport from one side of the membrane to the other (Gutman et al., 2003; Muth & Schuldiner, 2000; Rotem & Schuldiner, 2004). However, whilst the assays do demonstrate pumping of substrate, it was difficult to maintain a continuous pH gradient across a membrane due to the permeable nature of membranes to protons. Thus, a recent method have shown that the multidrug transporter can be co-reconstituted with a light driven proton pump bacteriorhodopsin (bR) into unilamellar vesicles (Basting, Lorch, Lehner, & Glaubitz, 2008). Thus, illuminating bR would generate a stable pH gradient, which EmrE requires for substrate transport. Hence, the sites that showed single distance components upon

binding of TPP^+ can be used to compare the distances between the same sites during substrate transport.

Effect of Detergent

The study where the crystal structure was determined using Nonyl-β-D-glucoside (NG) instead of Dodecyl-β-D-maltoside (β-DDM) to solubilize EmrE. Both detergents are non-ionic, but the hydrocarbon chain length of NG is shorter than β-DDM and may affect the conformation of the two monomers. In addition, it has been suggested that the detergents with the head group of the glucosides exhibit larger aggregation numbers and less spherical micelles compared to the maltosides for the same hydrocarbon chain length. Thus, the large head group of the maltosides as compared to the glucosides leads to stronger steric repulsion and, therefore, to smaller micelles (which, as a result, are more spherical) (Lipfert, Columbus, Chu, Lesley, & Doniach, 2007). Furthermore, a study has shown that extracting EmrE in NG detergent disrupts the oligomeric state of the protein (Soskine et al., 2006). Therefore, the differences in extraction of EmrE in our work and the crystal structure would have an effect in the inconsistencies observed in the packing of the helices of EmrE in the apo-state. In addition, our work shows that the detergent samples had similar EPR spectral line shape to the liposome samples (data not shown), thus, it may be an important consideration for future work to examine different detergents for solubilizing EmrE that may decrease the dynamic fluctuation without perturbing the overall tertiary structure.

Effect of Lipid Composition

Multidrug transporters bind to a variety of substrates. The flexibility in the transport protein binding pocket may be reflected in sensitivity to their surrounding lipids. Thus, lipid composition and global properties of the lipid bilayer play a key role in membranes, often modifying the function of membrane proteins. Recent work has shown that the lipid composition of EmrE reconstituted into liposomes modifies drug transport and that substrate translocation is dependent on *in vitro* lipid composition (Charalambous, Miller, Curnow, & Booth, 2008). This highlights the importance of investigating the influence of lipid environment on multidrug transport activity. Therefore, a long term goal is to learn the most efficient method for decreasing the resistance of specific substrates such as chemotherapeutic drugs that would have a major influence in successfully and selectively killing tumor cells.

APPENDIX

INTRA-SPIN LABEL INTERACTIONS

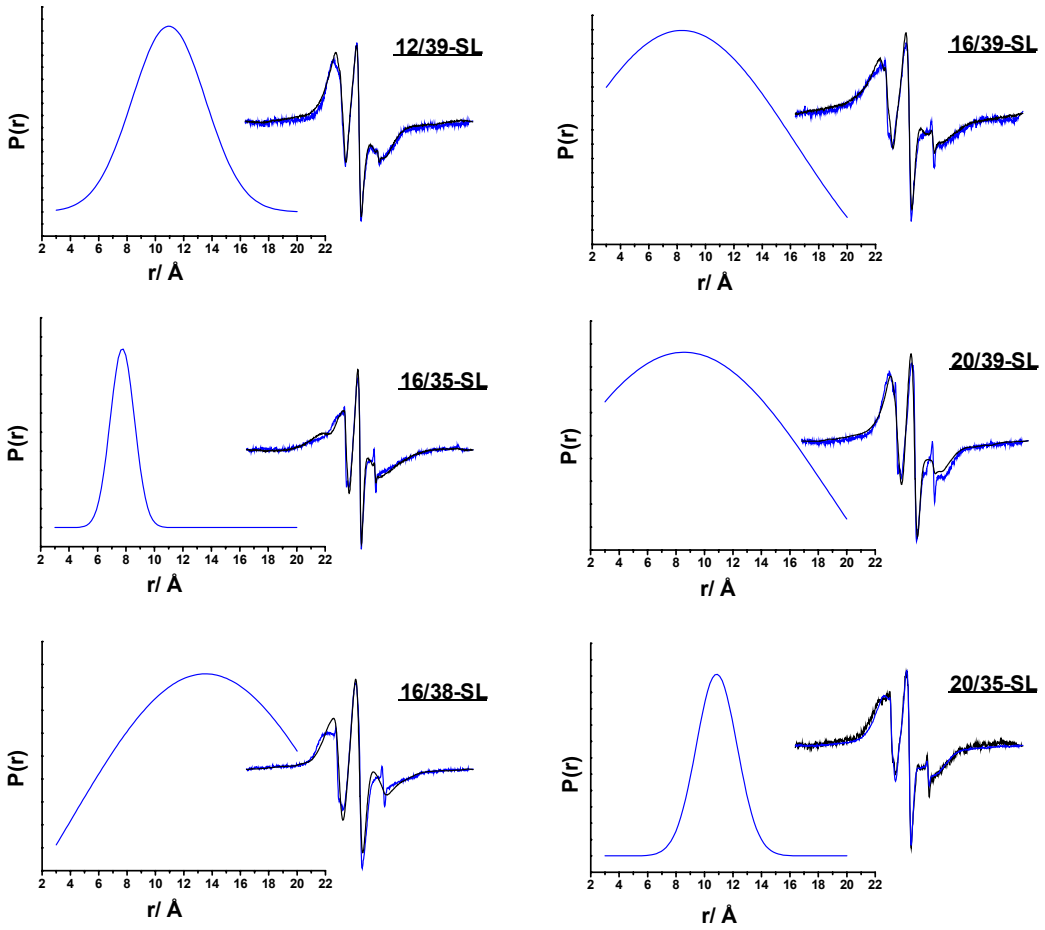

Intra-spin distance distributions using CW-EPR. Spin labeled double mutant located between TM1/TM2 (blue trace), simulated spectra (black trace).

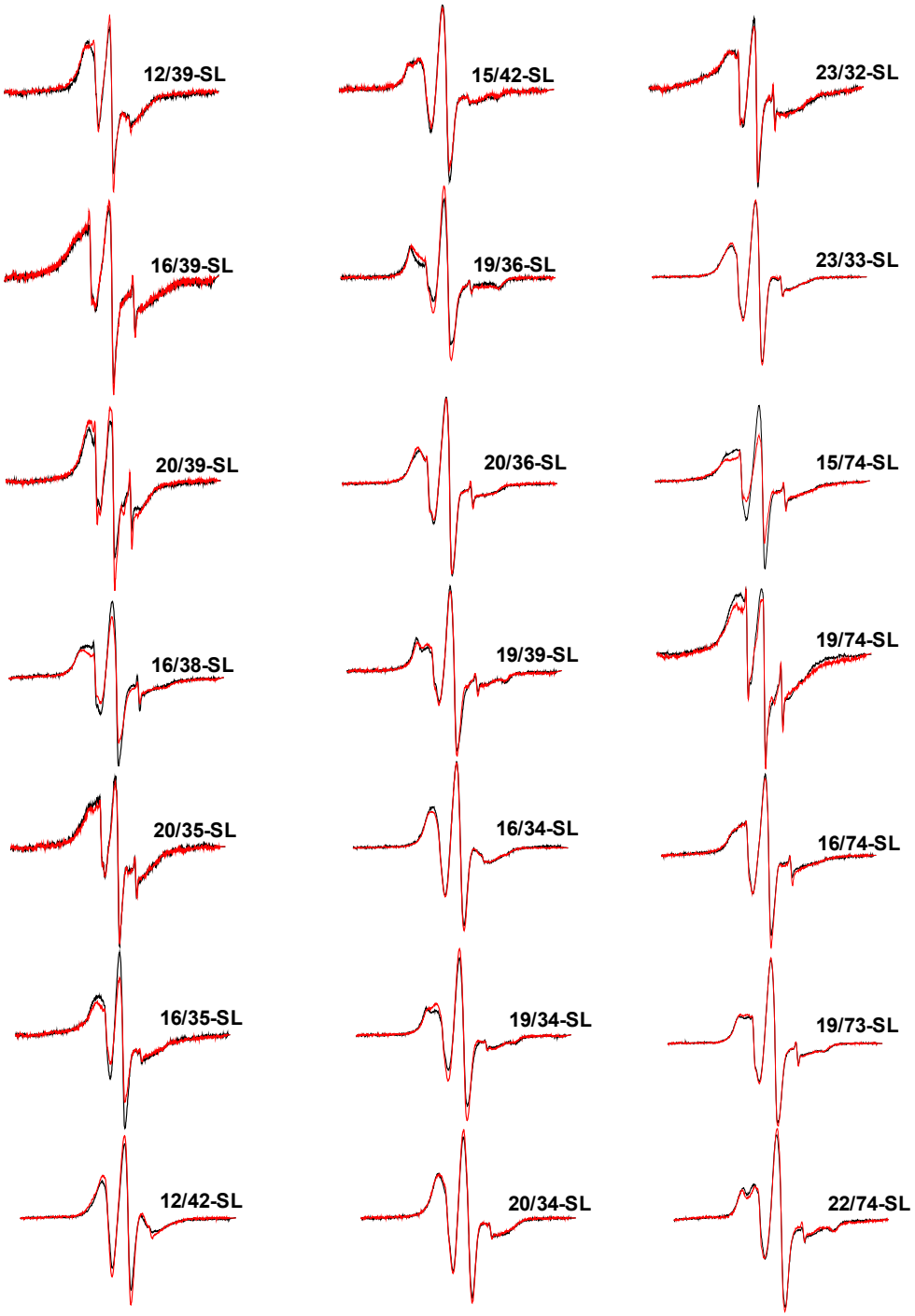

CW-EPR spectra of the intra-spin mutants. Spin labeled double mutants with (red trace) and without (black trace) TPP^{+}.

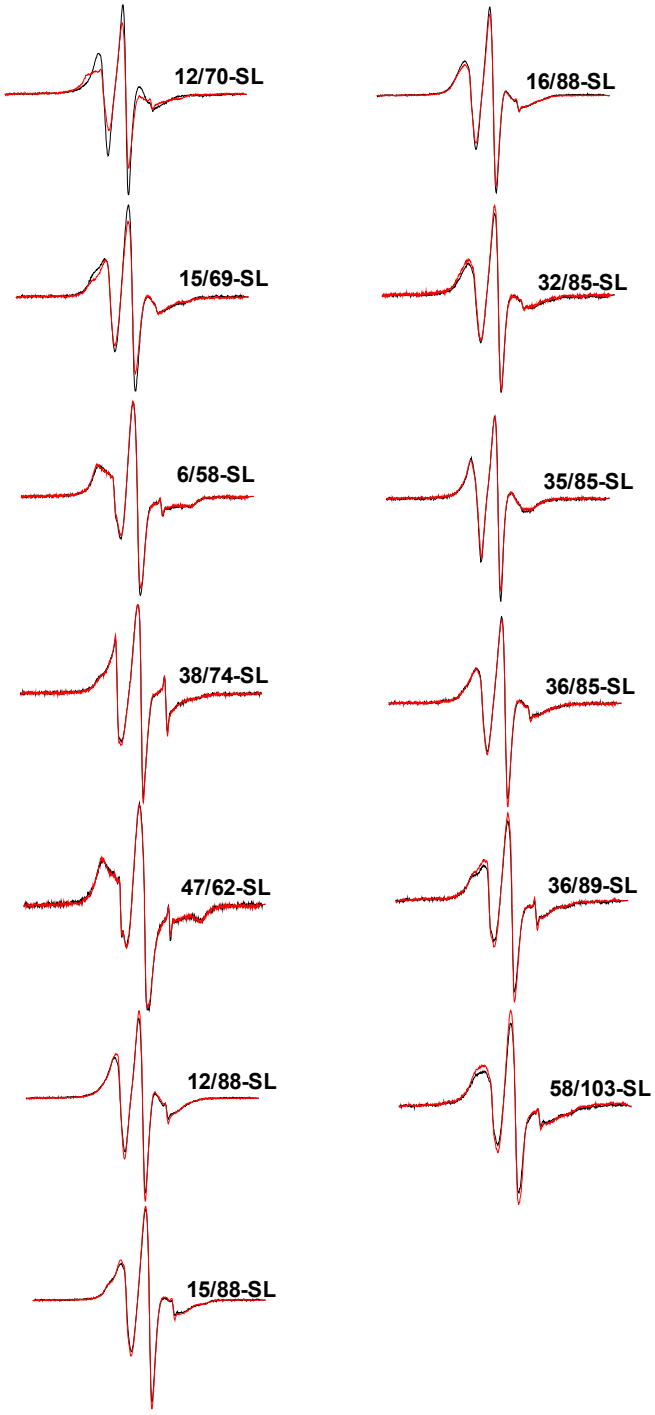

CW-EPR spectra of the intra-spin mutants. Spin labeled double mutants with (red trace) and without (black trace) TPP^{+}.

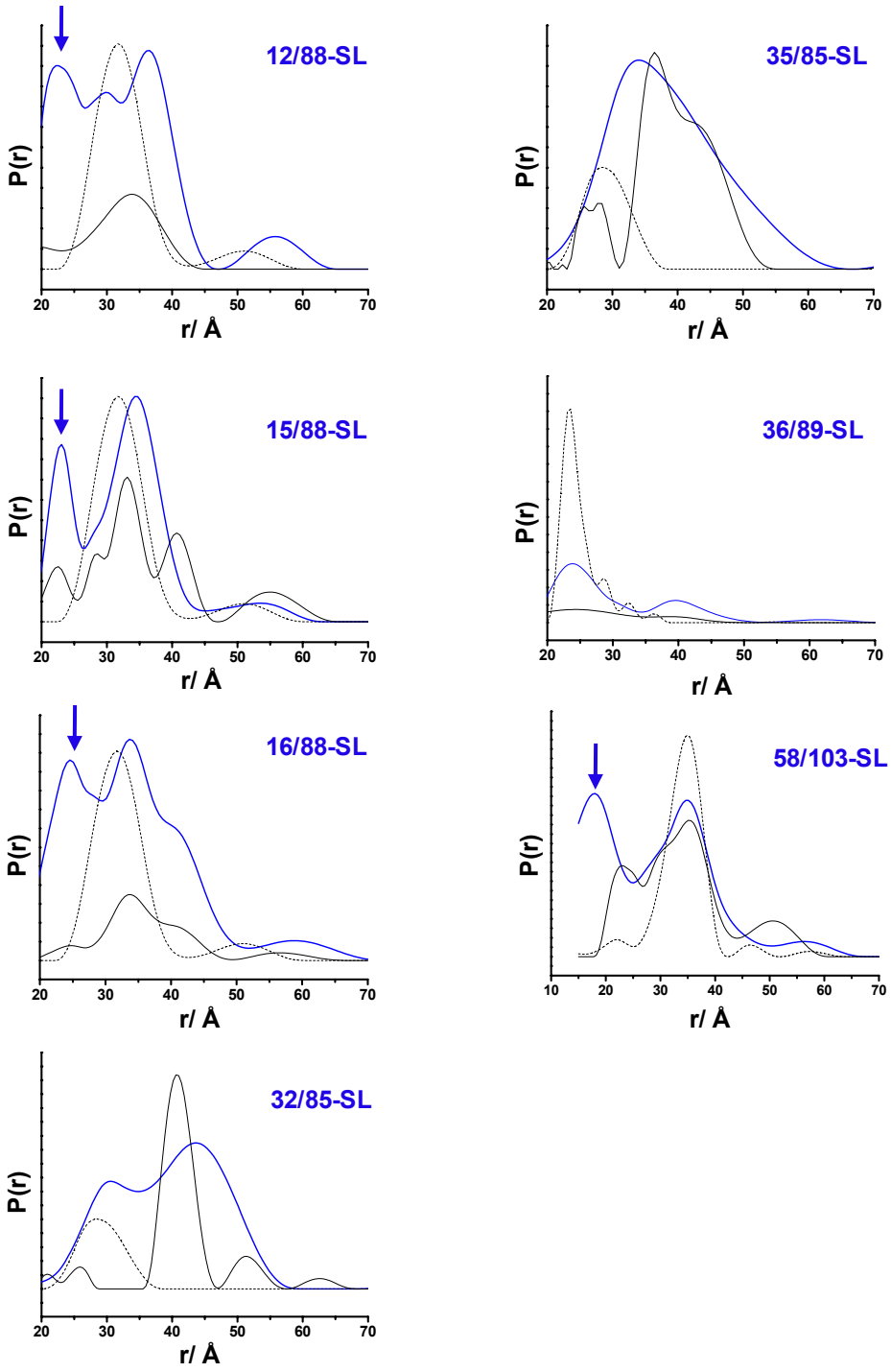

Intra-spin distance distributions using DEER. Spin labeled double mutants of sites located between TM1/TM4, TM2/TM4, and TM3/TM4 (blue trace). The blue arrow represents the average distance from the double mutants. The distance distribution of the corresponding single mutants (black and dotted trace, respectively) for comparison.

INTER-SPIN LABEL INTERACTIONS

Mutants	Location	Experimental distance, R_{av} (Å)		Calculated distance, C_α-C_α (Å)	Calculated distance of the spin label (Å)
		Apo	TPP^+		
3	TM1	35.5 ± 2.95			
4	TM1	35.6 ± 4.4			
5	TM1	46.7 ± 4.8			
6	TM1	40.3 ± 2.7	40.6 ± 2.9	30.2	34.31
8	TM1	30 ± 2.1	31 ± 1.9	30.1	22.95
9	TM1	41.8 ± 9.3		24.5	18.73
12	TM1	33.1 ± 9.5	32.4 ± 11	25.1	37.69
13	TM1	31.3 ± 6.8		20.4	19.48
15	TM1	33.8 ± 12.5	32.2 ± 3.4	21.6	34.21
16	TM1	35.1 ± 10.3		23.6	30.74
19	TM1	33.6 ± 5.7	36.4 ± 6.3	25.3	34.94
20	TM1	37.5 ± 2.8	39 ± 4.6	24.1	18.38
21	TM1	18.1 ± 2.7	19.2 ± 3.8	20.8	10.25
22	TM1	35.1 ± 4.9	36.3 ± 5.7	25.7	25.63
23	TM1	41.9 ± 4.2		30.5	32.23
25	Loop 1	44.3 ± 8.5	43.4 ± 6.6	31	32.41
26	Loop 1	37.6 ± 10.4		32.8	31.1
27	Loop 1	19.4 ± 4.7	20 ± 5.0	30.5	30.38
28	Loop 1	33.9 ± 17.7		29.2	29.41
29	Loop 1	43.9 ± 2.7		33	42.42
31	TM2	34.8 ± 15.1		33	42.69
32	TM2	40.8 ± 4.1		32	44.36
33	TM2	25.3 ± 4.7	25 ± 5.7	26.8	33.72
34	TM2	22.5 ± 5		22.4	24.31
35	TM2	39.4 ± 10		25	21.43
36	TM2	25.7± 18		24.4	30.92
38	TM2	23.7 ± 7.8		16.7	23.92
39	TM2	29.9 ± 15	29.4 ± 20	20.4	31.72
42	TM2	29.6 ± 6.6	32.1 ± 5.1	17.5	29.81
43	TM2	26.7 ± 18.4	26.2 ± 22.4	17.1	18.05
46	TM2	31.5 ± 19.5	35.3 ± 5.2	22.3	27.24
47	TM2	15 ± 27.5		18.9	4.8
52	Loop 2	44.6 ± 5.4	42.9 ± 9.1	33.4	42.6
53	Loop 2	43.9 ± 20	45 ±16.2	35.7	35.4
54	Loop 2	35.8 ± 3		35.9	35.78

Mutants	Location	Experimental distance, R_{av} (Å)		Calculated distance, C_α-C_α (Å)	Calculated distance of the spin label (Å)
		Apo	TPP^+		
56	Loop 2	29.8 ± 4		26.6	35.21
57	Loop 2	28.3 ± 16.2	28.4 ± 11.8	23.9	20.3
58	Loop 2	32.1 ± 14.8	32.6 ± 7.9	21.1	32.4
59	TM3	15 ± 30		15.3	19.5
61	TM3	22.7 ± 18		14.3	27.34
62	TM3	29.7 ± 4.5		14.6	23.44
66	TM3	35.4 ± 12.1	35.4 ± 1.0	16.6	19.77
67	TM3	29.7± 15		12.7	16.3
68	TM3	21.8 ± 3.4	23.4 ± 0.85	16.6	19.7
69	TM3	24.5 ± 13.5	24.1 ± 13.1	22.8	29.12
71	TM3	27.4 ± 14.6	30.2 ± 12.2	22	17.14
73	TM3	35 ± 7.6	34.4 ± 5.2	29.2	29
74	Loop 3	36 ± 10	37.2 ± 6.4	27.8	19.2
76	Loop 3	31 ± 27	40.9 ± 7.5	36.6	31.64
77	Loop 3	45 ± 12.4	51.3 ± 12.2	38.9	49.4
78	Loop 3	46.5 ± 13.6	48.7 ± 12.4	40.7	40.1
79	Loop 3	40.5 ± 10.2	39.7 ± 5.5	40.8	53.1
81	Loop 3	37.2 ± 9.9	38.1 ± 9.9	34.2	36.2
82	Loop 3	46.6 ± 6.5		35.7	34.86
83	Loop 3	31.6 ± 15.9		34.6	28.59
85	TM4	28.9 ±6.9		28.5	28.02
88	TM4	31.7 ± 6.8		28.3	38.51
89	TM4	23.6 ±3.1	24 ± 4	23	28.6
91	TM4	27.8 ± 18.4		18.9	30.69
95	TM4	14.4 ± 38.8		12.6	26.08
97	TM4	31.1 ± 26.9	30 ± 24.7	5.5	14.2
99	TM4	28 ± 6		14.2	21.7
100	TM4	25.5 ± 8.8		14.1	6.1
102	TM4	28 ± 5.0		18.1	21.3
103	Loop 4	34.5 ± 5.9			
104	Loop 4	32.6 ± 7			

Table of the average distances and the distribution of distances for the inter-spin label mutants in detergent micelles.

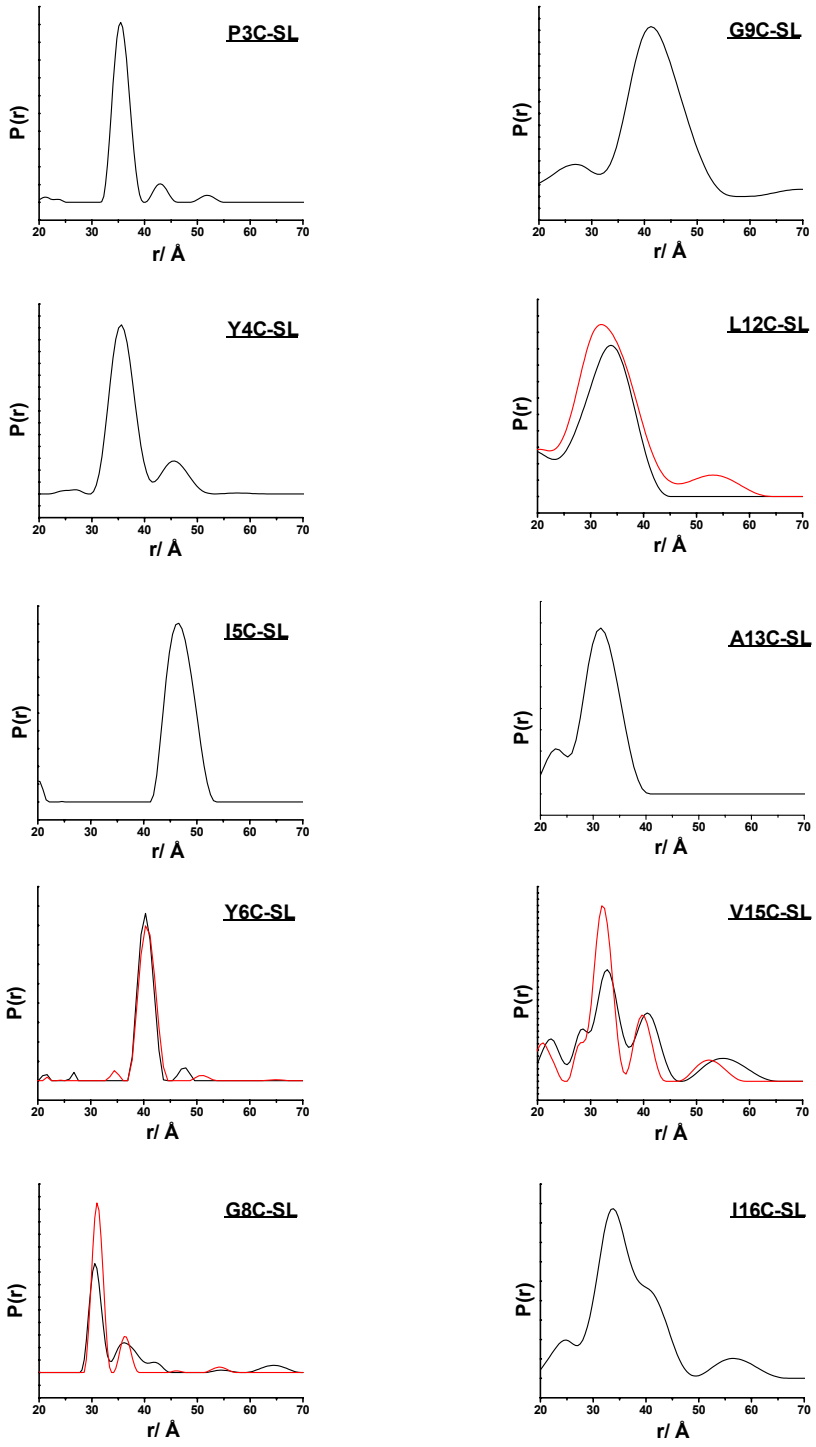

Inter-spin distance distributions using DEER. Changes in the average distance and distribution of distance between symmetry related spin labels with (red trace) and without (black trace) TPP^{+}.

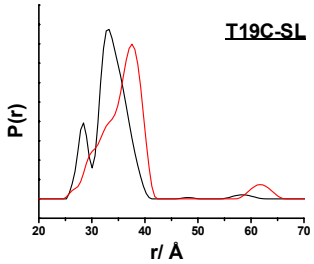
T19C-SL
P(r)
r/ Å

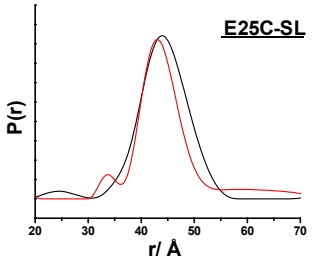
E25C-SL
P(r)
r/ Å

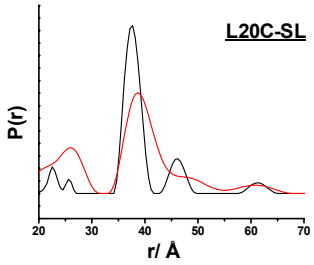
L20C-SL
P(r)
r/ Å

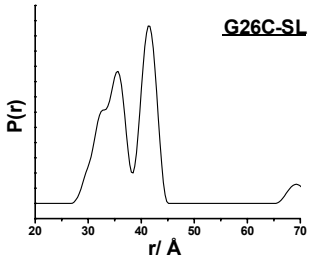
G26C-SL
P(r)
r/ Å

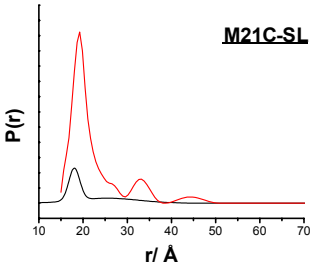
M21C-SL
P(r)
r/ Å

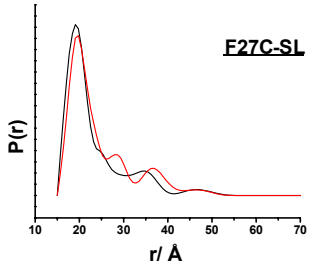
F27C-SL
P(r)
r/ Å

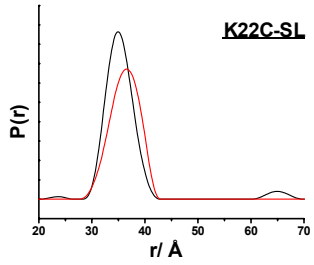
K22C-SL
P(r)
r/ Å

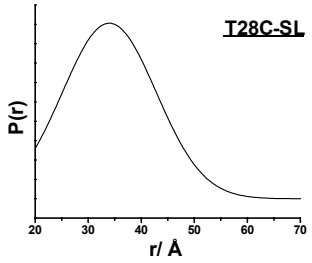
T28C-SL
P(r)
r/ Å

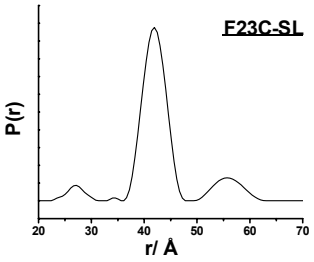
F23C-SL
P(r)
r/ Å

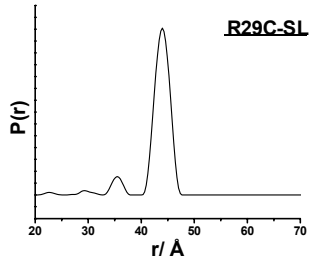
R29C-SL
P(r)
r/ Å

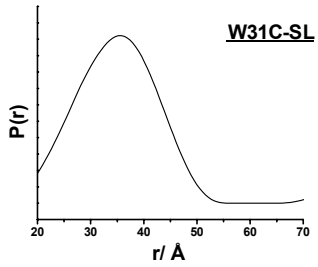
W31C-SL
P(r)
20 30 40 50 60 70
r/ Å

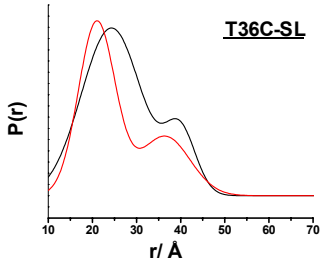
T36C-SL
P(r)
10 20 30 40 50 60 70
r/ Å

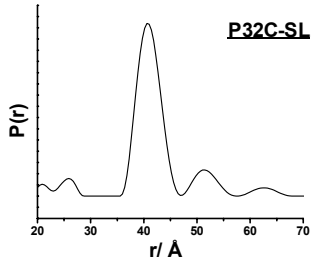
P32C-SL
P(r)
20 30 40 50 60 70
r/ Å

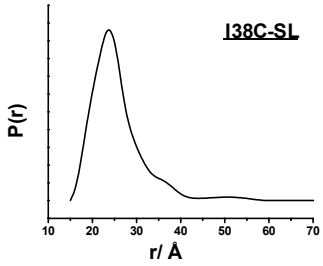
I38C-SL
P(r)
10 20 30 40 50 60 70
r/ Å

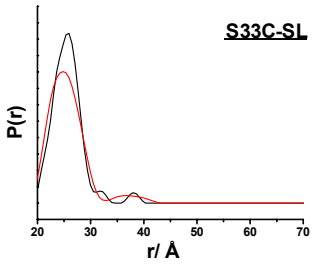
S33C-SL
P(r)
20 30 40 50 60 70
r/ Å

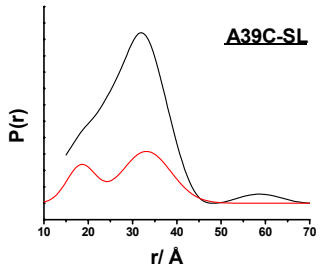
A39C-SL
P(r)
10 20 30 40 50 60 70
r/ Å

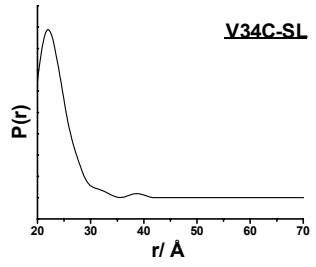
V34C-SL
P(r)
20 30 40 50 60 70
r/ Å

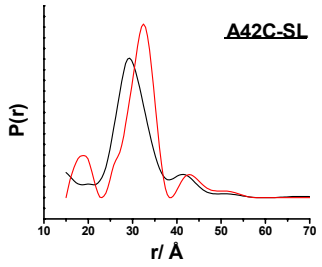
A42C-SL
P(r)
10 20 30 40 50 60 70
r/ Å

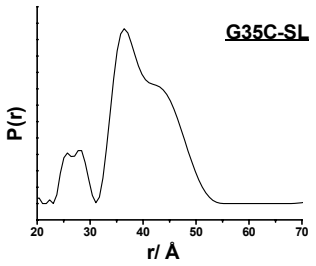
G35C-SL
P(r)
20 30 40 50 60 70
r/ Å

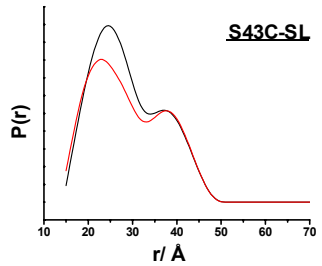
S43C-SL
P(r)
10 20 30 40 50 60 70
r/ Å

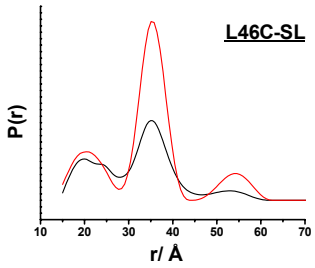
L46C-SL
P(r)
r/ Å

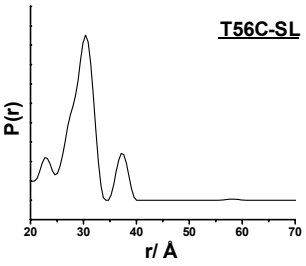
T56C-SL
P(r)
r/ Å

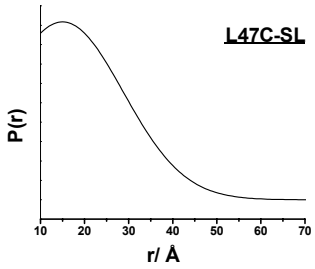
L47C-SL
P(r)
r/ Å

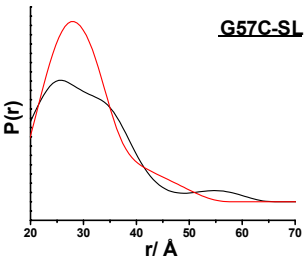
G57C-SL
P(r)
r/ Å

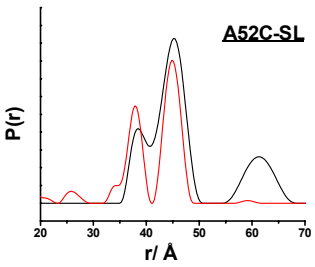
A52C-SL
P(r)
r/ Å

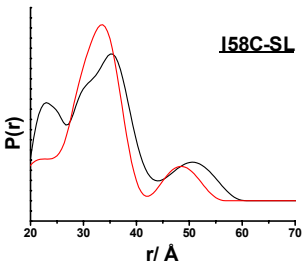
I58C-SL
P(r)
r/ Å

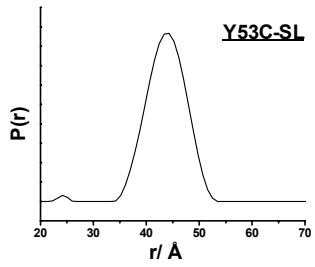
Y53C-SL
P(r)
r/ Å

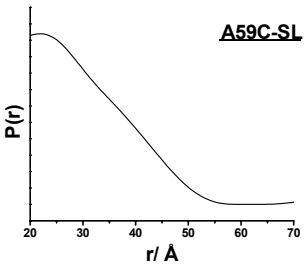
A59C-SL
P(r)
r/ Å

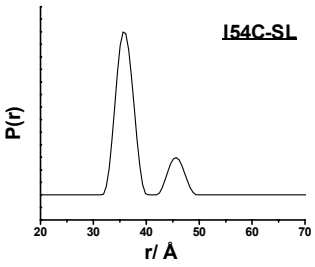
I54C-SL
P(r)
r/ Å

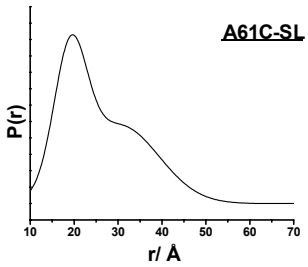
A61C-SL
P(r)
r/ Å

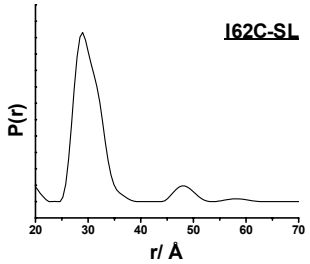
I62C-SL
P(r)
r/ Å

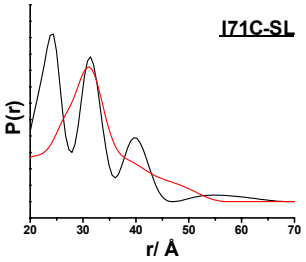
I71C-SL
P(r)
r/ Å

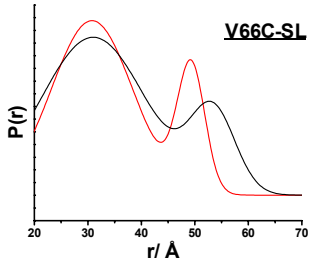
V66C-SL
P(r)
r/ Å

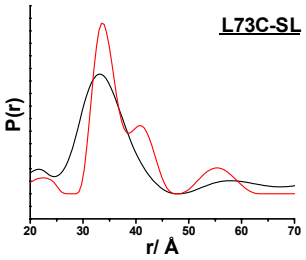
L73C-SL
P(r)
r/ Å

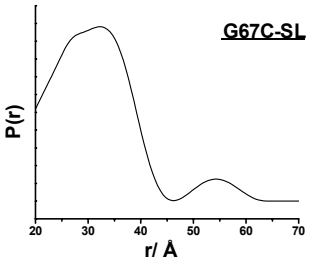
G67C-SL
P(r)
r/ Å

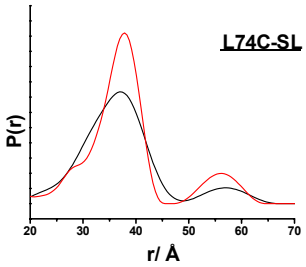
L74C-SL
P(r)
r/ Å

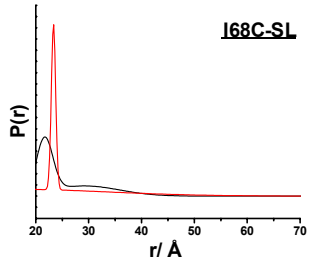
I68C-SL
P(r)
r/ Å

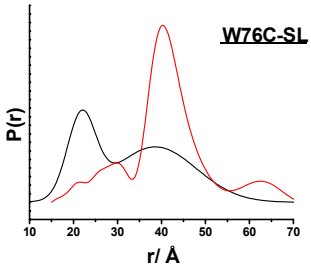
W76C-SL
P(r)
r/ Å

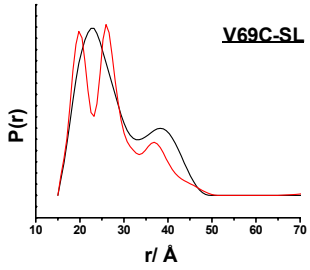
V69C-SL
P(r)
r/ Å

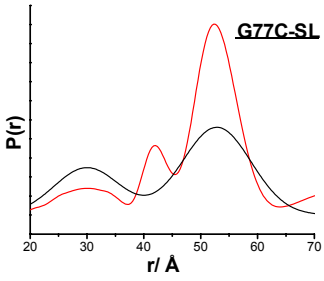
G77C-SL
P(r)
r/ Å

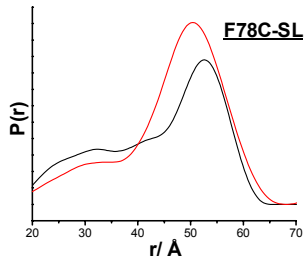
F78C-SL
P(r)
20 30 40 50 60 70
r/ Å

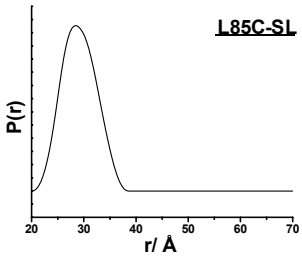
L85C-SL
P(r)
20 30 40 50 60 70
r/ Å

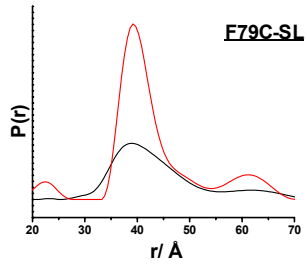
F79C-SL
P(r)
20 30 40 50 60 70
r/ Å

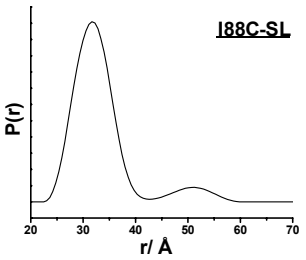
I88C-SL
P(r)
20 30 40 50 60 70
r/ Å

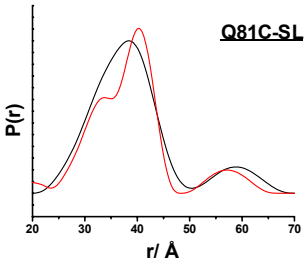
Q81C-SL
P(r)
20 30 40 50 60 70
r/ Å

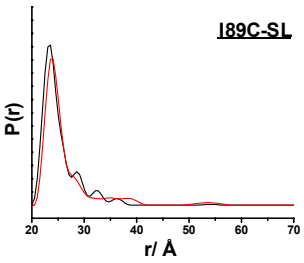
I89C-SL
P(r)
20 30 40 50 60 70
r/ Å

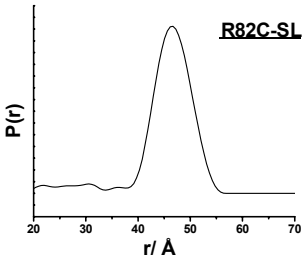
R82C-SL
P(r)
20 30 40 50 60 70
r/ Å

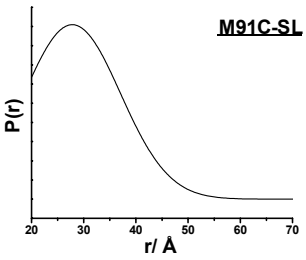
M91C-SL
P(r)
20 30 40 50 60 70
r/ Å

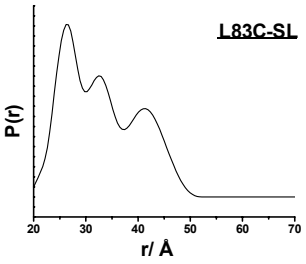
L83C-SL
P(r)
20 30 40 50 60 70
r/ Å

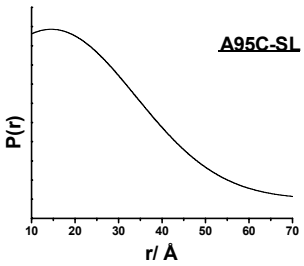
A95C-SL
P(r)
10 20 30 40 50 60 70
r/ Å

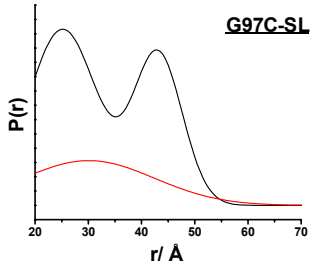
G97C-SL
P(r)
20
30
40
50
60
70
r/ Å

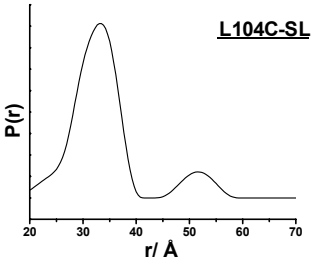
L104C-SL
P(r)
20
30
40
50
60
70
r/ Å

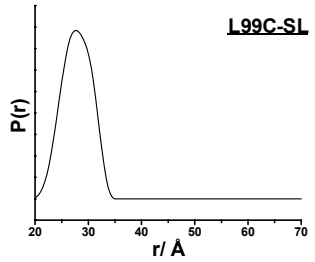
L99C-SL
P(r)
20
30
40
50
60
70
r/ Å

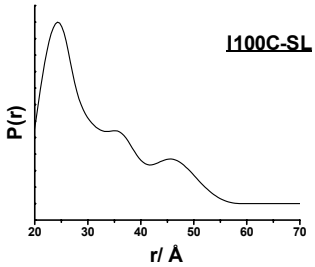
I100C-SL
P(r)
20
30
40
50
60
70
r/ Å

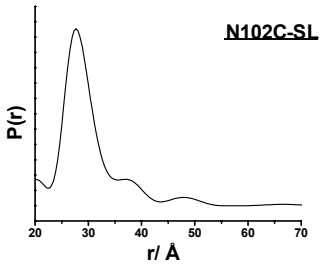
N102C-SL
P(r)
20
30
40
50
60
70
r/ Å

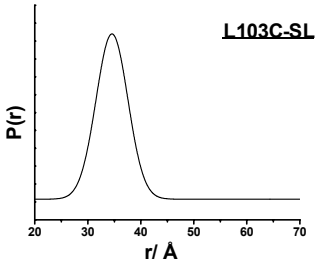
L103C-SL
P(r)
20
30
40
50
60
70
r/ Å

REFERENCE

Abraham, E. P., & Chain, E. (1988). An enzyme from bacteria able to destroy penicillin. 1940. *Rev Infect Dis, 10*(4), 677-678.

Abramson, J., Smirnova, I., Kasho, V., Verner, G., Kaback, H. R., & Iwata, S. (2003). Structure and mechanism of the lactose permease of Escherichia coli. *Science, 301*(5633), 610-615.

Adam, Y., Tayer, N., Rotem, D., Schreiber, G., & Schuldiner, S. (2007). The fast release of sticky protons: kinetics of substrate binding and proton release in a multidrug transporter. *Proc Natl Acad Sci U S A, 104*(46), 17989-17994.

Adler, J., & Bibi, E. (2005). Promiscuity in the geometry of electrostatic interactions between the Escherichia coli multidrug resistance transporter MdfA and cationic substrates. *J Biol Chem, 280*(4), 2721-2729.

Ahmed, M., Borsch, C. M., Taylor, S. S., Vazquez-Laslop, N., & Neyfakh, A. A. (1994). A protein that activates expression of a multidrug efflux transporter upon binding the transporter substrates. *J Biol Chem, 269*(45), 28506-28513.

Alexander, N., Bortolus, M., Al-Mestarihi, A., McHaourab, H., & Meiler, J. (2008). De novo high-resolution protein structure determination from sparse spin-labeling EPR data. *Structure, 16*(2), 181-195.

Aller, S. G., Yu, J., Ward, A., Weng, Y., Chittaboina, S., Zhuo, R., et al. (2009). Structure of P-glycoprotein reveals a molecular basis for poly-specific drug binding. *Science, 323*(5922), 1718-1722.

Altenbach, C., Froncisz, W., Hemker, R., McHaourab, H., & Hubbell, W. L. (2005). Accessibility of nitroxide side chains: absolute Heisenberg exchange rates from power saturation EPR. *Biophys J, 89*(3), 2103-2112.

Altenbach, C., Greenhalgh, D. A., Khorana, H. G., & Hubbell, W. L. (1994). A collision gradient method to determine the immersion depth of nitroxides in lipid bilayers: application to spin-labeled mutants of bacteriorhodopsin. *Proc Natl Acad Sci U S A, 91*(5), 1667-1671.

Altenbach, C., Marti, T., Khorana, H. G., & Hubbell, W. L. (1990). Transmembrane protein structure: spin labeling of bacteriorhodopsin mutants. *Science, 248*(4959), 1088-1092.

Arkin, I. T., Russ, W. P., Lebendiker, M., & Schuldiner, S. (1996). Determining the secondary structure and orientation of EmrE, a multi-drug transporter, indicates a transmembrane four-helix bundle. *Biochemistry, 35*(22), 7233-7238.

Banham, J. E., Baker, C. M., Ceola, S., Day, I. J., Grant, G. H., Groenen, E. J., et al. (2008). Distance measurements in the borderline region of applicability of CW EPR and DEER: a model study on a homologous series of spin-labelled peptides. *J Magn Reson, 191*(2), 202-218.

Barker, E. L., Moore, K. R., Rakhshan, F., & Blakely, R. D. (1999). Transmembrane domain I contributes to the permeation pathway for serotonin and ions in the serotonin transporter. *J Neurosci, 19*(12), 4705-4717.

Barnes, J. P., Liang, Z., McHaourab, H. S., Freed, J. H., & Hubbell, W. L. (1999). A multifrequency electron spin resonance study of T4 lysozyme dynamics. *Biophys J, 76*(6), 3298-3306.

Basting, D., Lorch, M., Lehner, I., & Glaubitz, C. (2008). Transport cycle intermediate in small multidrug resistance protein is revealed by substrate fluorescence. *FASEB J, 22*(2), 365-373.

Berengian, A. R., Bova, M. P., & McHaourab, H. S. (1997). Structure and function of the conserved domain in alphaA-crystallin. Site-directed spin labeling identifies a beta-strand located near a subunit interface. *Biochemistry, 36*(33), 9951-9957.

Berliner, L. J., Grunwald, J., Hankovszky, H. O., & Hideg, K. (1982). A novel reversible thiol-specific spin label: papain active site labeling and inhibition. *Anal Biochem, 119*(2), 450-455.

Beth, A. H., Robinson, B. H., Cobb, C. E., Dalton, L. R., Trommer, W. E., Birktoft, J. J., et al. (1984). Interactions and spatial arrangement of spin-labeled NAD+ bound to glyceraldehyde-3-phosphate dehydrogenase. Comparison of EPR and X-ray modeling data. *J Biol Chem, 259*(15), 9717-9728.

Blackburn, M. E., Veloro, A. M., & Fanucci, G. E. (2009). Monitoring inhibitor-induced conformational population shifts in HIV-1 protease by pulsed EPR spectroscopy. *Biochemistry, 48*(37), 8765-8767.

Bolin, K. A., Hanson, P., Wright, S. J., & Millhauser, G. L. (1998). An NMR investigation of the conformational effect of nitroxide spin labels on Ala-rich helical peptides. *J Magn Reson, 131*(2), 248-253.

Borbat, P. P., Costa-Filho, A. J., Earle, K. A., Moscicki, J. K., & Freed, J. H. (2001). Electron spin resonance in studies of membranes and proteins. *Science, 291*(5502), 266-269.

Borbat, P. P., McHaourab, H. S., & Freed, J. H. (2002). Protein structure determination using long-distance constraints from double-quantum coherence ESR: study of T4 lysozyme. *J Am Chem Soc, 124*(19), 5304-5314.

Borbat, P. P., Surendhran, K., Bortolus, M., Zou, P., Freed, J. H., & McHaourab, H. S. (2007). Conformational motion of the ABC transporter MsbA induced by ATP hydrolysis. *PLoS Biol, 5*(10), e271.

Bowie, J. U. (2004). Membrane proteins: a new method enters the fold. *Proc Natl Acad Sci U S A, 101*(12), 3995-3996.

Bowie, J. U. (2005). Solving the membrane protein folding problem. *Nature, 438*(7068), 581-589.

Burnside, J. M., & Groot Obbink, D. J. (1996). Plasmid pDGO100 contains a second integron with the trimethoprim resistance gene dfrA7 as the inserted cassette. *Plasmid, 35*(1), 67-70.

Butler, P. J., Ubarretxena-Belandia, I., Warne, T., & Tate, C. G. (2004). The Escherichia coli multidrug transporter EmrE is a dimer in the detergent-solubilised state. *J Mol Biol, 340*(4), 797-808.

Chang, G., & Roth, C. B. (2001). Structure of MsbA from E. coli: a homolog of the multidrug resistance ATP binding cassette (ABC) transporters. *Science, 293*(5536), 1793-1800.

Charalambous, K., Miller, D., Curnow, P., & Booth, P. J. (2008). Lipid bilayer composition influences small multidrug transporters. *BMC Biochem, 9*, 31.

Chen, C. J., Chin, J. E., Ueda, K., Clark, D. P., Pastan, I., Gottesman, M. M., et al. (1986). Internal duplication and homology with bacterial transport proteins in the mdr1 (P-glycoprotein) gene from multidrug-resistant human cells. *Cell, 47*(3), 381-389.

Chen, Y. J., Pornillos, O., Lieu, S., Ma, C., Chen, A. P., & Chang, G. (2007). X-ray structure of EmrE supports dual topology model. *Proc Natl Acad Sci U S A, 104*(48), 18999-19004.

Chiang, Y. W., Borbat, P. P., & Freed, J. H. (2005). The determination of pair distance distributions by pulsed ESR using Tikhonov regularization. *J Magn Reson, 172*(2), 279-295.

Chung, Y. J., & Saier, M. H., Jr. (2001). SMR-type multidrug resistance pumps. *Curr Opin Drug Discov Devel, 4*(2), 237-245.

Cobb, N. J., Sonnichsen, F. D., McHaourab, H., & Surewicz, W. K. (2007). Molecular architecture of human prion protein amyloid: a parallel, in-register beta-structure. *Proc Natl Acad Sci U S A, 104*(48), 18946-18951.

Columbus, L., & Hubbell, W. L. (2002). A new spin on protein dynamics. *Trends Biochem Sci, 27*(6), 288-295.

Columbus, L., & Hubbell, W. L. (2004). Mapping backbone dynamics in solution with site-directed spin labeling: GCN4-58 bZip free and bound to DNA. *Biochemistry, 43*(23), 7273-7287.

Columbus, L., Kalai, T., Jeko, J., Hideg, K., & Hubbell, W. L. (2001). Molecular motion of spin labeled side chains in alpha-helices: analysis by variation of side chain structure. *Biochemistry, 40*(13), 3828-3846.

Columbus, L., Lipfert, J., Jambunathan, K., Fox, D. A., Sim, A. Y., Doniach, S., et al. (2009). Mixing and matching detergents for membrane protein NMR structure determination. *J Am Chem Soc, 131*(21), 7320-7326.

Cuello, L. G., Cortes, D. M., & Perozo, E. (2004). Molecular architecture of the KvAP voltage-dependent K+ channel in a lipid bilayer. *Science, 306*(5695), 491-495.

Czogalla, A., Pieciul, A., Jezierski, A., & Sikorski, A. F. (2007). Attaching a spin to a protein -- site-directed spin labeling in structural biology. *Acta Biochim Pol, 54*(2), 235-244.

Daley, D. O., Rapp, M., Granseth, E., Melen, K., Drew, D., & von Heijne, G. (2005). Global topology analysis of the Escherichia coli inner membrane proteome. *Science, 308*(5726), 1321-1323.

Dano, K. (1973). Active outward transport of daunomycin in resistant Ehrlich ascites tumor cells. *Biochim Biophys Acta, 323*(3), 466-483.

Dawson, R. J., & Locher, K. P. (2006). Structure of a bacterial multidrug ABC transporter. *Nature, 443*(7108), 180-185.

Dong, J., Yang, G., & McHaourab, H. S. (2005). Structural basis of energy transduction in the transport cycle of MsbA. *Science, 308*(5724), 1023-1028.

Dutzler, R., Campbell, E. B., Cadene, M., Chait, B. T., & MacKinnon, R. (2002). X-ray structure of a ClC chloride channel at 3.0 A reveals the molecular basis of anion selectivity. *Nature, 415*(6869), 287-294.

Edgar, R., & Bibi, E. (1999). A single membrane-embedded negative charge is critical for recognizing positively charged drugs by the Escherichia coli multidrug resistance protein MdfA. *EMBO J, 18*(4), 822-832.

Edwards, R. A., & Turner, R. J. (1998). Alpha-periodicity analysis of small multidrug resistance (SMR) efflux transporters. *Biochem Cell Biol, 76*(5), 791-797.

Elbaz, Y., Salomon, T., & Schuldiner, S. (2008). Identification of a glycine motif required for packing in EmrE, a multidrug transporter from Escherichia coli. *J Biol Chem, 283*(18), 12276-12283.

Elbaz, Y., Tayer, N., Steinfels, E., Steiner-Mordoch, S., & Schuldiner, S. (2005). Substrate-induced tryptophan fluorescence changes in EmrE, the smallest ion-coupled multidrug transporter. *Biochemistry, 44*(19), 7369-7377.

Federici, L., Woebking, B., Velamakanni, S., Shilling, R. A., Luisi, B., & van Veen, H. W. (2007). New structure model for the ATP-binding cassette multidrug transporter LmrA. *Biochem Pharmacol, 74*(5), 672-678.

Feilmeier, B. J., Iseminger, G., Schroeder, D., Webber, H., & Phillips, G. J. (2000). Green fluorescent protein functions as a reporter for protein localization in Escherichia coli. *J Bacteriol, 182*(14), 4068-4076.

Fillingame, R. H. (1992). Subunit c of F1F0 ATP synthase: structure and role in transmembrane energy transduction. *Biochim Biophys Acta, 1101*(2), 240-243.

Fleishman, S. J., Harrington, S. E., Enosh, A., Halperin, D., Tate, C. G., & Ben-Tal, N. (2006). Quasi-symmetry in the cryo-EM structure of EmrE provides the key to modeling its transmembrane domain. *J Mol Biol, 364*(1), 54-67.

Fleming, A. (1980). Classics in infectious diseases: on the antibacterial action of cultures of a penicillium, with special reference to their use in the isolation of B. influenzae by Alexander Fleming, Reprinted from the British Journal of Experimental Pathology 10:226-236, 1929. *Rev Infect Dis, 2*(1), 129-139.

Forrest, L. R., & Rudnick, G. (2009). The rocking bundle: a mechanism for ion-coupled solute flux by symmetrical transporters. *Physiology (Bethesda), 24*, 377-386.

Forrest, L. R., Zhang, Y. W., Jacobs, M. T., Gesmonde, J., Xie, L., Honig, B. H., et al. (2008). Mechanism for alternating access in neurotransmitter transporters. *Proc Natl Acad Sci U S A, 105*(30), 10338-10343.

Frillingos, S., & Kaback, H. R. (1996). Cysteine-scanning mutagenesis of helix VI and the flanking hydrophilic domains on the lactose permease of Escherichia coli. *Biochemistry, 35*(16), 5333-5338.

Godsey, M. H., Zheleznova Heldwein, E. E., & Brennan, R. G. (2002). Structural biology of bacterial multidrug resistance gene regulators. *J Biol Chem, 277*(43), 40169-40172.

Gottschalk, K. E., Soskine, M., Schuldiner, S., & Kessler, H. (2004). A structural model of EmrE, a multi-drug transporter from Escherichia coli. *Biophys J, 86*(6), 3335-3348.

Gouldson, P. R., Snell, C. R., & Reynolds, C. A. (1997). A new approach to docking in the beta 2-adrenergic receptor that exploits the domain structure of G-protein-coupled receptors. *J Med Chem, 40*(24), 3871-3886.

Greener, T., Govezensky, D., & Zamir, A. (1993). A novel multicopy suppressor of a groEL mutation includes two nested open reading frames transcribed from different promoters. *EMBO J, 12*(3), 889-896.

Grigorieff, N., Ceska, T. A., Downing, K. H., Baldwin, J. M., & Henderson, R. (1996). Electron-crystallographic refinement of the structure of bacteriorhodopsin. *J Mol Biol, 259*(3), 393-421.

Grinius, L. L., & Goldberg, E. B. (1994). Bacterial multidrug resistance is due to a single membrane protein which functions as a drug pump. *J Biol Chem, 269*(47), 29998-30004.

Grkovic, S., Brown, M. H., Roberts, N. J., Paulsen, I. T., & Skurray, R. A. (1998). QacR is a repressor protein that regulates expression of the Staphylococcus aureus multidrug efflux pump QacA. *J Biol Chem, 273*(29), 18665-18673.

Grkovic, S., Brown, M. H., & Skurray, R. A. (2002). Regulation of bacterial drug export systems. *Microbiol Mol Biol Rev, 66*(4), 671-701, table of contents.

Gutman, N., Steiner-Mordoch, S., & Schuldiner, S. (2003). An amino acid cluster around the essential Glu-14 is part of the substrate- and proton-binding domain of EmrE, a multidrug transporter from Escherichia coli. *J Biol Chem, 278*(18), 16082-16087.

Hayes, J. D., & Wolf, C. R. (1990). Molecular mechanisms of drug resistance. *Biochem J, 272*(2), 281-295.

Heijne, G. V. (1986). The distribution of positively charged residues in bacterial inner membrane proteins correlates with the trans-membrane topology. *EMBO J, 5*(11), 3021-3027.

Heir, E., Sundheim, G., & Holck, A. L. (1999). Identification and characterization of quaternary ammonium compound resistant staphylococci from the food industry. *Int J Food Microbiol, 48*(3), 211-219.

Hessa, T., Meindl-Beinker, N. M., Bernsel, A., Kim, H., Sato, Y., Lerch-Bader, M., et al. (2007). Molecular code for transmembrane-helix recognition by the Sec61 translocon. *Nature, 450*(7172), 1026-1030.

Huang, Y., Lemieux, M. J., Song, J., Auer, M., & Wang, D. N. (2003). Structure and mechanism of the glycerol-3-phosphate transporter from Escherichia coli. *Science, 301*(5633), 616-620.

Hubbell, W. L., Cafiso, D. S., & Altenbach, C. (2000). Identifying conformational changes with site-directed spin labeling. *Nat Struct Biol, 7*(9), 735-739.

Hubbell, W. L., Gross, A., Langen, R., & Lietzow, M. A. (1998). Recent advances in site-directed spin labeling of proteins. *Curr Opin Struct Biol, 8*(5), 649-656.

Hubbell, W. L., McHaourab, H. S., Altenbach, C., & Lietzow, M. A. (1996). Watching proteins move using site-directed spin labeling. *Structure, 4*(7), 779-783.

Hustedt, E. J., & Beth, A. H. (1999). Nitroxide spin-spin interactions: applications to protein structure and dynamics. *Annu Rev Biophys Biomol Struct, 28*, 129-153.

Hustedt, E. J., Stein, R. A., Sethaphong, L., Brandon, S., Zhou, Z., & Desensi, S. C. (2006). Dipolar coupling between nitroxide spin labels: the development and application of a tether-in-a-cone model. *Biophys J, 90*(1), 340-356.

Inui, K. I., Masuda, S., & Saito, H. (2000). Cellular and molecular aspects of drug transport in the kidney. *Kidney Int, 58*(3), 944-958.

Jack, D. L., Storms, M. L., Tchieu, J. H., Paulsen, I. T., & Saier, M. H., Jr. (2000). A broad-specificity multidrug efflux pump requiring a pair of homologous SMR-type proteins. *J Bacteriol, 182*(8), 2311-2313.

Jacoby, G. A., & Carreras, I. (1990). Activities of beta-lactam antibiotics against Escherichia coli strains producing extended-spectrum beta-lactamases. *Antimicrob Agents Chemother, 34*(5), 858-862.

Jaud, S., Fernandez-Vidal, M., Nilsson, I., Meindl-Beinker, N. M., Hubner, N. C., Tobias, D. J., et al. (2009). Insertion of short transmembrane helices by the Sec61 translocon. *Proc Natl Acad Sci U S A, 106*(28), 11588-11593.

Jayasinghe, S. A., & Langen, R. (2004). Identifying structural features of fibrillar islet amyloid polypeptide using site-directed spin labeling. *J Biol Chem, 279*(46), 48420-48425.

Jeljaszewicz, J., Mlynarczyk, G., & Mlynarczyk, A. (2000). Antibiotic resistance in Gram-positive cocci. *Int J Antimicrob Agents, 16*(4), 473-478.

Jeschke, G., Bender, A., Schweikardt, T., Panek, G., Decker, H., & Paulsen, H. (2005). Localization of the N-terminal domain in light-harvesting chlorophyll a/b protein by EPR measurements. *J Biol Chem, 280*(19), 18623-18630.

Jiang, Y., Lee, A., Chen, J., Cadene, M., Chait, B. T., & MacKinnon, R. (2002). Crystal structure and mechanism of a calcium-gated potassium channel. *Nature, 417*(6888), 515-522.

Juliano, R. L., & Ling, V. (1976). A surface glycoprotein modulating drug permeability in Chinese hamster ovary cell mutants. *Biochim Biophys Acta, 455*(1), 152-162.

Kikukawa, T., Miyauchi, S., Araiso, T., Kamo, N., & Nara, T. (2007). Anti-parallel membrane topology of two components of EbrAB, a multidrug transporter. *Biochem Biophys Res Commun, 358*(4), 1071-1075.

Kikukawa, T., Nara, T., Araiso, T., Miyauchi, S., & Kamo, N. (2006). Two-component bacterial multidrug transporter, EbrAB: Mutations making each component solely functional. *Biochim Biophys Acta, 1758*(5), 673-679.

Kitayama, S., Shimada, S., Xu, H., Markham, L., Donovan, D. M., & Uhl, G. R. (1992). Dopamine transporter site-directed mutations differentially alter substrate transport and cocaine binding. *Proc Natl Acad Sci U S A, 89*(16), 7782-7785.

Korkhov, V. M., & Tate, C. G. (2008). Electron crystallography reveals plasticity within the drug binding site of the small multidrug transporter EmrE. *J Mol Biol, 377*(4), 1094-1103.

Koronakis, V., Sharff, A., Koronakis, E., Luisi, B., & Hughes, C. (2000). Crystal structure of the bacterial membrane protein TolC central to multidrug efflux and protein export. *Nature, 405*(6789), 914-919.

Koteiche, H. A., & McHaourab, H. S. (1999). Folding pattern of the alpha-crystallin domain in alphaA-crystallin determined by site-directed spin labeling. *J Mol Biol, 294*(2), 561-577.

Koteiche, H. A., Reeves, M. D., & McHaourab, H. S. (2003). Structure of the substrate binding pocket of the multidrug transporter EmrE: site-directed spin labeling of transmembrane segment 1. *Biochemistry, 42*(20), 6099-6105.

Kumar, A., & Schweizer, H. P. (2005). Bacterial resistance to antibiotics: active efflux and reduced uptake. *Adv Drug Deliv Rev, 57*(10), 1486-1513.

Kusnetzow, A. K., Altenbach, C., & Hubbell, W. L. (2006). Conformational states and dynamics of rhodopsin in micelles and bilayers. *Biochemistry, 45*(17), 5538-5550.

Lambert, B., & Le Pecq, J. B. (1984). Effect of mutation, electric membrane potential, and metabolic inhibitors on the accessibility of nucleic acids to ethidium bromide in Escherichia coli cells. *Biochemistry, 23*(1), 166-176.

Langen, R., Oh, K. J., Cascio, D., & Hubbell, W. L. (2000). Crystal structures of spin labeled T4 lysozyme mutants: implications for the interpretation of EPR spectra in terms of structure. *Biochemistry, 39*(29), 8396-8405.

Lau, F. W., & Bowie, J. U. (1997). A method for assessing the stability of a membrane protein. *Biochemistry, 36*(19), 5884-5892.

Lebendiker, M., & Schuldiner, S. (1996). Identification of residues in the translocation pathway of EmrE, a multidrug antiporter from Escherichia coli. *J Biol Chem, 271*(35), 21193-21199.

Lewinson, O., & Bibi, E. (2001). Evidence for simultaneous binding of dissimilar substrates by the Escherichia coli multidrug transporter MdfA. *Biochemistry, 40*(42), 12612-12618.

Li, X. Z., Poole, K., & Nikaido, H. (2003). Contributions of MexAB-OprM and an EmrE homolog to intrinsic resistance of Pseudomonas aeruginosa to aminoglycosides and dyes. *Antimicrob Agents Chemother, 47*(1), 27-33.

Lipfert, J., Columbus, L., Chu, V. B., Lesley, S. A., & Doniach, S. (2007). Size and shape of detergent micelles determined by small-angle X-ray scattering. *J Phys Chem B, 111*(43), 12427-12438.

Littlejohn, T. G., Paulsen, I. T., Gillespie, M. T., Tennent, J. M., Midgley, M., Jones, I. G., et al. (1992). Substrate specificity and energetics of antiseptic and disinfectant resistance in Staphylococcus aureus. *FEMS Microbiol Lett, 74*(2-3), 259-265.

Liu, Y., Engelman, D. M., & Gerstein, M. (2002). Genomic analysis of membrane protein families: abundance and conserved motifs. *Genome Biol, 3*(10), research0054.

Livshits, V. A., Kurad, D., & Marsh, D. (2006). Multifrequency simulations of the EPR spectra of lipid spin labels in membranes. *J Magn Reson, 180*(1), 63-71.

Ma, C., & Chang, G. (2004). Structure of the multidrug resistance efflux transporter EmrE from Escherichia coli. *Proc Natl Acad Sci U S A, 101*(9), 2852-2857.

Ma, C., & Chang, G. (2007). Structure of the multidrug resistance efflux transporter EmrE from Escherichia coli. *Proc Natl Acad Sci U S A, 104*(9), 3668.

Malo, G. D., Pouwels, L. J., Wang, M., Weichsel, A., Montfort, W. R., Rizzo, M. A., et al. (2007). X-ray structure of Cerulean GFP: a tryptophan-based chromophore useful for fluorescence lifetime imaging. *Biochemistry, 46*(35), 9865-9873.

Manoil, C., & Beckwith, J. (1986). A genetic approach to analyzing membrane protein topology. *Science, 233*(4771), 1403-1408.

Maxwell, A. (1992). The molecular basis of quinolone action. *J Antimicrob Chemother, 30*(4), 409-414.

Mazurkiewicz, P., Driessen, A. J., & Konings, W. N. (2004). Energetics of wild-type and mutant multidrug resistance secondary transporter LmrP of Lactococcus lactis. *Biochim Biophys Acta, 1658*(3), 252-261.

McDonnell, G., & Russell, A. D. (1999). Antiseptics and disinfectants: activity, action, and resistance. *Clin Microbiol Rev, 12*(1), 147-179.

McHaourab, H. S., Berengian, A. R., & Koteiche, H. A. (1997). Site-directed spin-labeling study of the structure and subunit interactions along a conserved sequence in the alpha-crystallin domain of heat-shock protein 27. Evidence of a conserved subunit interface. *Biochemistry, 36*(48), 14627-14634.

McHaourab, H. S., Kalai, T., Hideg, K., & Hubbell, W. L. (1999). Motion of spin-labeled side chains in T4 lysozyme: effect of side chain structure. *Biochemistry, 38*(10), 2947-2955.

McHaourab, H. S., Lietzow, M. A., Hideg, K., & Hubbell, W. L. (1996). Motion of spin-labeled side chains in T4 lysozyme. Correlation with protein structure and dynamics. *Biochemistry, 35*(24), 7692-7704.

McHaourab, H. S., Mishra, S., Koteiche, H. A., & Amadi, S. H. (2008). Role of sequence bias in the topology of the multidrug transporter EmrE. *Biochemistry, 47*(31), 7980-7982.

Merickel, A., Rosandich, P., Peter, D., & Edwards, R. H. (1995). Identification of residues involved in substrate recognition by a vesicular monoamine transporter. *J Biol Chem, 270*(43), 25798-25804.

Miriagou, V., Tassios, P. T., Legakis, N. J., & Tzouvelekis, L. S. (2004). Expanded-spectrum cephalosporin resistance in non-typhoid Salmonella. *Int J Antimicrob Agents, 23*(6), 547-555.

Mitchell, B. A., Brown, M. H., & Skurray, R. A. (1998). QacA multidrug efflux pump from Staphylococcus aureus: comparative analysis of resistance to diamidines, biguanidines, and guanylhydrazones. *Antimicrob Agents Chemother, 42*(2), 475-477.

Mordoch, S. S., Granot, D., Lebendiker, M., & Schuldiner, S. (1999). Scanning cysteine accessibility of EmrE, an H+-coupled multidrug transporter from Escherichia coli, reveals a hydrophobic pathway for solutes. *J Biol Chem, 274*(27), 19480-19486.

Morimyo, M., Hongo, E., Hama-Inaba, H., & Machida, I. (1992). Cloning and characterization of the mvrC gene of Escherichia coli K-12 which confers resistance against methyl viologen toxicity. *Nucleic Acids Res, 20*(12), 3159-3165.

Morin, B., Bourhis, J. M., Belle, V., Woudstra, M., Carriere, F., Guigliarelli, B., et al. (2006). Assessing induced folding of an intrinsically disordered protein by site-directed spin-labeling electron paramagnetic resonance spectroscopy. *J Phys Chem B, 110*(41), 20596-20608.

Morita, Y., Kodama, K., Shiota, S., Mine, T., Kataoka, A., Mizushima, T., et al. (1998). NorM, a putative multidrug efflux protein, of Vibrio parahaemolyticus and its homolog in Escherichia coli. *Antimicrob Agents Chemother, 42*(7), 1778-1782.

Murakami, S., Nakashima, R., Yamashita, E., Matsumoto, T., & Yamaguchi, A. (2006). Crystal structures of a multidrug transporter reveal a functionally rotating mechanism. *Nature, 443*(7108), 173-179.

Murata, K., Mitsuoka, K., Hirai, T., Walz, T., Agre, P., Heymann, J. B., et al. (2000). Structural determinants of water permeation through aquaporin-1. *Nature, 407*(6804), 599-605.

Muth, T. R., & Schuldiner, S. (2000). A membrane-embedded glutamate is required for ligand binding to the multidrug transporter EmrE. *EMBO J, 19*(2), 234-240.

Naroditskaya, V., Schlosser, M. J., Fang, N. Y., & Lewis, K. (1993). An E. coli gene emrD is involved in adaptation to low energy shock. *Biochem Biophys Res Commun, 196*(2), 803-809.

Neyfakh, A. A. (2002). Mystery of multidrug transporters: the answer can be simple. *Mol Microbiol, 44*(5), 1123-1130.

Ng, L. L., Davies, J. E., Siczkowski, M., Sweeney, F. P., Quinn, P. A., Krolewski, B., et al. (1994). Abnormal Na+/H+ antiporter phenotype and turnover of immortalized lymphoblasts from type 1 diabetic patients with nephropathy. *J Clin Invest, 93*(6), 2750-2757.

Nikaido, H. (1985). Role of permeability barriers in resistance to beta-lactam antibiotics. *Pharmacol Ther, 27*(2), 197-231.

Nikaido, H. (1989). Outer membrane barrier as a mechanism of antimicrobial resistance. *Antimicrob Agents Chemother, 33*(11), 1831-1836.

Nikaido, H., & Normark, S. (1987). Sensitivity of Escherichia coli to various beta-lactams is determined by the interplay of outer membrane permeability and degradation by periplasmic beta-lactamases: a quantitative predictive treatment. *Mol Microbiol, 1*(1), 29-36.

Ninio, S., Elbaz, Y., & Schuldiner, S. (2004). The membrane topology of EmrE - a small multidrug transporter from Escherichia coli. *FEBS Lett, 562*(1-3), 193-196.

Ninio, S., Rotem, D., & Schuldiner, S. (2001). Functional analysis of novel multidrug transporters from human pathogens. *J Biol Chem, 276*(51), 48250-48256.

Otsuka, M., Matsumoto, T., Morimoto, R., Arioka, S., Omote, H., & Moriyama, Y. (2005). A human transporter protein that mediates the final excretion step for toxic organic cations. *Proc Natl Acad Sci U S A, 102*(50), 17923-17928.

Pake, G. E. (1948). Nuclear Resonance Absorption in Hydrated Crystals: Fine Structure of the Proton Line. *The Journal of Chemical Physics, 16*(4), 327-336.

Pannier, M., Veit, S., Godt, A., Jeschke, G., & Spiess, H. W. (2000). Dead-time free measurement of dipole-dipole interactions between electron spins. *J Magn Reson, 142*(2), 331-340.

Paulsen, I. T., Brown, M. H., & Skurray, R. A. (1996). Proton-dependent multidrug efflux systems. *Microbiol Rev, 60*(4), 575-608.

Pedelacq, J. D., Cabantous, S., Tran, T., Terwilliger, T. C., & Waldo, G. S. (2006). Engineering and characterization of a superfolder green fluorescent protein. *Nat Biotechnol, 24*(1), 79-88.

Perozo, E., Kloda, A., Cortes, D. M., & Martinac, B. (2001). Site-directed spin-labeling analysis of reconstituted Mscl in the closed state. *J Gen Physiol, 118*(2), 193-206.

Pettersen, E. F., Goddard, T. D., Huang, C. C., Couch, G. S., Greenblatt, D. M., Meng, E. C., et al. (2004). UCSF Chimera--a visualization system for exploratory research and analysis. *J Comput Chem, 25*(13), 1605-1612.

Pfeiffer, M., Rink, T., Gerwert, K., Oesterhelt, D., & Steinhoff, H. J. (1999). Site-directed spin-labeling reveals the orientation of the amino acid side-chains in the E-F loop of bacteriorhodopsin. *J Mol Biol, 287*(1), 163-171.

Pornillos, O., Chen, Y. J., Chen, A. P., & Chang, G. (2005). X-ray structure of the EmrE multidrug transporter in complex with a substrate. *Science, 310*(5756), 1950-1953.

Poulsen, B. E., Rath, A., & Deber, C. M. (2009). The assembly motif of a bacterial small multidrug resistance protein. *J Biol Chem, 284*(15), 9870-9875.

Pritchard, J. B., & Miller, D. S. (1993). Mechanisms mediating renal secretion of organic anions and cations. *Physiol Rev, 73*(4), 765-796.

Purewal, A. S. (1991). Nucleotide sequence of the ethidium efflux gene from Escherichia coli. *FEMS Microbiol Lett, 66*(2), 229-231.

Purewal, A. S., Jones, I. G., & Midgley, M. (1990). Cloning of the ethidium efflux gene from Escherichia coli. *FEMS Microbiol Lett, 56*(1-2), 73-76.

Putman, M., Van Veen, H. W., Degener, J. E., & Konings, W. N. (2000). Antibiotic resistance: era of the multidrug pump. *Mol Microbiol, 36*(3), 772-773.

Rabenstein, M. D., & Shin, Y. K. (1995). Determination of the distance between two spin labels attached to a macromolecule. *Proc Natl Acad Sci U S A, 92*(18), 8239-8243.

Rapp, M., Granseth, E., Seppala, S., & von Heijne, G. (2006). Identification and evolution of dual-topology membrane proteins. *Nat Struct Mol Biol, 13*(2), 112-116.

Rapp, M., Seppala, S., Granseth, E., & von Heijne, G. (2007). Emulating membrane protein evolution by rational design. *Science, 315*(5816), 1282-1284.

Rosenberg, M. F., Velarde, G., Ford, R. C., Martin, C., Berridge, G., Kerr, I. D., et al. (2001). Repacking of the transmembrane domains of P-glycoprotein during the transport ATPase cycle. *EMBO J, 20*(20), 5615-5625.

Rotem, D., & Schuldiner, S. (2004). EmrE, a multidrug transporter from Escherichia coli, transports monovalent and divalent substrates with the same stoichiometry. *J Biol Chem, 279*(47), 48787-48793.

Rotem, D., Steiner-Mordoch, S., & Schuldiner, S. (2006). Identification of tyrosine residues critical for the function of an ion-coupled multidrug transporter. *J Biol Chem, 281*(27), 18715-18722.

Sanner, M. F., Olson, A. J., & Spehner, J. C. (1996). Reduced surface: an efficient way to compute molecular surfaces. *Biopolymers, 38*(3), 305-320.

Schuldiner, S. (2007a). Controversy over EmrE structure. *Science, 317*(5839), 748-751; author reply 748-751.

Schuldiner, S. (2007b). When biochemistry meets structural biology: the cautionary tale of EmrE. *Trends Biochem Sci, 32*(6), 252-258.

Schuldiner, S., Granot, D., Mordoch, S. S., Ninio, S., Rotem, D., Soskin, M., et al. (2001). Small is mighty: EmrE, a multidrug transporter as an experimental paradigm. *News Physiol Sci, 16*, 130-134.

Schulz, G. E. (1993). Bacterial porins: structure and function. *Curr Opin Cell Biol, 5*(4), 701-707.

Schwaiger, M., Lebendiker, M., Yerushalmi, H., Coles, M., Groger, A., Schwarz, C., et al. (1998). NMR investigation of the multidrug transporter EmrE, an integral membrane protein. *Eur J Biochem, 254*(3), 610-619.

Seeger, M. A., Schiefner, A., Eicher, T., Verrey, F., Diederichs, K., & Pos, K. M. (2006). Structural asymmetry of AcrB trimer suggests a peristaltic pump mechanism. *Science, 313*(5791), 1295-1298.

Sennhauser, G., Bukowska, M. A., Briand, C., & Grutter, M. G. (2009). Crystal structure of the multidrug exporter MexB from Pseudomonas aeruginosa. *J Mol Biol, 389*(1), 134-145.

Serrano-Vega, M. J., Magnani, F., Shibata, Y., & Tate, C. G. (2008). Conformational thermostabilization of the beta1-adrenergic receptor in a detergent-resistant form. *Proc Natl Acad Sci U S A, 105*(3), 877-882.

Seydel, U., Labischinski, H., Kastowsky, M., & Brandenburg, K. (1993). Phase behavior, supramolecular structure, and molecular conformation of lipopolysaccharide. *Immunobiology, 187*(3-5), 191-211.

Sharoni, M., Steiner-Mordoch, S., & Schuldiner, S. (2005). Exploring the binding domain of EmrE, the smallest multidrug transporter. *J Biol Chem, 280*(38), 32849-32855.

Sidhu, M. S., Langsrud, S., & Holck, A. (2001). Disinfectant and antibiotic resistance of lactic acid bacteria isolated from the food industry. *Microb Drug Resist, 7*(1), 73-83.

Sikora, C. W., & Turner, R. J. (2005). SMR proteins SugE and EmrE bind ligand with similar affinity and stoichiometry. *Biochem Biophys Res Commun, 335*(1), 105-111.

Silver, S., & Phung, L. T. (1996). Bacterial heavy metal resistance: new surprises. *Annu Rev Microbiol, 50*, 753-789.

Smirnova, I., Kasho, V., Choe, J. Y., Altenbach, C., Hubbell, W. L., & Kaback, H. R. (2007). Sugar binding induces an outward facing conformation of LacY. *Proc Natl Acad Sci U S A, 104*(42), 16504-16509.

Sorensen, T. L., Clausen, J. D., Jensen, A. M., Vilsen, B., Moller, J. V., Andersen, J. P., et al. (2004). Localization of a K+ -binding site involved in dephosphorylation of the sarcoplasmic reticulum Ca2+ -ATPase. *J Biol Chem, 279*(45), 46355-46358.

Soskine, M., Adam, Y., & Schuldiner, S. (2004). Direct evidence for substrate-induced proton release in detergent-solubilized EmrE, a multidrug transporter. *J Biol Chem, 279*(11), 9951-9955.

Soskine, M., Mark, S., Tayer, N., Mizrachi, R., & Schuldiner, S. (2006). On parallel and antiparallel topology of a homodimeric multidrug transporter. *J Biol Chem, 281*(47), 36205-36212.

Soskine, M., Steiner-Mordoch, S., & Schuldiner, S. (2002). Crosslinking of membrane-embedded cysteines reveals contact points in the EmrE oligomer. *Proc Natl Acad Sci U S A, 99*(19), 12043-12048.

Steiner-Mordoch, S., Soskine, M., Solomon, D., Rotem, D., Gold, A., Yechieli, M., et al. (2008). Parallel topology of genetically fused EmrE homodimers. *EMBO J, 27*(1), 17-26.

Steinhoff, H., Savitsky, A., Wegener, C., Pfeiffer, M., Plato, M., & Mobius, K. (2000). High-field EPR studies of the structure and conformational changes of site-directed spin labeled bacteriorhodopsin. *Biochim Biophys Acta, 1457*(3), 253-262.

Studier, F. W., Rosenberg, A. H., Dunn, J. J., & Dubendorff, J. W. (1990). Use of T7 RNA polymerase to direct expression of cloned genes. *Methods Enzymol, 185*, 60-89.

Tamai, I., Sai, Y., Ono, A., Kido, Y., Yabuuchi, H., Takanaga, H., et al. (1999). Immunohistochemical and functional characterization of pH-dependent intestinal absorption of weak organic acids by the monocarboxylic acid transporter MCT1. *J Pharm Pharmacol, 51*(10), 1113-1121.

Tate, C. G. (2006). Comparison of three structures of the multidrug transporter EmrE. *Curr Opin Struct Biol, 16*(4), 457-464.

Tate, C. G., Kunji, E. R., Lebendiker, M., & Schuldiner, S. (2001). The projection structure of EmrE, a proton-linked multidrug transporter from Escherichia coli, at 7 A resolution. *EMBO J, 20*(1-2), 77-81.

Tate, C. G., Ubarretxena-Belandia, I., & Baldwin, J. M. (2003). Conformational changes in the multidrug transporter EmrE associated with substrate binding. *J Mol Biol, 332*(1), 229-242.

Taubes, G. (2008). The bacteria fight back. *Science, 321*(5887), 356-361.

Thorgeirsson, T. E., Xiao, W., Brown, L. S., Needleman, R., Lanyi, J. K., & Shin, Y. K. (1997). Transient channel-opening in bacteriorhodopsin: an EPR study. *J Mol Biol, 273*(5), 951-957.

Tsuji, A., & Tamai, I. (1999). Organic anion transporters. *Pharm Biotechnol, 12*, 471-491.

Ubarretxena-Belandia, I., Baldwin, J. M., Schuldiner, S., & Tate, C. G. (2003). Three-dimensional structure of the bacterial multidrug transporter EmrE shows it is an asymmetric homodimer. *EMBO J, 22*(23), 6175-6181.

Ullrich, K. J. (1994). Specificity of transporters for 'organic anions' and 'organic cations' in the kidney. *Biochim Biophys Acta, 1197*(1), 45-62.

Vasquez, V., Sotomayor, M., Cordero-Morales, J., Schulten, K., & Perozo, E. (2008). A structural mechanism for MscS gating in lipid bilayers. *Science, 321*(5893), 1210-1214.

Vasquez, V., Sotomayor, M., Cortes, D. M., Roux, B., Schulten, K., & Perozo, E. (2008). Three-dimensional architecture of membrane-embedded MscS in the closed conformation. *J Mol Biol, 378*(1), 55-70.

Ward, A., Reyes, C. L., Yu, J., Roth, C. B., & Chang, G. (2007). Flexibility in the ABC transporter MsbA: Alternating access with a twist. *Proc Natl Acad Sci U S A, 104*(48), 19005-19010.

Weinglass, A. B., Smirnova, I. N., & Kaback, H. R. (2001). Engineering conformational flexibility in the lactose permease of Escherichia coli: use of glycine-scanning mutagenesis to rescue mutant Glu325-->Asp. *Biochemistry, 40*(3), 769-776.

Weinglass, A. B., Soskine, M., Vazquez-Ibar, J. L., Whitelegge, J. P., Faull, K. F., Kaback, H. R., et al. (2005). Exploring the role of a unique carboxyl residue in EmrE by mass spectrometry. *J Biol Chem, 280*(9), 7487-7492.

Weiss, M. S., & Schulz, G. E. (1992). Structure of porin refined at 1.8 A resolution. *J Mol Biol, 227*(2), 493-509.

White, S. H., & Wimley, W. C. (1999). Membrane protein folding and stability: physical principles. *Annu Rev Biophys Biomol Struct, 28*, 319-365.

Yerushalmi, H., Lebendiker, M., & Schuldiner, S. (1995). EmrE, an Escherichia coli 12-kDa multidrug transporter, exchanges toxic cations and H+ and is soluble in organic solvents. *J Biol Chem, 270*(12), 6856-6863.

Yerushalmi, H., Lebendiker, M., & Schuldiner, S. (1996). Negative dominance studies demonstrate the oligomeric structure of EmrE, a multidrug antiporter from Escherichia coli. *J Biol Chem, 271*(49), 31044-31048.

Yerushalmi, H., Mordoch, S. S., & Schuldiner, S. (2001). A single carboxyl mutant of the multidrug transporter EmrE is fully functional. *J Biol Chem, 276*(16), 12744-12748.

Yerushalmi, H., & Schuldiner, S. (2000a). A common binding site for substrates and protons in EmrE, an ion-coupled multidrug transporter. *FEBS Lett, 476*(1-2), 93-97.

Yerushalmi, H., & Schuldiner, S. (2000b). An essential glutamyl residue in EmrE, a multidrug antiporter from Escherichia coli. *J Biol Chem, 275*(8), 5264-5269.

Yin, Y., He, X., Szewczyk, P., Nguyen, T., & Chang, G. (2006). Structure of the multidrug transporter EmrD from Escherichia coli. *Science, 312*(5774), 741-744.

Zacharias, N., & Dougherty, D. A. (2002). Cation-pi interactions in ligand recognition and catalysis. *Trends Pharmacol Sci, 23*(6), 281-287.

Zgurskaya, H. I., & Nikaido, H. (1999). AcrA is a highly asymmetric protein capable of spanning the periplasm. *J Mol Biol, 285*(1), 409-420.

Zhang, L., Sato, Y., Hessa, T., von Heijne, G., Lee, J. K., Kodama, I., et al. (2007). Contribution of hydrophobic and electrostatic interactions to the membrane integration of the Shaker K+ channel voltage sensor domain. *Proc Natl Acad Sci U S A, 104*(20), 8263-8268.

Zhang, Z., Ma, C., Pornillos, O., Xiu, X., Chang, G., & Saier, M. H., Jr. (2007). Functional characterization of the heterooligomeric EbrAB multidrug efflux transporter of Bacillus subtilis. *Biochemistry, 46*(17), 5218-5225.

Zheleznova, E. E., Markham, P. N., Neyfakh, A. A., & Brennan, R. G. (1999). Structural basis of multidrug recognition by BmrR, a transcription activator of a multidrug transporter. *Cell, 96*(3), 353-362.

Zhou, Y., Guan, L., Freites, J. A., & Kaback, H. R. (2008). Opening and closing of the periplasmic gate in lactose permease. *Proc Natl Acad Sci U S A, 105*(10), 3774-3778.

Zou, P., & McHaourab, H. S. (2009). Alternating access of the putative substrate-binding chamber in the ABC transporter MsbA. *J Mol Biol, 393*(3), 574-585.